Dennis Trebbels

Broadband Measurement Techniques for Impedance Spectroscopy- and Time Domain Reflectometry Applications

Cuvillier Verlag Göttingen
Internationaler wissenschaftlicher Fachverlag

Dieses Werk ist copyrightgeschützt und darf in keiner Form vervielfältigt werden noch an Dritte weitergegeben werden.
Es gilt nur für den persönlichen Gebrauch.

Broadband Measurement Techniques for Impedance Spectroscopy- and Time Domain Reflectometry Applications

Dissertation
zur Erlangung des Doktorgrades der Technischen Fakultät der
Albert-Ludwigs-Universität Freiburg im Breisgau

vorgelegt von
Dennis Trebbels

Freiburg im Breisgau 2012

Dieses Werk ist copyrightgeschützt und darf in keiner Form vervielfältigt werden noch an Dritte weitergegeben werden.
Es gilt nur für den persönlichen Gebrauch.

Bibliografische Information der Deutschen Nationalbibliothek
Die Deutsche Nationalbibliothek verzeichnet diese Publikation in der Deutschen Nationalbibliographie; detaillierte bibliographische Daten sind im Internet über http://dnb.d-nb.de abrufbar.
1. Aufl. - Göttingen: Cuvillier, 2013
Zugl.: Freiburg im Breisgau, Univ., Diss., 2012

978-3-95404-360-6

Dekan

Prof. Dr. Yiannos Manoli

Referenten

Prof. Dr. Roland Zengerle
Prof. Dr. Yiannos Manoli

Tag der Prüfung

12.02.2013

Dennis Trebbels
HSG-IMIT
Wilhelm-Schickard-Str. 10
78052 Villingen-Schwenningen

© CUVILLIER VERLAG, Göttingen 2013
Nonnenstieg 8, 37075 Göttingen
Telefon: 0551-54724-0
Telefax: 0551-54724-21
www.cuvillier.de

Alle Rechte vorbehalten. Ohne ausdrückliche Genehmigung des Verlages ist es nicht gestattet, das Buch oder Teile daraus auf fotomechanischem Weg (Fotokopie, Mikrokopie) zu vervielfältigen.
1. Auflage 2013
Gedruckt auf säurefreiem Papier.

978-3-95404-360-6

Dieses Werk ist copyrightgeschützt und darf in keiner Form vervielfältigt werden noch an Dritte weitergegeben werden.
Es gilt nur für den persönlichen Gebrauch.

Contents

Dieses Werk ist copyrightgeschützt und darf in keiner Form vervielfältigt werden noch an Dritte weitergegeben werden.
Es gilt nur für den persönlichen Gebrauch.

Dieses Werk ist copyrightgeschützt und darf in keiner Form vervielfältigt werden noch an Dritte weitergegeben werden.
Es gilt nur für den persönlichen Gebrauch.

List of Figures

Dieses Werk ist copyrightgeschützt und darf in keiner Form vervielfältigt werden noch an Dritte weitergegeben werden.
Es gilt nur für den persönlichen Gebrauch.

Dieses Werk ist copyrightgeschützt und darf in keiner Form vervielfältigt werden noch an Dritte weitergegeben werden.
Es gilt nur für den persönlichen Gebrauch.

Dieses Werk ist copyrightgeschützt und darf in keiner Form vervielfältigt werden noch an Dritte weitergegeben werden.
Es gilt nur für den persönlichen Gebrauch.

Dieses Werk ist copyrightgeschützt und darf in keiner Form vervielfältigt werden noch an Dritte weitergegeben werden.
Es gilt nur für den persönlichen Gebrauch.

List of Publications

Peer-reviewed journal papers

1. D. Trebbels, F. Fellhauer, M. Jugl, G. Haimerl, M. Min, R. Zengerle; **On-line Tissue Discrimination for Transcutaneous Needle Guidance Applications Using Broadband Impedance Spectroscopy** IEEE Transactions on Biomedical Engineering, VOL. 59, NO 2, pp. 494-503, February 2012

2. D. Trebbels, A. Kern, F. Fellhauer, C. Huebner, R. Zengerle; **Miniaturized high resolution FPGA based Time Domain Reflectometer** IEEE Transactions on Instrumentation and Measurement, accepted for publication, October 2012

3. D. Trebbels, R. Zengerle; **Capacitive On-line Hematocrit Measurement in Extracorporeal Circuits** IEEE Transactions on Biomedical Engineering, submitted July 2012

4. M. Min, R. Land, T. Paavle, T. Parve, P. Annus, D. Trebbels; **Broadband spectroscopy of dynamic impedances with short chirp pulses** Physiological Measurement, Vol 32, Number 7, July 2011, pp. 945-958.

Peer-reviewed conference publications

1. D. Trebbels, R. Zengerle, D. Hradetzky; **Concepts for Non-Contact Hematocrit Measurement based on high precision Impedance Spectroscopy at low cost** ISEMA 2009, 8th International Conference on Electromagnetic Wave Interaction with Water and Moist Substances, Conference Proceedings, pp. 183-189, Helsinki, June 1-5, 2009

2. D. Trebbels, R. Zengerle, D. Hradetzky; **Hematocrit Measurement - A high precision on-line measurement system based on impedance spectroscopy for use in hemodialysis machines** World Congress 2009, 11th International Congress of the IUPESM Medical Physics and Biomedical Engineering, IFMBE Proceedings 25/VII, pp. 247-250, Munich, September 7-12, 2009

Dieses Werk ist copyrightgeschützt und darf in keiner Form vervielfältigt werden noch an Dritte weitergegeben werden.
Es gilt nur für den persönlichen Gebrauch.

3. D. Trebbels, D. Hradetzky, R. Zengerle; **Capacitive on-line hematocrit sensor design based on Impedance Spectroscopy for use in hemodialysis machines** IEEE EMBC 2009, 31st Annual International Conference of the IEEE EMBS, pp. 1208-1211, Minneapolis/USA, September 3-6, 2009

4. D. Trebbels, D. Woelki, R. Zengerle; **High Precision Phase Measurement Technique for Cell Impedance Spectroscopy**, ICEBI 2010, 14th International Conference on Electrical Bioimpedance, Journal of Physics: Conference Series 224 (2010) 012159, Gainesville/Florida, April 4-8, 2010

5. D. Trebbels, M. Jugl, R. Zengerle; **Real-Time Cannula Navigation in Biological Tissue with high temporal and spatial resolution based on Impedance Spectroscopy**, IEEE EMBC 2010, 32nd Annual International Conference of the IEEE EMBS, pp. 1886-1889, Buenos Aires, August 31-September 4, 2010

6. D. Trebbels, C. Huebner, R. Becker, R. Zengerle; **Digital low-cost Time Domain Reflectometer Circuit optimized for use in Field Applications**, AQUAMETRY 2010, 1st European Conference on Moisture Measurement, Conference Proceedings, pp. 174-181, Weimar, October 5-7, 2010

7. D. Trebbels, M. Jugl, R. Zengerle; **Impedance Spectroscopy based Tissue Classification for the Navigation of a Cannula during Vessel Puncture**, BMT 2010, 44th DGBMT Jahrestagung, Biomed Tech 2010, 55 (Suppl. 1), Rostock, October 5-8, 2010

8. D. Trebbels, F. Fellhauer, C. Huebner, R. Zengerle; **Miniaturized TDR-meter for large scale Field Experiments** ISEMA 2011, 9th International Conference on Electromagnetic Wave Interaction with Water and Moist Substances, Conference Proceedings, Kansas City, May 31 - June 3, 2011

9. D. Trebbels, M. Jugl, R. Zengerle; **Fluid Compartment Estimation in Dialysis Patients by use of regional and continuous Bioimpedance Spectroscopy**, BMT 2011, 45th DGBMT Jahrestagung, Freiburg, September 27-30, 2011

10. T. Paavle, M. Min, D. Trebbels; **Low-Energy Chirps for Bioimpedance Measurement** IEEE TSP2011, 34th International Conference on Telecommunications and Signal Processing, Budapest, August 18-20, 2011

Dieses Werk ist copyrightgeschützt und darf in keiner Form vervielfältigt werden noch an Dritte weitergegeben werden.
Es gilt nur für den persönlichen Gebrauch.

Peer-reviewed workshops and symposia contributions

1. D. Trebbels, M. Jugl, D. Anselmi, R. Zengerle; **Miniaturized low-cost Time-Domain-Reflectometer circuit for wideband impedance spectroscopy measurement applications**, IWIS 2010, 3rd International Workshop on Impedance Spectroscopy, Chemnitz, October 13-15, 2010

2. D. Trebbels, M. Jugl, D. Anselmi, R. Zengerle; **Digital chirp signal processing for broadband impedance spectroscopy - practical considerations for fast measurements**, IWIS 2010, 3rd International Workshop on Impedance Spectroscopy, Chemnitz, October 13-15, 2010

3. D. Trebbels, M. Jugl, D. Anselmi, R. Zengerle; **Biological tissue classification for needle guidance - a fast impedance measurement method based on chirp signals**, IWIS 2010, 3rd International Workshop on Impedance Spectroscopy, Chemnitz, October 13-15, 2010

4. D. Trebbels, M. Jugl, R. Zengerle; **Impedanzspektroskopie mittels Zeitbereichsreflektometrie: Einsatz des Delta-Modulations-Verfahrens zur Realisierung effizienter Messelektronik**, 15. Heiligenstaedter Kolloquium, Technische Systeme fuer die Lebenswissenschaften, Heilbad Heiligenstadt, September 27-29, 2010

5. D. Trebbels, M. Min; **Fast FPGA based Chirp Signal Processing for Broadband Impedance Estimation**, IWIS 2011, 4th International Workshop on Impedance Spectroscopy, Chemnitz, September 28-30, 2011

6. D. Trebbels, F. Fellhauer, C. Huebner, R. Zengerle; **Miniaturized self contained Spatial-TDR Field Measurement System**, IWIS 2011, 4th International Workshop on Impedance Spectroscopy, Chemnitz, September 28-30, 2011

Patent applications related to this doctoral thesis

1. D. Trebbels, M. Jugl, R. Zengerle; **Vorrichtung und Verfahren zur elektrischen und dielelektrischen Charakterisierung von biologischen Materialien unter Verwendung einer Reflexionsmessung**; DE102010039797

2. D. Trebbels, M. Jugl, R. Zengerle; **Vorrichtung und Verfahren zur elektrischen und dielektrischen Charakterisierung von biologischen Materialien unter Verwendung eines Chirp- oder MLS-Signals** ; DE102010039790

Dieses Werk ist copyrightgeschützt und darf in keiner Form vervielfältigt werden noch an Dritte weitergegeben werden.
Es gilt nur für den persönlichen Gebrauch.

Dieses Werk ist copyrightgeschützt und darf in keiner Form vervielfältigt werden noch an Dritte weitergegeben werden.
Es gilt nur für den persönlichen Gebrauch.

Zusammenfassung

Die vorliegende Arbeit beschäftigt sich mit der Anwendung der breitbandigen elektrischen Impedanzmessung, häufig auch Impedanzspektroskopie genannt, sowie verwandten breitbandigen Messmethoden wie der Zeitbereichsreflektometrie. Breitbandige Messungen der komplexen elektrischen Impedanz einer Probe werden bereits seit rund einem Jahrhundert erfolgreich eingesetzt, um charakteristische frequenzabhängige elektrische und dielektrische Materialeigenschaften zu ermitteln. Anhand gewonnener Messdaten und mittels geeigneter Auswerteverfahren und Modelle kann in vielen Fällen eine Aussage über den Zustand der Probe gemacht werden. Das potentielle Anwendungsgebiet der Impedanzspektroskopie und der verwandten Zeitbereichsreflektometrie umfasst fast alle Bereiche des täglichen Lebens und reicht von medizinischen, biologischen und chemischen Anwendungen über KFZ-, Industrie- und Umweltmesstechnik bis hin zur Pharmazie und Lebensmittelanalyse. Obwohl dieses Forschungs- und Arbeitsgebiet bereits seit langem bekannt ist und unzählige Publikationen existieren, gibt es bis heute vergleichsweise wenige technische Realisierungen in Form von Produkten. Ein Grossteil der publizierten Forschungs- und Entwicklungsarbeiten behandelt theoretische Grundlagen und weist die prinzipielle Machbarkeit in einer Vielzahl unterschiedlicher Anwendungen nach. In vielen Fällen ist zu beobachten, dass die bereits publizierten Ergebnisse auf der Basis von Laborversuchen mittels teurer und aufwendiger Labormesstechnik beruhen. Ein Nachweis der prinzipiellen Anwendbarkeit der Messmethode ist damit meist zwar geführt, zu einer Umsetzung in Form eines real nutzbaren Produktes kommt es jedoch in vielen Fällen aufgrund der hohen Kosten nicht. Neben den zahlreichen bereits untersuchten Anwendungsfällen gibt es auch immer noch viele Aufgaben- und Problemstellungen, die sich zwar mit Hilfe breitbandiger Messverfahren prinzipiell lösen lassen, aber noch nicht bzw. nicht ausreichend untersucht wurden. Viele dieser noch nicht untersuchten Anwendungsgebiete befinden sich in Marktsegmenten, die zusätzliche oder spezielle Anforderungen an entsprechende Produkte stellen wie z.B. eine miniaturisierte Bauform, energieeffizientes und batteriebetriebenes Messen und nicht zu letzt niedrige Kosten.

Die vorliegende Arbeit ist inhaltlich in zwei Teile gegliedert. Im ersten Teil beschäftigt sie sich mit der ausführlichen Untersuchung von drei praktischen Aufgabenstellungen. Zwei davon aus dem Bereich der Medizintechnik sowie eine weitere aus dem Bereich Feuchtemesstechnik. Im zweiten Teil der Arbeit werden neu entwickelte universelle elektronische Schaltungskonzepte und Messkonzepte erläutert, mit denen es möglich ist die untersuchten Anwendungen kostengünstig in reale Produkte zu überführen.

In der ersten medizintechnischen Anwendung wird ein kapazitiver Sensor entwickelt, der basierend auf Impedanzmessungen in der Lage ist, den Hämatokritwert (HCT) von Blut zu bestimmen. Besonderheit dieses Sensors ist, dass er in bestehenden Systemen mit extrakorporalen Blutkreisläufen von aussen an einem Schlauch angebracht werden kann, ohne direkten Kontakt zum Blut zu haben. Mit dem neu entwickelten Sensor wurde im Labor eine Messgenauigkeit von 4 % HCT erreicht bei einer Auflösung von etwa 0,1 % HCT. In der zweiten untersuchten medizintechnischen Anwendung wird biologisches Gewebe an der Spitze einer Kanüle während des dynamischen Einstechvorgangs impedanzspektroskopisch analysiert und klassifiziert. Dies ermöglicht eine genaue Positionierung der Kanülenspitze in einem bestimmten Zielgewebe mit minimalem technischem Auf-

Dieses Werk ist copyrightgeschützt und darf in keiner Form vervielfältigt werden noch an Dritte weitergegeben werden.
Es gilt nur für den persönlichen Gebrauch.

wand. Durch die Verwendung eines koaxialen Kanülenaufbaus wird eine hohe örtliche Auflösung erreicht die in etwa dem Durchmesser der Kanüle entspricht. Der Einsatz von kurzen Chirp-Signalen als Messsignal ermöglicht eine Gewebeerkennung innerhalb einer Mess- und Auswertezeit von unterhalb einer Millisekunde. Die dritte untersuchte Anwendung kommt aus dem Bereich der Feuchtemesstechnik. Hier wird mithilfe der Zeitbereichsreflektometrie eine ortsaufgelöste Erkennung des Wasserstandes von Grundwasser bzw. die Erkennung von eindringendem Fremdwasser in Gebäude realisiert. Die entwickelte Messelektronik ermöglicht durch den Einsatz geeigneter Abtast- und Auswerteverfahren eine Detektion von Wasser entlang der verwendeten Messleitung mit einer örtlichen Auflösung im Bereich weniger Millimeter und einer Genauigkeit von etwa +/- 3 cm.

Durch den universellen und modularen Aufbau und Charakter der entwickelten Elektroniken eignen sich diese darüber hinaus hervorragend auch zur Lösung weiterer messtechnischer Aufgaben in verwandten Themengebieten. Ziel der Schaltungsentwicklungen ist es, den Platzbedarf, die Stromaufnahme und die Kosten gegenüber dem aktuellen Stand der Messtechnik deutlich zu senken, so dass sich basierend auf den entwickelten Prototypen leicht anwendungsspezifische Produkte realisieren lassen. Obwohl die breitbandige Impedanzmesstechnik kein neues wissenschaftliches Arbeitsgebiet ist, herrscht derzeit immer noch ein grosser Mangel an miniaturisierter und kostengünstiger Messtechnik. In den letzten Jahren gab es jedoch insbesondere im Bereich der programmierbaren bzw. konfigurierbaren digitalen Logikschaltungen einigen technischen Fortschritt, so dass heute extrem leistungsfähige Bausteine zu sehr geringen Kosten zur Verfügung stehen. Die in dieser Arbeit entwickelten Schaltungskonzepte basieren auf dem Einsatz solcher programmierbarer Logikschaltungen. Die technischen Moglichkeiten der verwendeten Bausteine werden genutzt in Verbindung mit geeigneten Messsignalen und Abtastprinzipien. Als Ergebnis dieser Arbeit stehen zwei unterschiedliche Plattformen zur Verfügung. Die erste Plattform ist optimiert für statische Anwendungen, in denen die Messdauer ein unkritischer Parameter ist, jedoch hohe Anforderungen an die (virtuelle) zeitliche Auflösung des gemessenen Signals gestellt werden. Das technische Abtastprinzip dieser Plattform basiert auf dem Verfahren der Unterabtastung eines periodischen Messsignals, wobei zur Abtastung eine digitale Variante eines Delta-Modulators verwendet wird. Die zweite entwickelte Plattform ist optimiert für dynamische Anwendungen, bei denen die benötigte Messdauer zur Aufnahme eines komplexen Impedanzspektrums ein kritischer Parameter ist. Aufgrund der hervorragenden Skalierbarkeit in Bezug auf Signaldauer, Signalamplitude und Signalbandbreite sowie der Möglichkeit einer sehr schnellen digitalen Verarbeitung der abgetasteten Signale in Hardware werden hier Chirp-Signale als Messsignale eingesetzt.

Basierend auf den messtechnischen Überlegungen wurden jeweils Prototypen - Schaltungen aufgebaut und erfolgreich getestet. Die Plattform zur Messung mit virtuell sehr hoher zeitlicher Auflösung wurde zusätzlich im Rahmen eines Projektes mit der University of Queensland, Brisbane, Australien, weiterentwickelt zu einem miniaturisierten hochauflösenden Zeitbereichsreflektometer. Derzeit werden in Pilotstudien in der Nähe von Brisbane 20 dieser Geräte genutzt zur ortsaufgelösten Messung des Grundwasserpegels. Weitere 20 Geräte wurden in Kooperation mit der TU Darmstadt modifiziert und werden erfolgreich in der Gebäudetechnik zur Feuchtemessung eingesetzt.

Dieses Werk ist copyrightgeschützt und darf in keiner Form vervielfältigt werden noch an Dritte weitergegeben werden.
Es gilt nur für den persönlichen Gebrauch.

Abstract

The following thesis focuses on the application of broadband impedance measurements, often referred to as impedance spectroscopy, as well as similar measurement methods such as Time Domain Reflectometry (TDR). Broadband complex impedance measurements of a sample have been successfully conducted since about a century for obtaining characteristic frequency dependent electric and dielectric material properties. The condition of a sample can be determined based on measured data as well as suitable data processing methods and models. Potential practical applications for impedance spectroscopy are widely found in almost all areas of the daily life and include medical, biological, chemical, automotive, industrial, environmental, pharmaceutical and food quality applications. Although impedance spectroscopy is a well known scientific field with a huge amount of existing publications, there are only few real products based on this technology available today. Most scientific publications elaborate on the theoretical background and demonstrate the applicability of the method within many different applications. In most cases it can be observed that presented research results are based on measurements which have been conducted with expensive state-of-the-art laboratory equipment. The suitability of the impedance spectroscopy method is proven in many cases but mostly there is no resulting product available due to the high cost of the measurement equipment. In addition to the already studied applications there are still a lot of applications and problems where impedance spectroscopy could be used but which are not or not fully investigated yet. Many of these applications can be found in market segments where additional requirements exist such as miniaturization, low-power and battery operation and last but not least low cost.

The content of the following thesis is subdivided into two parts. The first part is about the detailed analysis of three practical measurement applications. Two applications belong to the field of biomedical engineering and the third application belongs to the field of moisture measurement. Within the second part of this thesis new developed circuits and measurement concepts are presented. Based on these new concepts it is possible to implement cost sensitive real products for the investigated applications.

Within the first medical application a capacitive sensor is developed which is able to determine the hematocrit value (HCT) of a blood sample based on impedance measurements. This sensor can be attached to standard plastic tubing in existing machines with an extracorporeal blood circulation system without the need for a direct contact with the blood. Laboratory experiments with the new developed sensor show an accuracy of approximately 4 % HCT and a resolution of approximately 0,1 %. Within the second investigated medical application the biological tissue which is close to the tip of a needle is continuously analysed during the dynamic insertion process and based on the obtained impedance data the tissue type is classified. This allows for positioning the tip of a needle or cannula within a well defined target tissue type with a minimum technical effort. By using a coaxial cannula design the achieved high spatial resolution is in the range of the diameter of the cannula. Short chirp signals are used as measurement signals and allow for a short measurement and processing time of below 1 ms for recognizing a tissue type. The third investigated application is in the field of moisture measurement. Here a water

Dieses Werk ist copyrightgeschützt und darf in keiner Form vervielfältigt werden noch an Dritte weitergegeben werden.
Es gilt nur für den persönlichen Gebrauch.

detection system with spatial resolution along a transmission line is implemented which allows for groundwater level monitoring and detection of penetrating water in buildings.

The second part of the thesis deals with the development of suitable electronic measurement equipment and circuits which cover the requirements given by the previously studied applications. Goal of the development is to dramatically reduce the size, the power consumption and the cost compared to existing standard measurement devices. In combination with the flexible design of the developed circuits and systems this allows for implementing real products in similar other applications as well. In spite of the fact that broadband impedance measurement is not a new field of work, there is still a lack of available miniaturized and cheap measurement equipment. However, in the recent past there was a lot of progress in the field of programmable and reconfigurable digital hardware. Today there are very cheap but powerful logic components available. The measurement circuits developed within this thesis are based on such programmable logic components. The technical benefits of these components are used in conjunction with suitable measurement signals and sampling methods. As a result of this thesis there are two independent platforms available. One platform is optimized for static applications where the total acquisition time is of minor importance but the requirements for a (virtual) very high temporal resolutions are present. In this case the employed sampling concept is conventional undersampling of a periodic measurement signal. The sampling system itself is based on a digital variation of a delta modulator circuit. The second developed measurement platform is optimized for dynamic applications where the required acquisition time for obtaining an impedance spectrum is a critical parameter. Chirp signals are used due to the excellent scalability with respect to signal duration, signal amplitude and signal bandwidth as well as the option for fast digital hardware signal processing.

Prototype circuits have been constructed and successfully tested based on the two developed measurement concepts. In addition the first platform which employs the undersampling scheme is used within a research project in cooperation with the University of Queensland, Brisbane, Australia. The platform is modified and used for soil moisture measurements based on the Time-Domain-Reflectometry (TDR) principle. Currently 20 TDR-meter devices are installed near Brisbane, Australia within a ground water monitoring experiment. Another 20 TDR-meter prototype devices have been built in cooperation with the University of Darmstadt and are used for water detection and moisture measurement in buildings.

Dieses Werk ist copyrightgeschützt und darf in keiner Form vervielfältigt werden noch an Dritte weitergegeben werden.
Es gilt nur für den persönlichen Gebrauch.

1 Introduction

Broadband electrical impedance measurement, often referred to as impedance spectroscopy (IS), is a well known method for characterizing the electric and dielectric properties of a material under test (MUT). This method applies an alternating voltage signal or current signal via electrodes to the MUT and monitors the system response which is the resulting current through the MUT or the developed voltage across the MUT. The frequency of the excitation signal is varied within a defined frequency window. The response of the MUT is typically a complex function which results in a characteristic amplitude and phase shift of the flowing current with respect to the signal voltage. An application specific analysis and interpretation of the measured complex impedance transfer function can give valuable information about the state of the MUT. Often model based analysis methods are found which usually try to explain and describe the transfer function by physical properties of the MUT and associated additional side effects caused e.g. by measurement electrode polarization, stray capacitances or long measurement cables.

Impedance spectroscopy is used in almost all scientific and technical fields within a frequency range from below 1 Hz up to several ten GHz. Applications include battery and fuel cell analysis [1], analysis of organic and inorganic chemical substances [2, 3] and electrochemical systems [4, 5], characterization of electrical machines, drives and transformers [6–9], microfluidic applications [10, 11], soil moisture measurement [12–16], flow sensors [17, 18], infrastructure and construction monitoring [19, 20], characterization of organic and inorganic semiconductors [21], readout of piezo sensors [22], biological tissue analysis [23, 24] food and drug analysis and quality monitoring [25], biosensors [26] and moisture measurement of granular materials [27]. The given list is not complete but shows that impedance spectroscopy is a powerful tool in many applications.

A more detailed analysis of the above listed applications shows, that each application has specific requirements for the impedance measurement. Measurement parameters such as the bandwidth of the excited measurement signal, measurement signal amplitude and signal duration must be adjusted to fulfil the specific needs. For applying the measurement signal to the MUT and for recording the system response it is usually required to either attach electrodes to the MUT or installing the MUT inside a defined test cell such as e.g. a parallel plate capacitor. Depending on the properties of the MUT and the used measurement setup measurement errors will occur and must be taken into account. The following sections within the first chapter describe the physical basics of broadband impedance measurement, impedance spectra representation, different types of measurement signals, suitable measurement equipment and typical electrode configurations. Last but not least an overview about current activities and advances in electronic measurement equipment dedicated for impedance spectroscopy is presented. Although several interesting measurement concepts have been introduced within the last decades, there is still a lack of simple, small and efficient electronic measurement solutions which could be used in a real product outside the laboratory.

Dieses Werk ist copyrightgeschützt und darf in keiner Form vervielfältigt werden noch an Dritte weitergegeben werden.
Es gilt nur für den persönlichen Gebrauch.

1.1 Impedance Basics

Most materials can be characterized by analysing their frequency dependent electric and dielectric properties. The measured values are a function of the sample geometry and the individual characteristic material properties. In the field of impedance spectroscopy there are two effects which are measured and analysed when a voltage signal is applied to a sample and a current flows through the sample. The first effect are losses in the material which always occur when a current is flowing. The second effect is the capability of the material to store energy. Usually the losses are described by a material specific characteristic conductivity which results in an effective conductance for a given geometry. The capability of storing energy is usually described by the (relative) permittivity of the material. Each material has a characteristic permittivity which leads to a measured capacitance when a sample of a defined geometry is placed between electrodes such as e.g. a parallel plate capacitor. Figure 1.1 A illustrates an often found model for a material placed between two parallel plates which serve as electrodes. The size A of the electrodes

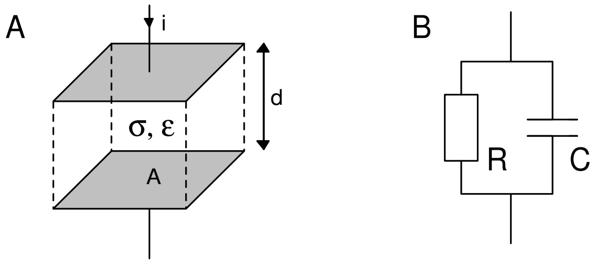

Figure 1.1: A: Model of a typically used test cell geometry for measuring material specific properties such as conductivity σ and permittivity ε. B: Equivalent electrical schematic describing the test cell with a lossy material between the electrodes.

$$G = \frac{\sigma * A}{d} \tag{1.1}$$

$$C = \frac{\varepsilon_0 * \varepsilon_r * A}{d} \tag{1.2}$$

$$R = \frac{1}{G} \tag{1.3}$$

In the scientific literature it is common to express the two material properties "conductivity" and "permittivity" by either a complex conductivity $\underline{\sigma}$ or by a complex permittivity $\underline{\varepsilon}$. The definition for complex conductivity is given by equation 1.4 and the

Dieses Werk ist copyrightgeschützt und darf in keiner Form vervielfältigt werden noch an Dritte weitergegeben werden.
Es gilt nur für den persönlichen Gebrauch.

definition for complex permittivity is given by 1.5. If the complex conductivity is used the real part represents the losses in the material and the imaginary part represents all energy storage effects. If the complex permittivity is used the real part represents all energy storage effects and the imaginary part represents all losses in the material. Both notations can be used to express complex material properties. The relationship between the complex conductivity and the complex permittivity is given by equation 1.6 [3].

$$\underline{\sigma} = \sigma' + j\sigma'' \tag{1.4}$$

$$\underline{\varepsilon_r} = \varepsilon_r' + j\varepsilon_r'' \tag{1.5}$$

$$\underline{\sigma} = j\omega\varepsilon_0\underline{\varepsilon_r} \tag{1.6}$$

The resulting relationship between the four variables is given by equations 1.7 and 1.8. A comprehensive derivation of the presented equations can be found in [3].

$$\sigma'' = \omega\varepsilon_0\varepsilon_r' \tag{1.7}$$

$$\varepsilon_0\varepsilon_r'' = \frac{\sigma'}{\omega} \tag{1.8}$$

If a sinusoidal voltage U is applied to the electrodes (equation 1.9) a sinusoidal current I (equation 1.10) will flow through the material. The ratio between the voltage signal amplitude and the resulting current signal amplitude is expressed by the complex impedance $\underline{Z}$ (equation 1.11). Figure 1.2 A illustrates typical sinusoidal voltage and current signals which can be measured over a complex load with a characteristic frequency dependent impedance Z_0 and phase shift $\varPhi$.

$$U = U_0 e^{j(\omega t + \varphi_u)} \tag{1.9}$$

$$I = I_0 e^{j(\omega t + \varphi_i)} \tag{1.10}$$

$$\underline{Z} = \frac{U}{I} = \frac{U_0 e^{j(\omega t + \varphi_u)}}{I_0 e^{j(\omega t + \varphi_i)}} = \frac{U_0}{I_0} * e^{j(\varphi_u - \varphi_i)} = Z_0 e^{j\phi} \tag{1.11}$$

In the field of electrical engineering it is common to express the complex impedance $\underline{Z}$ in terms of a real part R and an imaginary part X (equation 1.12). The imaginary part X is called reactance. Figure 1.2 B shows an often used graphical representation of the complex impedance as a pointer. The length $|\underline{Z}|$of the pointer is given by equation 1.13 and the angle $\varPhi$ is given by equation 1.14. Vice versa the real part R and the imaginary part X can be calculated out of a measured amplitude ratio and a measured phase shift by equations 1.15 and 1.16.

$$\underline{Z} = |\underline{Z}|\, e^{j\varPhi} = Z' + jZ'' = R + jX \tag{1.12}$$

$$|\underline{Z}| = \sqrt{R^2 + X^2} \tag{1.13}$$

$$\varPhi = arctan(\frac{X}{R}) = arctan(\frac{Z''}{Z'}) \tag{1.14}$$

Dieses Werk ist copyrightgeschützt und darf in keiner Form vervielfältigt werden noch an Dritte weitergegeben werden.
Es gilt nur für den persönlichen Gebrauch.

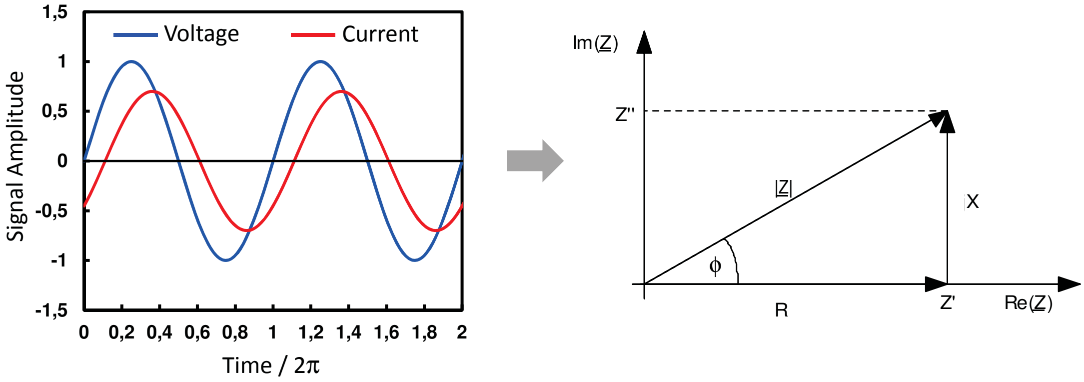

Figure 1.2: Left side: Typical sinusoidal voltage and current signal for a randomly selected complex impedance. A frequency dependent amplitude ratio and phase shift can be observed when varying the frequency. Right side: Representation of the complex impedance in the complex plane as commonly used in the field of electronics. The complex impedance consists of a real part and an imaginary part.

The frequency dependent electric behaviour of the equivalent circuit presented in figure 1.1 B can be calculated by the parallel connection of the capacitor C and the resistor R. For parallel combinations it is often easier to express the overall electric behaviour by the complex admittance $\underline{Y}$ which is the inverse of the complex impedance $\underline{Z}$. Equation 1.17 derives the admittance and equation 1.18 derives the impedance of the equivalent circuit.

$$\underline{Y} = G + j\omega C = \frac{A}{d}(\sigma + j\omega C\varepsilon_0\varepsilon_r) \tag{1.17}$$

$$\underline{Z} = Z' + jZ'' = \frac{1}{\underline{Y}} = R + jX = \frac{G - j\omega C}{G^2 + (\omega C)^2} \tag{1.18}$$

1.2 Impedance Spectra Representation

The measured impedance is a function of the frequency. Thus a plot of the frequency dependent impedance values of a MUT is often referred to as "impedance spectrum". There are several ways for graphically presenting the complex impedance data. In the field of impedance spectroscopy there are typically two types of diagrams found: the Bode Diagram and the Nyquist Diagram. The Bode Diagram of the equivalent electrical schematic is shown in figure 1.3 (left side). There are two plots in the Bode Diagram, one plot shows the modulus and the second plot shows the phase. Modulus and phase can be calculated by equations 1.13 and equation 1.14 when the real part Re($\underline{Z}$) and the imaginary part Im($\underline{Z}$) are known. For the equivalent circuit in figure 1.1 B the real and imaginary parts are given by equations 1.19 and 1.20. Advantage of this representation is the fact that both plots are functions of the frequency and it is intuitive to discover interesting frequency dependent areas within a measured broad frequency

Dieses Werk ist copyrightgeschützt und darf in keiner Form vervielfältigt werden noch an Dritte weitergegeben werden.
Es gilt nur für den persönlichen Gebrauch.

w
a
ir

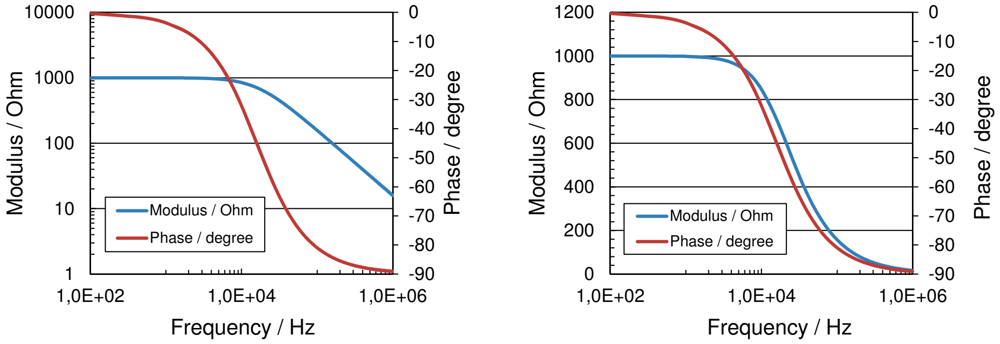

Figure 1.3: Left side: Bode Diagram of a lossy dielectric. Magnitude and phase are plotted against the frequency. Magnitude and frequency axes are logarithmic. Right side: Modified Bode Diagram with linear magnitude axis as sometimes used within this thesis.

$$Re(\underline{Z}) = \frac{\frac{1}{R}}{(\frac{1}{R})^2 + (\omega C)^2} \tag{1.19}$$

$$Im(\underline{Z}) = \frac{-\omega C}{(\frac{1}{R})^2 + (\omega C)^2} \tag{1.20}$$

As an alternative to the Bode Diagram a Nyquist Diagram can be used. In this case the imaginary part Im($\underline{Z}$) of the impedance is plotted against the real part Re($\underline{Z}$) of the impedance as shown in figure 1.4. The characteristic curve of the equivalent schematic shown in figure 1.1 B is a semicircle. Drawback of this representation is the fact that there is no intuitive link to the frequency which belongs to each pair of real and imaginary components. Advantage is that it is possible to obtain the impedance values at a frequency of zero and at infinite frequency by extrapolation of the data practically measured within a limited frequency range. In addition it is relatively easy to discover even small changes in the complex impedance at very low or at very high frequencies. This type (ıpedance spectroscop

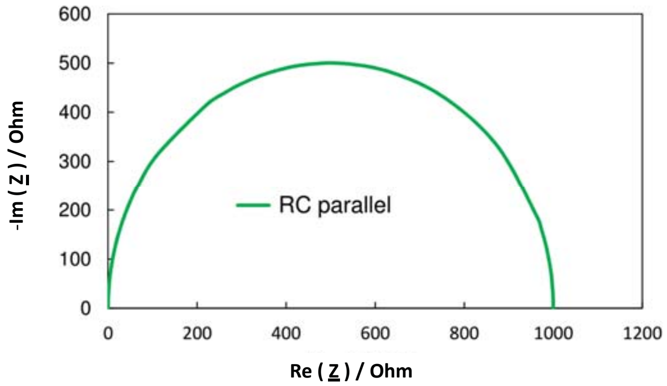

Figure 1.4: Nyquist Diagram of a lossy dielectric. Real part and imaginary part are plotted against each other. Each point of the curve belongs to a defined frequency.

Dieses Werk ist copyrightgeschützt und darf in keiner Form vervielfältigt werden noch an Dritte weitergegeben werden.
Es gilt nur für den persönlichen Gebrauch.

1.3 Broadband Measurement Signals

Goal of the broadband impedance measurement is to derive the frequency dependent complex transfer function of the unknown system formed by the electrodes and the attached test sample. Therefore it is required to apply stimulus signals (e.g. voltage signals or current signals) which contain multiple frequency components inside the band of interest. There are two options for applying multiple frequencies to the unknown MUT: sweeping the signal within a defined frequency range which means hopping from one frequency to the next frequency or alternatively applying a broadband signal which contains multiple frequencies at a time. Sweeping the measurement signal is often referred to as measuring in the "Frequency Domain" and applying a signal which contains multiple frequencies at a time is usually referred to as measuring in the "Time Domain". The following section describes typical signals which are often found in impedance measurement systems. Each signal has its inherent advantages and disadvantages. The choice of the best stimulus signal for a given application depends on several individual boundary parameters such as measurement time, required signal to noise ratio (SNR), achievable bandwidth and last but not least efficient and robust signal processing of the captured raw data.

One of the best known and frequently found measurement signals is the pure sine wave signal. A sinusoidal excitation voltage or current is applied to the MUT. If a passive MUT is measured within a linear range the resulting response signal (either a current or voltage signal) is a sinusoidal signal as well. Both signals can be captured and it is a straight forward way to compute the complex impedance as shown in equations 1.12 to 1.16. After measuring the impedance at one specific frequency it is switched to the next frequency and the measurement cycle is repeated. Great advantage of this method is the high SNR which can be achieved with this method because the whole signal energy is concentrated at a single frequency. Figure 1.5 shows a sine wave signal in time domain (left diagram) and in the frequency domain (right diagram). In addition it is relatively easy to generate a sinusoidal excitation signal and there are lots of analog and digital circuits and signal processing methods for processing sine wave signals with high accuracy. However - drawback of a sine wave sweep is the long measurement time which is required when sweeping over several decades of frequency. It is often not possible to measure for such a long time e.g. when fast applications such as single cell sorting in microfluidic systems have to be processed in real-time. In addition there are systems where the MUT varies with time such as e.g. a heart muscle which is continuously moving. In this thesis the sine wave signal is used for measuring the phase shift with very high accuracy and resolution in a slow medical system. The target application is hematocrit measurement in closed loop blood circulation systems found in dialysis machines. An electronic circuit is developed which can precisely measure within a frequency range of a few Hz up to several MHz.

An often used alternative to a pure sine wave signal is a so called multisine signal. Such a signal consists of multiple sinusoidal signals which are superposed to each other and applied at the same time to the MUT. Figure 1.6 shows such a multisine signal in the time domain (left diagram) and in the frequency domain (right diagram) which consists of five discrete sine wave signals. On the first view it looks attractive to use such a signal since it is straight forward to understand. But there are several drawbacks which often limit the usability within real applications. Major concern is the fact that superposing multiple sinusoidal signals often leads to very high excitation signal amplitudes. Such high amplitudes are difficult to generate and in many cases the MUT does not behave linear when large signal amplitudes are applied. There are several interesting methods

Dieses Werk ist copyrightgeschützt und darf in keiner Form vervielfältigt werden noch an Dritte weitergegeben werden.
Es gilt nur für den persönlichen Gebrauch.

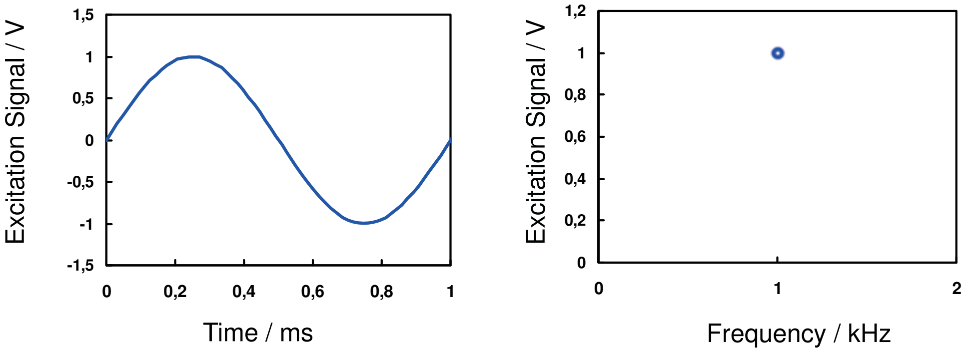

Figure 1.5: Plot of a pure sine wave signal in time domain (left) and frequency domain (right). The whole signal energy is concentrated at one discrete frequency and allows for measuring with an excellent SNR.

and approaches which show how to carefully select the frequencies and which phasing relative to the other frequencies should be used in order to obtain a low overall amplitude of the resulting sum signal [28–31]. These methods work quite well for a low number of frequencies but the problem of optimization becomes very difficult for a larger number of frequencies. A further drawback of the multisine signal is that it is not so easy to generate. If an analog circuit should be used for signal generation then for each frequency component one signal source is required which results in a large overall circuit when a large as a sig lex shap

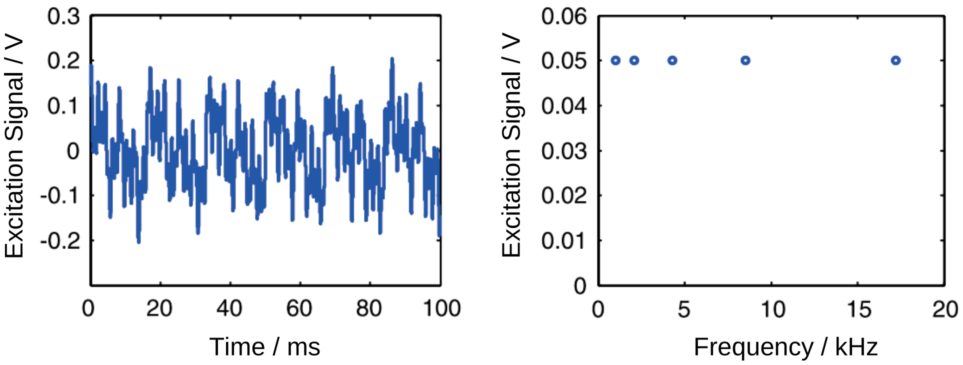

Figure 1.6: Graphical presentation of a multisine signal composed of five discrete sinusoidal signals. The total signal energy is distributed over the five contained discrete frequencies [25].

Another very interesting type of excitation signals with attractive properties is a so called chirp signal. A chirp signal usually is a sinusoidal excitation signal which continuously varies its frequency according to some kind of "ramping function". The most common type of a chirp signal is a linear chirp C(t) which can be expressed by equation 1.21 where A denotes the amplitude, f_0 denotes the initial and f_{fin} denotes the final frequency of the chirp signal and T_{ch} denotes the duration of the chirp signal.

$$C(t) = Asin(2\pi(f_0 t + (f_{fin} - f_0)t^2/2T_{ch}) \tag{1.21}$$

Equation 1.21 shows one of the advantages that a chirp signal has compared to many other broadband signals: its excellent scalability. The parameters f_0 and f_{fin} determine

Dieses Werk ist copyrightgeschützt und darf in keiner Form vervielfältigt werden noch an Dritte weitergegeben werden.
Es gilt nur für den persönlichen Gebrauch.

the bandwidth $B = f_{fin} - f_0$ and can be chosen independent from each other and independent from the remaining parameters such as amplitude and duration. The chirp signal properties can therefore easily be adjusted to the individual requirements given by each application. Figure 1.7 shows a linear chirp signal with a duration of 20 ms and a bandwidth up to 8 kHz. The amplitude spectrum on the right side shows a further advantage of the chirp signal compared to many other signals. The amplitude spectrum is flat which allows for measuring the impedance of the MUT at all covered frequencies with an acceptable SNR. Drawback of the chirp signal is that it is required to have an appropriate high sampling rate for generating the excitation signal and for capturing the response signal. The energy of the chirp signal is spread over the entire bandwidth which of course leads to a lower SNR for each discrete impedance value computed out of the sampled raw data. A detailed overview over chirp signals, modified chirp signals and correspo

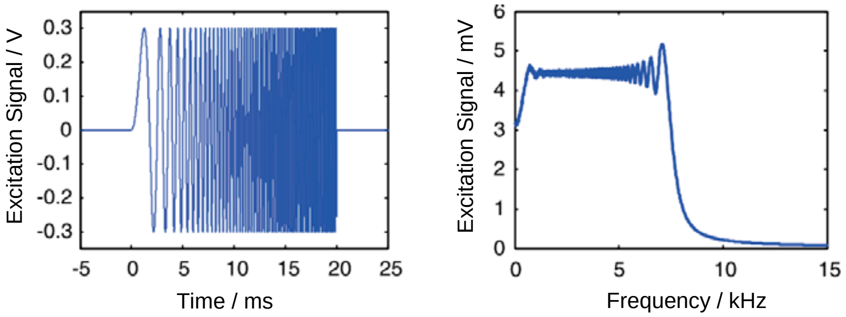

Figure 1.7: Graphical presentation of a linear chirp signal with a duration of 20 ms covering a bandwidth of several kHz. The flat amplitude spectrum shown on the right side allows for measuring at all covered frequencies with an acceptable SNR [25].

Besides sinusoidal signals there are often pulsed signals found in impedance measurement systems. The simplest broadband signal which can be generated is a step pulse signal or a square wave signal as shown in figure 1.8. Such a signal is simple to understand and there are many known and straight forward to implement signal processing methods available. Major drawback of such a pulsed signal is the low amplitude of the higher frequency components which follows a $\frac{sin(x)}{x}$ envelope. For broadband impedance measurement systems which cover a few decades of frequencies this often means a poor SNR for the higher frequency measurement results. However - there are several interesting ways to use the properties of a square wave signal in combination with special "electrodes" e.g. in die field of Time Domain Reflectometry (TDR). Furthermore in some applications it is possible to fit the sampled response signal to a known model of the MUT and achieve a quite good overall measurement result.

Dieses Werk ist copyrightgeschützt und darf in keiner Form vervielfältigt werden noch an Dritte weitergegeben werden.
Es gilt nur für den persönlichen Gebrauch.

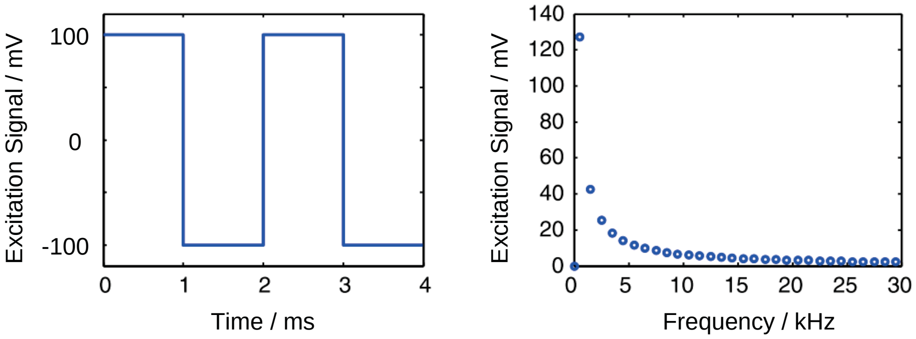

Figure 1.8: Graphical presentation of a square wave signal and its amplitude spectrum. The square wave signal is easy to generate but the decaying amplitude of higher frequency components is a problem in many applications which require a certain SNR [25].

A frequently found and smart method for improving the SNR at higher frequencies is to replace the standard square wave signal by a defined pulse train which follows certain mathematical boundary conditions. The probably best known method is based on so called "Maximum Length Sequence" (MLS) signals. Figure 1.9 shows such a MLS signal and the corresponding amplitude spectrum. On one hand it can be said that the spectrum is not as flat and ideal as it is in the case of a chirp signal. On the other hand the spectrum shows improved signal energy in the higher frequency ranges compared to a standard pulse. A MLS sequence is very easy to generate and processing of the sampl … uch as the " … ls and relate

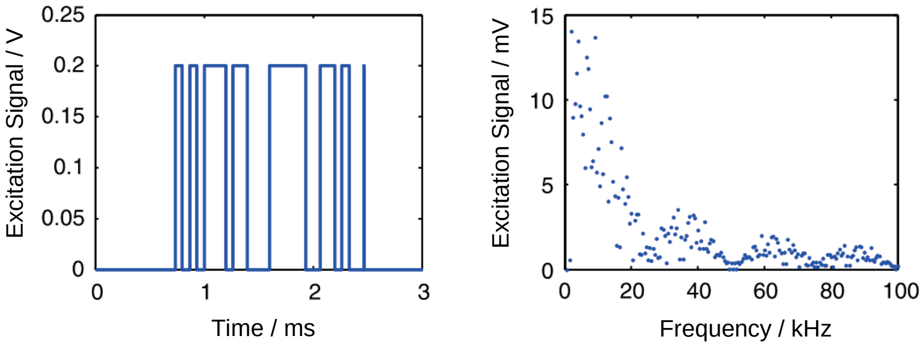

Figure 1.9: Graphical presentation of a Maximum Length Sequence (MLS). The MLS pulse train follows certain mathematical boundary conditions. The resulting amplitude spectrum allows for measuring impedances even at higher frequencies with an improved SNR compared to a simple square wave signal [25].

Dieses Werk ist copyrightgeschützt und darf in keiner Form vervielfältigt werden noch an Dritte weitergegeben werden.
Es gilt nur für den persönlichen Gebrauch.

1.4 Laboratory Measurement Equipment

Usually the target application of interest is investigated and analysed in the laboratory first. Goal of the laboratory measurements is to find interesting characteristic areas within the impedance spectrum which can be analysed according to the applications specific requirements. Here the key component of each measurement setup is a precision laboratory impedance measurement device. There are several manufacturers which offer a broad range of measurement devices optimized for the field of impedance spectroscopy. However, in many cases it is not required to use such (expensive) special equipment if an electronic laboratory is available . There are a few typical devices which are widely found in electronic laboratories and which are ideally suited for first experimental measurements.

One precision type of laboratory impedance measurement devices are so called "LCR-Meters" with programmable measurement frequency. Many devices allow to switch the measurement frequency from a few Hz up to a few MHz. For example this frequency range is ideal for most biological applications. LCR-Meters typically achieve high precision measurement results due to the fact that they operate based on pure sinusoidal excitation signals where the signal energy is concentrated at the selected measurement frequency. Drawback is the long acquisition time which limits the system to be used for static MUTs only. Figure 1.10 A shows one state-of-the-art LCR meter (Agilent E4980A) which is widely used for impedance spectroscopy applications.

Another well known type of impedance measurement devices is a network analyser. Usually they offer a wider bandwidth than LCR-meters and can measure up to a frequency range of several GHz. However - many devices cannot measure in the low frequency range of a few Hz or a few hundred Hz. Figure 1.10 B shows one modern network analyser (Agilent E5061B) which covers an exceptionally wide frequency range from 5
H
re
su

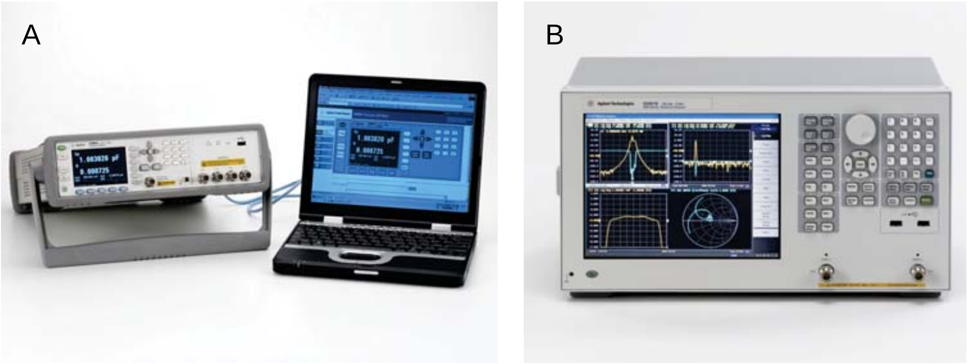

Figure 1.10: State-of-the-Art Laboratory Measurement Equipment for broadband impedance measurement. Figure A shows a precision LCR-Meter for covering a frequency range from 20 Hz to 2 MHz. Figure B shows a modern network analyser covering a frequency range from 5 Hz to 3 GHz. (Reproduced with Permission, Courtesy of Agilent Technologies, Inc.)

Dieses Werk ist copyrightgeschützt und darf in keiner Form vervielfältigt werden noch an Dritte weitergegeben werden.
Es gilt nur für den persönlichen Gebrauch.

1.5 Electrode Configurations and Interfacing

One of the most challenging tasks in the field of Impedance Spectroscopy is to interface the MUT to the electronic measurement device or circuit. On one hand the interface should be as simple as possible, on the other hand the interface and its properties should not interact with the MUT and the measurement procedure. One common method is to directly contact the MUT with a set of at least two electrodes. Usually the electrodes are made out of metal or an alternative conductor or semiconductor. Figure 1.11 A shows such a two-electrode circuit. A current source injects a defined alternating current with adjustable frequency into the MUT. The resulting voltage drop across the MUT which arises from the current flowing through the MUT is measured between the electrodes. In some applications this setup works well, but major drawback is the measurement error caused by a potentially unknown transfer impedance between the surface of the electrode and the surface of the MUT. Especially at low frequencies electrode polarisation may cause significant measurement errors [52–55]. One well known method for compensating for such effects is to use a four-electrode configuration as illustrated in Figure 1.11 B. Here the current is injected via two electrodes similar to the two-electrode configuration. However, the resulting voltage drop across the MUT is measured with separate electrodes which are connected to a high impedance voltage measurement circuit. Any unknown transfer impedance between the electrode surface and the MUT is in series with the very high input impedance of the measurement device and therefore plays no significant role. Drawback of the four-electrode interface is the fact that it might be difficult to attach 4 electrodes with a defined geometry on the surface of the MUT. Especially when the MUT is very small (e.g. single cell analysis) this is a practical limitation.

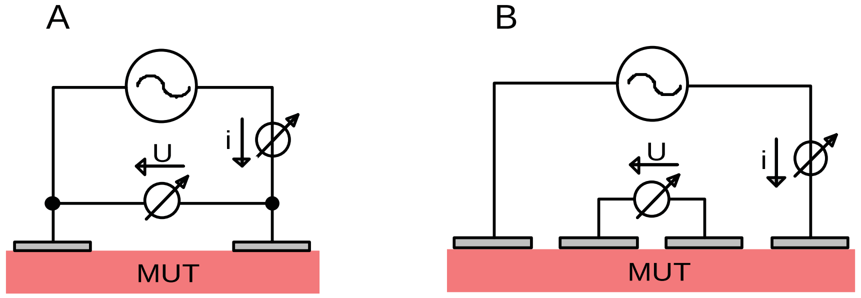

Figure 1.11: One of the best known and widely found methods for interfacing a MUT to a measurement device is to directly attach electrodes. Usually either a two-electrode configuration (A) or a four-electrode configuration (B) is used. The four-electrode interface eliminates major measurement errors caused by a unknown or unstable transfer impedance between the electrode surface and the MUT.

When the losses in the MUT are relatively small and the capability of storing energy is relatively high a capacitive measurement approach is often used. The simplest method is to build a parallel plate capacitor with a well known geometry. The MUT is installed between the plates and has direct contact to the plates as illustrated in Figure 1.12 A. If the MUT is a granular material or a liquid a coaxial test cell setup is often preferred. Here the MUT can flow inside the test cell and there is almost no unknown fringing field. Figure 1.12 B illustrates such a setup. Several industrial and automotive applications such as oil quality monitoring sensors are based on coaxial test cells.

When it is not possible to install the MUT inside a capacitive test cell and when it is difficult to attach electrodes to the MUT (e.g. due to restricted space) sometimes an

Dieses Werk ist copyrightgeschützt und darf in keiner Form vervielfältigt werden noch an Dritte weitergegeben werden.
Es gilt nur für den persönlichen Gebrauch.

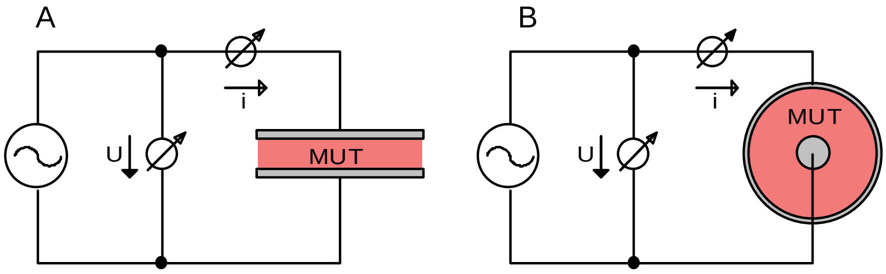

Figure 1.12: Measurement of electric and dielectric parameters of a material under test using a capacitive test cell. Often the geometry of the cell is either a parallel plate capacitor (A) or a coaxial capacitor (B).

open ended coaxial line is used. Especially when high frequency signals up to several GHz are of interest this type of probe is often found. The measurement signal is fed into a coaxial line which ends at the surface of the MUT. The injected measurement signal travels along the line until it reaches the open end. Here a reflection occurs and the reflected signal is travelling back to the measurement device. The reflection coefficient depends on the properties of the MUT which forms a complex electrical load. In most cases the end of the line has a special geometry in order to redirect the fringing field which occurs at the end of the line. The fringing field penetrates the MUT and is influenced by its electric and dielectric properties. Figure 1.13 illustrates such a setup.

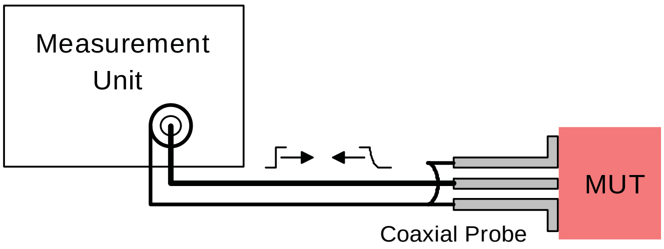

Figure 1.13: Measurement of electric and dielectric parameters of a MUT using an open ended coaxial probe. The probe end is attached to the surface of the MUT. This type of interface is often used when the space is restricted and when high frequency signals up to several GHz are of interest.

A similar approach to the open ended coaxial line is to embed a suitable sensor line into the MUT as illustrated in Figure 1.14. In applications such as e.g. soil moisture measurement it is common to use flat ribbon cables as sensor lines. Flat ribbon cables have a large fringing field which penetrates the surrounding media. The electric and dielectric properties of the media influence the characteristic wave impedance of the embedded transmission line. Any injected broadband measurement signal is distorted in a characteristic way while travelling along the line. The distorted signal is captured by the measurement electronics and analysed. In many practical applications a step pulse with sharp rising edges is used as a broadband measurement signal. The injected pulse is travelling along the line until it reaches the open end of the line. Here a positive reflection

Dieses Werk ist copyrightgeschützt und darf in keiner Form vervielfältigt werden noch an Dritte weitergegeben werden.
Es gilt nur für den persönlichen Gebrauch.

occurs and the signal is travelling back to the beginning of the line. This measurement principle is often referred to as "Time Domain Reflectometry". In this thesis this principle is used to measure the water content of soil by using a transmission line as sensor element and a suitable miniaturized electronic measurement circuit is developed. In addition the Time Domain Reflectometry measurement principle is investigated for tissue recognition at the tip of a needle.

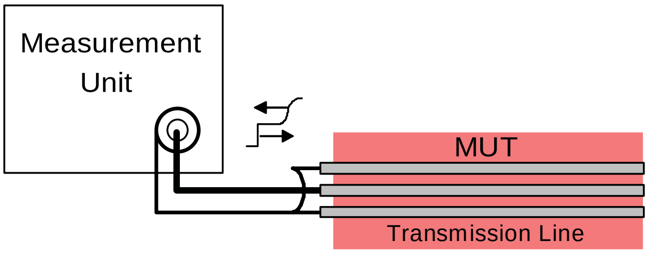

Figure 1.14: Measurement of electric and dielectric parameters of a MUT using an embedded open ended transmission line. The geometry of the line is designed in such a way that a large fringing field is penetrating the surrounding media.

If only high frequency signals are of interest it is sometimes possible to use optimized antennas for sending electromagnetic waves towards the MUT and for receiving either the transmitted or the reflected signals. Figure 1.15 A shows a typical setup for transmission measurement and Figure 1.15 B shows a typical setup for reflection measurement. Target applications for this method are mainly found in the field of moisture measurement where free and bound water molecules interact with high frequency microwave signals. For low frequency applications such as e.g. broadband impedance analysis of biological cells and tissue this method is not suitable due to the resulting large wavelengths of the signals.

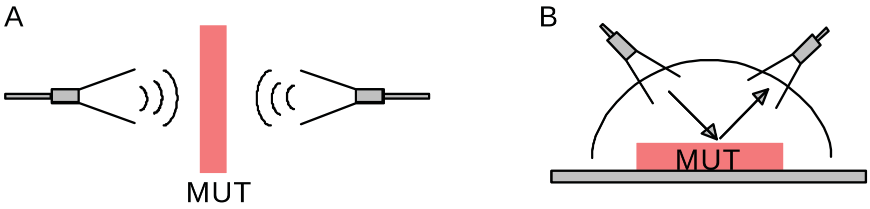

Figure 1.15: Free space measurement of dielectric properties of a MUT using two antenna positions. In A a setup for a transmission measurement is shown and in B a setup for a reflection measurement is shown. All antenna based setups are only suitable at high frequencies in the microwave range.

Dieses Werk ist copyrightgeschützt und darf in keiner Form vervielfältigt werden noch an Dritte weitergegeben werden.
Es gilt nur für den persönlichen Gebrauch.

1.6 State of the Art in Impedance Spectroscopy Measurement Circuits and Systems

Broadband impedance spectroscopy as a measurement method can only be successfully employed in real applications and products when there is a suitable electronic measurement circuit or system available. Conventional expensive laboratory measurement equipment does not fulfil the typical requirements of small size, low cost, low power consumption and simple integration into the target application. The interesting frequency range for different applications reaches from below 1 Hz up to several 10 GHz which means a potential bandwidth of approximately 10 decades. Of course there is almost no technical, physical or biological application where the entire frequency range is of interest. This automatically implies that it absolutely makes sense to classify different applications according to their corresponding "frequency windows". Within these frequency windows there are individual interesting frequency dependent properties of the MUT which allows to derive interesting information about the state of the MUT. Now it makes sense to develop efficient electronic measurement circuits and systems which are able to measure within such a defined frequency window. This allows for optimizing the system by setting appropriate boundary conditions for the electronic circuit. However, sometimes it is still a challenge to develop a broadband measurement circuit which covers several decades of frequency when a special boundary condition such as e.g. extremely fine resolution of amplitude or phase shift has to be measured or if the measurement of the whole impedance spectrum must be accomplished within a very short period of time. Unfortunately the individual boundary conditions vary from application to application and in many cases this does not allow to reuse circuits. It would be very efficient to have one or more concepts for universal electronic measurement circuits which can be employed "out of the box" for a variety of applications with a minimum of changes. In the ideal case there would be a set of adjustable parameters only which allow to set the measurement circuit properties such as e.g. bandwidth, measurement time, resolution or the measurement signal amplitude. In the past when the first broadband impedance measurement experiments have been done there was only the option to build analog measurement circuits. Of course analog circuits may lead to a good measurement result but it is almost impossible to optimize analog circuits in such a way that they could be reused by changing parameters only. Nowadays the situation is different: there are many programmable electronic devices available at very low cost which offer new and attractive options for smart measurement concepts and circuits. It is possible to add flexibility to the circuit by employing software e.g. inside a Microcontroller (MCU) or Digital Signal Processor (DSP) or by using reconfigurable logic devices such as Complex Programmable Logic Devices (CPLDs) or Field Programmable Gate Arrays (FPGAs). In combination with an optimized analog front end which forms the "bridge" to the electrodes on the MUT it is now possible to use complex measurement signals and process measurement results with efficient signal processing methods optimized for the employed signals.

In many scientific articles (see below) broadband impedance measurement is performed with a custom made measurement setup. One common method is to use programmable measurement components such as AD-Converter modules and DA-Converter modules with an interface connection to a host computer. As an alternative standard oscilloscopes and arbitrary waveform generators are used for signal generation and acquisition. The computer is controlling the measurement setup and is processing the acquired measurement signals. Main reasons for building up such individual measurement systems are often the need for an optimized analog front end to the MUT or optimized measurement

Dieses Werk ist copyrightgeschützt und darf in keiner Form vervielfältigt werden noch an Dritte weitergegeben werden.
Es gilt nur für den persönlichen Gebrauch.

signals, methods and strategies which have application specific advantages compared to standard laboratory measurement equipment such as e.g. LCR-Meters. Pliquett et al. proposed such a computer based system for fast time domain based impedance measurement of biological tissues [56]. Kozlowska et al. analysed electric and dielectric properties of biological tissue within a test cell based on a computer controlled setup [57]. Xu et al. propose a computer controlled setup for sensor readout in structural health monitoring applications [58]. Maertens et al. developed a measurement system for fast broadband readout of piezo sensors [59], Hoja et al. developed a computer based system for anti corrosion coating spectroscopy based on pulsed measurement signals [60] and Lentka et al. show how to efficiently obtain an impedance spectrum based on Laplace Transform algorithms for a computerized measurement system [61]. Palani et al. demonstrate how to build a computerized high resolution measurement system for the broadband characterization of transformers [7]. Da Silva et al. developed a system for high speed measurement of the complex permittivity of fluids [18] and Yoo et al. developed a computer based impedance spectroscopy system for real-time measurement of complex impedances of a MUT within electrochemical experiments [2]. In all named applications there are interesting aspects and ideas for optimized measurement of the broadband impedance, but all these systems are quite expensive and bulky and are far away from being integrated into a real product. In most scientific articles a new measurement approach is examined and verified within experiments, but there is no transfer of the whole system into a small and efficient electronic circuit which could be incorporated into cost sensitive products.

Several other scientific articles elaborate on the optimization of the analog front end which is usually employed between the sampling circuit (e.g. AD-Converter or laboratory instrument) and the electrodes. Typical circuits deal with the development of stable and error free broadband current sources or impedance matching circuits. Yelamos et al. present an amplifier circuit for improving the measurement range and accuracy of a conventional laboratory impedance analyser within measurements on biological tissue samples [62]. Aroom et al. developed a universal electronic front end circuit based on a modified Howland Bridge [63], Mathis et al. developed a measurement circuit for cross correlation based impedance estimation [64]. Almasi developed a measurement front end circuit for precision very low frequency measurements [65]. Seoane et al. developed an optimized wideband current source circuit based on a single operational amplifier [66] and Weereld et al. developed a circuit for bipolar pulsed measurement of impedances within tomography applications [67]. There are several more interesting circuits and front ends proposed in the literature, but all of them can only be used in combination with a complete measurement system comprising a signal source and a signal acquisition module as often found e.g. in a computerized measurement setup. In some cases the researchers developed a whole measurement system which is mainly intended to be used in the laboratory only. Such equipment may give precision measurement results but is usually not optimized for low cost, small size and low power consumption. Examples for such custom build laboratory systems are the multi channel measurement systems developed by Thiel et al. [68] and Hartov et al. [69]. A very interesting and promising approach for a modular broadband impedance measurement unit is the IMPSPEC system. Nacke et al. and Pliquett et al. present the functionality and the system concept within several scientific and technical articles [30, 70–72]. The system is developed as a real product which can be used "out of the box" for various applications. The different frequency ranges are covered by different measurement principles and signals. For instance the system can measure at low frequencies by applying (multi) sinusoidal measurement signals and it can measure at high frequencies up to a few GHz by applying Maximum

Dieses Werk ist copyrightgeschützt und darf in keiner Form vervielfältigt werden noch an Dritte weitergegeben werden.
Es gilt nur für den persönlichen Gebrauch.

Length Sequence (MLS) signals. In contrast to many computer based measurement setups the IMPSPEC system is capable of processing the measurement signals by built in logic modules and processors. The IMPSPEC system is a powerful and precision system which can be considered as a "bridge" between conventional computer based systems and a standardized measurement unit dedicated for impedance spectroscopy. However, the IMPSPEC system is still too large in size for several applications such as e.g. wearable medical and textile products. In addition the price is too high for mass production and integration in consumer products. In most cases only certain special applications or industrial processes can justify the high price of the system which is in the range of several thousand Euro depending on the individual system configuration.

Within the last 5 to 10 years there was some progress in the development of electronic platforms and concepts for efficient broadband impedance measurement. All platforms and systems which are presented in the literature show several identical aspects: they employ modern and powerful programmable devices such as Microprocessors, Digital Signal Processors or Field Programmable Gate Arrays. All developed circuits have the same idea of optimizing the overall system by combining efficient and smart measurement signals and fast and robust signal processing algorithms. One very interesting and promising approach is developed by Schneider at al. [73]. The presented system measures with a sinusoidal signal which can arbitrarily be adjusted in frequency. The signal is sampled by conventional AD-Converters and is then processed with optimized algorithms. One key consideration of this system is to enhance the signal to noise ratio (SNR) by employing oversampling and by fitting sinusoidal functions to the sampled signal points. The system is intended to be used in industrial measurement applications e.g. in combination with capacitive sensor front ends. However, although this system shows several positive aspects, there are some major drawbacks. One drawback is the required long measurement time because the sinusoidal excitation signal has to be swept over the entire frequency range of interest. This prohibits to use the system in fast or dynamic applications. A second drawback may be the employed direct sampling scheme of the signals. It is a straight forward approach but causes a relatively complex electronic circuit which is capable to handle the resulting high data rates. Memory space and signal processing power must be adjusted to the large amount of raw data. In addition the resulting power consumption of the system will be relatively high. Other interesting broadband impedance measurement platforms are developed by Min et al. [74–76]. The authors propose new concepts especially for a simplified excitation signal design and corresponding effective signal processing concepts. The presented electronic prototype system employs a fast DSP for calculation of cross correlation functions and the Fast Fourier Transform (FFT). Due to the proposed different excitation signals the system is quite flexible and shows good potential for further optimization and miniaturization. One potential drawback might be the required signal processing time in very fast applications. Here the serial processing of the captured raw data is a potential limitation in the current architectural design of the system. However, the platform has potential to be enhanced in terms of processing speed by replacing the serial data processing path by a parallel processing concept implemented e.g. inside a standard FPGA. In addition to these systems the authors already proposed a FPGA based concept for high speed measurements for biomedical applications [77]. Here synchronous sampling of a repetitive waveform is employed as a measurement concept. The concept has great advantage compared to several traditional systems, but the synchronous sampling scheme is limited in its flexibility because it is not possible to excite any frequency of interest without violating the fundamental working concept of the proposed efficient data processing. This might be

Dieses Werk ist copyrightgeschützt und darf in keiner Form vervielfältigt werden noch an Dritte weitergegeben werden.
Es gilt nur für den persönlichen Gebrauch.

a limitation in applications where a narrow frequency band has to be captured with a high frequency resolution e.g. in resonant circuits, crystals or piezos. Other FPGA based impedance measurement applications are presented by Patz et al. [78] and Yoo et al. [79]. The system developed by Patz is intended for use in multichannel applications such as tomography and is capable of sampling up to 14 channels. The developed system is relatively slow and a few hundred milliseconds are required for the impedance measurement and signal processing. The system is not optimized for size, cost and power consumption. The FPGA based system proposed by Yoo et al. is based on a very traditional sinusoidal measurement signal source and traditional direct sampling of the voltage and current signals. The processing is done by a FPGA and a DSP. The overall circuit complexity is very high compared to the obtained speed and accuracy. A much smaller system with even better accuracy, resolution and a higher bandwidth is proposed by Beckmann et al. [80]. The small system is based on a cheap standard microcontroller and the size of the electronic circuit is very small compared to most other systems and solutions. The miniaturized system is also using sinusoidal measurement signals and is optimized for a frequency window starting at a few kHz and ending at 1 MHz. Target application of the circuit are battery powered wearable textiles with integrated electrodes. The system looks attractive for such applications especially because of the expected low production price of the electronic circuit. However, because of the employed sinusoidal sweep the system is slow and can only be used for static or quasi static applications. Last but not least there is the option to embed a full broadband measurement system into one single chip. This allows for the smallest size and gives very good options for optimizing the power consumption. Lerch et al. developed a programmable Mixed-Signal ASIC for data acquisition systems in medical implants [81]. The circuit contained flexible measurement options, integrated data storage options, a wireless communication interface and various additional functions such as watchdog and power management modules. Another interesting system is currently commercially available on the market (AD5933 from Analog Devices [82]). The integrated circuit AD5933 is tested in various applications and the results are published in the literature [83–85]. According to the different authors and the datasheet there are several limitations of the circuit. Most significant limitation is the frequency range which allows to measure only up to 100 kHz. This is usually not enough for many applications such as e.g. biomedical tissue analysis or biological cell analysis. Second limitation is the requirement for relatively complex external amplifier circuits. Of course it is possible to build such amplifier circuits, but then the great advantage of having a complete system on one single chip is lost. In addition the price for the AD5933 is very high (in the range of approximately 30 Euro per chip) which prohibits to use the chip in cost sensitive applications. Sachs et al. developed an interesting and promising ultra wideband measurement circuit based on MLS-Signals for measuring within an extraordinary large frequency window reaching from near zero up to approximately 5 GHz [45]. But the presented chip mainly contains the components for signal generation and sampling and therefore requires an additional external processing system. Yufera et al. developed a chip for measuring the impedance of a 2D array of biological cells [86]. All components of the measurement system including the electrodes are manufactured on one chip. The measurement system is interesting for a small number of applications only because the integrated measurement electrodes can not be connected to external hardware such as external electrodes or external amplifier circuits.

In summary the literature survey shows that there is still a broad gap between state of the art experimental laboratory measurement equipment and the requirements which are given by most practical applications. A few interesting approaches for lightweight mea-

Dieses Werk ist copyrightgeschützt und darf in keiner Form vervielfältigt werden noch an Dritte weitergegeben werden.
Es gilt nur für den persönlichen Gebrauch.

surement systems and smart signal processing methods have been published yet but the large amount of potential target applications and its individual requirements currently cannot be covered by these techniques. Goal of this thesis is to fill the existing gap by developing smart measurement concepts which can be used for real products especially when it comes to requirements such as low cost, small size and low power consumption. A detailed analysis of many potential target applications shows, that there are mainly two groups of applications. In a first group there are static or quasi static applications where the measurement time is not critical but in many cases a high accuracy and high resolution of the measurement result is required. The second group of applications are mainly fast and dynamic systems which require to measure and process impedance data within a very short period of time. In order to derive optimized measurement strategies and universal electronic circuit concepts for all applications it makes sense to distinguish at least between these two groups of applications and develop an individual optimized measurement platform for each group. Within this thesis the focus is on target applications in the field of biomedical engineering and environmental engineering. Two biomedical applications have been investigated in detail and the developed electronic circuits have successfully been tested within these applications. In addition one environmental engineering application has been analysed and a miniaturized version of one measurement circuit has successfully been developed. The applications are examined in chapters 2 and 3 of this thesis, the developed two measurement concepts and the electronic circuits are discussed in detail in chapter 4.

Dieses Werk ist copyrightgeschützt und darf in keiner Form vervielfältigt werden noch an Dritte weitergegeben werden.
Es gilt nur für den persönlichen Gebrauch.

2 Biomedical Applications

One of the largest scientific fields within impedance spectroscopy applications is the analysis of biological cells and tissue. In all applications the frequency dependent electric and dielectric properties of cells and tissue are measured and examined. Applications reach from single cell analysis in microfluidic structures [11, 41, 46–48, 84, 87–91] and biosensors [26, 42, 92–94] to full body impedance measurement [95–105]. Even complex tissues such as blood are characterized for different applications [106–112]. Interesting is the potential of impedance spectroscopy for detecting breast cancer [68, 113–118] and for analysing properties of the skin [119–126]. In dialysis applications the hydration state of the body is measured by impedance spectroscopy [97, 127–131] and even 2D and 3D impedance "pictures" can be obtained by Electrical Impedance Tomography (EIT) [69, 132–138].

Within this thesis two biomedical applications are examined in detail. The first application is hematocrit measurement of blood. The idea of measuring the hematocrit value based on impedance spectroscopy is not new, but in this particular case the blood has to be analysed inside a standard plastic tubing as always found in extracorporeal blood circulation systems. This means that there is no direct access to the blood and it is not possible to insert conductive electrodes into the blood sample. As a solution a capacitive measurement approach is presented and analysed in detail. The research results have been submitted as a regular paper to the journal "IEEE Transactions of Biomedical Engineering" and major parts will be published there. In addition preliminary results have been published at the IEEE conference "EMBC 2009" and are available as conference proceedings paper via the database IEEE Xplore. Details about cited sections of the publications are given in the appropriate chapters.

The second biomedical application which is examined in detail is a tissue discrimination based needle navigation system. The exact type of tissue close to the tip of a needle or a cannula has to be recognized in real time during the needle insertion process into the body. Since the needle insertion is a dynamic process the impedance spectrum of the tissue sample must be measured within a very short time. In order to solve for the problems a coaxial cannula design is proposed and analysed in detail. For the fast measurement of the impedance spectrum short broadband chirp signals with a duration of only 100 microseconds are used. The obtained research results have been published as a regular paper in the journal "IEEE Transactions on Biomedical Engineering" in February 2012 (Vol. 59, No. 2, pp. 494-503). Major parts of the corresponding chapter within this thesis cite the published article. In addition preliminary research results for coaxial needle designs and TDR-measurement signals have been published as a conference paper at the IEEE conference "EMBC 2010".

In both applications the measurements have been done with suitable laboratory equipment first. The measurement results especially show which accuracy and which resolution is required by each application. These parameters are taken as a part of the specification for an electronic measurement circuit which can replace the laboratory measurement setup. The development of the electronic circuits and concepts for both applications is explained in detail in chapter 4.

Dieses Werk ist copyrightgeschützt und darf in keiner Form vervielfältigt werden noch an Dritte weitergegeben werden.
Es gilt nur für den persönlichen Gebrauch.

2.1 Physiological Background

Biological tissue shows a frequency dependent electric and dielectric behaviour. According to the literature there are several physical and physiological effects which explain the observed behaviour. Commonly there are three frequency regions for a biological tissue where dispersion effects occur. In the literature these different dispersion effects are known as α-dispersion, β-dispersion and γ-dispersion [72, 139, 140]. In the newer literature the α-dispersion is sometimes subdivided into a first α_1-dispersion and a second α_2-dispersion. The α-dispersion typically occurs at low frequencies up to a few kHz. The β-dispersion can usually be observed within a frequency window of a few kHz and a few MHz. The γ-dispersion occurs at very high frequencies in the GHz range. Figure 2.1 illustrates the typical dispersion effects and shows the real part and the imaginary part of the complex permittivity as a function of the frequency. Each observed dispersion effect has its unique physical and physiological mechanisms. For the α-dispersions in the low frequency range the literature lists several different effects. According to most experiments and investigations major effect is the frequency dependent relaxation of counter-ions which are found on a charged cellular surface. A further effect is the frequency dependent conductance of channel-proteins which exist in the plasma membrane [83]. The β-dispersion can be explained by a simplified modell of a cell as shown in Figure 2.3. The cell membrane (lipid layers) has a low conductance but acts as a capacitive structure which becomes low-impedance at high frequencies. The inner cell volume is modelled by a resistor and the extracellular fluids are modelled by a parallel resistor. The γ-dispersion which can be observed at high frequencies is caused by dipolar mechanisms. Polar molecules such as e.g. water molecules and large protein molecules are influenced by an externally applied electric field. The γ-dispersion can therefore be

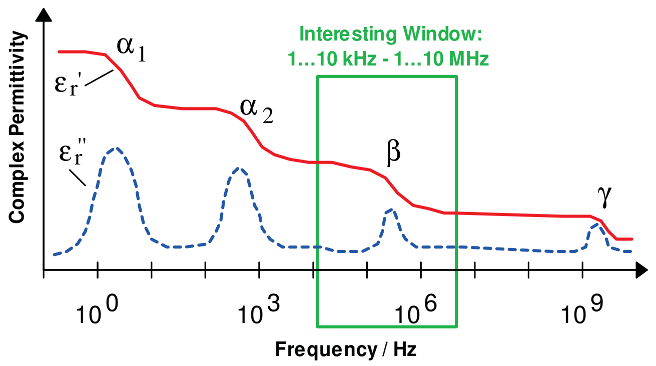

Figure 2.1: Modified illustration of the three known dispersion effects as originally published by H.P. Schwan [139]. The β-dispersion effect is often used in tissue analysis applications. The typical frequency range in which the β-dispersion can be observed is between a few kHz and a few MHz.

Dieses Werk ist copyrightgeschützt und darf in keiner Form vervielfältigt werden noch an Dritte weitergegeben werden.
Es gilt nur für den persönlichen Gebrauch.

In the literature the frequency dependent impedance model of a tissue sample is often simplified and shown as an ideal semicircle in a Nyquist diagram as illustrated in Figure 2.2. In contrast to the semicircle of a lossy dielectric material shown in Figure 1.4 there is a typical offset on the real axis. This offset can be modelled by adding a serial resistor R_{offset} to the equivalent schematic as shown in Figure 2.2. This equivalent schematic is sometimes used in the scientific literature to model the β-dispersion but it does not reflect any physical or physiological structures. As mentioned above a cell (or a tissue sample consisting of multiple cells) can be modelled by a simplified electrical schematic when taking the cell structure into account. The cell membrane acts as a capacitor C_m, the inner cell volume is replaced by a resistor R_i and the extracellular fluids are represented by a parallel resistor R_p. Figure 2.3 illustrates this simplified model for a single cell on the right side. This model is also often used in the literature for modelling the frequency dependent electric and dielectric behaviour of biological tissue. However, the two presented models are identical and describe the same impedance transfer function

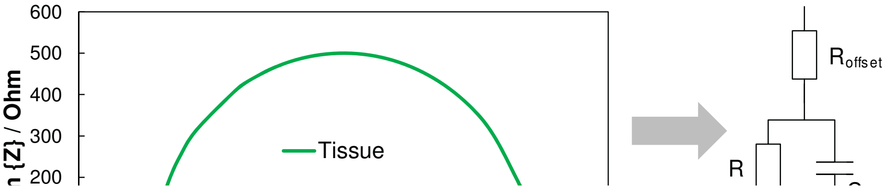

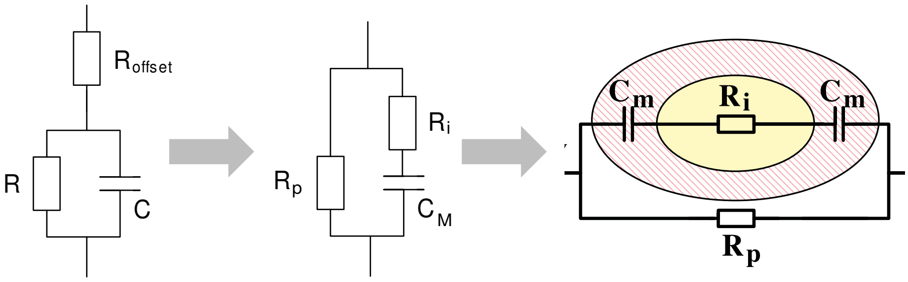

Figure 2.3: Equivalent electrical circuit for the observed tissue behavior. The circuit can be transformed to a circuit with equivalent electrical properties and which represents biological structures of a biological cell. The two illustrated cell membrane capacitors C_m are in series and can be summarized into one equivalent capacitor C_M as shown in the equivalent schematic in the middle.

R&D STMI Trebbels

Dieses Werk ist copyrightgeschützt und darf in keiner Form vervielfältigt werden noch an Dritte weitergegeben werden.
Es gilt nur für den persönlichen Gebrauch.

In the field of electrical engineering the Bode Diagram is often the preferred representation of a complex frequency dependent function. A typical transfer function of the biological tissue model is shown in figure 2.4. The upper graph shows the amplitude transfer function and the lower graph shows the phase transfer function. In both graphs it can easily bee seen that there is an "interesting" frequency window. At frequencies below or above the interesting window the tissue behaves like a pure resistive component. Only within the window there is a characteristic frequency dependent effect which might be used for evaluating the state or the condition of the tissue sample. In the literature, especially in the medical field, the pure resistive behaviour of tissue at low frequencies and at high frequencies outside the window is often illustrated by a simplified model for the current paths inside a tissue sample. Figure 2.5 shows a tissue sample between two parallel electrode plates. In A the current paths for low frequencies is illustrated. The current can only flow between the cells inside the extracellular fluids (equivalent to R_p). In B the current paths for high frequencies is illustrated. Here the current can flow through the cells as well because the capacitive cell membranes become low-impedance.
H
of

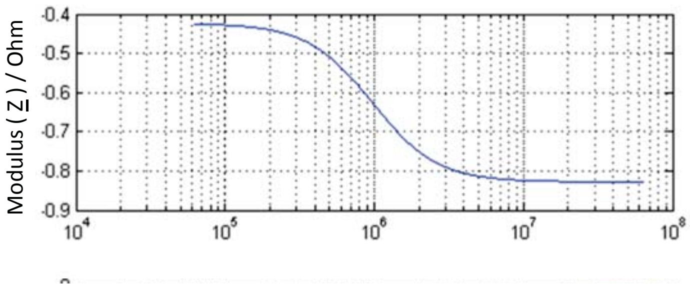

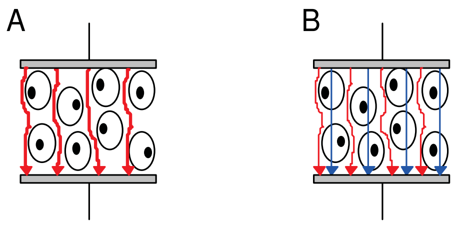

Figure 2.5: In A the typical current paths through a tissue sample is illustrated for low frequencies where the capacitive cell membrane is a high impedance. The current flows mainly between the cells. In B the current paths for high frequency signals is illustrated where the cell membranes become low impedance and current can flow through the cells.

Dieses Werk ist copyrightgeschützt und darf in keiner Form vervielfältigt werden noch an Dritte weitergegeben werden.
Es gilt nur für den persönlichen Gebrauch.

As mentioned earlier the representation of a complex impedance transfer function can either be done in a Nyquist Diagram or in a Bode Diagram. Both representations are useful and have individual advantages and drawbacks. Both types of 2D-diagrams can be drawn in one 3D-diagram as shown in 2.6. All three graphs of the Nyquist- and Bode-Plots are drawn. The resulting complex frequency dependent tissue transfer function

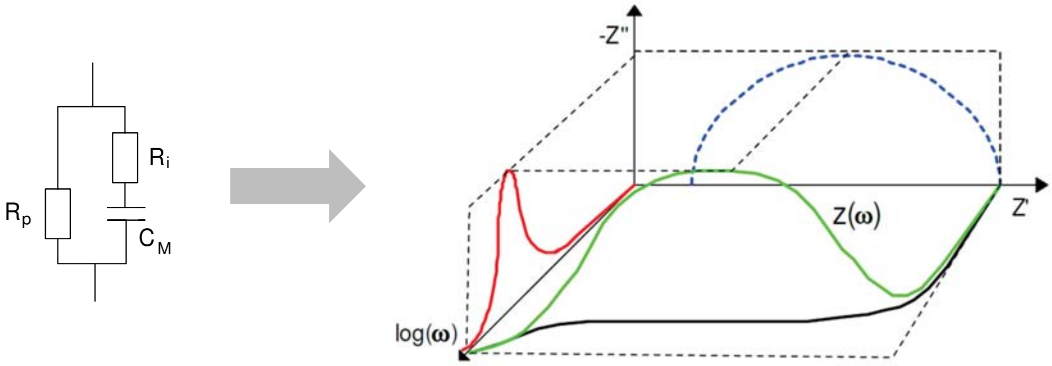

Figure 2.6: 3D-View of a typical tissue transfer function according to the simplified equivalent circuit. The 3D-View contains the Nyquist-Plot and the two "Bode-Plots" for real part and imaginary part of the frequency dependent tissue impedance.

R&D STMI Trebbels

Dieses Werk ist copyrightgeschützt und darf in keiner Form vervielfältigt werden noch an Dritte weitergegeben werden.
Es gilt nur für den persönlichen Gebrauch.

2.2 Hematocrit Measurement

The text of the following section about hematocrit measurement mainly consists of merged text parts of two previously written scientific articles. The first article which is partly cited here is a regular conference paper and has been published, the second article which is cited here is submitted as a regular journal paper. In addition to the cited sections of the paper the introduction to the topic hematocrit measurement is enhanced within this thesis and in the simulation section and the prototype section the two different sensor geometry concepts which have originally been published in the two articles are compared to each other. The numbering of the subsections, figures and references are adapted to the overall numbering of this dissertation. A detailed description of the originally written and published work and the individual contributions of the author and the co-authors is given below.

D. Trebbels, D. Hradetzky, R. Zengerle:

Capacitive on-line hematocrit sensor design based on Impedance Spectroscopy for use in hemodialysis machines
IEEE EMBC 2009, 31st Annual International Conference of the IEEE EMBS, pp. 1208-1211, Minneapolis/USA, September 3-6, 2009

Contributions to this publication:

1. D. Trebbels: Development of the Sensor Concept and Design, FEM Simulation, Laboratory Measurements and Manuscript Preparation including Literature Reserach.
2. D. Hradetzky: Organisational Support during Experiments and Scientific Advice and Discussions
3. R. Zengerle: Planning of Experiments, Discussion of Results and Scientific Advice during Manuscript Preparation

D. Trebbels, R. Zengerle:

Capacitive On-line Hematocrit Measurement in Extracorporeal Circuits
IEEE Transactions on Biomedical Engineering, submitted July 2012

Contributions to this publication:

1. D. Trebbels: Literature Reserach, Development of the Sensor Concept and Design, FEM Simulation, Laboratory Measurements and Manuscript Preparation.
2. R. Zengerle: Discussion of Results and Scientific Advice during Manuscript Preparation

Dieses Werk ist copyrightgeschützt und darf in keiner Form vervielfältigt werden noch an Dritte weitergegeben werden.
Es gilt nur für den persönlichen Gebrauch.

2.2.1 Introduction to Hematocrit Measurement

Measuring the hematocrit value (HCT) of a blood sample is a common task during many medical interventions and treatments [144] and can give valuable additional information about the health status of the patient. The HCT value is defined as the fraction of the blood volume which is occupied by cells. Since approximately 99% of the cell volume is occupied by erythrocytes only, it can be said as a rule of thumb that the HCT value is equal to the fraction of red blood cells [145]. This article focuses on applications, where an extracorporeal blood circulation system is already available such as life support machines and hemodialysis machines. It is desirable to continuously measure the HCT value of the blood flowing inside standard medical tubing without the need for extracting a blood sample out of the circuit and without direct contact to the blood. Figure 2.7 illustrates a simplified hemodialysis circuit in which such a sensor is desired for monitoring the blood of the patient during hemodialysis treatment. The blood of the patient is flowing through a primary circuit and the volume of the plasma is reduced by the dialysis machine. Therefore the relative amount of red blood cells is increasing during the treatment and can be used as an indicator e.g. for estimating the end of a dialysis procedure. Since the plastic tubing is a very price sensitive disposable product it is required not to integrate the HCT-sensor into the tubing but it is a solution to incorporate a HCT-Sensor into the dialysis machine and attach it to the tubing. Drawback from the measurement point of view is the fact that the isolating plastic walls of the tubing are now between the sensor and the blood and there is no direct contact possible. This does not allow to measure the HCT value by e.g. measuring the direct electric conductivity of the blood by using conductive metal electrodes. In addition it is difficult to modify the plastic tubing by e.g. integrating a cheap conductive metal electrode because any disturbing object within the blood path is subject to cause coagulation. In addition any modification of the tubing would increase the production cost which is absolutely critical in this case.

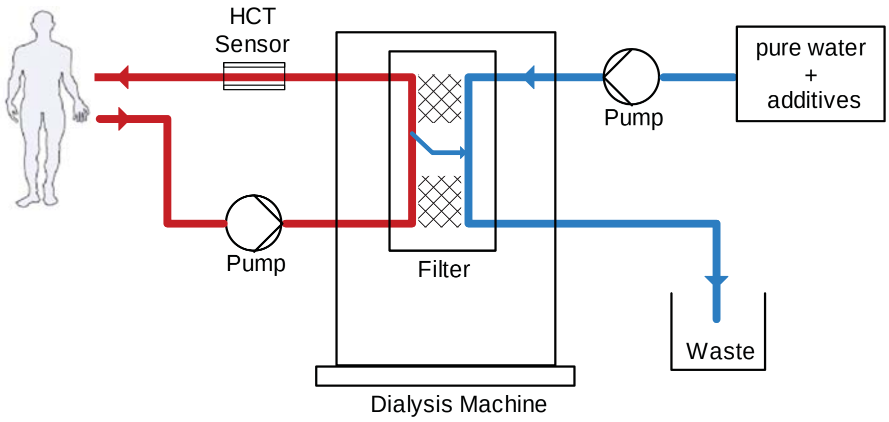

Figure 2.7: Simplified structure of a hemodialysis machine. The blood of the patient flows through a primary circuit and a fluid volume is removed within the filter and disposed via a secondary circuit. Measuring the HCT-value of the blood within the primary circuit can give additional information about the dialysis treatment procedure.

Dieses Werk ist copyrightgeschützt und darf in keiner Form vervielfältigt werden noch an Dritte weitergegeben werden.
Es gilt nur für den persönlichen Gebrauch.

2.2.2 Existing Measurement Techniques

There are several well known HCT measurement techniques which are commonly used. One straight forward method is based on centrifugation [146] where the cells and the plasma are separated from each other and the HCT value can be directly read after the centrifugation. An established alternative method is Complete Blood Count (CBC) [147]. Here a blood sample is analysed in a special cell cytometer which counts the number of cells (e.g. thrombocytes, leukocythes and erythrocytes) in the sample. Both methods give precise results but require expensive laboratory equipment and trained staff. Further drawback of these methods is the fact, that a blood sample must be extracted from the extracorporeal circuit. The procedure is laborious and in addition there is a potential risk for infections because of the direct contact to the blood. Therefore both methods are not suited for continuous on-line monitoring of the HCT value. In the past several interesting alternative measurement approaches for continuous on-line HCT measurement were presented based on different physical sensor principles. Schneditz et al. developed an ultrasound based sensor system which can be attached to the tubing [148–150]. The system works well, but the coupling between the ultrasound transducers and the tubing wall as well as the stability of the acoustic properties of the tubing material over temperature is a major concern. Another measurement approach is based on optical measurement principles. Drawback is the need for inserting a short glass tube or a similar device with defined optical properties in the tubing. This causes additional cost and again there is the risk for infections due to opening the sterile circuit. Oshima et al. propose an advanced optical system which measures the HCT through the tubing walls without the need for inserting an optical device, but according to [151, 152] at the current stage this is a theoretical approach only and there is no available system on the market yet. Another well known method is to estimate the HCT value based on impedance measurements. There is a broad range of concepts which reach from single frequency to broadband frequency measurements and evaluating parameters such as conductivity or permittivity of the blood sample [112, 153–157]. However, in all cases there is the need for bringing electrodes into direct contact with the blood which does not permit a HCT measurement through the electrically isolating plastic tubing walls. Last but not least there are several approaches for a non-invasive on-line measurement of the HCT value by directly attaching sensors to the human body instead of attaching them to the tubing. The sensor principles are generally the same as already introduced above and reach from ultrasound over optical methods to impedance measurements [158–162]. However, these concepts typically deal with problems associated with the undefined interface to the human body and sometimes related poor measurement resolution and accuracy [106].

2.2.3 New Capacitive System Concept

In order to eliminate problems associated with a human-machine interface it is proposed to measure the HCT value of the blood through the plastic tubing walls with a sensor attached to the tubing from the outside. In this thesis a new capacitive sensor design is proposed which is based on electrodes encapsulating the tubing. Figure 2.8 shows two possible electrode designs which have been analysed in depth. Each design has individual advantages and disadvantages. On the left side two simple half-shell electrodes form a capacitor and the tubing filled with blood serves as a laminated dielectric between the electrodes. On the right side the electrodes are formed as rings which enclose the tubing. The resulting capacitance between two adjacent rings partly depends on the dielectric properties of the tubing and the blood inside the tubing. In both cases the

Dieses Werk ist copyrightgeschützt und darf in keiner Form vervielfältigt werden noch an Dritte weitergegeben werden.
Es gilt nur für den persönlichen Gebrauch.

basic measurement concept is to measure the impedance of the resulting capacitor and derive the HCT value of the blood from the measurement data. According to [10] the permittivity of blood depends on the HCT value. The resulting capacitance of the formed capacitor is measured with a laboratory LCR-meter. In addition the LCR-meter measures the phase angle between the applied voltage signal and the resulting current flow. For an ideal capacitor the phase angle is expected to be 90 degrees. However, in this case there are some frequency dependent losses caused by the blood which serves as part of the dielectric and therefore the phase angle will vary from 90 degrees. In order to achieve a sensor element with good sensitivity the shape of the two proposed electrode designs is investigated and optimized with finite element method simulations. Based on the simulation results two sensor prototypes have been constructed. In the laboratory in-vitro measurements have been done in order to investigate the expected dependency of the complex sensor impedance on the HCT value of the blood. The measurement results are presented and analysed within this thesis.

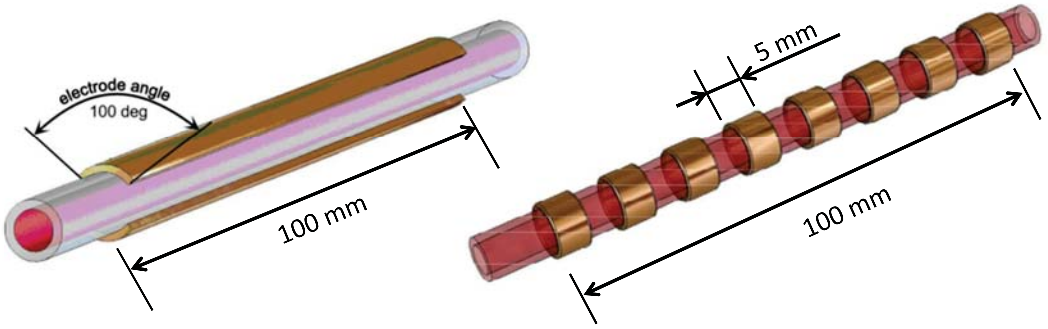

Figure 2.8: Two possible electrode designs which form a capacitor around the tubing. In both designs the total capacitance partly depends on the electric and dielectric properties of the tubing wall material and the blood inside the tubing.

2.2.4 Finite Element Method Simulation

Goal of the simulation is to obtain a detailed understanding of the expected sensor behavior and to show potential limits of this concept caused by side effects such as temperature drift of the dielectric properties of the tubing wall material. In addition the geometry of the electrodes is optimized in order to obtain the best sensitivity of the sensor towards the dielectric properties of the medium flowing inside the tubing. The simulation is done using the free software package "FEMM4.2" [163]. Each sensor design is investigated in depth. The following sections describe the simulation for each design with all details and results.

Half-Shell Electrode Design

The first sensor design based on two half-shell electrodes is modelled as a planar electrostatic problem as shown in Fig. 2.9. The depth of the model (which is equivalent to the length of the electrodes) is set to 10 cm as a compromise between overall sensor size and resulting total capacitance. The potential of the upper electrode is set to $+1.0$ Volt, the lower electrode is at ground potential as well as the boundaries of the system. The outer diameter of the simulated plastic tubing is 6.4 mm and the wall thickness is 0.8

Dieses Werk ist copyrightgeschützt und darf in keiner Form vervielfältigt werden noch an Dritte weitergegeben werden.
Es gilt nur für den persönlichen Gebrauch.

mm which is equivalent to the dimension of the medical sample tubing which is also used in the laboratory for experiments. The material of the tubing wall is PVC and according to the manufacturers data sheet has a relative permittivity ε_r of 3.1.

Within the first simulation the distribution of the electrical field inside the capacitor is investigated. Fig. 2.9 shows several simulated field patterns. Fig. 2.9 A and B show the electrical field strength, in 2.9 A the tubing is filled with air ($\varepsilon_r = 1$) and in 2.9 B the tubing is filled with water ($\varepsilon_r = 80$). Fig. 2.9 C and D show the electric potential, in 2.9 C the tubing is filled with air and in 2.9 D the tubing is filled with water. It can be seen that in 2.9 B and 2.9 D the resulting field strength inside the tubing wall material is very high compared to the field strength inside the media when the tubing is filled with water. Reason for this behaviour is the resulting capacitive voltage divider created by the tubing wall material and the medium inside the tubing. The relative permittivity of water (and blood) is by a factor of approximately 25 higher than the permittivity of PVC and thus the field is heavily distorted. Fig. 2.10 A illustrates a virtual lateral cut through the capacitor from the inner surface of the upper electrode down to the inner surface of the lower electrode. The graph in Fig. 2.11 shows the corresponding potential along the virtual cut for the tubing filled with water as shown in Fig. 2.9 B. According to the graph approximately 90 % of the applied voltage signal drops in the tubing walls. Only around 10% of the applied voltage signal drop inside the medium. Therefore as a matter of principle the overall sensor is much more sensitive to the dielectric properties of the tubing wall material than to the dielectric properties of the medium. As a result the stability of the dielectric properties of the tubing wall material is a critical point. Especially the temperature drift must be tested and evaluated in detail.

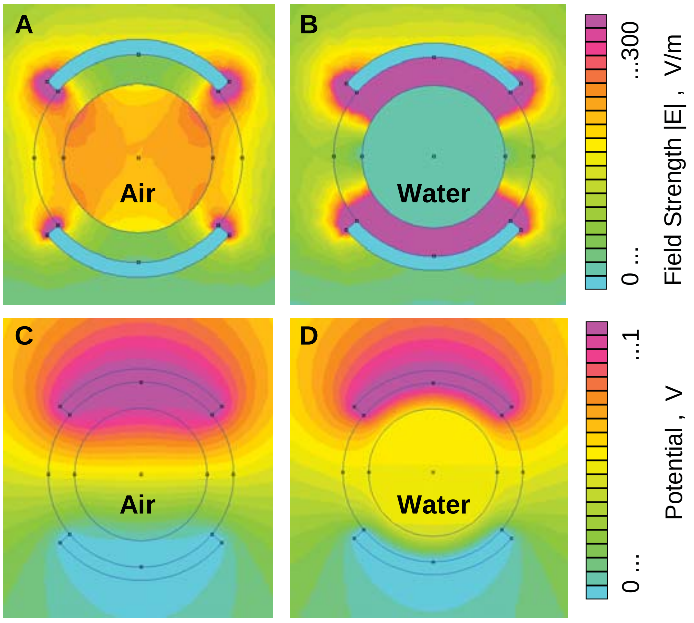

Figure 2.9: Simulated electrical field patterns within the capacitor. A and B show the field strength, C and D show the absolute potential. In A and C the tubing is filled with air, in B and D the tubing is filled with water. Due to the high permittivity of water compared to the PVC tubing walls the field is distorted and the highest field strength is found in the tubing walls.

Dieses Werk ist copyrightgeschützt und darf in keiner Form vervielfältigt werden noch an Dritte weitergegeben werden.
Es gilt nur für den persönlichen Gebrauch.

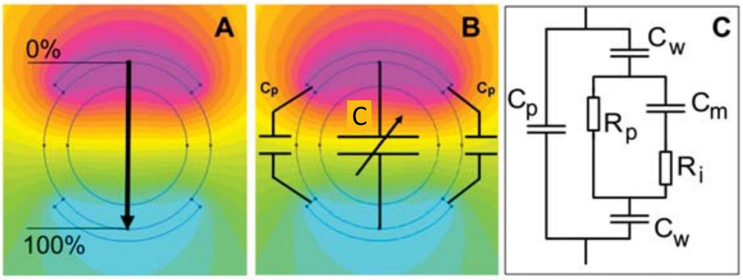

Figure 2.10: A virtual lateral cut through the capacitor is shown in A. The corresponding voltage signal is shown in Fig. 2.11. B illustrates two unavoidable parasitic parallel capacitors C_p and the variable inner "measurement capacitor" C. In C an equivalent electrical schematic for the overall sensor structure is presented. C_p is the parasitic parallel capacitor and C_w models the tubing walls. The blood is modelled by an equivalent circuit for tissue where C_m is the cell membrane capacitance of the erythrocytes, R_i the inner resistivity of the cells and R_p the resistivity of the plasma.

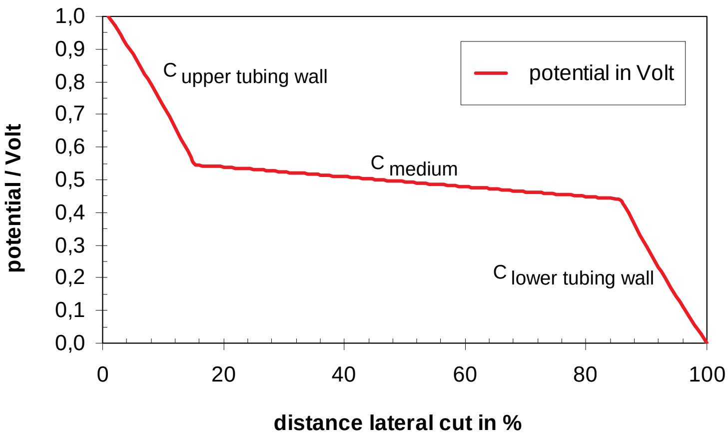

Figure 2.11: Potential along a virtual lateral cut through the sensor between the upper and the lower electrode as illustrated in Fig. 2.10 A. Approximately 90 % of the applied voltage signal drop in the tubing walls and only 10 % drop inside the media.

Due to the fact that the sensitivity towards a change of the dielectric properties of the medium inside the tubing is relatively small, it is mandatory to optimize the shape and geometry of the sensor electrodes in such a way that the optimum relative sensitivity is obtained. Interesting parameters are the electrode angle (see Fig. 2.8) and the strength of the electrode material. Fig. 2.12 shows the capacitance as a function of the electrode angle for different electrode material strengths from 0.035 mm to 1.5 mm for the tubing filled either with water or air. As expected the total capacitance is rising when the size of the electrodes is increased. Especially at electrode angles of 160 degrees and higher the capacitance dramatically increases due to the parasitic parallel capacitors C_p which are formed by the electrodes (see Fig. 2.10 B). It is obvious that there must be an optimum between very small electrode angles which result in a very low capacitance and very large electrode angles which result in a large sensor offset signal caused by C_p. Fig. 2.13 shows the relative change of the total sensor capacitance between air and water calculated from the graphs presented in Fig. 2.12. The result is an optimum electrode angle of approximately 100 degree where the sensor shows the best achievable sensitivity to a change of the dielectric properties of the medium for a given diameter and wall

Dieses Werk ist copyrightgeschützt und darf in keiner Form vervielfältigt werden noch an Dritte weitergegeben werden.
Es gilt nur für den persönlichen Gebrauch.

thickness. In addition it can be seen that a thin electrode gives slightly better results than a massive electrode because of the resulting lower value of C_p. In summary the simulation results demand for an electrode angle of 100 degree, a thin electrode material and from the graph shown in Fig. 2.11 it is clear that the tubing wall material must either provide stable dielectric properties (e.g. over temperature) or alternatively a resulting drift in the signal must be compensated for by a suitable method.

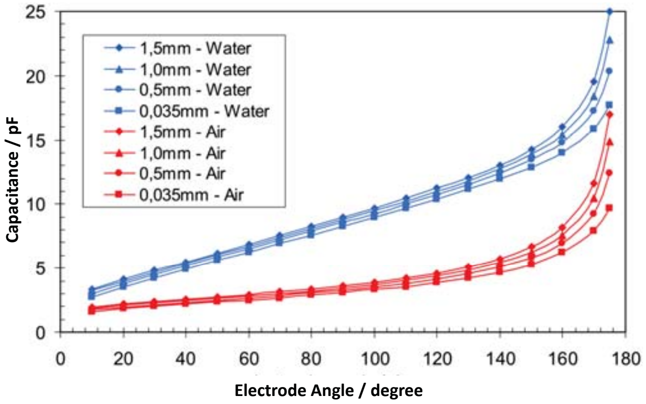

Figure 2.12: Capacitance as a function of the electrode angle for several electrode material strengths between 0.035 mm and 1.5 mm. The graphs are calculated for a tubing filled with water and air.

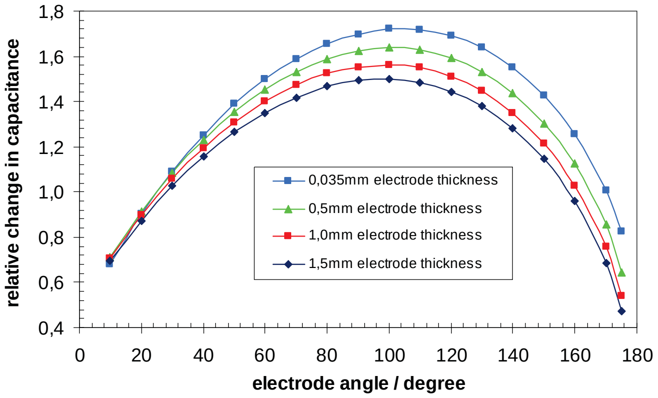

Figure 2.13: Relative change of the total sensor capacitance as a function of the electrode angle. The graph is calculated from the data presented in Fig. 2.12 and assumes a change of the media inside the tubing from air to water.

Ring Electrode Design

The second electrode design which is investigated in depth are ring electrodes as shown in Fig. 2.8 on the right side. Fig. 2.14 shows how the rings are connected to each other. Two adjacent rings always have opposite polarity. In order to form one large capacitor out of multiple rings all electrodes having the same potential are tied together. The electric field between two rings partly penetrates the tubing wall and therefore the measured capacitance partly depends on the dielectric properties of the medium which flows inside the tubing. Similar to Fig. 2.10 B and C there is an equivalent electric schematic which describes the resulting capacitive system. Fig. 2.15 A illustrates this

Dieses Werk ist copyrightgeschützt und darf in keiner Form vervielfältigt werden noch an Dritte weitergegeben werden.
Es gilt nur für den persönlichen Gebrauch.

capacitive system in a simplified way by subdividing it into three parallel capacitances. The first capacitance C_1 is directly between the rings with air as dielectric. The second capacitance C_2 represent the electric field lines which follow the tubing wall and the third capacitance C_3 represents the field lines which penetrate the tubing wall and interact with the medium inside the tubing. Fig. 2.15 B shows the parallel connection of the three capacitances and the connection to a measurement device such as a network analyser. Since only C_3 interacts with the medium inside the tubing C_1 and C_2 create an offset for the overall capacitance of the system.

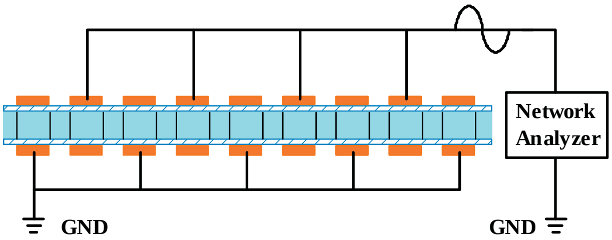

Figure 2.14: The electrodes are formed as rings around the tubing. Adjacent rings always have opposite polarity. All rings having the same potential are connected to each other. In total one large capacitor is formed. The electric field between two rings partly penetrates the tubing wall and therefore the total measured capacitance partly depends on the dielectric properties of the medium inside the tubing.

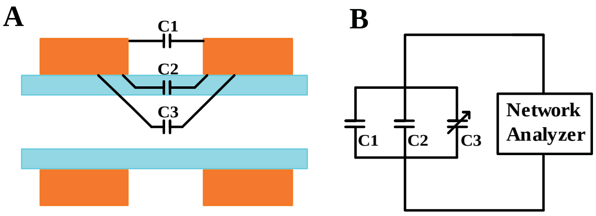

Figure 2.15: Two adjacent ring electrodes form a capacitor. The electric field distribution and the resulting equivalent capacitance is illustrated by a parallel connection of several capacitive effects.

The finite element method simulation of the ring electrode design is done in order to investigate the sensitivity of the sensor towards a change of the dielectric properties of the medium in the tubing. In order to optimize the sensitivity of the sensor, the shape and the distance of the ring electrodes have to be optimized and adapted to the given dimensions of the plastic tubing. The graphical simulation results in Fig. 2.16 show a strong field distortion caused by the high permittivity of the water (blood) and the relatively low permittivity of the plastic tubing walls. Fig. 2.16 A shows a normal field pattern as expected. The simulation was done with air inside the plastic tubing. Fig. 2.16 B shows the distorted field pattern for the real situation with water (blood) inside the tubing. Due to this field distortion, the electrical field strength inside the tubing walls is approximately ten times higher than inside the blood and therefore causes a large sensor offset. Referring to Fig. 2.15 the modelled capacitor C_2 is large compared to C_1 and C_3. The large sensor offset is a result of the tubing wall material and can not be fully eliminated. Since the geometry of the plastic tubing is given by the application, the goal of the simulation is to find a reasonable ratio between the distance of the electrodes and the width of each electrode. Both parameters have been investigated in parallel in Finite Element Simulations. For the simulation the following parameters of the tubing

Dieses Werk ist copyrightgeschützt und darf in keiner Form vervielfältigt werden noch an Dritte weitergegeben werden.
Es gilt nur für den persönlichen Gebrauch.

have been used: the tubing consists of PVC and therefore has a relative permittivity of approximately 3.1. The inner diameter of the tubing is 4.8 mm and the outer diameter is 6.4 mm. The simulation results for electrodes having a width of 1 mm, 3 mm and 5 mm is shown in Fig. 2.17 . The solid line shows the relative change of the sensor signal as a function of the distance between two adjacent electrodes. The dashed line shows the resulting overall capacitance of the sensor. Since the overall capacitance of the sensor is just in the range of a few pF, major goal of the simulation is to find a reasonable compromise between the sensitivity and the overall capacitance. On the one hand the graphs in Fig. 2.17 show that a small distance between the electrodes causes a large overall sensor capacitance but only a poor sensitivity. Referring to Fig. 2.15 this can be explained by an increased C_1 as well as an increased C_2. Large values for C_1 and C_2 cause an additional sensor offset signal and therefore minimize the relative change in capacitance. On the other hand a large distance between two electrodes causes an optimized sensitivity but the sensor will have a relatively low overall capacitance which makes it difficult to measure the low absolute values. In this particular case a reasonable compromise between both scenarios has been chosen. The width of the ring electrodes is set to 5 mm and the distance between two adjacent electrodes is set to 3 mm.

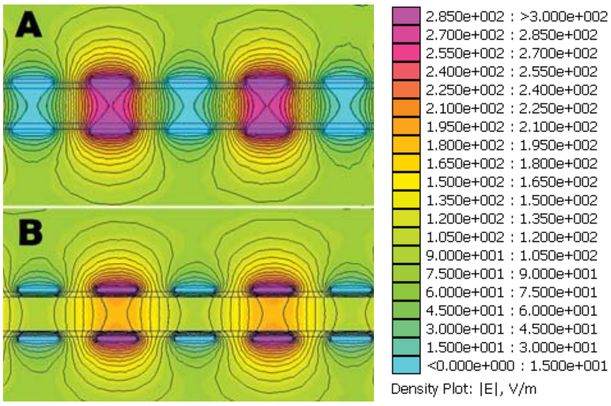

Figure 2.16: Electrical field pattern between the ring electrodes. In A the tubing is filled with air, in B the tubing is filled with water. Due to the high relative permittivity of water compared to the low relative permittivity of the tubing wall material the electric field is distorted and the highest field strength is found in the tubing wall.

Summary of the FEM simulation results

The simulation and analysis of the electric field pattern for both electrode configurations shows that in either case there is a higher sensitivity of the sensor towards the dielectric properties of the tubing wall material than towards a change of the dielectric properties of the medium inside the tubing. The reason for this sensor behaviour is the fact that the tubing wall material typically has a significantly lower relative permittivity than water or similar fluids such as blood inside the tubing. This "offset" is not a problem as long as it remains constant. But since the material for the disposable tubing must be as cheap as possible PVC is chosen in most medical blood circulation circuits. PVC has the drawback that its relative permittivity drifts over temperature which potentially makes the resulting sensor very sensitive to the ambient temperature. However, by analysing the sensor geometry it was possible to optimize the electrode shape and therefore to optimize the remaining small sensitivity of the sensor towards the medium inside the tubing.

Dieses Werk ist copyrightgeschützt und darf in keiner Form vervielfältigt werden noch an Dritte weitergegeben werden.
Es gilt nur für den persönlichen Gebrauch.

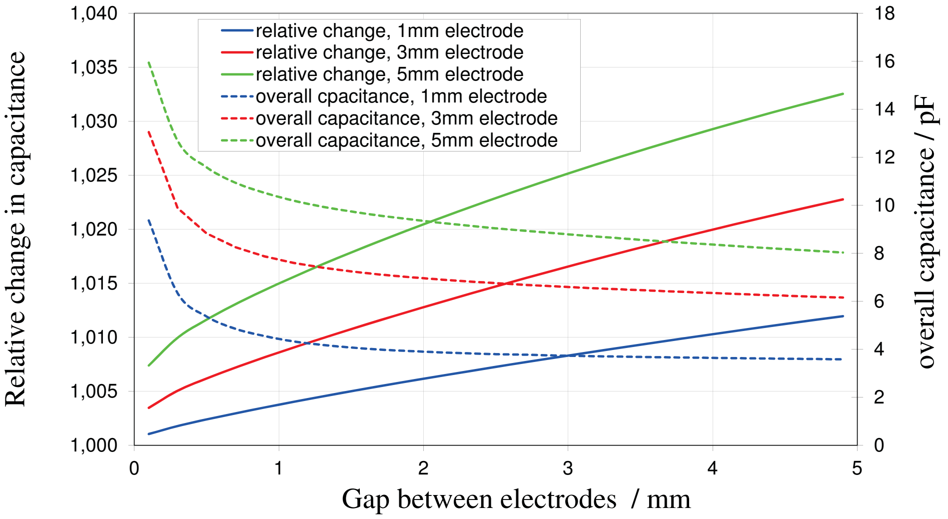

Figure 2.17: FEM simulation result for the sensitivity analysis of the sensor design based on ring electrodes. The graphs show that for each simulated combination the relative sensitivity of the sensor becomes high when the spacing of the electrodes is increased. On the other hand the total capacitance of the sensor is decreased by a wider spacing which makes it more difficult to measure, especially when longer cables have to be attached to the sensor.

2.2.5 Sensor Prototypes

The FEM simulation shows that there is a significant sensitivity of the sensor towards the electric and dielectric properties of the tubing wall. On one hand this means that the tubing wall material parameters itself must be investigated for stability. On the other hand this means that a real construction of a sensor should be done in such a way that the tubing wall geometry remains constant after attaching the sensor to the tubing. Especially PVC has temperature dependent mechanical properties. At higher temperatures (e.g. blood at 37 °C) the PVC material becomes very smooth and any force which is applied to the tubing by an attached sensor can easily cause mechanical deformations which may influence the sensor capacitance. However, it is absolutely required to apply a certain force to the tubing to ensure that there are no air gaps between the tubing and the electrodes which may degrade the sensitivity and which may vary in an undefined way during a longer measurement. Figure 2.18 illustrates this effect for the half-shell electrode design when a force is applied to the tubing via the electrodes. In A the open construction allows for deforming the sensor even with small forces. In B the tubing is completely embedded into the cavity of the solid block of the sensor material and no deformation can occur.

In order to test the two proposed electrode designs two sensor prototypes have been constructed. Both sensor housings are machined out of a solid block of PEEK and have an identical length of 10 cm. Fig. 2.19 shows the construction of the first electrode configuration based on half-shells. Fig. 2.20 shows the second configuration based on ring electrodes. Several laboratory tests over temperature show, that the design with two half-shell electrodes is much more stable and reliable than the design based on ring electrodes. Based on the practical experience gained during the laboratory experiments one important factor is to completely embed the tubing into a cavity of the solid sensor block. This ensures that the shape of the tubing remains constant and yields a stable measurement signal for many hours e.g. during the hemodialysis treatment of the patient. In

Dieses Werk ist copyrightgeschützt und darf in keiner Form vervielfältigt werden noch an Dritte weitergegeben werden.
Es gilt nur für den persönlichen Gebrauch.

most experiments with the ring electrode based prototype the PVC tubing wall material became to weak at temperatures of 37 °C and the tubing was "pressed" inside the free space cavities between the rings. This mechanical deformation and displacement leads to measurement errors in the range of approximately 20 to 50 % and are not reproducible. In theory it would be possible to construct a ring electrode based sensor in such a way that the electrodes are embedded into the solid block of the sensor housing. However, this would require an extensive technical effort for building a prototype as well as for building a real product. Since the half-shell electrode based sensor design is much easier to build and in addition gives stable measurement results in the laboratory experiments this type of sensor is preferred for building a real product. The following in-vitro laboratory measurements have been done with the stable and reliable sensor version based on two half-shell electrodes.

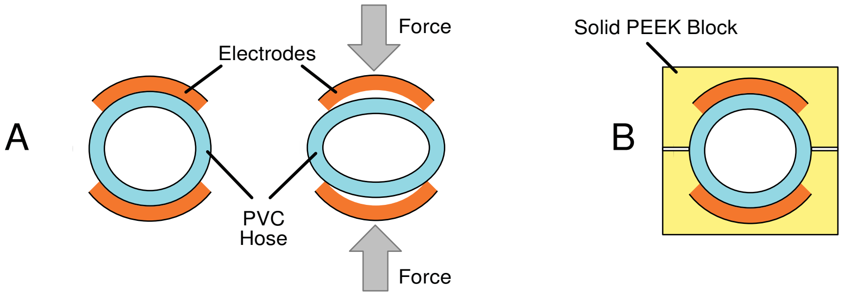

Figure 2.18: Illustration of a possible deformation of the plastic tubing inside the capacitive sensor. Practical experiments in the laboratory show that it is important to completely embed the tubing into a solid block in order to avoid any mechanical deformation and instability.

Figure 2.19: Prototype of a HCT sensor based on the concept with two half-shell electrodes having an optimized electrode angle of 100 degree.

Dieses Werk ist copyrightgeschützt und darf in keiner Form vervielfältigt werden noch an Dritte weitergegeben werden.
Es gilt nur für den persönlichen Gebrauch.

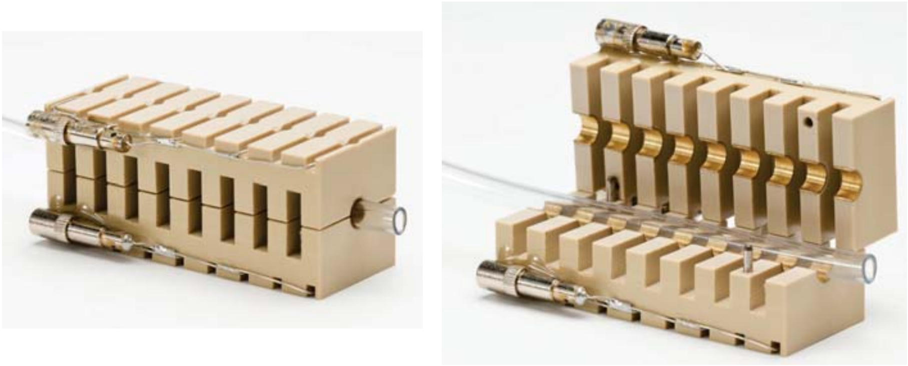

Figure 2.20: Prototype of a HCT sensor based on the concept with ring electrodes having a width of 5 mm and a distance of 3 mm to each other.

2.2.6 Laboratory Measurement Setup

In the laboratory an experimental setup is constructed to simulate an extracorporeal blood circulation system. A block schematic of the setup is shown in Fig. 2.21. A portion of heparinized pork blood is continuously stirred and the blood temperature is regulated to 37.0 °C. A peristaltic pump with an adjustable flow rate of 100 to 500 ml/min pumps the blood through the tubing. The prototype sensor is attached to the tubing and kept inside a controlled temperature chamber. The chamber allows for changing the ambient temperature of the sensor between 10 and 50 °C. The sensor is connected to a programmable remote controlled RLC-Meter (Fluke PM6304). The RLC-Meter measures the capacitance and the phase angle as a function of frequency by applying a sweep starting at 100 Hz and ending at 1.0 MHz. 10 measurements per decade are recorded. The data is automatically transferred to a connected computer for further analysis and evaluation. As a reference method we use an established photometer (Diaglobal Vario Photometer DP 300) with disposable HCT measurement capillaries. According to the documentation the accuracy of the photometer is +/- 2 %, the resolution is 0.1 %. In all experiments the HCT value is measured 8 times with the photometer and the average value is calculated. According to our experience this leads to very reproducible results. Within the first experiment the temperature of the sensor inside the chamber is kept constant at room temperature of 25 °C. The pump is adjusted to a fixed flow rate of 300 ml/min. At the beginning the original blood is used as derived from the pig. After measuring the sensor impedance with the RLC-meter the HCT value is changed by diluting the blood several times with plasma. The plasma is derived from the same original blood sample by centrifugation. Within each dilution cycle the sensor impedance is measured again. Within a second experiment the influence of the temperature to the sensor is examined. In a first measurement setup the tubing is empty in order to exclude frequency dependent effects caused by the fluid. The ambient temperature of the sensor is varied from 10 to 50 °C which already represents a broader range than commonly requested by applications such as hemodialysis or life support machines. The resulting capacitance and the phase angle are measured from 100 Hz to 1.0 MHz at temperature steps of 10 °C. In a second measurement setup the tubing is then filled with blood at 37.0 °C. The blood is diluted with plasma several times as already described for the first experiment. In addition the ambient temperature of the sensor is varied from 15 to 35 °C within 2 steps of 10 °C each. The ambient temperature is limited to this window in order

Dieses Werk ist copyrightgeschützt und darf in keiner Form vervielfältigt werden noch an Dritte weitergegeben werden.
Es gilt nur für den persönlichen Gebrauch.

to protect the blood. In a last experiment the influence of the flow rate is examined. The flow rate of the blood is varied from 100 to 500 ml/min in steps of 100 ml/min. The temperature of the blood is kept constant at 37.0 °C and the ambient temperature of the sensor is kept constant at 25 °C. The HCT value of the blood is varied by dilution with plasma in order to examine the effects of the flow rate for different cell concentrations. All measurement results are presented in detail in the following section V.

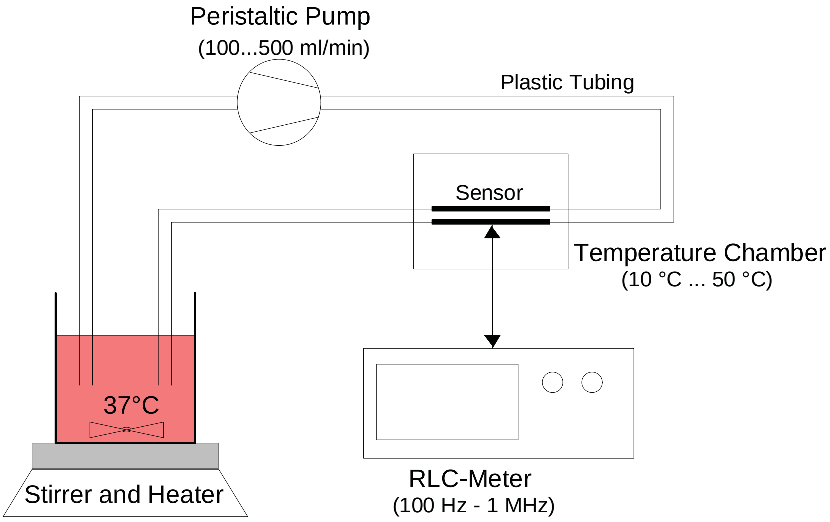

Figure 2.21: Illustration of the laboratory measurement setup constructed for evaluation of the HCT sensor prototype. The setup simulates an extracorporeal blood circulation system as often found in medical systems such as hemodialysis machines.

2.2.7 Hematocrit Measurement Results

Within the first experiment the capacitance and the resulting phase angle of the sensor are measured as a function of frequency for several HCT values. Fig. 2.22 shows a typical plot of the measured capacitance as a function of the frequency at a constant ambient temperature of 25 °C and a blood temperature of 37.0 °C. It can be seen that there is an optimum measurement frequency window in the range of several kHz up to approximately 100 kHz. Here the distance between the plotted curves indicate a good sensitivity of the sensor. At very high frequencies the distance between the plots and thus the sensitivity of the sensor drop. This behaviour is expected and can be explained by the equivalent electrical circuit schematic shown in Fig. 2.10 C. At low frequencies the membrane capacitance C_m of the erythrozytes is high impedant and any displacement current within the dielectric of the capacitor can only flow through the plasma which is represented by R_p. According to [10] the conductivity of the blood depends on the HCT value and therefore R_p will vary. At very high frequencies the cell membrane is virtually short circuited and the current can flow through the plasma as well as through the intracellular volume represented by R_i. The resulting overall conductivity of the blood can be understood as a parallel combination of R_p and R_i and remains almost constant independent of the HCT value. Fig. 2.23 shows the capacitance as a function of the HCT value for three selected frequencies. The plots show the average value of the measurements taken within 7 independent experiments using the blood of seven different pigs. The error bars show the absolute maximum deviation of a measurement from the average value. As expected the slope of the curve and thus the sensitivity of the sensor

Dieses Werk ist copyrightgeschützt und darf in keiner Form vervielfältigt werden noch an Dritte weitergegeben werden.
Es gilt nur für den persönlichen Gebrauch.

is almost equal for the frequencies 10 kHz and 100 kHz but decreases at 1 MHz. At 100 kHz we obtained the smallest variations within all 7 experiments and the sensitivity of the prototype sensor is 32.1 fF per 1 % HCT. It is remarkable that the total measured sensor capacitance of approximately 8 to 9 pF is very close to the FEM simulation result presented in Fig. 2.12 for the tubing filled with water. In addition to the capacitance of the sensor the phase angle between the applied voltage signal and the resulting current is measured by the RLC-meter. For an ideal capacitor a constant phase of 90 degree is expected. However, in this case there are losses caused by the conductivity of the blood which serves as part of the dielectric between the electrodes. The losses are represented by R_i and R_p in the equivalent schematic shown in Fig. 2.10 C. Therefore the phase angle of the sensor shows a typical curve as a function of the frequency. In Fig. 2.24 a typical plot of the phase is presented. Fig. 2.25 shows the derived plot for the phase angle as a function of the HCT value. As in Fig. 10 the graph represents the averaged values obtained in 7 experiments with blood from 7 different pigs and the error bars show the maximum deviation of a sample to the averaged value. The samples are taken at a frequency of 60 kHz since the distance between the plots and thus the sensitivity of the sensor is at its maximum. The resulting sensitivity of the prototype sensor is 0.21 degree phase shift per 1% HCT.

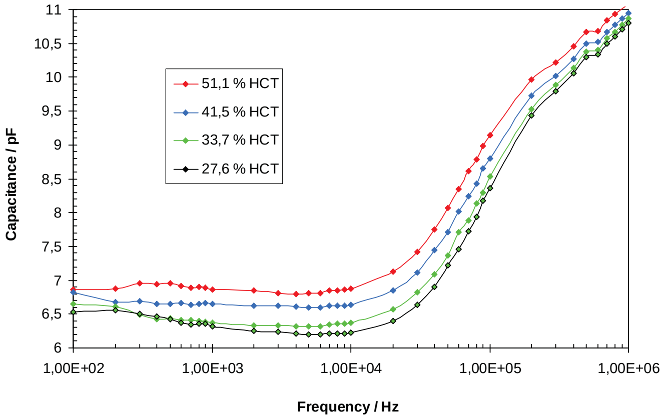

Figure 2.22: The graphs show the measured sensor capacitance as a function of the frequency for different HCT values of the blood. Obviously the sensitivity of the sensor drops at higher frequencies.

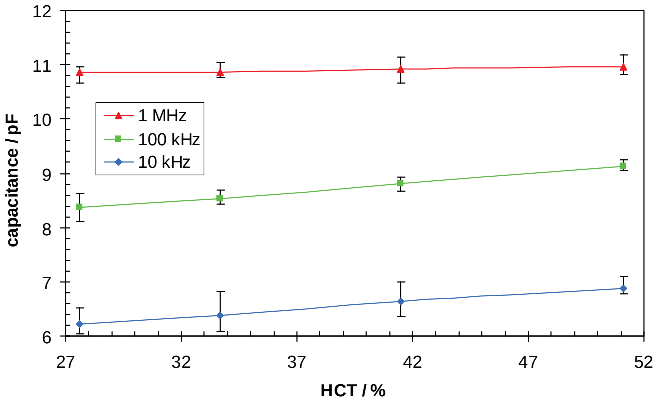

Figure 2.23: The graphs show the measured sensor capacitance as a function of the HCT value of the blood for three selected frequencies. At 10 kHz and at 100 kHz the sensitivity is significantly higher than at 1 MHz.

Dieses Werk ist copyrightgeschützt und darf in keiner Form vervielfältigt werden noch an Dritte weitergegeben werden.
Es gilt nur für den persönlichen Gebrauch.

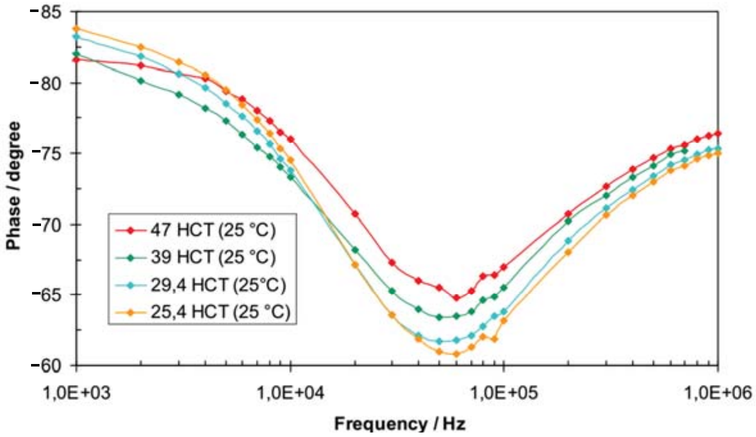

Figure 2.24: The graphs show the measured phase angle as a function of the frequency for selected HCT values of the blood. It can be observed that there is an optimum sensitivity at a frequency of approximately 60 kHz for the prototype sensor.

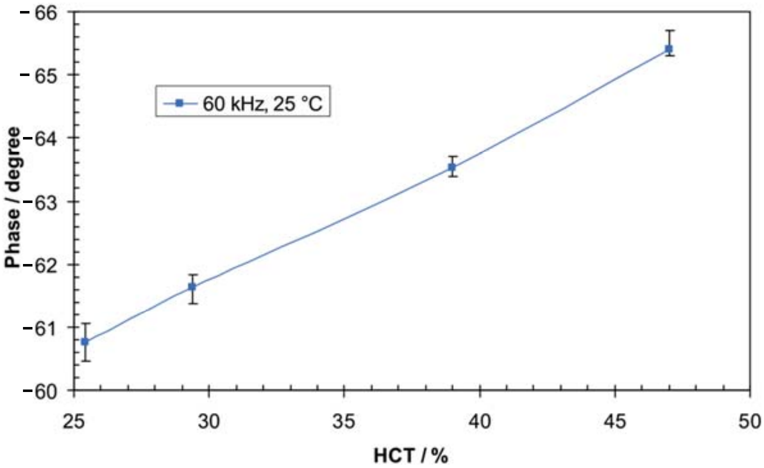

Figure 2.25: The graph shows the measured phase angle as a function of the HCT value for a selected frequency of 60 kHz. According to fig. 2.24 the optimum sensitivity is reached at approximately 60 kHz.

Dieses Werk ist copyrightgeschützt und darf in keiner Form vervielfältigt werden noch an Dritte weitergegeben werden.
Es gilt nur für den persönlichen Gebrauch.

2.2.8 Temperature Drift Measurement

Within the second experiment the influence of the ambient temperature is investigated. The sensor is placed inside a temperature chamber and the ambient temperature is varied from 10 °C to 50 °C. The blood temperature is constant at 37.0 °C. It is expected that the permittivity of the tubing wall material will drift over temperature and therefore decrease the accuracy of the sensor. Fig. 2.26 shows the measured capacitance as a function of the frequency for the empty tubing at three temperatures. The three upper curves are measured with a standard medical grade PVC tubing. The lower three curves are measured just for comparison using PE tubing with the same dimensions. It can be seen that the PVC material shows a large temperature drift whereas PE shows a significantly lower drift. However, PVC is the standard material for cheap medical tubing and replacing the material is not applicable in many situations. Fig. 2.27 shows the capacitance of the sensor as a function of the temperature for two selected frequencies. At 100 kHz the drift is in the range of 22 fF per degree Celsius and at 1 MHz the drift is in the range of 15 fF per degree Celsius. In addition to the capacitance the phase angle is measured. The result is shown in Fig. 2.28 for PVC tubing at three different temperatures. Obviously the phase angle is only slightly affected by the temperature. The random variations within the graph are caused by the limited accuracy and resolution of the RLC-meter. Fig. 2.29 shows a plot for the phase angle as a function of the temperature for the two frequencies 100 kHz and 1 MHz. In the next experiment the tubing is filled with blood at 37.0 °C and the ambient temperature of the sensor is varied in two equal steps of 10 °C from 15 °C to 35 °C. The blood is diluted with plasma and the resulting sensor impedance is measured. Since the temperature drift of the capacitance is very large compared to the sensor signal, the phase angle measurement method is preferred in a later design. Details are discussed in the following section. Fig. 2.30 shows multiple phase angle plots as a function of the frequency for three different temperatures and 4 different HCT values. The data is obtained during three independent dilution series using the same original blood sample from one pig. Fig. 2.31 shows the phase angle as a function of the HCT value for the three dilution series at different temperatures. The three curves are almost identical which means that the phase measurement is almost not affected by the ambient temperature. This result fits very well to the graph shown in Fig. 2.29 where the very low drift of approximately 0.0075 degrees per 1 °C is presented.

Dieses Werk ist copyrightgeschützt und darf in keiner Form vervielfältigt werden noch an Dritte weitergegeben werden.
Es gilt nur für den persönlichen Gebrauch.

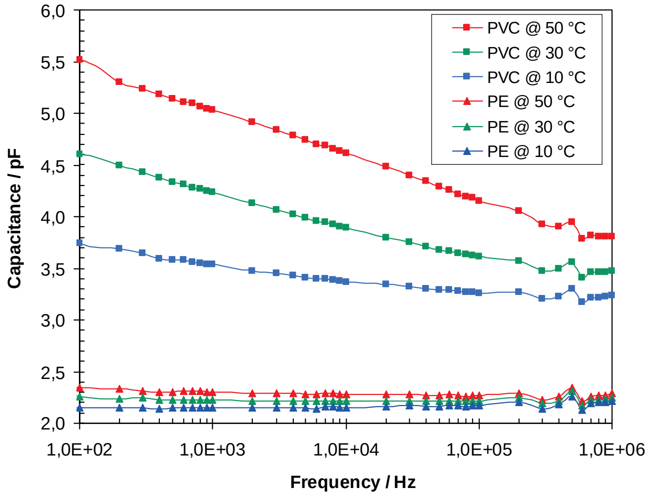

Figure 2.26: Capacitance as a function of the frequency for three selected temperatures. The three upper curves are for PVC tubing material and the three lower curves are for a PE tubing.

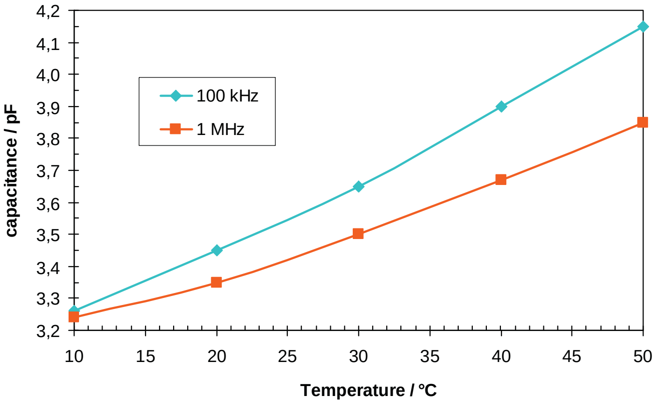

Figure 2.27: Capacitance as a function of the temperature for two selected frequencies. The graph shows that the sensor is significantly influenced by the temperature at both frequencies. The gradient is approx. 22 fF per degree Celsius at the measurement frequency of 100 kHz.

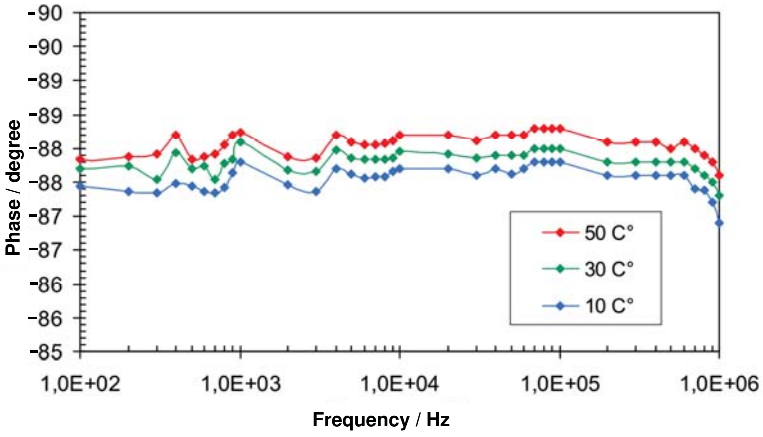

Figure 2.28: Measured phase angle as a function of frequency for three selected ambient temperatures of the sensor. The resulting temperature drift is presented in Fig. 2.29

Dieses Werk ist copyrightgeschützt und darf in keiner Form vervielfältigt werden noch an Dritte weitergegeben werden.
Es gilt nur für den persönlichen Gebrauch.

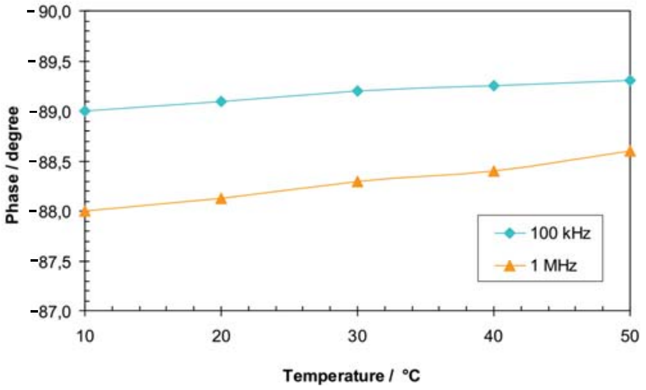

Figure 2.29: Phase angle as a function of the temperature for two selected frequencies. The drift is almost independent of the frequency and is approximately 0.0075 degrees per 1 °C.

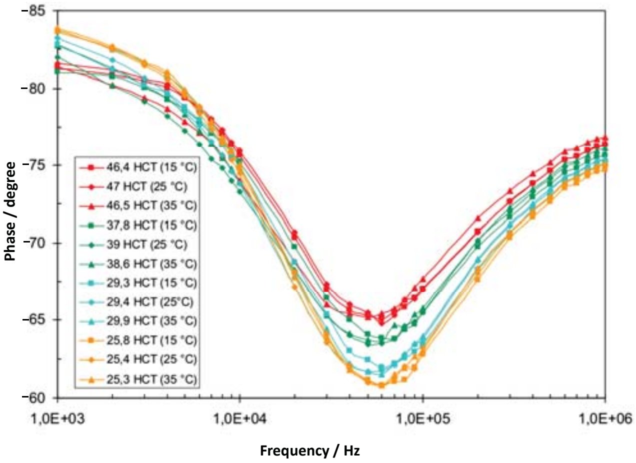

Figure 2.30: Phase angle as a function of the frequency for 4 different HCT values at three different temperatures. The best sensitivity of the sensor is found at approximately 60 kHz where the spacing between the curves is maximized.

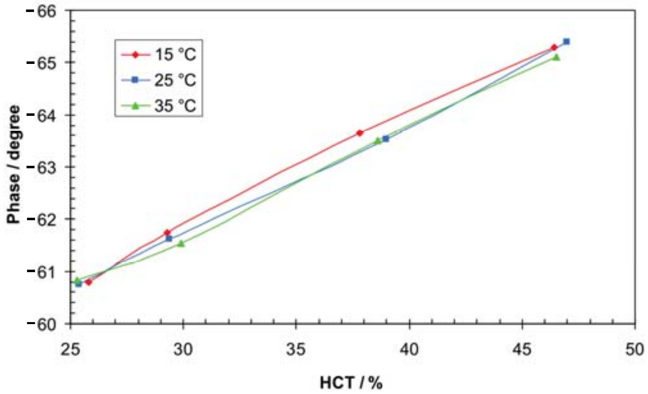

Figure 2.31: Phase angle as a function of the HCT value for three different ambient temperatures of the sensor. All three graphs are almost identical and show a constant gradient of approx. 0.21 degree phase shift per 1 % HCT which means that the phase measurement principle is almost not affected by a change in the ambient temperature of the sensor.

Dieses Werk ist copyrightgeschützt und darf in keiner Form vervielfältigt werden noch an Dritte weitergegeben werden.
Es gilt nur für den persönlichen Gebrauch.

2.2.9 Measurement at different Flow Rates

In the last experiment the influence of the blood flow rate to the measurement is investigated. A blood sample at 37.0 °C is pumped with different flow rates from 100 ml/min to 500 ml/min through the sensor. The ambient temperature of the sensor is 25 °C. Fig. 2.32 shows the measured capacitance and Fig. 2.33 shows the measured phase angles as a function of the flow rate for three different HCT values. The capacitance is measured at a frequency of 100 kHz as in Fig. 2.27, the phase angle is measured at a frequency of 60 kHz. The curves in both diagrams are parallel which means there is no visible influence of the flow rate on the measurement within the tested range and for the given tubing dimensions with an outer diameter of 6.4 mm and a wall thickness of 0.8 mm.

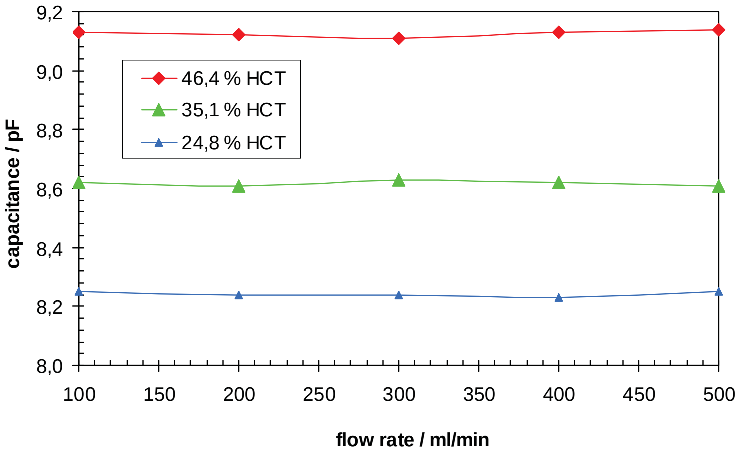

Figure 2.32: Capacitance as a function of the flow rate for three different HCT values. The measurement is done at a frequency of 100 kHz where a good sensitivity is expected.

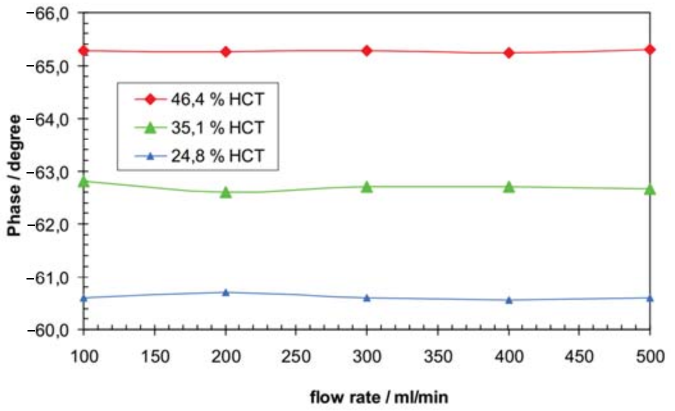

Figure 2.33: Phase angle as a function of the flow rate for four different HCT values. The phase measurement is done at a frequency of 60 kHz where the sensitivity is expected to be in a good range.

Dieses Werk ist copyrightgeschützt und darf in keiner Form vervielfältigt werden noch an Dritte weitergegeben werden.
Es gilt nur für den persönlichen Gebrauch.

2.2.10 Analysis and Discussion of Measurement Results

The measurement results clearly show that in principle both measurement methods (capacitance and phase angle) individually allow to measure the HCT value of a blood sample inside plastic tubing. However, the simulation results already showed that the capacitive sensor will always be more sensitive to the dielectric tubing wall material properties than to the fluid inside the tubing because of the large voltage divider effect caused by the large difference in the permittivity between PVC and water (or blood). As a result the influence of the temperature to the measurement of the capacitance is very large. According to Fig. 2.23 the sensor output signal varies 32.1 fF per 1 % change of the HCT value and according to Fig. 2.27 the influence of the ambient temperature causes a change of approximately 22 fF per 1 °C change of the ambient temperature. In other words, a change of 1 °C in the ambient temperature is equal to the signal change caused by a HCT variation of 0.68 %. Within the tested ambient temperature range of 10 to 50 °C the sensor can drift up to 40 * 22 fF = 880 fF in the capacitance which is equal to a change of 27.4 % in the HCT value. This means the sensor is very sensitive to the ambient temperature and the resulting accuracy is poor when there is no additional temperature compensation. One interesting concept for intrinsic temperature compensation is to measure the capacitance at least at two different frequencies. According to Fig. 2.22 and Fig. 2.23 the sensitivity of the sensor towards a change of the HCT value is frequency dependent. At a frequency of 100 kHz there is a much larger sensitivity observed than at a frequency of 1 MHz. At 1 MHz the sensor is already very insensitive to the HCT value, but according to Fig. 2.27 the sensor is still sensitive to the ambient temperature. A partial temperature compensation scheme can be implemented by measuring the capacitance at two frequencies and then correcting the HCT value. The HCT measurement is done at 100 kHz and the temperature information is derived at a higher frequency of 1 MHz. If the sensor would be completely insensitive to the HCT value at the high frequency measurement, in theory a perfect compensation could be reached. However, within the tested range of up to 1 MHz this is not the case and therefore only a partial compensation can be achieved. With the data of the graph shown in Fig. 2.27 we could mathematically compensate the drift to a level, where an accuracy of approximately 8 % is reached. We assumed that the curves in Fig. 2.27 are linear.

The second measurement principle is based on the frequency dependent phase angle. The capacitor is not ideal because of losses inside the dielectric (blood). Since the conductivity of the plastic tubing material is extremely low compared to blood and the used measurement frequencies are still relatively low, there are almost no dielectric losses expected within the tubing walls. According to Fig. 2.29 this assumption is true since the measured phase angle of an empty tubing is close to 90 degrees. In addition it can be expected that the temperature has only a minor impact to the phase angle. At least within the tested temperature range this assumption could also be proved as shown in Fig. 2.29. The measured drift is only approx. 0.0075 degrees per 1 °C. Compared to the sensitivity of the phase angle towards a change in the HCT value of approx. 0.21 degrees per 1 % HCT the temperature drift is almost negligible. Within the tested range of 10 to 50 °C the temperature drift could potentially cause a drift in the phase angle of 40 * 0.0075 ° = 0.3 ° which is equal to only 1.4% HCT value. This effect is already below the accuracy of the used reference measurement method of 2 %. As a result temperature compensation is not required for the phase measurement method. Without any temperature compensation the measurement results of all 7 pig blood samples show an accuracy better than 4%.

Dieses Werk ist copyrightgeschützt und darf in keiner Form vervielfältigt werden noch an Dritte weitergegeben werden.
Es gilt nur für den persönlichen Gebrauch.

2.2.11 Summary and Conclusions

A new capacitive sensor for on-line HCT measurement of a blood sample inside a plastic tubing without direct contact to the blood is developed. The proposed capacitive sensor design is investigated in detail within several FEM simulations and multiple in-vitro experiments in the laboratory. The FEM simulation results clearly show how to optimize the sensitivity of the sensor by choosing the right electrode geometry and furthermore leads to a understanding of potential limits such as the expected temperature drift caused by the material of the tubing walls. The measurement results derived in the laboratory support the simulation results very well. The two different "sensor signals" capacitance and phase angle have been measured within several experiments. As an overall result both concepts will work in theory whereas the phase measurement approach shows much better accuracy and especially no problems associated with a drift of the ambient temperature of the sensor. Another more practical advantage of the phase measurement principle against the capacitance measurement principle is the fact, that it is much easier to built a precision electronic circuit for measuring the phase of a sensor signal than measuring a relatively small total capacitance of a few pF with an accuracy of a few fF. This allows for practically replacing the used laboratory RLC-meter by a small and cheap phase-measurement electronic. The development of such a circuit is described in chapter 4.

Advantages of the proposed phase measurement concept compared to other state-of-the-art measurement methods such as ultrasound and optical methods is the low sensitivity to tolerances of the tubing wall material since the measured losses do not occur in the tubing wall material. The colour of the material and the optical properties are not relevant and the temperature has only a very small influence. Especially to ultrasound systems this is an advantage since they commonly rely on stable acoustic properties of the tubing material and a stable coupling of the ultrasound signal between the transducer and the tubing.

Dieses Werk ist copyrightgeschützt und darf in keiner Form vervielfältigt werden noch an Dritte weitergegeben werden.
Es gilt nur für den persönlichen Gebrauch.

2.3 Tissue Discrimination for Needle and Cannula Guidance

The presented research results of this section have previously been published as a regular conference paper and as a regular journal paper. The following section mainly consists of merged text of the published articles. In addition each introduction has slightly been adapted to the text flow of this dissertation. At the beginning of this section the preliminary results obtained for a solid coaxial needle in combination with the TDR measurement principle are presented which have been published at the conference. Afterwards an improved system concept based on a hollow coaxial cannula and chirp measurement signals is presented which has identically been published as a journal paper. The numbering of the subsections, figures and references are adapted to the overall numbering of this dissertation. A detailed description of the originally published work and the individual contributions of the author and the co-authors is given below.

D. Trebbels, M. Jugl, R. Zengerle:

Real-Time Cannula Navigation in Biological Tissue with high temporal and spatial resolution based on Impedance Spectroscopy
IEEE EMBC 2010, 32nd Annual International Conference of the IEEE EMBS, pp. 1886-1889, Buenos Aires, August 31-September 4, 2010

Contributions to this publication:

1. D. Trebbels: Development of the System Concept, FEM Simulation, Laboratory Measurements and Manuscript Preparation including Literature Reserach.
2. M. Jugl: Construction of Coaxial Cannulas, Preparation of Mechanical Drawings
3. R. Zengerle: Discussion of Results, Scientific Advice during Manuscript Preparation

D. Trebbels, F. Fellhauer, M. Jugl, G. Haimerl, M. Min, R. Zengerle:

On-line Tissue Discrimination for Transcutaneous Needle Guidance Applications Using Broadband Impedance Spectroscopy
IEEE Transactions on Biomedical Engineering, VOL. 59, NO 2, pp. 494-503, Feb. 2012

Contributions to this publication:

1. D. Trebbels: Literature Reserach, Development of the Measurement Concept and Laboratory Equipment, FEM Simulation, Data Analysis, Supervision of Felix Fellhauer (Student) and Manuscript Preparation.
2. F. Fellhauer: Assistance in the Laboratory (as a Part of his Student Internship)
3. M. Jugl: Construction of Coaxial Cannulas, Assistance during Experiments, Preparation of Mechanical Drawings
4. G. Haimerl: Organisational Assistance for In-Vivo Experiments
5. M. Min: Conceptual Discussions about Measurement Signals and Processing
6. R. Zengerle: Discussion of Results, Scientific Advice during Manuscript Preparation

Dieses Werk ist copyrightgeschützt und darf in keiner Form vervielfältigt werden noch an Dritte weitergegeben werden.
Es gilt nur für den persönlichen Gebrauch.

2.3.1 Introduction and Overview

Needle and cannula guidance during transcutaneous surgical interventions is a common challenge in many medical applications such as fine needle biopsies [23], regional anaesthesia [164], drug delivery [164], catheter insertion [165], vessel puncture [166] and brachytherapy [167]. In all of the listed applications it is important to place the needle tip inside a well defined tissue type of the human body whereas often the exact 3D-orientation of the needle is of minor importance.

Within this thesis a coaxial needle design and a coaxial cannula design are proposed. The coaxial design gives the option to have two conductors which reach up to the end of the needle or cannula tip and which can be used for feeding broadband measurement signals to the tissue which is in contact to the tip. A finite element simulation has been done for a solid coaxial needle and for a hollow coaxial cannula in order to investigate the size of the sensitive area in which the resulting current distribution inside the tissue generates a tissue specific complex measurement signal. Prototypes of a solid needle and a hollow cannula have been constructed and tested in the laboratory. The solid coaxial needle was a preliminary step in the development cycle because it is relatively easy to build and test. As a broadband measurement signal a step pulse signal was used. Based on the laboratory measurement results it was decided to further improve the measurement strategy and the step pulse signal was replaced by short chirp signals and an appropriate signal processing scheme has been developed. The chirp signal based measurement approach has been done with the coaxial hollow cannula design. Focus of both measurement signals and methods was to measure the impedance of the tissue at the needle tip within a short period of time in order to obtain a "real-time" system which can be used during surgical interventions and which gives direct feedback to the surgeon during the dynamic needle insertion process.

All above mentioned experiments have been done with laboratory measurement devices. Based on the obtained measurement results parameters for a specification of an electronic measurement circuit have been derived. Appropriate electronic circuits and signal processing is developed for each signal (step pulse and chirp signals). The development of the electronic circuits is described in detail in chapter 4 in this thesis.

2.3.2 Existing Needle Guidance Methods

Today there are several approaches to accomplish the exact needle placement based on 2D or 3D imaging systems which allow for controlling the needle orientation and position and support the surgeon during the needle insertion procedure. Three well known systems are Magnetic Resonance Imaging (MRI), Computer Tomography (CT) and X-Ray fluoroscopy [168–170]. All systems work very well and give good spatial resolution but are too expensive for widespread use. In addition CT and X-Ray fluoroscopy expose the patient to ionizing radiation. Furthermore fluoroscopy provides only a limited contrast for soft-tissues which is a crucial point for needle guidance. Alternative imaging systems are based on ultrasound (US) [171, 172]. There are several ultrasound systems available on the market but major drawbacks are the limited penetration depth and the limited field of view. In addition it is difficult to analyse the exact type of soft tissue close to the needle tip by using US. The use of force-feedback systems [173] in combination with imaging based systems or robots [174] can improve the needle steering process but the overall system again becomes quite complicated and expensive. In some actual research projects micro sensors are integrated in the needle tip [175] but deal with the inherent lack of space given by the thin needle geometry and the low-cost requirements for disposable medical

Dieses Werk ist copyrightgeschützt und darf in keiner Form vervielfältigt werden noch an Dritte weitergegeben werden.
Es gilt nur für den persönlichen Gebrauch.

equipment. A promising alternative approach for exact on-line tissue classification at the needle tip during the insertion process into the human body is broadband impedance measurement, often referred to as impedance spectroscopy. This method is based on the continuous measurement of the characteristic impedance spectrum of a small volume of tissue around the needle tip. The measured spectrum is analysed and the exact type of tissue can be determined. Kalvoy et al. already presented preliminary results of their configuration based on a monopolar needle electrode where the impedance is measured against a reference electrode [176,177]. The results look promising but a drawback of the system is the need for the additional reference electrode and due to the current density distribution the achievable spatial resolution is limited to a spherical volume having a diameter of approximately 3 to 4 times the needle diameter. The new coaxial needle design which is introduced in this thesis enhances the spatial resolution of the system because the current flows only through a small tissue volume very close to the needle tip. An exact analysis of the achievable spatial resolution is given in the following sections based on FEM simulation results.

2.3.3 Needle Guidance based on Step-Pulse Measurements

This chapter shows and explains the first implemented coaxial needle system which employs step pulse signals as a broadband measurement signal. Objective of the developed measurement system is to gain information about the tissue type close to the tip of the cannula. Because of the thin cannula design there is almost no space for placing electrodes or other sensing equipment on the cannula tip. Therefore the proposed cannula design shown in 2.34 forms a coaxial probe which serves as a waveguide. Remote measurement equipment is connected to the waveguide probe via a coaxial cable. The complete measurement setup is shown in Fig. 2.35. An arbitrary signal generator feeds a step pulse measurement signal into the cable. The signal travels along the cable and the cannula until it reaches the cannula tip. From the electrical point of view the tip forms an open ended coaxial cable and therefore the signal is reflected. The reflected signal travels back along the cable and superposes to the input signal. The resulting waveform is continuously sampled by a high-speed sampling unit such as a fast digital oscilloscope. If the cannula tip is in contact with biological tissue not all measurement signal components are fully reflected since the tissue acts as a complex load impedance at the end of the waveguide as illustrated in Fig. 2.37. According to the Cole- Cole model for tissue the load impedance is frequency dependent and characteristic for each tissue [139–141]. The resulting shape of the partially reflected and phase shifted measurement signal superposed to the input signal carries tissue specific information which can be analysed and potentially be used for tissue classification. For measuring an impedance spectrum of a sample many impedance spectroscopy based systems use sine wave sweeps. The drawback of a sweep is the duration required for capturing the complete impedance spectrum within the relevant frequency range. Since the developed system is intended to be used for dynamic cannula guidance, Time- Domain-Reflectometry (TDR) is used as an alternative method. Therefore the signal generator in Fig. 2.35 generates a periodic rectangular signal. According to Fourier such a signal is composed of the fundamental superposed by harmonics and has a broad spectrum. The traditionally required frequency sweep is replaced by applying all relevant frequencies at the same time by a rectangular pulse. Fig. 2.38 illustrates the Fourier-Components of a step pulse signal as superposed harmonics.

Dieses Werk ist copyrightgeschützt und darf in keiner Form vervielfältigt werden noch an Dritte weitergegeben werden.
Es gilt nur für den persönlichen Gebrauch.

Figure 2.34: Prototype of a solid coaxial needle as constructed for the first experiments. The measurement signal is fed to the needle tip on the inner conductor. The outer wall of the needle serves as a grounded reference electrode which is isolated from the inner conductor.

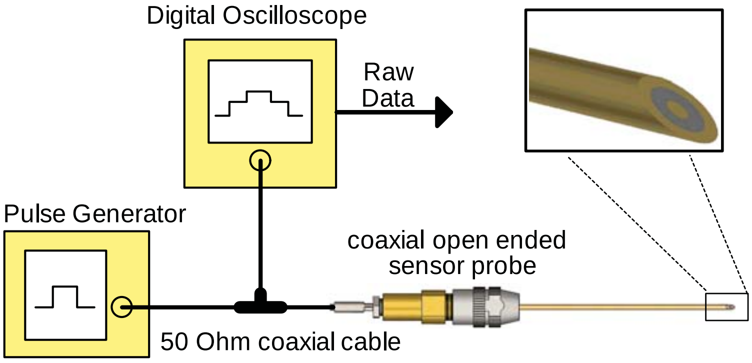

Figure 2.35: Laboratory measurement setup for experiments with a coaxial needle. A signal generator injects periodic rectangular step pulses into the cable. The resulting waveform is captured by a fast oscilloscope and can be analysed.

Figure 2.36: Photograph of a coaxial needle tip which is inserted into biological tissue during laboratory experiments.

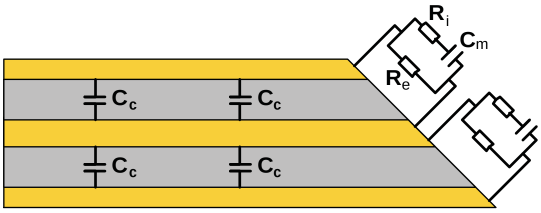

Figure 2.37: The biological tissue forms a frequency dependent electric load at the open end of the coaxial needle.

Dieses Werk ist copyrightgeschützt und darf in keiner Form vervielfältigt werden noch an Dritte weitergegeben werden.
Es gilt nur für den persönlichen Gebrauch.

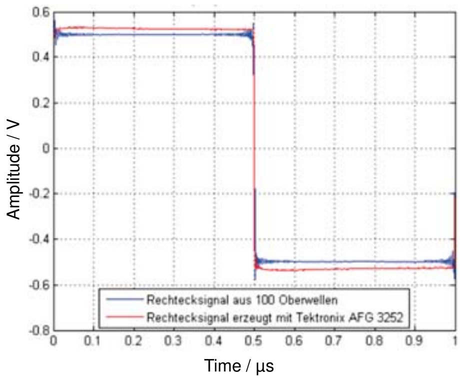

Figure 2.38: A periodic step pulse signal consists of a fundamental and superposed harmonics. Such a signal can be used for broadband impedance measurement. In case of the coaxial needle design each component is individually reflected at the needle tip depending on the tissue properties.

2.3.4 FEM Simulation of a solid Coaxial Needle

In order to investigate the achievable spatial resolution of the coaxial needle design the current flow inside the tissue close to the needle tip is simulated with finite element simulations. The investigated needle has an outer diameter of 1.25 mm, an inner diameter of 0.8 mm and a coaxial inner wire of 0.3 mm. The tip has an angle of 30 degrees. A low frequency finite element simulation shows the resulting current density distribution in a homogeneous tissue when a voltage signal is applied to the inner coaxial wire and the outer wall of the needle is at ground potential as well as the boundaries of the simulated tissue volume (10 x 10 x 10 cm^3). Fig. 2.39 illustrates the created FEM Model with enhanced resolution close to the tip of the needle. Fig. 2.40 A shows the voltage pattern and Fig. 2.40 B the resulting current density pattern. The absolute values are dependent on the applied signal level and the tissue parameters but are not relevant for a relative sensitivity analysis. Fig. 2.40 C illustrates the investigated volume in longitudinal direction in front of the tip. The volume is virtually subdivided into thin slices with a thickness of 0.1 mm.

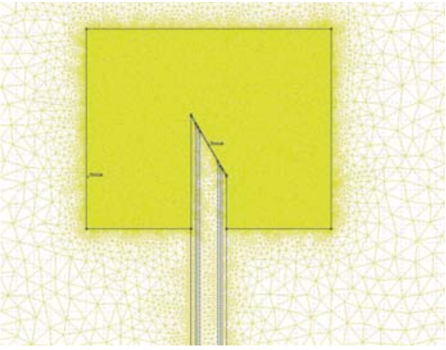

Figure 2.39: FEM simulation model for the coaxial needle tip. The mesh size is reduced around the needle tip for increased simulation resolution.

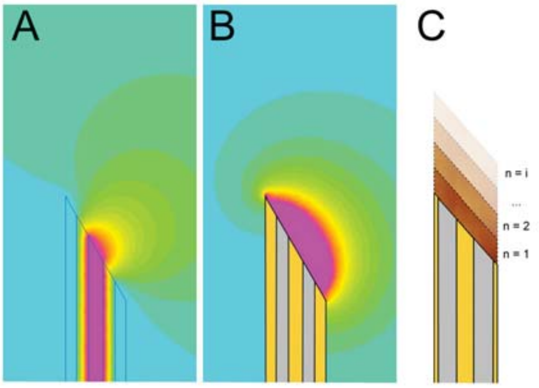

Figure 2.40: FEM simulation results for a solid coaxial needle tip. A shows the potential, B the resulting current density pattern and C the virtual subdivision of the tissue volume in front of the tip for the sensitivity analysis.

Dieses Werk ist copyrightgeschützt und darf in keiner Form vervielfältigt werden noch an Dritte weitergegeben werden.
Es gilt nur für den persönlichen Gebrauch.

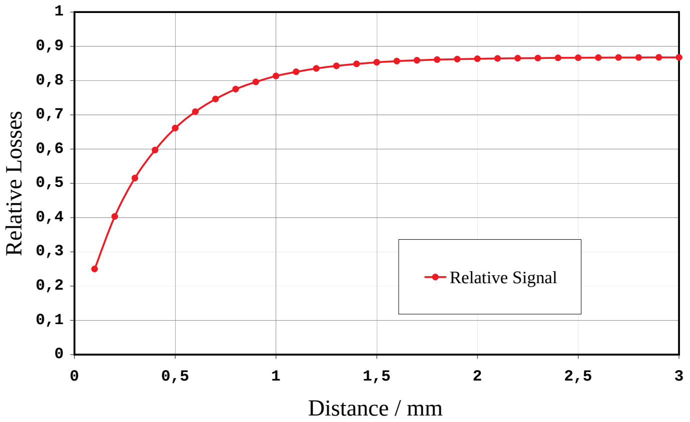

Figure 2.41: FEM simulation result for the sensitivity study of the needle tip. Approximately 81 % of all losses are generated within a distance of 1.0 mm to the tip.

The losses generated by the tissue within the slices are compared to the total tissue losses. The result is presented in Fig. 2.41. The graph shows the relative losses as a function of the distance to the cannula tip. According to the simulation results approximately 81 % of all losses are generated within a distance of 1.0 mm and 85 % within a distance of 1.5 mm.

2.3.5 Laboratory Measurements with a solid Coaxial Needle

The previously described coaxial cannula is tested in the laboratory during in-vitro experiments. A Tektronix AFG 3252 is used as stable signal generator and feeds rectangular pulses with sharp rising edges into the coaxial line and the connected coaxial needle at a fundamental frequency of 5 kHz. The resulting waveform is captured using a fast digital oscilloscope (LeCroy WaveRunner 104 Xi). The laboratory setup is prepared as shown in Fig. 2.35. The cannula tip is inserted into three different pork tissues: fat, muscle and blood. Fig. 2.42 shows the measured waveforms of the resulting signal. The first rising edge arises out of the voltage divider created by the inner generator impedance and the characteristic wave impedance of the cable. Then the signal level remains constant while the rising edge travels to the cannula tip and back to the signal generator. The partially reflected signal superposes to the input signal and forms the second rising edge. Only the shape of the second rising edge contains information about the tissue impedance on the cannula tip. This signal is analysed in time domain. Fig. 2.43 compares the average signal level of all tissues after t = 14.0 ns which have been derived in 9 experiments. The error bars show the maximum absolute deviation from the average values.

Dieses Werk ist copyrightgeschützt und darf in keiner Form vervielfältigt werden noch an Dritte weitergegeben werden.
Es gilt nur für den persönlichen Gebrauch.

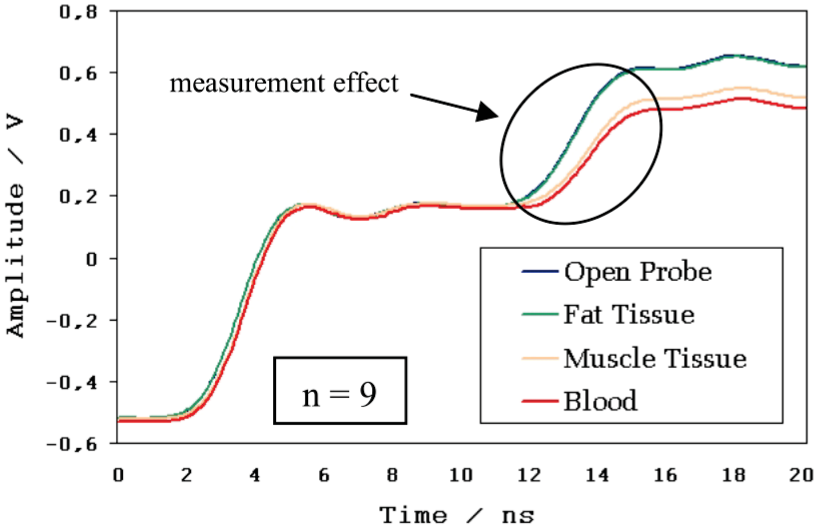

Figure 2.42: Captured TDR traces with different tissue types at the coaxial needle tip. The first rising edge is caused by the voltage divider between the signal generator output impedance and the wave impedance of the cable. The second rising edge is the reflected and superposed measurement signal which carries information about the load at the needle tip.

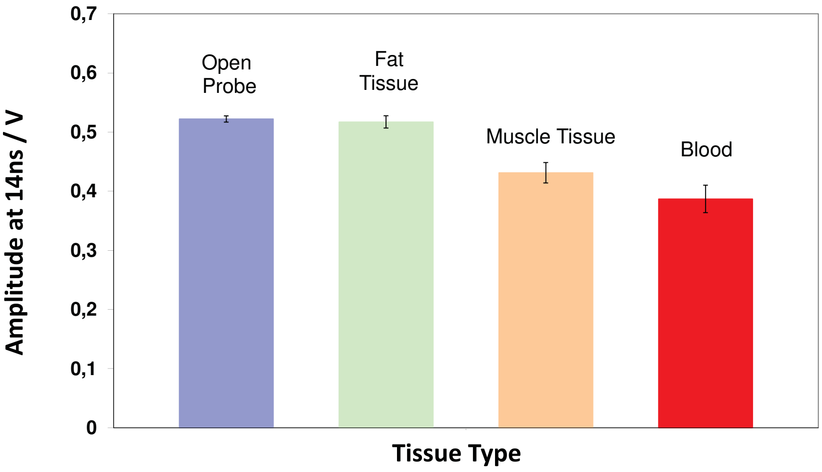

Figure 2.43: Comparison of the characteristic measurement signal amplitude at a fixed delay of 14 ns after exciting the pulse. All tested tissues cause individual signal distortions and it is possible to distinguish between the tested three tissue types. It is not possible to distinguish between an open probe end and fat tissue because of the low conductivity of fat. The presented result is the average of 9 measurements.

Dieses Werk ist copyrightgeschützt und darf in keiner Form vervielfältigt werden noch an Dritte weitergegeben werden.
Es gilt nur für den persönlichen Gebrauch.

2.3.6 Conclusions for the Step-Pulse Signal based Coaxial Needle Concept

The FEM-Simulation results of the new coaxial design show a very good spatial resolution. More than 80 % of the measurement signal of the prototype cannula with an outer diameter of 1.25 mm are generated in a distance smaller than 1.0 mm to the cannula tip. Advantage of the coaxial cannula tip compared to monopolar needles is the small distance between the inner conductor and the outer conductor which leads to a small and well defined sensitivity zone. The open end of the coaxial waveguide simply forms two electrodes and allows for measuring the tissue impedance without the need for an additional reference electrode. In order to optimize the measurement speed of the system Time-Domain-Reflectometry as fast measurement method has been chosen. For determination of characteristic tissue impedance within a short period of time broadband rectangular pulses are applied to the tissue and the response is analysed in time domain. The in-vitro experiments and the measurement signal analysis show that the system concept works and that it is possible to distinguish between the different tested tissue types. However, the reflected signal amplitudes are relatively close to each other so that the reliability and the robustness of a tissue classification might be poor. In addition it is expected that it will be not possible to distinguish between a large quantity of tissues, only a few tissues which have significantly different conductivities such as fat, muscle and blood can be classified. In theory it would be possible to analyse the reflected signal in the frequency domain after transforming the captured time domain signal. In reality there are two main problems associated with this approach: First the incident and the reflected signal components have to be separated from each other and second the amplitude of the higher harmonics is very low which means a poor signal to noise ratio (see also Fig. 2.38). The mentioned drawbacks of the step-pulse signal and the TDR measurement principle lead to the conclusion, that a different short broadband signal with better spectral properties should be used in order to generate a measurement signal with a good signal to noise ratio over the entire covered frequency range. Captured measurement signals with such robust broadband properties can be evaluated in the frequency domain after transformation and often yield precise results. The next sections describe an improved system based on broadband chirp signals which replace the step-signals.

Dieses Werk ist copyrightgeschützt und darf in keiner Form vervielfältigt werden noch an Dritte weitergegeben werden.
Es gilt nur für den persönlichen Gebrauch.

2.3.7 Improved System Concept and Model for a Coaxial Cannula

The previously described system based on a solid coaxial needle showed good simulation results for the spatial resolution of the measurement. For this reason the coaxial design is kept and a second coaxial prototype is constructed for laboratory measurements. However, in most medical applications a hollow cannula is required instead of a solid coaxial needle. The second constructed prototype is a coaxial hollow cannula as illustrated in Fig. 2.44. There are two stainless steel tubes isolated by a thin layer of non conductive material.

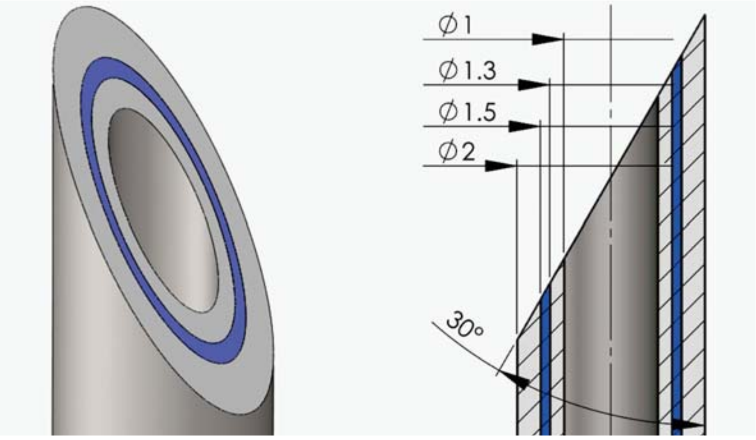

Figure 2.44: Drawing of the coaxial hollow cannula prototype. Two stainless steel tubes are electrically isolated against each other by a thin PTFE layer.

The inner stainless steel tube serves as electrical conductor for the measurement signal whereas the outer stainless steel tube is at ground potential. Current can only flow from the inner conductor to the outer conductor when the cannula tip is inserted into a conductive media. When the cannula is inserted into biological tissue, the tissue forms a frequency dependent electrical load on the cannula tip as already illustrated in Fig. 2.37 for the solid coaxial needle. In Fig. 2.45 A the equivalent schematic is enhanced by a second schematic which approximates the frequency dependent impedance of a polarisation layer which is typically found when a metal electrode is in direct contact with an aqueous electrolyte [52, 54]. The effect can be explained by a rigid double layer which is caused by metal ions on the electrode surface and corresponding counter ions in the electrolyte. Often this layer is referred to as Helmholtz layer. In addition there is a weaker diffusion layer caused by the electrostatic coulomb forces of the charged metal surface, often referred to as Gouy-Chapman layer (see Fig. 2.45 C). The equivalent circuit model for the two layers consist of a common layer capacitance C_{pol} and the two elements R_{pol} and ZW. R_{pol} represents the resistive behaviour of the charge transfer within the Helmholtz layer and is almost frequency independent. ZW represents the impedance of the Gouy-Chapman layer and is frequency dependent. Often this frequency dependency is modelled by a constant phase element. The resistive properties of the electrolyte bulk material are already represented by R_p of the tissue model and therefore here not included in the double layer model. Fig. 2.46 shows the effect of a typical polarization layer. The measured impedance of a tissue sample is significantly influenced at low frequencies up to several kHz. At higher frequencies above 10 kHz the capacitive effect of the layer becomes low-impedance and does almost not affect the measurement accuracy. For tissue classification it would be ideal to measure the broadband impedance of the tissue only and eliminating the parasitic effects caused by the electrode polarization. However, this

Dieses Werk ist copyrightgeschützt und darf in keiner Form vervielfältigt werden noch an Dritte weitergegeben werden.
Es gilt nur für den persönlichen Gebrauch.

is practically impossible due to the 2-electrode interface formed by the needle tip. All measurement results will always be a combination of the tissue transfer function and the electrode polarization transfer function. Calibration and precision correction of the polarization effects is also practically not applicable because the polarization itself depends on characteristic tissue properties such as the conductivity of the bulk material as well as on measurement signal parameters such as the applied voltage level and the resulting current density. In addition a calibration (e.g. in saline) for each hollow needle means a significant amount of effort. In the ideal case it would be possible to measure directly without the need for any calibration procedure. Throughout the following sections in this thesis it was decided to go a straight way and simply measure the resulting overall electrode impedance as a function of frequency inside different types of tissue including all polarization effects. Multiple complex impedance curves are recorded for each type of tissue. An averaged curve for each individual tissue type is calculated out of the recorded data and serves as library function. Tissue classification is done by comparing these tissue library functions on-line with continuously measured impedance curves. The comparison is made by correlation and the tissue classification is based on the resulting correlation coefficients. It is accepted that the measured impedance curves do not exactly represent the specific tissue impedance only, especially not at low frequencies. However, the focus of this development is on tissue classification between several types of tissue and not on precise tissue analysis of one specific single tissue. The obtained measurement results discussed later in this thesis show that a robust classification can be achieved by this method and there is no need for an additional calibration procedure using e.g. a reference electrolyte.

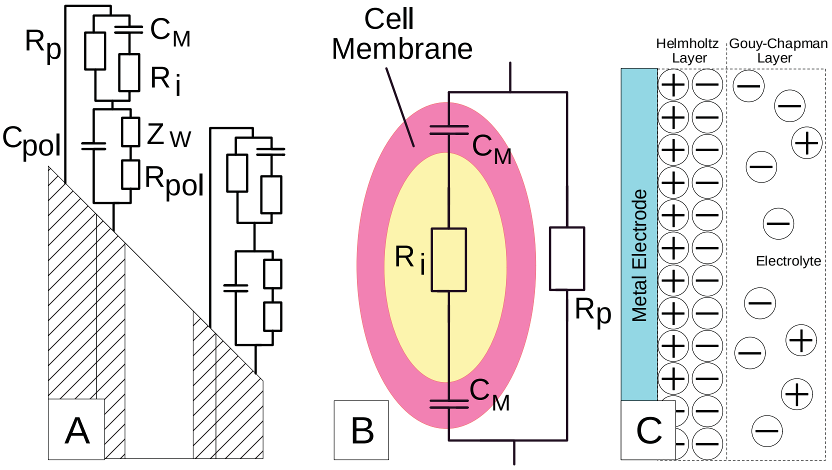

Figure 2.45: A: Equivalent electrical schematic of the tissue on the needle tip in series to a model for the electrode polarisation. B: Model for the tissue only. C: Illustration of a typical double layer polarisation effect which occurs when a metal electrode is used within an aqueous electrolyte.

Dieses Werk ist copyrightgeschützt und darf in keiner Form vervielfältigt werden noch an Dritte weitergegeben werden.
Es gilt nur für den persönlichen Gebrauch.

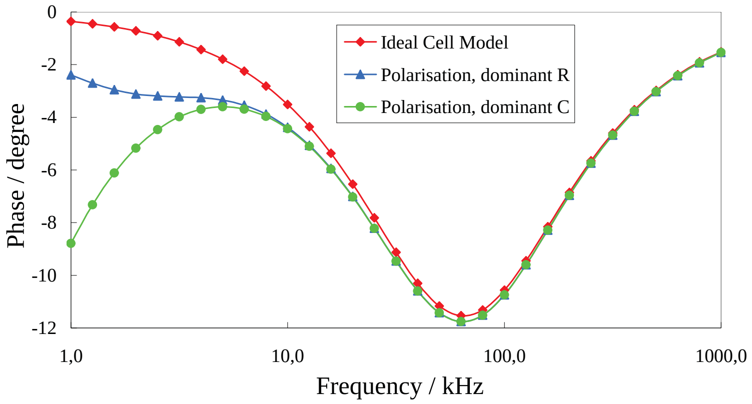

Figure 2.46: Graphical presentation of a typical parasitic effect caused by electrode polarization. The exact values depend on the chemical properties of the electrode and the aqueous solution. The shown graph is a typical example and illustrates the expected signal distortion especially at low frequencies.

2.3.8 FEM Simulation of the hollow Coaxial Cannula Tip

A low frequency finite element simulation is done in order to evaluate the current density distribution and the resulting spatial sensitivity for a needle with the geometry shown in Fig. 2.44. The simulation is done at a frequency of 100 kHz. The maximum mesh size is set to 30 μm, the boundaries of the simulated volume are at ground potential. The excitation signal amplitude is set to 1V and the conductivity of the bulk material is set to 1 S/m. However, the absolute values of the resistive bulk material and the excitation signal amplitude are not relevant, since the relative losses are calculated. This means the losses within a small tissue volume close to the needle tip are calculated and compared to the total losses in the simulated system caused by the measurement signal. Any absolute material properties such as the specific conductivity cancel out. The resulting relative losses represent the sensitivity as a function of the needle tip geometry only. The electrical losses are proportional to the square of the current density within a small volume of tissue. Fig. 2.47 A shows a simulated current density pattern for the needle tip inserted into homogeneous resistive media. As expected, the highest current density and therefore the highest sensitivity are found close to the needle tip which serves as two-electrode-pair. For further detailed analysis of the sensitivity the volume in front of the needle tip is virtually cut into thin slices with a thickness of 0.1 mm each as shown in Fig. 2.47 B. Fig. 2.48 presents the simulation result. The graph shows the accumulated relative losses inside a volume in front of the needle tip as illustrated in Fig. 2.47 B. The graph shows that approximately 90 percent of the total losses are generated within a distance of only 1 mm to the needle tip. In addition the effect of the needle insertion depth is investigated. The current density on the outer needle wall surface is very low but in total the needle has a large surface compared to the needle tip. Fig. 2.48 contains two graphs, one for 10 mm insertion depth and one for 40 mm insertion depth. Both graphs are almost identical which means the sensitivity is almost independent of the insertion depth of the needle. The result looks reasonable since almost all losses (90 %) are generated directly in front of the needle tip. The simulation result leads to the conclusion that the hollow coaxial needle design yields a very good spatial

Dieses Werk ist copyrightgeschützt und darf in keiner Form vervielfältigt werden noch an Dritte weitergegeben werden.
Es gilt nur für den persönlichen Gebrauch.

resolution of the measurement and is ideally suited for precision needle tip positioning. In addition to the simulation an in-vitro experiment is conducted to verify the expected spatial resolution. The obtained results support the simulation result very well and are described in detail within the experimental sections of this chapter.

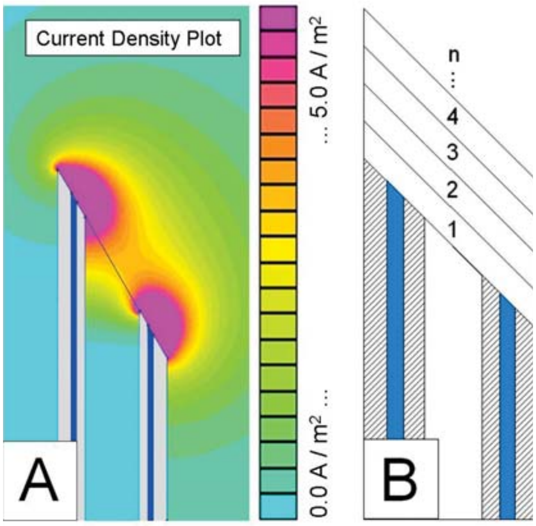

Figure 2.47: A shows the FEM simulation result of the current density distribution in the tissue close to the tip of the hollow cannula. The current mainly flows directly in front of the tip at the shortest distance between the inner and the outer conductive stainless steel tube. B illustrates the volume in front of the tip which is virtually cut into thin slices for the sensitivity analysis.

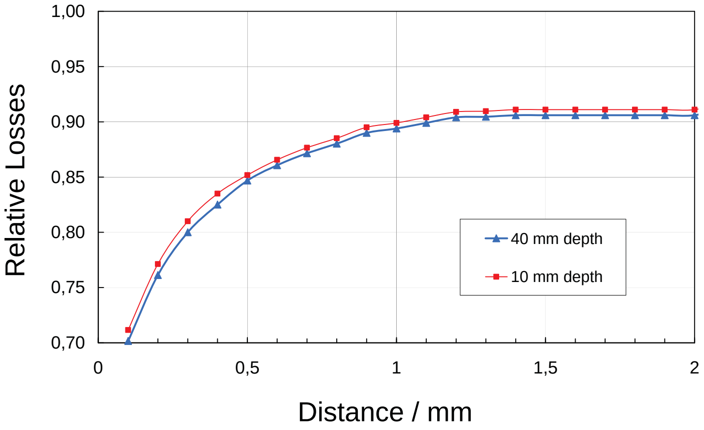

Figure 2.48: FEM-Simulation results: Relative losses as a function of the volume in front of the needle tip. The volume is indicated by the distance to the needle tip according to the slices shown in Fig. 2.47

Dieses Werk ist copyrightgeschützt und darf in keiner Form vervielfältigt werden noch an Dritte weitergegeben werden.
Es gilt nur für den persönlichen Gebrauch.

2.3.9 Chirp Measurement Signals and Processing

Linear Chirp Signal

As already mentioned the broadband measurement of the complex tissue transfer function at the tip of the cannula must be accomplished within a very short time frame. The needle insertion procedure is a dynamic process and in an ideal case the measurement time window is so short that the complex tissue load on the needle tip remains quasi-stable for one complete measurement cycle. However, this requirement can not be achieved by using conventional measurement techniques such as applying several frequencies within one slow sweep. The step-pulse signal which has been used in the first laboratory experiments is also not ideally suited because of the decaying amplitude of the higher frequency harmonics which lead to a poor signal to noise ratio. In the improved system the step-pulse is replaced by a linear chirp signal. Chirp signals have already been introduced as a promising signal for impedance measurement [33]. The sine wave based chirp signal has a general expression

$$C(t) = A\ sin\ \phi(t) = A\ sin \int \omega(t)dt + \phi_0 \tag{2.1}$$

with amplitude A, running phase $\phi(t)$, instantaneous angle frequency $\omega(t)$ and initial phase angle ϕ_0. A simple linear chirp has an instantaneous frequency $\omega(t) = d\phi(t)/dt$, which changes linearly during the excitation interval T_{exc} with constant acceleration $d\omega(t)/dt = d^2\phi(t)/dt^2 = k_{ch}$. Expressing $\omega = 2\pi f$ and denoting f_0 as an initial, and f_{fin} as a final frequency, also taking $\phi_0 = 0$ and marking T_{ch} as duration of the chirp pulse, we obtain the following expression for the linear chirp excitation:

$$C_1(t) = A\ sin\ \{2\pi(f_0 \cdot t + (f_{fin} - f_0)\frac{t^2}{2 \cdot T_{ch}}\} \tag{2.2}$$

The excitation bandwidth $B_{exc}= f_{fin} - f_0$ remains the same when the excitation time $T_{exc} = T_{ch}$ changes. Only the chirping rate $k_{ch} = (f_{fin} - f_0)/T_{ch}$ and signal energy $E = (A^2/2)T_{ch}$ vary together with T_{ch}.

A linear chirp signal calculated by equation 2.2 gives maximum flexibility in scaling the signal to the needs of the application. In this case amplitude, signal duration and covered bandwidth can be controlled independently. Fig. 2.49 and Fig. 2.50 show a linear chirp signal in time domain and frequency domain. One advantageous property of such a chirp signal is the flat spectrum in the frequency domain.

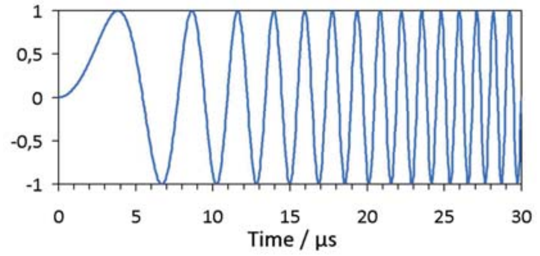

Figure 2.49: Normalized linear chirp signal plot in time domain. The presented sample signal has a duration of 30 μs and its frequency ranges from 5 kHz to 1 MHz.

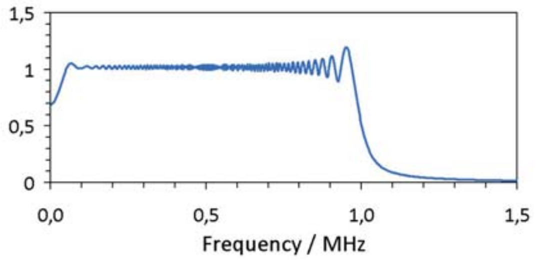

Figure 2.50: Normalized amplitude spectrum of the chirp signal presented in Fig. 2.49.

Dieses Werk ist copyrightgeschützt und darf in keiner Form vervielfältigt werden noch an Dritte weitergegeben werden.
Es gilt nur für den persönlichen Gebrauch.

The amplitude of all contained frequency bins remains stable over the entire frequency range (see Fig. 2.50). This property allows for measuring the impedance over the full bandwidth with stable signal to noise ratio and therefore leads to precision transfer functions of the measured complex impedance at the tip of the cannula.

Signal Processing Concept

Goal of the measurement is to derive the complex transfer function of the load impedance caused by the tissue under investigation in the frequency domain. Therefore the unknown tissue is stimulated by a broadband chirp voltage signal and the resulting response current is recorded. Both signals are synchronously sampled by a two-channel AD-converter and transformed into frequency domain (Fig. 2.51). The quotient of both signals is the complex transfer function.

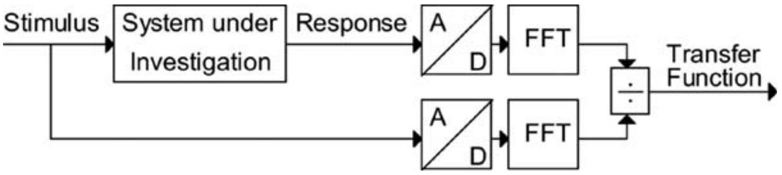

Figure 2.51: Block schematic of the signal processing chain as implemented in the developed system. The system under investigation is the load impedance caused by the unknown tissue located at the needle tip. Stimulus and response signals are voltage and current signals, respectively. Both signals are sampled and converted into frequency domain for calculation of the transfer function.

Measurement Signal Properties and Boundary Conditions

As already mentioned before, the chirp signal properties can independently be adjusted to the specific requirements of the application. In this case the bandwidth of interest is set to 5 kHz to 1.0 MHz because here we expect a characteristic impedance spectrum for each biological tissue. Furthermore the covered frequency range is a compromise between the excitation signal bandwidth, excitation signal duration and the resulting amount of sampled raw data which must be processed on-line with a reasonable amount of computing effort. Key consideration is the required sampling rate of the two synchronous AD-converters shown in Fig. 2.51. According to the Shannon theorem the minimum sampling rate must be at least twice the frequency of the highest frequency component in the signal. Therefore the maximum frequency component f_{max} in the chirp signal dictates the minimum sampling frequency $f_{sample-min}$ of both AD-converters which is $f_{sample-min} = 2 \cdot f_{max}$. The resulting minimum total number of samples N_{min} required to capture one full chirp excitation signal can be calculated and expresses as $N_{min}= T_{chirp} \cdot f_{sample-min} = 2 \cdot f_{max}/f_{min}$. This equation shows that the number of samples N_{min} is an exponential function and becomes quite large for signals with a broad bandwidth covering several decades. Therefore we choose a compromise and use a chirp signal with a duration of 200 μs. This results in a frequency resolution δf $= 1/T_{chirp} = 1/200$ μs $=$ 5 kHz and a minimum number of samples $N_{min} = 400$. In addition we decide to use an oversampling rate of a factor 10, resulting in 4000 samples. The next matching power of 2 is 4096 samples. The sampling frequency and thus the trigger frequency for

Dieses Werk ist copyrightgeschützt und darf in keiner Form vervielfältigt werden noch an Dritte weitergegeben werden.
Es gilt nur für den persönlichen Gebrauch.

the AD-converter is therefore adjusted to 20.48 MHz for capturing a chirp with $f_{max} = 1$ MHz. Our developed software running on a laptop computer can perform a complex 4096 point FFT within 2.4 ms and allows for fast on-line signal processing. Another critical parameter is the excitation signal amplitude. Extremely low amplitudes in the mV or even sub-mV range cause difficulties associated with noise and the dynamic range of AD-converters. In contrast very high amplitudes in the range of several volts may significantly cause measurement errors due to the resulting high current densities and nonlinear behaviour or even damage of the tissue under investigation. Based on our experience we choose the chirp signal amplitude to be 100 mV as a compromise and use this value within all experiments.

2.3.10 Laboratory Measurement Setup

For experiments a laboratory measurement setup is developed using state of the art equipment. Fig. 2.52 shows a block schematic of the implemented setup. The chirp signal is generated by a programmable arbitrary waveform generator (AWG, Tektronix AFG3252) which drives the coaxial cable connected to the needle via a current measurement resistor. The stimulating voltage signal and the resulting current signal are synchronously sampled by a digital storage oscilloscope (DSO, LeCroy WaveRunner 104 Xi). Fig. 2.53 illustrates the sampled voltage signal connections. The AWG generates an additional trigger signal with stable phase relative to the chirp measurement signal and allows for a stable triggering and sampling. Both oscilloscope input channels have a limited input impedance of 1 MOhm and a relatively high input capacitance of approximately 20 pF. Especially at higher frequencies the high input capacitance causes a low input impedance and lead to frequency dependent measurement errors. This unwanted effect is avoided by employing two identical buffer amplifiers connected to the oscilloscope inputs as shown in Fig. 2.52. The amplifiers have an input capacitance of approximately 1 pF. Fig. 2.54 shows a photograph of the employed laboratory measurement setup.

A custom software has been programmed which calculates the chirp signal and controls the signal generation and sampling process via LAN and USB. In addition the software processes the measured raw data and directly calculates the transfer function.

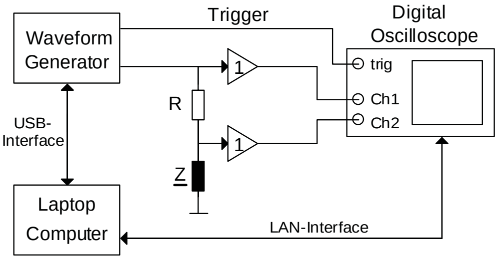

Figure 2.52: Block schematic of the laboratory setup. The unknown impedance Z and the current measurement resistor are connected in series and the waveform generator excites the measurement signal. In addition an adjustable trigger signal for the oscilloscope is generated which allows for a customized sampling rate.

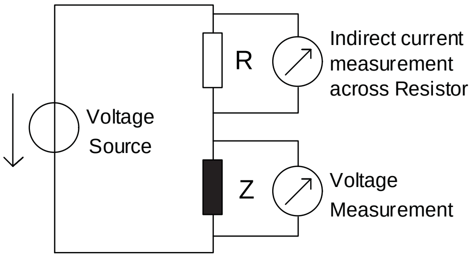

Figure 2.53: Illustration of the connection scheme for voltage and current sensing. The stimulus signal is a voltage source and the resulting current is measured as voltage drop across a known serial resistor.

Dieses Werk ist copyrightgeschützt und darf in keiner Form vervielfältigt werden noch an Dritte weitergegeben werden.
Es gilt nur für den persönlichen Gebrauch.

Figure 2.54: Photograph of the developed chirp signal measurement setup. A custom software running on a laptop computer controls the laboratory measurement devices and processes the sampled raw data.

In principle the transfer function can directly be calculated out of the measured voltage and current signals as illustrated in Fig. 2.51. Drawbacks of this direct method are measurement errors caused by inherent parasitic effects such as unwanted capacitive and resistive elements in the setup. Fig. 2.55 shows an equivalent circuit including major effects such as the cable capacitance C_c and the connector cable resistance R_c. In order to minimize such measurement errors we perform a one time system calibration by measuring the transfer function of the open system (no load at the needle tip) and the shortened system (short circuit at the needle tip). The measured transfer functions of the open circuit and the shortened circuit are used to directly correct measurement errors of the tissue transfer functions in frequency domain. First the open calibration has to be performed. In an ideal setup no current is expected to flow under the open condition. In reality a frequency dependent current can be measured. This alternating current mainly flows through the parallel cable capacitance C_c. The equivalent schematic for an open condition is presented in Fig. 2.55 A. The measured transfer function TF{open} is directly the transfer function of the capacitive element TF$\{C_c\}$. Fig. 2.55 B shows the equivalent circuit for a short condition on the needle tip. In parallel to the capacitance C_c there is two times the cable resistance R_c. The transfer function TF$\{R_c\}$ can be obtained by calculating TF$\{R_c\}$ = TF{short} − TF$\{C_c\}$. Now all relevant parasitic components are known and the corresponding transfer functions can directly be taken into account during the calculation of any measured tissue transfer function. Fig. 2.56 shows two plots for a laboratory measurement result obtained by placing the needle tip into a resistive saline bath with a measured conductivity of 16.2 mS/cm (almost isotonic). In the test setup we used a coaxial cable of type RG174A with a length of 1.5m to connect the needle with our measurement setup. In case of no calibration and no error correction a signal degradation at high frequencies is observed. This is mainly caused by the parasitic coaxial cable capacitance. Applying the above described calibration procedure virtually eliminates the parasitic effects and shows a stable modulus and phase value as expected for a pure resistive load within this frequency range. Any polarization effects at low frequencies could not be observed within this experiment because polarization mainly occurs at low frequencies. The lowest frequency component of the generated chirp signal is 5 kHz which is already outside the range in which polarization effects dominate.

Dieses Werk ist copyrightgeschützt und darf in keiner Form vervielfältigt werden noch an Dritte weitergegeben werden.
Es gilt nur für den persönlichen Gebrauch.

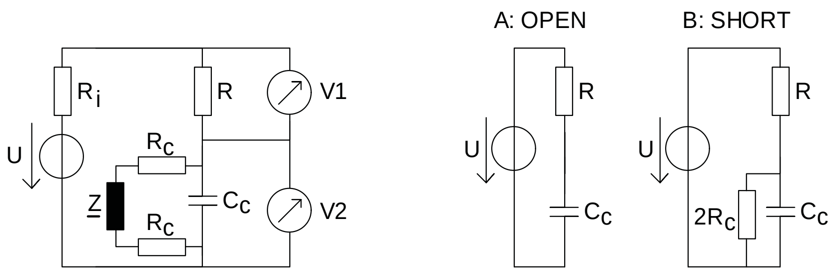

Figure 2.55: Equivalent electrical schematic of the system including relevant parasitic components that cause measurement errors. R_i is the output resistance of the generator, R_c is the DC-resistance of the copper wires that connect the measurement setup with the needle and C_c is the cable capacitance of the used coaxial cable. A: C_c can be estimated by an open calibration. B: R_c can be estimated by a short calibration if C_c is known.

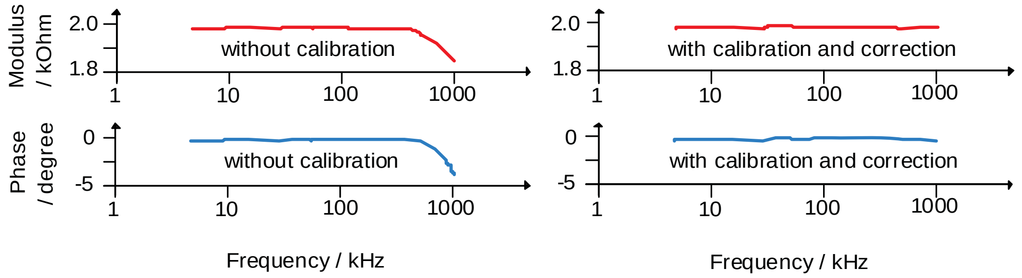

Figure 2.56: Influence of parasitic components and result of calibration and error correction illustrated by the result of an experiment obtained in resistive saline bath.

2.3.11 Description of Laboratory Experiments

Overview

Within this thesis several in-vivo- and in-vitro experiments have been conducted. Goal of the in-vivo experiments was to derive measurement data especially in order to investigate the possibility of tissue classification. Details of the in-vivo experiments are presented in the following sections. In addition to the in-vivo experiments three in-vitro experiments have been done in order to investigate side effects and robustness of the measurement principle as well as verifying the presented FEM-simulation results. Details about the in-vitro experiments are given in the appropriate sections. All measurements have been done with the developed laboratory setup described above. The measurement resistor R (see Fig. 2.54) is set to 100 Ohm. The excited chirp signal has a duration of 200 μs, an amplitude of 100 mV and coveres a bandwidth from 5 kHz to 1 MHz. The signals have been captured by a DSO with a sampling rate of 20.48 MHz and an amplitude resolution of 8 bits resulting in a total number of 4096 samples per sampled chirp signal. The sampled waveforms of the stimulus chirp signal and resulting current signal have been stored on file for later analysis.

Dieses Werk ist copyrightgeschützt und darf in keiner Form vervielfältigt werden noch an Dritte weitergegeben werden.
Es gilt nur für den persönlichen Gebrauch.

Description of the in-vivo Experiments

All in-vivo experiments have been conducted on anesthetized pigs. For the study it was measured on three pigs. On each pig the three tissue types muscle, fat and blood have been measured on two locations with a prototype needle having the dimensions presented in Fig. 2.44. A picture of the used prototype needle is shown in Fig. 2.57 (C). First measurement location was the neck of the pig, second measurement location the hip of the pig. A veterinarian carefully cut the skin of the pig and dissected the named three tissue samples. The measurement locations on the pig were prepared in such a way, that the measurement needle could be inserted into either plain muscle, plain fat or arterial blood without any visible inhomogeneity. Placement of the needles was done manually.

Description of the in-vitro Experiments

Goal of the first in-vitro experiment was to verify the simulation result for the expected spatial resolution of the tissue classification on the needle tip. Therefore the needle was inserted into a well prepared peace of pork tissue (see Fig. 2.57 (D)) using a programmable linear actuator. We started with the needle tip embedded inside homogeneous muscle tissue. In steps of 0.1 mm the needle was moved towards the fat tissue. On each step the impedance spectrum of the tissue load was measured. The actuator was stopped when the needle tip was fully embedded inside fat tissue.

The second in-vitro experiment was conducted with the same setup, but the needle was moved within homogeneous muscle tissue only. The needle was continuously moved with various speeds from 0 to 14 mm*s-1 and it was continuously measured during the movement. Goal was to evaluate if a moving needle shows different results compared to a non moving needle due to disturbance effects of the expected polarization layer on the electrodes.

The third in-vitro experiment was done with three different types of prototype needles with various dimensions as shown in Fig. 2.57. All three needles were placed into homogeneous muscle and fat tissue and the impedance spectra have been recorded. The results are compared to each other and give a first overview about the impact of mechanical parameter

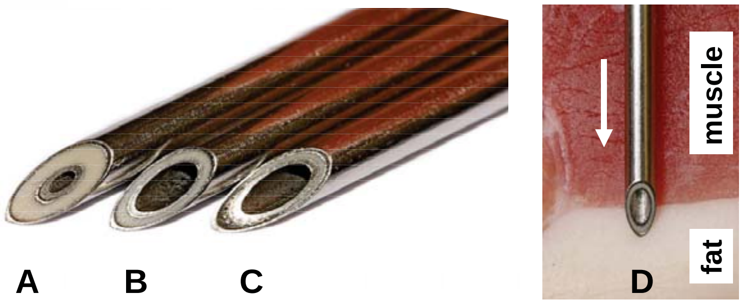

Figure 2.57: Photograph of three constructed prototype needles. Needle C is used for all experiments, needles A and B for investigating mechanical tolerance effects. D: Photograph of the needle and a prepared tissue sample with sharp boundaries for a sensitivity experiment.

Dieses Werk ist copyrightgeschützt und darf in keiner Form vervielfältigt werden noch an Dritte weitergegeben werden.
Es gilt nur für den persönlichen Gebrauch.

2.3.12 Measurement Results

In-vivo Experiments

During the in-vivo experiments the three different tissue types muscle, fat and arterial blood have been measured. The sampled raw data of the stimulus voltage signal and the response current signal have been processed by a custom analysis software according to the scheme presented in Fig. 2.51. The output of the signal processing software is a diagram similar to a Bode Diagram for each measurement but with a linear axis for the modulus of the impedance. Since the measured impedance is complex there are two plots for each measurement: the modulus plot and the phase plot as a function of frequency. Below are the obtained results for the three tissues. The measurement was conducted on 3 pigs with 2 samples per pig resulting in a total of 6 measurements per tissue. However, for muscle tissue only 5 measurements are shown since one extreme outlier was excluded. The outlier was caused by accidentally scratching a blood vessel and almost reflected the blood curve only. In some diagrams the plotted graphs are on lying on top of each other.

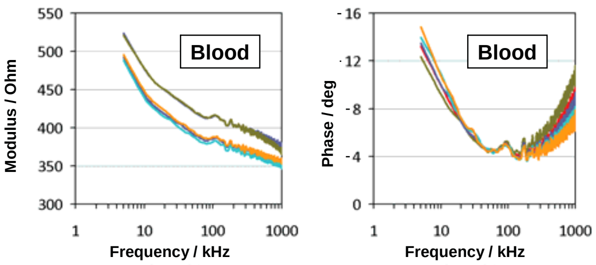

Figure 2.58: Diagrams for blood measured using a 200μs chirp signal. The left diagram shows the modulus and the right diagram shows the phase.

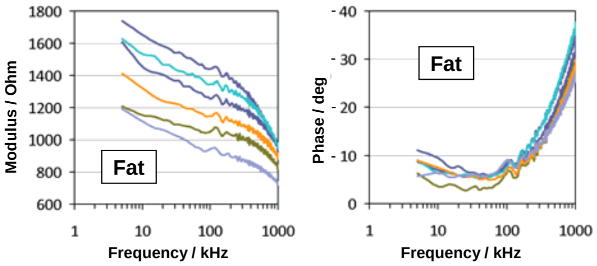

Figure 2.59: Diagrams for fat measured using a 200μs chirp signal. The left diagram shows the modulus and the right diagram shows the phase.

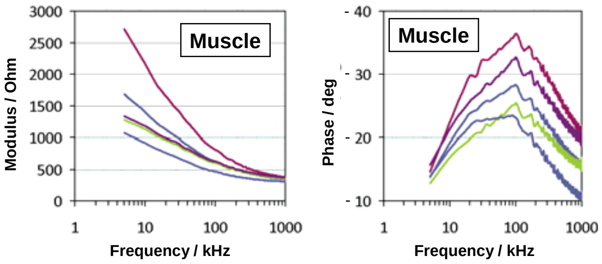

Figure 2.60: Diagrams for muscle measured using a 200μs chirp signal. The left diagram shows the modulus and the right diagram shows the phase.

Dieses Werk ist copyrightgeschützt und darf in keiner Form vervielfältigt werden noch an Dritte weitergegeben werden.
Es gilt nur für den persönlichen Gebrauch.

In-vitro Experiments

The first in-vitro experiment was done in order to verify the simulation result presented in Fig. 2.48. The experiment was conducted as described above. Measurements were obtained for the cannula transition from muscle to fat tissue. Fig. 2.61 A, B and C illustrate the cannula position as also indicated in the associated graph in Fig. 2.62. The graph shows the measured phase as a function of the penetration depth for a fixed frequency of 100 kHz. A frequency of 100 kHz was chosen because according to Fig. 2.59 and Fig. 2.60 at this frequency a significant change in the signal is expected depending on which tissue we have in front of the cannula tip. The second in-vitro experiment was done in order to verify the impact of speed when the needle is moving inside the tissue during the measurement cycle. The graphs in Fig. 2.63 show the measured amplitude and phase values at a frequency of 100 kHz for muscle and fat tissue as a function of speed. The maximum speed which could be achieved with the given linear actuator was 14 mm*s-1 which already represents a quite fast insertion process. During conventional surgical operations the cannula insertion speed is usually lower.

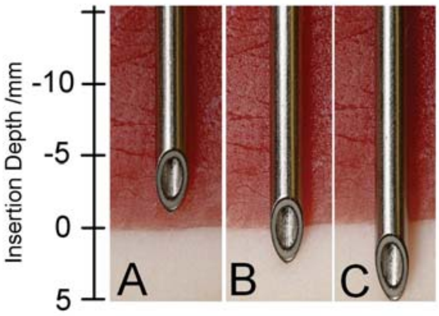

Figure 2.61: Three remarkable needle positions are shown in A,B,and C.The corresponding positions are also marked with A, B, and C in the phase diagram in Fig. 2.62.

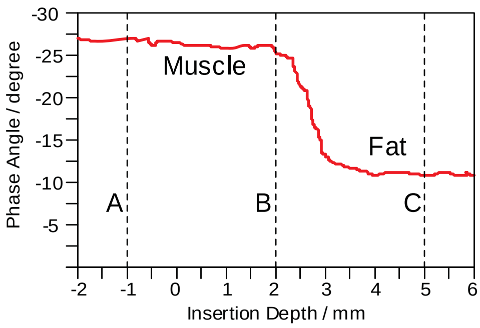

Figure 2.62: Phase signal as a function of the cannula insertion depth. The plotted phase curve shows the phase angle at a frequency of 100kHz. The marked positions A, B and C correspond to Fig. 2.61.

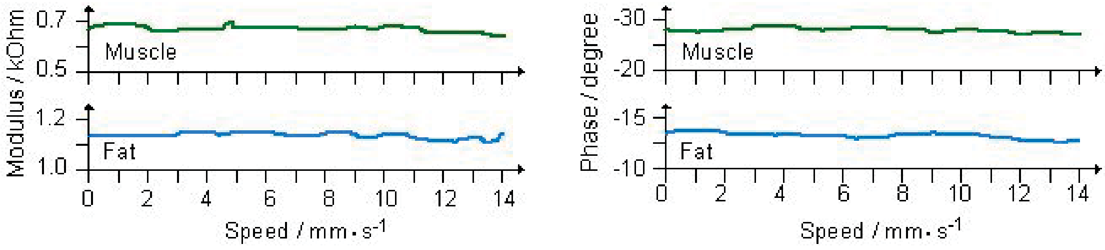

Figure 2.63: Modulus and phase angle of the impedance as a function of cannula insertion speed for muscle and fat tissue. The diagram represents the values for 100kHz obtained from the measured impedance spectra.

Dieses Werk ist copyrightgeschützt und darf in keiner Form vervielfältigt werden noch an Dritte weitergegeben werden.
Es gilt nur für den persönlichen Gebrauch.

2.3.13 Evaluation and Discussion of Measurement Results

In vivo Experiments

The presented diagrams in Fig. 2.58, 2.59 and 2.60 show the measured complex impedance formed by the tissues on the needle tip. The data includes characteristic tissue properties as well as characteristic electrode polarization effects which can not be separated from each other. However, on the first view the three tissues seem to have individual characteristic shapes of the plotted curves. Especially the phase curves show significant differences in the shape and it looks attractive to classify the different tissue types based on their individual spectra. The classification approach is done using correlation and is described in detail within the following sections. It is remarkable that all measured curves for blood show an almost perfect match to each other whereas especially the impedance curves for fat and the phase curves for muscle show some variations between the lines. According to the gained practical measurement experience this is mainly caused by the quality of the contact between the tissue and the needle. Blood is liquid and always has an ideal contact to the cannula tip whereas the contact of fat and muscle tissue depends on the pressure which is generated by the cannula. A high pressure ensures a good contact whereas a low pressure may significantly affect the measured values. However, the pressure is given by the mechanical tissue properties, the cannula geometry and the insertion speed. In real applications this may vary and can not be optimized or stabilized. For tissue classification this circumstance should be included in the tests and a resulting classification scheme should be robust enough to correctly identify the different tissues despite the unknown quality of the contact to the needle. In addition to the variations caused by imperfections of the contact, there is the possibility that small inhomogeneities in the tested tissues caused variations as well.

In-vitro Experiments

The measurement results for the first in-vitro experiment are presented in Fig. 2.62. The graph shows the measured phase angle as a function of the insertion depth at a frequency of 100 kHz. The measurement values were picked out of the measured impedance spectrum which has been recorded for each measurement position. The graph clearly shows that the measured phase value for muscle remains stable until the boundary layer of muscle and fat is reached with the center of the cannula tip, indicated with position B. Shortly after reaching position B the signal drops to the value measured for fat where is remains stable again. It is remarkable that there is a spatial delay between position B and the falling signal edge which is approximately 0.5 to 1.0 mm. This is caused by the higher electrical conductivity of the muscle tissue compared to the fat tissue (according to Fig. 2.63 approximately by a factor of two). As long as the needle tip still has contact to the muscle tissue with higher conductivity, the fat tissue is partially shortened. This limits the steepness of the falling edge as well. However, according to the presented simulation results the sensitivity of the system should be within 1 mm of the needle tip. The obtained measurement results support the simulation results very well. The falling signal edge occurs within 1 mm and the location of the falling edge is within 1 mm to the position B. In summary the FEM simulation and the experimental results lead to the conclusion that the sensitivity is approximately within 1 mm to the needle tip for a needle with an outer diameter of 2 mm and therefore yields a very good spatial resolution which is ideal for precision needle tip placement inside a specific target tissue. The second in-vitro experiment shows the amplitude and phase values for muscle and fat tissue at 100 kHz as a function of speed of the moving needle. The results are presented in Fig.

Dieses Werk ist copyrightgeschützt und darf in keiner Form vervielfältigt werden noch an Dritte weitergegeben werden.
Es gilt nur für den persönlichen Gebrauch.

2.63. The speed was varied from 0 to 14 mm*s-1. Obviously the measured values remain quite stable which indicates that moving the needle within the tested speed regions and within the tested tissues does not significantly affect the measurements.

2.3.14 Tissue Classification

Goal of the studies is to implement an on-line tissue classification system which enables to identify the type of tissue on the needle tip in real-time during the insertion process. Key component of such a system is a method which allows for identification of a specific tissue based on the characteristic properties of its spectrum. In this thesis traditional correlation technique is proposed for comparing the shape of a measured spectrum with the shape of several known tissues contained in a tissue transfer function library. Within the research experiments the library functions were obtained for each tissue by simply averaging the measured curves presented in Fig. 2.58, 2.59 and 2.60. The averaged result for each tissue is presented in Fig. 2.64. The obtained measurement data (modulus and phase diagrams) for each single measurement within each type of tissue is correlated to all three library functions presented in Fig. 2.64. The resulting correlation coefficients for the modulus of the impedance are presented in Fig. 2.65, the results for phase in Fig. 2.67. Fig. 2.66 and Fig. 2.68 show the same correlation data but in a different scale. Then the tiny error bars become visible for each correlation coefficient. The tables show the obtained average value and the standard deviation enclosed in brackets. A correlation factor of 1 means both correlated curves are identical and therefore indicate a perfect match between the measured transfer function and the library transfer function. A coeffic ndicates
a perfec

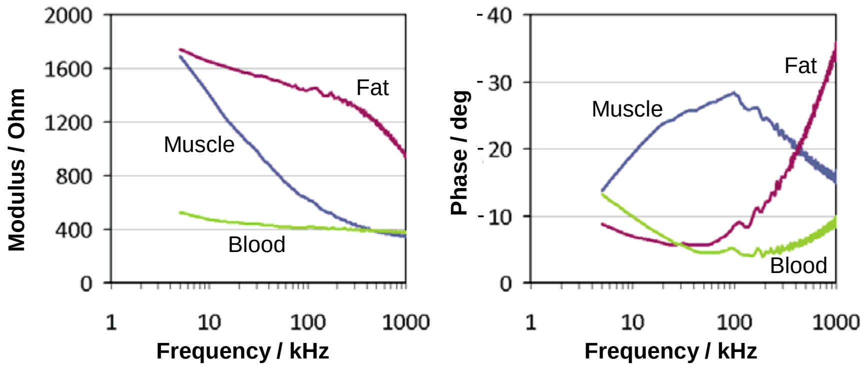

Figure 2.64: Transfer functions of different tissue types which are used as "library functions" for the correlation based tissue classification. The curves have been obtained by averaging multiple single measurements.

In order to derive a robust tissue classification scheme, it is desirable to obtain a correlation coefficient close to 1 for the matching curves (e.g. measured blood curve correlated with library blood curve) and a coefficient as close to zero as possible for non matching curves (e.g. measured blood curve correlated with library muscle curve). Second important factor for a robust classification scheme is a tight standard deviation of all correlated values. This ensures proper classification even in the case that two average correlation factors for different tissues are relatively close to each other (e.g. blood to library blood = 0.9 and blood to library muscle = 0.8). The data presented in Fig. 2.66

Dieses Werk ist copyrightgeschützt und darf in keiner Form vervielfältigt werden noch an Dritte weitergegeben werden.
Es gilt nur für den persönlichen Gebrauch.

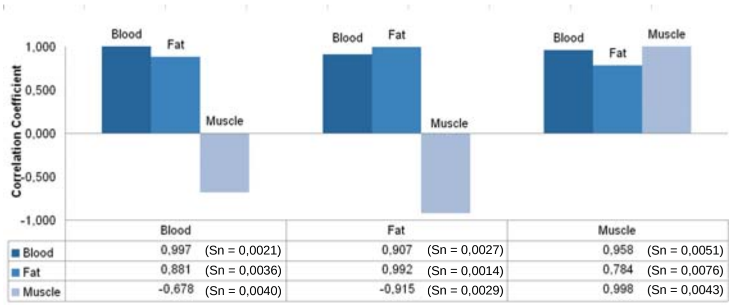

	Blood	Fat	Muscle
■ Blood	0,997 (Sn = 0,0021)	0,907 (Sn = 0,0027)	0,958 (Sn = 0,0051)
■ Fat	0,881 (Sn = 0,0036)	0,992 (Sn = 0,0014)	0,784 (Sn = 0,0076)
■ Muscle	-0,678 (Sn = 0,0040)	-0,915 (Sn = 0,0029)	0,998 (Sn = 0,0043)

Figure 2.65: The table shows the average correlation coefficients for the impedance modulus curves for each type of tissue correlated to each other averaged transfer function. The standard deviation is enclosed in brackets.

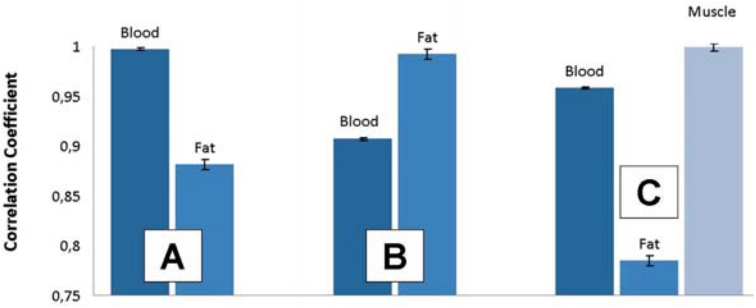

Figure 2.66: Detailed view of the correlation results shown in Fig. 2.65 on a different scaling. The bigger scaling enables to see the tiny error bars.

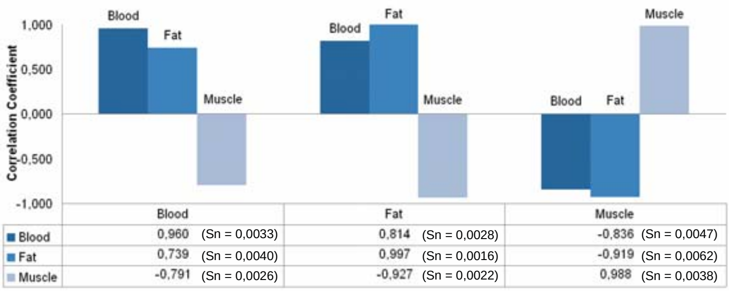

	Blood	Fat	Muscle
■ Blood	0,960 (Sn = 0,0033)	0,814 (Sn = 0,0028)	-0,836 (Sn = 0,0047)
■ Fat	0,739 (Sn = 0,0040)	0,997 (Sn = 0,0016)	-0,919 (Sn = 0,0062)
■ Muscle	-0,791 (Sn = 0,0026)	-0,927 (Sn = 0,0022)	0,988 (Sn = 0,0038)

Figure 2.67: The table shows the average correlation coefficients for the impedance phase curves for each type of tissue correlated to each other averaged transfer function. The standard deviation is enclosed in brackets.

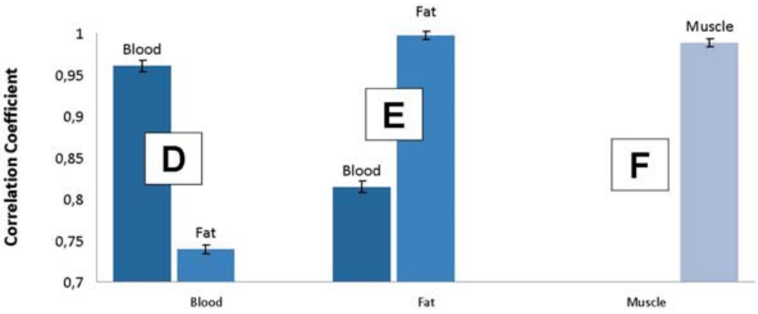

Figure 2.68: Detailed view of the correlation results shown in Fig. 2.67 on a different scaling. The bigger scaling enables to see the tiny error bars.

Dieses Werk ist copyrightgeschützt und darf in keiner Form vervielfältigt werden noch an Dritte weitergegeben werden.
Es gilt nur für den persönlichen Gebrauch.

and Fig. 2.68 shows that a tissue classification of the three tested tissues can be done without any trouble based on the experimental data set. Classification can either be done on modulus or phase curves only whereas the phase curves show slightly better correlation results for classification. The standard deviation is at least by a factor of approximately 30 smaller than the smallest absolute difference in correlation coefficients e.g. fat impedance correlated with library fat vs. fat impedance curve correlated with library blood yields an average difference in the correlation coefficient of $0.992 - 0.907 = 0.085$ whereas the standard deviation is 0.0027 for fat.

Another interesting point which has to be investigated is the effect of mechanical variations. Any variation in the needle geometry, variation in size and mechanical tolerances as well as imperfections of the metal surface have impact on the effective electrode surface and thus affect the electrode transfer impedance to the tissue as well as the resulting current density inside the tissue. Since it is difficult to quantitatively cover the impact of all possible tolerances and variations, we simply manufactured two more needles with the same outer diameter of 2 mm but different inner conducting tubes and different PTFE insulation thicknesses. The two additional needles are shown in Fig. 2.57 A and B. Needle A has an inner diameter of 0.4 mm and 0.4 mm PTFE insulation, needle B has an inner diameter of 0.8 mm and 0.2 mm PTFE insulation. All three needles are used within the same in-vitro experiment and it is measured 10 times inside muscle and fat tissue with each needle. The derived transfer functions of all three needles have been correlated to library functions obtained by only averaging the values from the original needle C. That means we compare the measurement results from needles A and B to needle C using the correlation technique despite the needles have significantly different dimensions. The resulting correlation coefficients are presented in table 2.69. Tissue classification is still possible, but the average coefficients become closer to each other compared to the values shown in Fig. 2.66 and Fig. 2.68. That means less buffer for a definite tissue classification. However, it shows that the correlation method has good potential to be robust enough against mechanical imperfections caused by manufacturing of a needle with a well defined geometry.

Needle C library functions	Impedance		Phase Angle	
	Needle A		Needle A	
	Muscle	Fat	Muscle	Fat
Muscle	0,932	-0,883	0,953	-0,901
Fat	0,661	0,928	-0,898	0,966
	Needle B		Needle B	
	Muscle	Fat	Muscle	Fat
Muscle	0,944	-0,957	0,979	-0,934
Fat	0,707	0,948	-0,933	0,972

Figure 2.69: The table shows the resulting correlation coefficients which have been obtained during measurement with two different needle geometries. The correlation becomes weaker but despite the geometry is significantly different a tissue classification is still possible.

Dieses Werk ist copyrightgeschützt und darf in keiner Form vervielfältigt werden noch an Dritte weitergegeben werden.
Es gilt nur für den persönlichen Gebrauch.

2.3.15 Conclusions

Throughout this chapter a novel system approach for on-line broadband impedance measurement and on-line tissue classification on the tip of a hollow needle is presented. The developed system architecture shows good potential for building up a stand-alone needle guidance system or it could be integrated into existing needle steering systems. Here it can potentially improve the weakness of such systems that they often can not perfectly classify between different types of soft tissue. The presented system architecture successfully uses short broadband chirp signals with well chosen parameters and a following effective signal processing scheme for obtaining transfer functions of the load on the needle tip within a very short measurement time as required by an on-line system. Tissue classification is done by simple correlation of the measured complex transfer functions. The measured functions are compared to known library functions and based on the correlation coefficients the type of tissue is identified. The in-vivo experiments show excellent results and allow for a clear tissue identification using either the modulus or the phase curve of the transfer function whereas the results obtained by analysing the phase curve are slightly better. Additional in-vitro experiments indicate that the system has good potential to be robust against mechanical tolerances of the needle tip electrodes as well as to be almost immune against dynamic needle movement within the tested speed range up to 14 mm*s-1. A FEM simulation and a corresponding in-vitro experiment show an excellent spatial resolution of the sensitive cannula tip, approximately 90% of the signal is derived within 1 mm to the cannula tip for cannula with an outer diameter of 2 mm. This is a better resolution than existing prototype systems based on monopolar electrodes can achieve. According to [176] a spherical shaped monopolar electrode tip measures 70% of the total signal within a relatively large volume having a 3.3 times greater diameter than the needle. Clear advantage of the proposed coaxial needle design is the close proximity of the two electrodes at the needle tip and the resulting well defined current path.

Dieses Werk ist copyrightgeschützt und darf in keiner Form vervielfältigt werden noch an Dritte weitergegeben werden.
Es gilt nur für den persönlichen Gebrauch.

Dieses Werk ist copyrightgeschützt und darf in keiner Form vervielfältigt werden noch an Dritte weitergegeben werden.
Es gilt nur für den persönlichen Gebrauch.

3 Time Domain Reflectometry Applications for Moisture Measurement

Measuring the water content of a substance such as e.g. soil or detecting water in different applications is a common task in many technical fields. There are different measurement methods which allow for estimating the water content of a sample. Often such sensor systems work in the microwave frequency range and detect losses caused by the dipolar water molecules in the fast changing electromagnetic field.

One specific but very interesting method for estimating the water content of a substance is based on Time-Domain-Reflectometry (TDR). This method is based on exciting a broadband measurement signal which contains high frequency components such as e.g. a rectangular pulse with sharp rising edges or short needle pulses. The excited measurement signal is usually injected into a special transmission line which serves as sensor element. The measurement signal travels along the transmission line and the electromagnetic field interacts with the surrounding medium. The water content of the surrounding medium influences the permittivity of the medium and thus the characteristic impedance of the transmission line. The propagation velocity of the injected signal depends on the characteristic line impedance. Thus any injected measurement signal will be distorted in a specific way while travelling along the sensor line. By capturing the fast signals with high temporal resolution the shape of the distorted signal can be analysed. The analysis can give precise results about the absolute water content of the surrounding media as well as information about the exact location of the moisture along the line. It is even possible to reconstruct a complete moisture profile along the transmission line when appropriate algorithms and calibration are used [178].

Within this thesis two moisture measurement applications have been analysed. The first application is soil moisture measurement and ground water measurement. The second application is an alarm system for water detection in buildings. The soil moisture measurement project was done in collaboration with the University of Queensland, Brisbane, Australia. The project with the moisture detection system in buildings was done in cooperation with the Technical University of Darmstadt, Germany. In both cases a complete measurement system was constructed including measurement electronics. The development of the measurement electronics is described in chapter 4 in this thesis.

The obtained research results have been published as regular conference papers at the ISEMA2011 entitled "Miniaturized TDR-meter for large scale field experiments " and at the AQUAMETRY2010 entiteld "Digital low-cost Time Domain Reflectometer circuit optimized for use in field applications". In addition a comprehensive paper about the developed system with focus on the electronic measurement circuits is accepted for publication at the journal IEEE Transactions on Instrumentation and Measurement entitled "Miniaturized FPGA based high resolution Time Domain Reflectometer". The following sections partly cite the mentioned publications.

Dieses Werk ist copyrightgeschützt und darf in keiner Form vervielfältigt werden noch an Dritte weitergegeben werden.
Es gilt nur für den persönlichen Gebrauch.

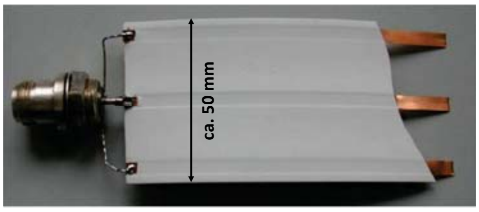

Figure 3.1: Flat ribbon cable as often found in TDR measurement applications. The inner conductor carries the measurement signal while the outer two conductors serve as reference.

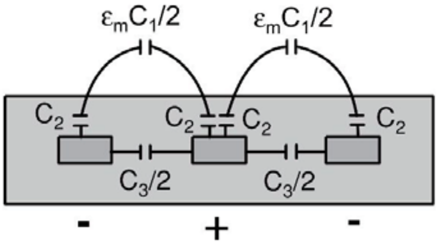

Figure 3.2: Equivalent electrical schematic of the flat ribbon cable capacitances. C_1 depends on the permittivity of the surrounding medium of the cable.

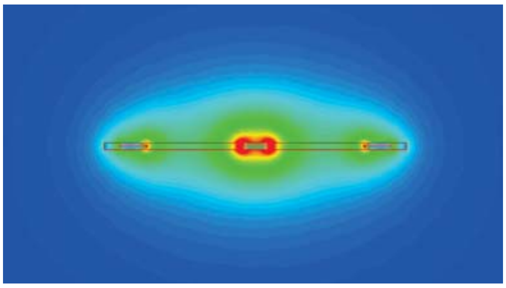

Figure 3.3: FEM Simulation of the electrical field strength of a flat ribbon cable.

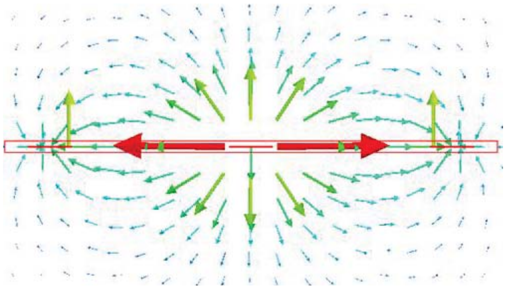

Figure 3.4: Simulation of the electric field of a flat ribbon cable having three conductors.

3.1 State of the Art in TDR-Moisture-Measurement

Moisture measurement based on the TDR principle is a well known technique and research results have been published for a wide variety of applications where the moisture content of a material or a substance is of interest. Such applications include soil moisture measurement [13, 27, 179, 180], agro-food applications [27], grain moisture measurement [27], snow moisture measurement [181, 182], wood moisture estimation [183] or moisture monitoring in concrete [90]. In all listed applications a special transmission line is used as a sensor element. The transmission line is constructed in such a way that a large fringing field is penetrating the surrounding media. The electromagnetic field of the injected measurement signal which travels along the line interacts with the medium and thus the shape of the signal is distorted. One common architecture of such a transmission line with a large fringing field is a flat ribbon cable as shown in Fig. 3.1. The measurement signal is travelling along the inner conductor while the outer two conductors are at a fixed reference potential such as e.g. ground. The resulting equivalent schematic is shown in Fig. 3.2. The capacitance C_3 is created by the plastic material of the cable which isolates the conductors from each other. Capacitance C_2 is virtually connected in series to C_1 because the electromagnetic field has to penetrate the cable isolation first before it can interact with the surrounding medium. The capacitance C_1 is created by the surrounding medium which serves as dielectric and depends on the permittivity (water content) of the medium. Fig. 3.3 and Fig. 3.4 illustrate the resulting field when the transmission line is embedded inside a homogeneous material.

Dieses Werk ist copyrightgeschützt und darf in keiner Form vervielfältigt werden noch an Dritte weitergegeben werden.
Es gilt nur für den persönlichen Gebrauch.

A complete TDR measurement setup requires multiple components including a TDR-measurement device (TDR-meter), a control unit such as e.g. a computer and the sensor transmission lines. Due to the fact that many available TDR-meters on the market are very expensive it is often required to connect multiple sensor transmission lines to one TDR-meter by a high frequency multiplexer switch matrix in order to reduce the overall system cost. The switch matrix is usually also controlled by the computer in the setup. In addition a suitable power supply must be ensured which causes certain effort especially in autarkic outdoor measurement sites as often found e.g. in geological long term monitoring applications. Fig. 3.5 shows some of the currently available TDR-meters which are widely used for such measurement experiments. Especially the TDR100 and the Tektronix 1502C are widely found in scientific field applications. However, all these TDR-meters can not operate without the above mentioned additional equipment and the price for the components is high. Fig. 3.6 illustrates the typical structure of a TDR-measurement setup and Fig. 3.7 shows three examples of TDR-meter field stations where a complete measurement system is remotely measuring soil moisture profiles. It becomes very clear that all systems mainly have scientific character and are quite complicated to handle. Due to the high cost and the size of such a system currently it can not be used as a standard measurement method in many technical fields. One goal of the developments made in this thesis is to replace such a large and expensive measurement system by a small and cheap measurement electronics. In the ideal case such a measurement electronic can replace all typical components of the presented systems including control and power management. Furthermore it is desired to dramatically reduce the price of a TDR-meter measurement solution which potentially enables for using one dedicated low-cost TDR-meter directly at the end of each measurement transmission line. This would eliminate the need for the high frequency multiplexer and thus enhance the signal quality. No long feeding cables, no impedance matching problems to e.g. 50 Ohm components and no signal distortion in the multiplexer switches enhance the overall accuracy of such a desirable system. Fig. 3.8 illustrates such a desired miniaturized system where the complete TDR-meter including all system components is embedded inside a small and robust housing. If the total power consumption could be reduced to a minimum a standard battery pack would allow even for autarkic long term monitoring applications. In addition in many cases a flexible interface for data transmission is required. The exact type of interface depends on the target application and reaches from USB for laboratory measurements over RS-485 for industrial and outdoor applications to wireless connections for autarkic remote operation.

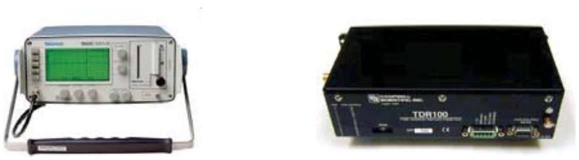

Tektronix 1502C

Campbell Scientific TDR 100

Mohr CT100

Sympuls TDR 3000

Figure 3.5: Some TDR-meters which are currently available on the market and which are widely found in measurement applications. Especially the TDR100 from Campbell Scientific and the 1502C from Tektronix have been successfully used in a variety of scientific experiments.

Dieses Werk ist copyrightgeschützt und darf in keiner Form vervielfältigt werden noch an Dritte weitergegeben werden.
Es gilt nur für den persönlichen Gebrauch.

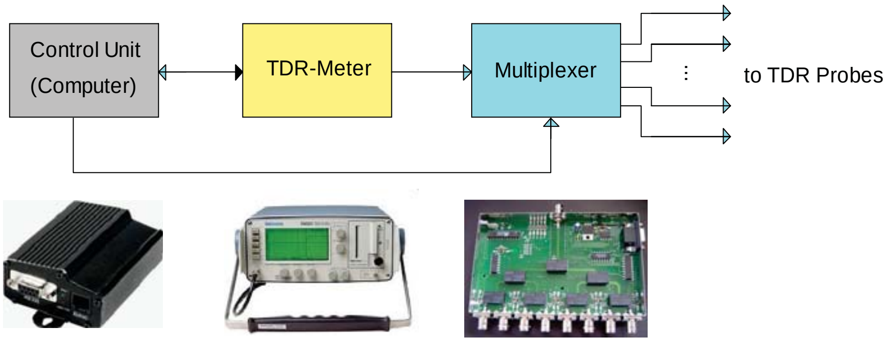

Figure 3.6: Block schematic of the typically used TDR-meter field setup for autarkic measurement and long term monitoring of several transmission lines. A multiplexer reduces the overall system cost by connecting multiple sensor transmission lines to one expensive TDR-meter.

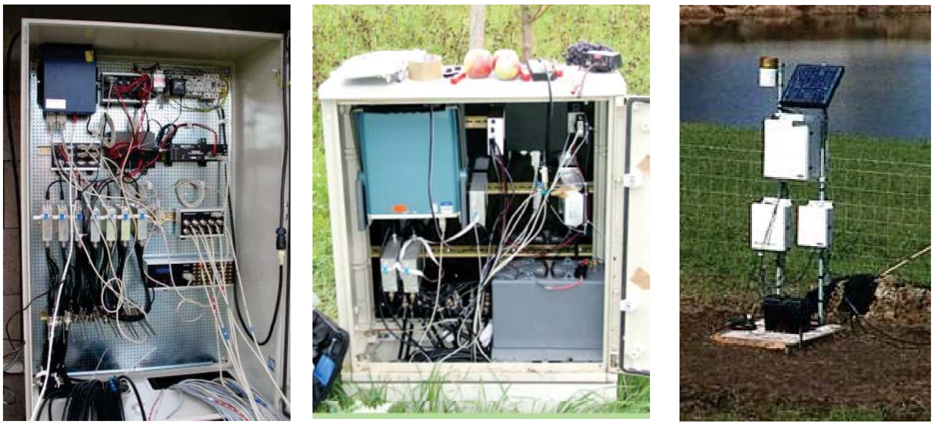

Figure 3.7: Three examples of real constructed TDR-field measurement systems. The system on the left has been developed by the MFPA Weimar, the system in the middle has been constructed by the HS Mannheim and the KIT Karlsruhe, the photograph of the system on the right side shows a setup available from Campbell Scientific and has been taken from the corresponding website [184].

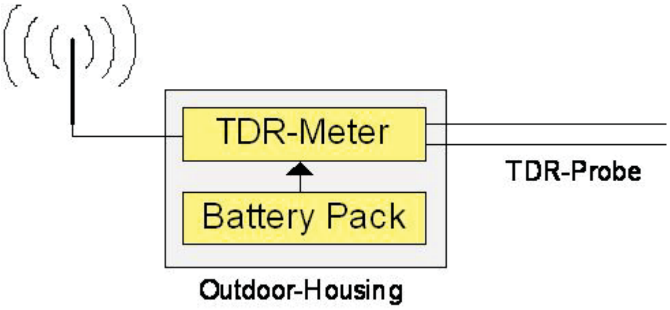

Figure 3.8: It would be ideal to have a miniaturized TDR-meter available which is cheap, small, consumes low power and which can operate completely independent of an external control setup such as e.g. a computer.

Dieses Werk ist copyrightgeschützt und darf in keiner Form vervielfältigt werden noch an Dritte weitergegeben werden.
Es gilt nur für den persönlichen Gebrauch.

In the recent past several concepts for new and innovative TDR-meter circuits and systems were presented. Lee et al. developed a random equivalent sampling TDR-meter with a 16 ps sampling resolution based on needle pulse excitation [185]. According to their publication the concept works well, but a drawback of the system is the requirement for two extremely stable crystal oscillators with very low frequency tolerances and low drift and well known frequency in order to derive a defined sampling timebase. Xudong et al. developed a TDR based cable fault diagnosis system, but the system was implemented using expensive off the shelf laboratory equipment such as a pulse generator and a fast sampling oscilloscope [186]. Purisima et al. developed a FPGA based TDR system using prototyping boards but due to the implemented direct sampling scheme the temporal resolution is limited by the FPGA clock frequency to a few nano seconds and therefore is very low compared to state-of-the-art TDR- meters [187]. Negrea et al. introduced a small microcontroller based sequential sampling TDR-meter which employs three programmable delay lines for generating appropriate trigger signals for the sampling circuit. According to [188] the achieved temporal sampling resolution is only 250 ps. Schimmer et al. developed a portable high frequency TDR- meter which is capable of generating and capturing signals with very high frequency components up to a few GHz [189, 190]. The system is also based on programmable delay lines. In this case a strong drawback of the delay line concept is the limited number of programmable steps which results either in a very limited overall recording time or in a limited temporal resolution as already presented in [188]. In addition delay lines have some more drawbacks such as high power consumption, the need for calibration and sometimes limited availability on the market. Recently Schimmer et al. improved their TDR sampling concept and replaced the programmable delay lines by two programmable but free running oscillators [191]. The system shows an excellent performance and high accuracy up to very high frequencies in the GHz range. However, the developed system is optimized and intended for use with short waveguide probes such as open ended coaxial lines. The system cannot easily be adapted for long transmission lines as required in many geological and agricultural applications [19, 192, 193] due to the fact that the tuning accuracy of the free running oscillators only allows for a rough frequency adjustment. As a consequence the excited repetitive measurement signal must be kept in the range of several MHz in order to retain the excellent temporal resolution of a few picoseconds. Furthermore the overall system is still expensive due to the optimization for very high frequency applications. Despite all advancements and achievements made within the past years, there is still a lack of available low-cost TDR measurement equipment which can easily be employed within large scale outdoor field applications.

3.2 Moisture Detection in Buildings

3.2.1 Problem Description and proposed Solution

The first target application which was investigated within the work of this thesis is an alarm system for large buildings which can detect incoming water. Especially in older buildings as well as in modern buildings with poor construction incoming water (usually rain and groundwater) may significantly damage the building. In modern buildings often the incoming water is not immediately recognized because is flows in "hidden channels" such as e.g. below the floor screed between the isolation layers and the massive concrete construction of the building as illustrated in Fig. 3.9. Here the incoming water may lead to mold and other unwanted effects such as causing corrosion and weakening the con-

Dieses Werk ist copyrightgeschützt und darf in keiner Form vervielfältigt werden noch an Dritte weitergegeben werden.
Es gilt nur für den persönlichen Gebrauch.

struction. Traditionally incoming water is detected by simple sensors which measure the conductance between two electrodes. This principle works well, but has the disadvantage that only one point of the building can be monitored at a time. In a large building this would require an extensive amount of sensors for monitoring all areas. Larger conductive electrodes connected to such simple sensors may detect incoming water in a wide area but then can not give any information about the exact position of the incoming water. This is a significant drawback because usually the building has to be sealed by different technologies exactly at the point where the water comes in. In order to keep the sealing and the corresponding work as simple and as cheap as possible the weak point of the building structure such as e.g. a hole in a wall should be located as precise as possible.

As a solution for the measurement task this thesis proposes to use a transmission line which is mounted between the concrete floor and the insulation as illustrated in Fig. 3.9. As transmission line a flat ribbon cable is ideal as described in Fig. 3.1. Such a cable is robust and because of its flat geometry can easily be installed on top of the concrete floor. When the flat cable is glued to the concrete floor with an appropriate adhesive any incoming water is forced to flow over the cable. When water flows over the cable then it interacts with the fringing field of the measurement signal. Due to the high relative permittivity of water (approximately 80) the characteristic wave impedance of the transmission line is changed at this point. Any high frequency measurement signal which travels along the line is partially reflected and distorted when reaching this point. The reflected signal parts travel back to the beginning of the line. When the signal is captured with a high temporal resolution, the position of the water on the line can be precisely calculated by evaluating the travel time of the signal on the cable. Corresponding measurement signals are shown in the next section. Advantage of such a system is that the measurement cables are robust and passive components. On one hand such a cable is very cheap, on the other hand there is no need for maintenance or repair and the cable will most likely last as long as the building itself. The measurement electronics (TDR-meter) can be installed at the end of the transmission line in such a way that later maintenance or replacement is possible with little effort. In contrast any electronic water detection sensors which measure only at a single point have to be spread over a large area and a later replacement, maintenance or repair might become difficult.

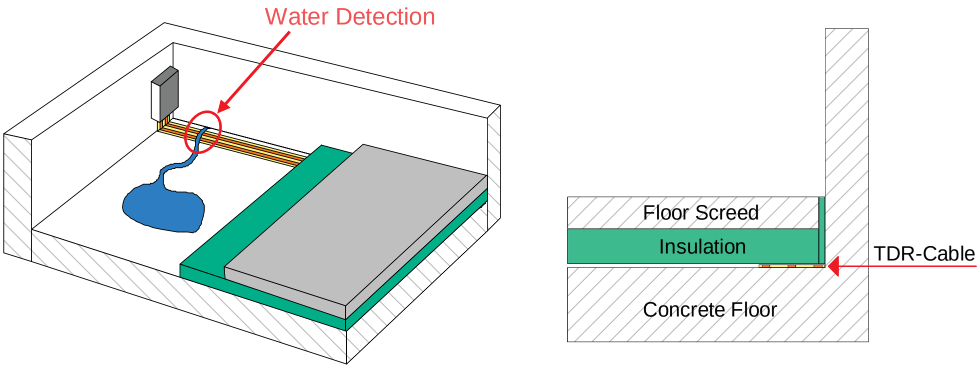

Figure 3.9: Installation of a TDR measurement system in a building for detecting hidden incoming water which flows under the floor screed in the isolation layer. The incoming water has to pass the transmission line and causes a change in the characteristic wave impedance of the cable which can be detected by the measurement system.

Dieses Werk ist copyrightgeschützt und darf in keiner Form vervielfältigt werden noch an Dritte weitergegeben werden.
Es gilt nur für den persönlichen Gebrauch.

3.2.2 Laboratory Experiments and Measurement Results

Before the system is installed within the target building a laboratory experiment is done in order to verify the sensitivity of the system and to prove that it is realistic to detect incoming water. The laboratory setup consists of the developed miniaturized TDR-meter shown in Fig. 3.10 connected to a flat ribbon cable as shown in Fig. 3.1. The incoming water on the line is simulated by placing a wet sponge on top of the cable at different positions. The size of the wet sponge is 4 cm x 4 cm and the thickness is 5 mm. Fig. 3.11 shows the captured measurement signal. In the lower left diagram one complete period of the periodic rectangular measurement signal is shown. The signal is injected into the transmission line with a sharp rising edge. When the signal generator output impedance is matched to the characteristic wave impedance of the cable the resulting voltage divider creates the characteristic step in the edge. The signal amplitude remains constant at 50 % of the injected level for two times the travel time of the signal on the line. After reaching the unterminated open end of the line the signal is reflected and travels back to the beginning of the line where it superposes to the incident signal resulting in a full amplitude. When the characteristic wave impedance of the transmission line is not constant (e.g. because of water on top of the line) parts of the signal are reflected back to the beginning of the line earlier. These signal parts can be seen as short pulses. The upper graph is a zoomed view of such two pulses created by two wet sponges on top of the cable. It is now straight forward to detect such pulses and calculate the position of the wet sponges on top of the transmission line by evaluating the travel time of the measurement signal. The lower right graph shows the corresponding opposite signal which occurs in a mirrored way at the falling edge of the rectangular measurement signal. It carries the same information as the rising edge and therefore it makes no difference if either the rising or the falling edge of the signal is evaluated. Because of the implemented sampling scheme of the developed TDR-meter circuit there is always some ripple and noise present superposed to the signal. However, the signal is highly oversampled which means it is easily possible to low-pass filter the noisy signal by a moving averaging filter without creating a noticeable additional phase shift of the signal which is equal to a virtual displacement of the wet sponge. Fig. 3.12 A shows the sampled raw signal and Fig. 3.12 B shows the low pass filtered signal.

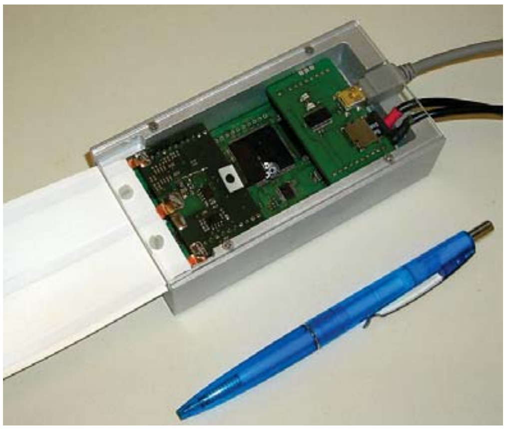

Figure 3.10: Miniaturized TDR-meter prototype circuit for installation into a water detection application into a building. The size of the TDR-meter is so small that it can easily be installed. No additional components are required, the TDR-meter can operate completely independent e.g. from a control computer.

Dieses Werk ist copyrightgeschützt und darf in keiner Form vervielfältigt werden noch an Dritte weitergegeben werden.
Es gilt nur für den persönlichen Gebrauch.

A moving averaging filter with a window size of 128 samples has been used, the virtual sampling rate of the TDR-meter was set to 1 ps which is equal to 1000 GHz (achieved by equivalent time sampling). The filtered signal clearly shows the exact positions of the wet sponges and allows for a spatial resolution accuracy of a few cm on the cable. Even smaller peaks in the signal can potentially be detected when the signal is filtered. A detailed description of the developed TDR-meter circuit is given in the following chapter of this thesis where the electronic developments are described in detail.

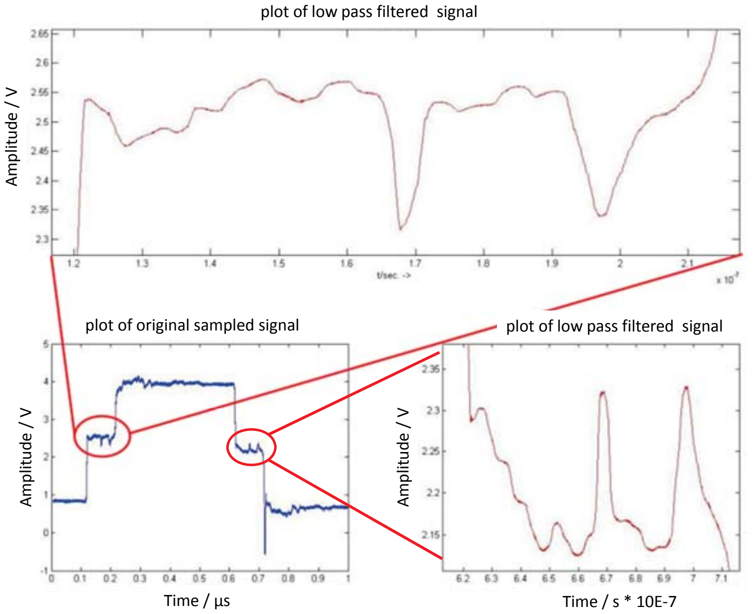

Figure 3.11: Measured TDR Traces for water detection along the transmission line. There are two peaks visible in the signal which are caused by the distorted characteristic wave impedance of the line because of the high relative permittivity of water.

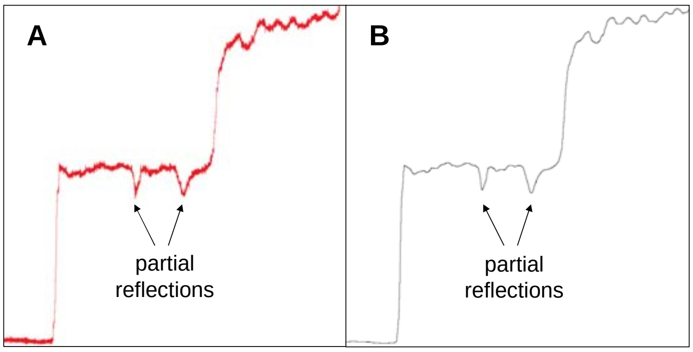

Figure 3.12: A shows the raw data of a measured TDR trace, B shows the low pass filtered signal. Because of the very high oversampling rate the low pass filtering adds no remarkable phase shift to the signal. The filtered signal allows for easy and precise location of the characteristic peaks.

Dieses Werk ist copyrightgeschützt und darf in keiner Form vervielfältigt werden noch an Dritte weitergegeben werden.
Es gilt nur für den persönlichen Gebrauch.

3.2.3 Installation of a TDR Measurement System in a Building

Within a project in cooperation with the Technical University of Darmstadt a complete measurement system was developed and installed in a building where water is expected to penetrate the building walls in the cellar floors. The following figures show photographs of the installation of the cable. The white cable is glued to the floor along the outer walls of the building. Then additional layers of isolation and floor screed are installed on top of the cable. After installation of the cables several tests and experiments have been done similar to the laboratory experiment described above. In all cases it was possible to detect the water in the line. Only one boundary condition was made: the length of the measurement cables was limited to a maximum of approximately 10 m. Longer cables would cause a significant degradation in the signal quality because of losses on the cable and other dispersion effects.

Figure 3.13: A shows the flat ribbon cable on a spool. The cable is cheap and easy to handle. B shows how the cable is glued to the concrete floor to avoid that water can flow under the cable without direct contact to the cable surface. C shows how the cable is installed along the outer walls of the building and D shows how the cable is bent around corners. Bending the cable also distorts the measurement signal and causes partial reflections. Therefore there should be only one corner per cable to ensure that the signal still can be evaluated.

3.3 Groundwater Monitoring

A similar application to the water detection system in buildings is to measure the level of the ground water. Traditionally a borehole is required with clean water inside. Then a level sensor such as e.g. a water pressure sensor, an ultrasound sensor or similar

Dieses Werk ist copyrightgeschützt und darf in keiner Form vervielfältigt werden noch an Dritte weitergegeben werden.
Es gilt nur für den persönlichen Gebrauch.

devices are installed inside the borehole. However, the measured water level only reflects the level inside the borehole which might be different to the level in the surrounding soil. Especially when multiple wet and dry soil layers are expected then a different measurement method is preferred which can give information about the moisture profile of the soil. One approach is to embed a transmission line into the soil and measure the characteristic TDR signal distortion caused by the different moisture contents along the line. Fig. 3.14 illustrates the installation of such a transmission line into the soil. A borehole is drilled with a depth of several meters and the open ended transmission line (white flat ribbon cable) is inserted into the borehole. Then the borehole is refilled with the same material in such a way that the transmission line is completely embedded in the soil. At the upper end of the cable a TDR-meter is connected. The electronic TDR-meter circuit is encapsulated inside the grey water resistant tubing. Fig. 3.15 shows a virtual cut through the housing. The white flat cable is fastened and sealed by a developed special O-Ring sealing which works like a cable gland for the flat cable. The electronic circuit board of the developed TDR-meter is directly attachted to the end of the cable by soldering the wires to the PCB. No disturbing connectors which potenitally degrade the signal quality are used.

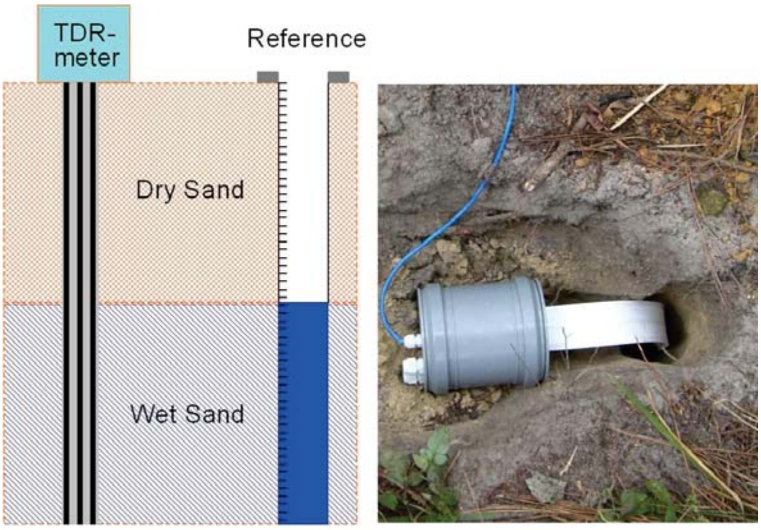

Figure 3.14: Installation of a TDR-meter at a borehole for measuring the ground water level. The white flat ribbon cable is installed into the hole and the hole is refilled with soil.

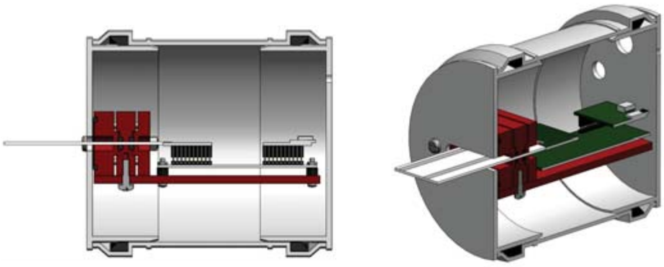

Figure 3.15: The developed miniaturized TDR-meter circuit is encapsulated by a water resistant and robust housing. The white cable is sealed by a special O-Ring cable gland which has been constructed for this application.

Dieses Werk ist copyrightgeschützt und darf in keiner Form vervielfältigt werden noch an Dritte weitergegeben werden.
Es gilt nur für den persönlichen Gebrauch.

The described system is tested in a laboratory experiment by evaluating multiple measured moisture levels. As a reference method a borehole is used as illustrated in Fig. 3.14. The captured TDR signal is analysed by searching for the characteristic steps in the signal as illustrated in Fig. 3.16. A tangent is fitted to each rising edge of the signal and the travel time is derived by measuring the distance of the midpoints of the tangents. The calculated water level is compared to the measurement results obtained with the reference method. Fig. 3.17 shows a histogram which contains the absolute deviation from the measured reference level. According to the histogram the accuracy of this method is approximately 5 cm for a transmission line length of 4 m. The resolution of the system is much better and in the range of a few mm. However, in real applications the ground water level is only changing slowly and allows for averaging multiple measurements in order to obtain a stable result.

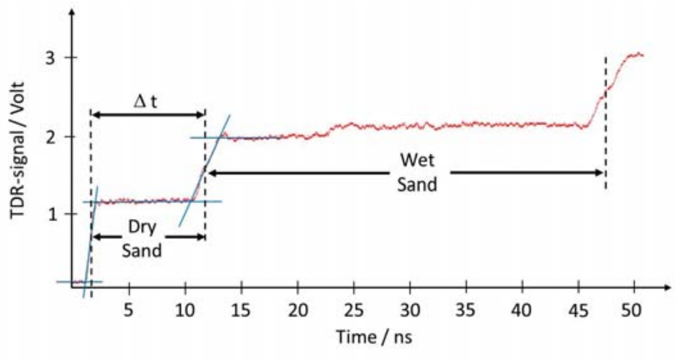

Figure 3.16: Measured TDR-Trace as a sample measurement result which was obtained with the cable embedded in soil. The characteristic steps in the signal can be evaluated and a simple moisture profile can be reconstructed.

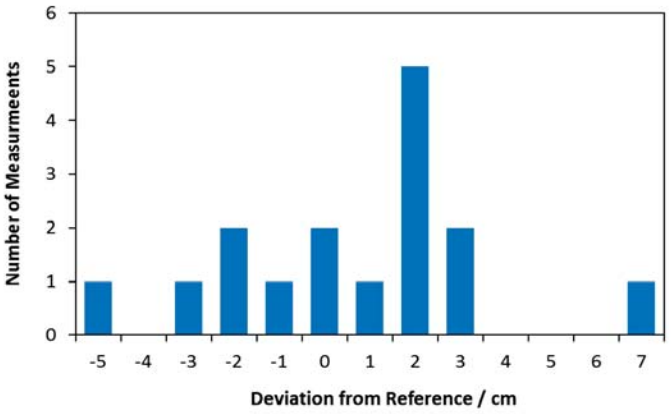

Figure 3.17: In the test site multiple water levels have been measured with the TDR-meter and the trace has been evaluated according to the scheme illustrated in Fig. 3.16. The histogram shows the deviation of the measurement result to the reference method.

Dieses Werk ist copyrightgeschützt und darf in keiner Form vervielfältigt werden noch an Dritte weitergegeben werden.
Es gilt nur für den persönlichen Gebrauch.

Dieses Werk ist copyrightgeschützt und darf in keiner Form vervielfältigt werden noch an Dritte weitergegeben werden.
Es gilt nur für den persönlichen Gebrauch.

4 Broadband Measurement Electronics

The previous chapters elaborate on the fundamentals of broadband impedance measurement and on practical applications such as biomedical tissue analysis or Time Domain Reflectometry. Throughout this thesis different applications have been investigated and different solutions for broadband impedance measurement have been proposed based on different measurement signals such as a slow sine sweep, step pulse signals or chirp signals. However, all applications have one thing in common: a cheap but precise electronic measurement circuit for broadband measurement is required to build real products based on the results of this thesis.

From an electronic point of view the requirements set by the different applications can be classified into two groups: A first group in which the required measurement time is not a critical parameter because the system is static compared to the measurement time and a second group in which the measurement time is critical because the system is dynamic.

In this thesis the applications HCT measurement in the extracorporeal circuit as well as moisture measurement applications based on Time Domain Reflectometry belong to the first group. Despite both applications have a totally different electrode design and different measurement signals, there is one thing which is identical: in both circuits a high temporal resolution of the sampled signal is required. In case of the HCT measurement the phase angle of a capacitor has to be measured with an accuracy better than approximately 0.1 degree in a frequency window of a few kHz up to 1 MHz. The resolution of the system may even be better by a factor of ten in order to see a drift of the measurement signal. The phase information of the sensor is directly related to a high temporal resolution of the measurement circuit. In case of the TDR measurements the travel time of a measurement signal on a transmission line has to be captured. In order to obtain an equivalent spatial resolution in the mm range the sampling rate must be very high. A sampling resolution in the ps range is mandatory.

In case of the needle guidance application where the tissue at the needle tip has to be analysed in real-time the requirements for the temporal resolution of the system are "normal" and a sampling rate which is a bit higher than the Nyquist-Rate is sufficient. But on the other hand the full frequency range of interest (a few kHz up to a few MHz) has to be captured within fractions of a second. In case of a needle guidance system which supports the surgeon during the needle insertion process at least 20 measurements of the complete impedance spectrum have to be done and evaluated within 1 second in order to have a "video-like" real time information about the position of the needle tip.

Within the work of this thesis two independent concepts for universal electronic circuits have been developed. The first circuit allows for capturing a (repetitive) measurement signal with a very high temporal resolution based on equivalent time sampling. The second universal circuit is based on the excitation and the sampling of broadband chirp signals. In both cases the developed circuit structures have a universal character and allow for very easy adaptation or modification to fit the needs of other applications. Focus during the development was to keep the complexity of the circuits as low as possible (much lower than the complexity of traditionally used laboratory measurement devices!) while keeping the size, cost and power consumption low. Especially the cost of such

Dieses Werk ist copyrightgeschützt und darf in keiner Form vervielfältigt werden noch an Dritte weitergegeben werden.
Es gilt nur für den persönlichen Gebrauch.

an electronic measurement circuit is a key factor which must fulfil certain requirements in order to allow for building a real product. Modern electronic components allow for building efficient circuits which fulfil all the listed requirements. Especially programmable digital devices such as CPLDs and FPGAs allow for flexible and lightweight systems at low cost. In case of the real time measurement platform based on chirp signals an FPGA provides sufficient signal processing capabilities at low cost and in case of the sampling circuit for slow systems based on repetitive measurement signals a smart modulation scheme (Delta-Modulation) is employed for reducing the overall component count and cost.

Within the following chapter the development and the functionality of the electronic circuits is described in detail. The first section elaborates on the development of a miniaturized TDR-meter for moisture measurement applications. The second section shows how this circuit concept can easily be modified in such a way that precision phase measurement is possible for HCT measurement. The last section of this chapter describes the chirp signal based measurement platform which is required by the needle guidance system. For all three applications real prototypes have been constructed and tested. In case of the miniaturized TDR-meter there was a great interest from other research institutes such as the University of Queensland, Brisbane, Australia and the Technical University of Darmstadt, Germany. In collaboration with these two institutions a small series of 60 TDR-meters was built and successfully installed within real applications.

Dieses Werk ist copyrightgeschützt und darf in keiner Form vervielfältigt werden noch an Dritte weitergegeben werden.
Es gilt nur für den persönlichen Gebrauch.

4.1 Miniaturized Time Domain Reflectometer

The following section describes the development of an efficient and miniaturized electronic circuit which can replace standard TDR-meters such as e.g. the Campbell Scientific TDR100 or the Tektronix 1502C in most applications but at a much lower cost. The developed system has been described within a regular paper for the journal IEEE Transactions on Instrumentation and Measurement which is accepted for publication. The following text is based on this paper and cites most sections without modifications. The numbering of the subsections, figures and references are adapted to the overall numbering of this dissertation. A detailed description of the originally published work and the individual contributions of the author and the co-authors is given below.

D. Trebbels, A. Kern, F. Fellhauer, C. Huebner, R. Zengerle:

Miniaturized high resolution FPGA based Time Domain Reflectometer
IEEE Transactions on Instrumentation and Measurement, accepted for publication, October 2012

Contributions to this publication:

1. D. Trebbels: Literature Reserach, Development of the System Concept, Development of Prototype Circuits and Software, Laboratory Measurements, Supervision of Felix Fellhauer (Student) and Manuscript Preparation
2. A. Kern: Support in Circuit Design and Prototype Programming
3. F. Fellhauer: Assistance in Circuit Design and Prototype Development (as Part of his Student Internship)
4. C. Huebner: Conceptual Discussions, Assistance during Field Experiments and Installations
5. R. Zengerle: Discussion of Results, Scientific Advice during Manuscript Preparation

Dieses Werk ist copyrightgeschützt und darf in keiner Form vervielfältigt werden noch an Dritte weitergegeben werden.
Es gilt nur für den persönlichen Gebrauch.

4.1.1 System Concept

The new developed TDR-meter circuit is based on repetitive rectangular pulses with a duty cycle of 50 %. A voltage source with defined output impedance (e.g. 50 Ohm) excites the measurement signal which is fed into an open ended transmission line. The resulting voltage signal at the beginning of the line is sampled with a high temporal resolution. Fig. 4.1 illustrates the general concept based on a typical laboratory setup using a step pulse generator as signal source and a fast digital sampling oscilloscope for capturing the waveform of the measurement signal. Fig. 4.2 A shows the equivalent circuit model of the system. Fig. 4.3 A illustrates the resulting typical waveform at the beginning of the line. The first rising edge at t_0 up to approximately UG/2 in the signal is caused by the voltage divider formed by the generator output impedance R_{out} and the matching wave impedance Z_W of the coaxial line. After travelling along the coaxial line the signal enters the connected flat ribbon cable. Due to impedance mismatching caused by the typically higher characteristic wave impedance of the flat ribbon cable a partial reflection occurs. The partially reflected signal can be observed at t_1. The transmitted part of the signal travels along the ribbon cable and is distorted along the cable depending on the dielectric properties of the surrounding media (e.g. soil). After reaching the end of the open line the signal is reflected and travels back to the generator. The last rising edge at t_2 can be observed at the beginning of the line. As illustrated in Fig. 4.3 A only a small fraction of the signal contains relevant measurement information and only a fraction of the vertical resolution is used. In an optimized TDR system it is desired to directly connect the output of the generator to the input of the sensor transmission line. This allows for maximizing the injected signal energy by adjusting the output impedance of the TDR-meter to the characteristic wave impedance of the sensor transmission line. A corresponding equivalent electrical circuit model is shown in Fig. 4.2 B and the resulting typical waveform is shown in Fig. 4.3 B.

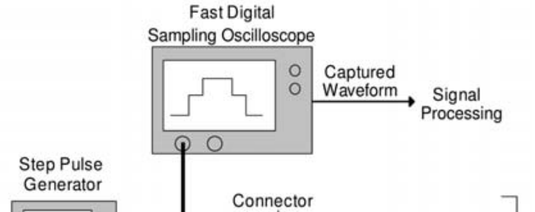

Figure 4.1: Typical laboratory setup for TDR measurements based on a step pulse generator and a fast sampling oscilloscope for capturing the waveform.

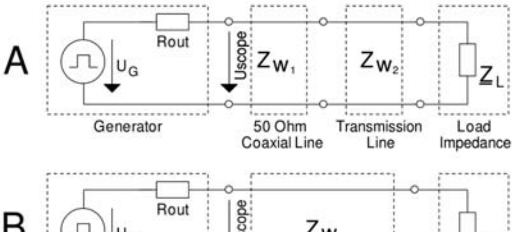

Figure 4.2: A: Equivalent electrical circuit model for the laboratory setup presented in Fig. 4.1. B: Equivalent electrical circuit model for an optimized TDR system where the generator is directly connected to the sensor transmission line and the generators output impedance matches the line impedance.

Dieses Werk ist copyrightgeschützt und darf in keiner Form vervielfältigt werden noch an Dritte weitergegeben werden.
Es gilt nur für den persönlichen Gebrauch.

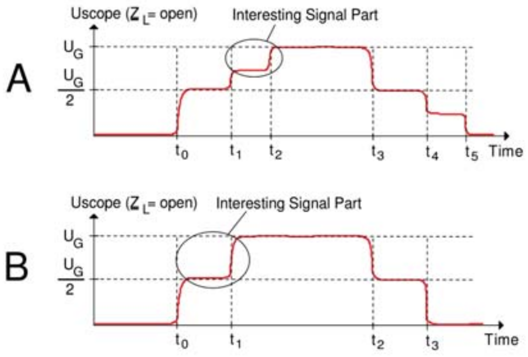

Figure 4.3: Typical resulting waveforms which can be observed at the beginning of the transmission line. For simplification multiple reflections are not drawn. The step pulse is generated and injected at t_0. A: typical signal expected from a sensor line which is connected via a non matching coaxial feeding line. B: typical waveform for an ideal system with no feeding line and matched impedance between the sensor line and generator.

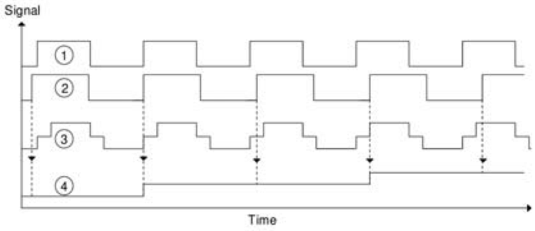

Figure 4.4: Equivalent time sampling scheme as implemented in the developed TDR-meter. Two slightly different frequencies (signals 1 and 2) are required, one frequency is used as excitation signal and the second frequency is used as trigger signal for the electronic sampling circuit. The sampled signal 3 is then reconstructed on a slower timescale (signal 4).

4.1.2 Sampling Concept

Equivalent Time Sampling

Goal of the new TDR-meter circuit is to capture a waveform with high temporal resolution in the picosecond range. Direct real-time sampling is therefore not applicable. In order to reduce the sampling speed sequential equivalent time sampling as fundamental concept is used. Fig. 4.4 illustrates the sampling process. Signal 1 is the generated step signal of the generator, signal 3 the corresponding typical double step signal at the beginning of the line. Signal 2 is a trigger signal with a slightly lower frequency than signal 1. On each rising edge of signal 2 one sample is taken of signal 3. Within each period of the repetitive signals there is a short delay of the trigger signal which results in sequentially scanning signal 3. The original signal 3 can be reconstructed out of the samples but on a slower timescale as illustrated by signal 4. A more quantitative description of the method is given in the following sections where the system dynamics and the limitations of the developed TDR-meter circuit are discussed.

Delta Modulation

As discussed above, on each rising edge of the trigger signal one sample of the repetitive measurement signal is taken. In conventional sampling systems there is usually a standard AD- converter employed for digitizing the analog voltage level on the line. This conventional approach is straight forward and usually works fine, but major drawback is the resulting huge amount of sampled raw data when capturing a signal with very high temporal resolution. Storing and processing of large data sets is technically possible but again makes the overall system more complex and gives rise to the cost, size and the power consumption. In order to drastically reduce the amount of raw data we replace a standard AD-converter by a digital Delta- Modulator (DM). Such a DM-based concept has already been successfully introduced in [13] but was implemented as analog circuit with some drawbacks and limitations as well as resulting nonlinearities. Advantage of a

Dieses Werk ist copyrightgeschützt und darf in keiner Form vervielfältigt werden noch an Dritte weitergegeben werden.
Es gilt nur für den persönlichen Gebrauch.

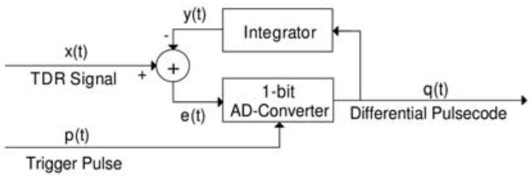

Figure 4.5: Abstract block schematic of a Delta Modulator. The input signal x(t) is digitized by the circuit and output as digital pulse code modulated bitstream q(t). One sample (= one bit) is digitized on each trigger pulse p(t).

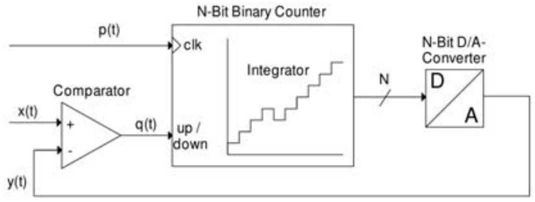

Figure 4.6: Block schematic of the DM shown in Fig. 4.5 as implemented in the developed electronic sampling circuit. A comparator serves as 1-bit AD- converter and a binary counter serves as integrator in the feedback loop.

DM is the fact that instead of one n-bit absolute value per sample with n-bit amplitude resolution only the change of the signal amplitude between two following samples is encoded by 1 bit. This removes any redundancy and compresses the amount of sampled raw data by a factor n compared to a standard AD- converter with n-bit amplitude resolution. For a 10-bit AD- converter this means 90 % reduction of raw data. Fig. 4.5 shows an abstract model of a DM. Fig. 4.6 shows the corresponding block schematic of the DM as implemented in the developed electronic circuit. The measurement signal x(t) is continuously compared to a feedback signal y(t) by a fast comparator which serves as 1-bit AD-converter. On each incoming trigger signal p(t) the output e(t) of the comparator is latched and depending on the state of the output an integrator (digital counter) in the feedback loop is forced to either count up or down. The closed loop structure forces the integrator to virtually continuously track the measurement signal x(t) but on a much slower time scale. A quantitative description is given in the following section. The bit stream output of the comparator q(t) is the pulse code modulated form of the signal x(t) which is equivalent to the derivative of x(t).

System Dynamics and Limitations

The resulting virtual temporal resolution of the equivalent time sampling circuit and the resulting system dynamics of the DM depend on the fundamental measurement signal repetition frequency f_{pulse} and the fundamental trigger signal frequency $f_{trigger}$. By controlling both frequencies the temporal resolution of the system can be adjusted. The total acquisition time t_s required to capture one full period of the measurement signal by sampling one sample per period is

$$t_s = \frac{1}{f_{pulse} - f_{trigger}} = \frac{1}{\Delta f} \tag{4.1}$$

The achieved virtual temporal sampling resolution t_{res} can be calculated by equation(4.2).

$$t_{res} = T_{trigger} - T_{pulse} = \frac{f_{pulse} - f_{trigger}}{f_{pulse} \cdot f_{trigger}} \tag{4.2}$$

Combination of equations (4.1) and (4.2) lead to the following expressions for the acquisition time t_s and the required delta frequency Δf as a function of the measurement signal frequency with the given parameter t_{res}

Dieses Werk ist copyrightgeschützt und darf in keiner Form vervielfältigt werden noch an Dritte weitergegeben werden.
Es gilt nur für den persönlichen Gebrauch.

$$t_s = \frac{1}{f_{pulse}} + \frac{1}{(f_{pulse})^2 \cdot t_{res}} \tag{4.3}$$

$$\Delta f = \frac{(f_{pulse})^2 \cdot t_{res}}{f_{pulse} \cdot t_{res} + 1} \tag{4.4}$$

In an equivalent time sampling system with extensive undersampling Δf is usually much smaller than f_{pulse} which allows us to simplify equations 4.3 and 4.4 to equations 4.5 and 4.6 by assuming that $f_{pulse} = f_{trigger}$. Equations 4.5 and 4.6 show that there is a quadratic dependency between t_s or t_{res} on one side and f_{pulse} on the other side. However, the following sections and theoretical analysis are based on the exact equations 4.3 and 4.4.

$$t_s = \frac{1}{t_{res} \cdot (f_{pulse})^2} \tag{4.5}$$

$$\Delta f = t_{res} \cdot (f_{pulse})^2 \tag{4.6}$$

Fig. 4.7 is a plot of equation 4.3 for three selected sampling resolutions t_{res} of 1 ps, 10 ps and 100 ps equivalent to a virtual sampling rate of 1000 GHz, 100 GHz and 10 GHz. The graph in Fig. 4.8 is a plot of equation 4.4 and shows the required delta frequency Δf between the measurement signal and the trigger signal for the same three selected sampling resolutions t_{res}.

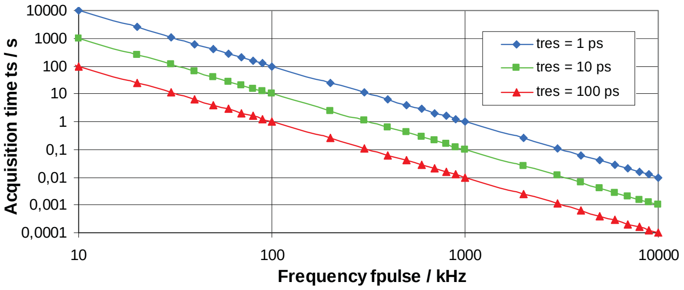

Figure 4.7: Resulting acquisition time t_s for capturing one period of the measurement signal as a function of the measurement signal frequency f_{pulse} for three selected temporal sampling resolutions t_{res}.

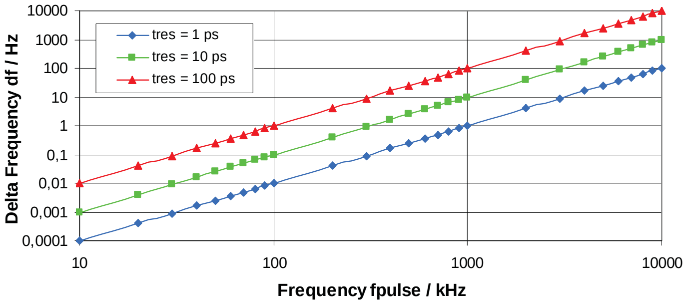

Figure 4.8: Required delta frequency Δf as a function of the measurement signal frequency f_{pulse} for three selected temporal sampling resolutions t_{res}.

Fig. 4.7 and Fig. 4.8 clearly show that the equivalent time sampling concept works very well for higher frequencies in the MHz range whereas lower frequencies result in a

Dieses Werk ist copyrightgeschützt und darf in keiner Form vervielfältigt werden noch an Dritte weitergegeben werden.
Es gilt nur für den persönlichen Gebrauch.

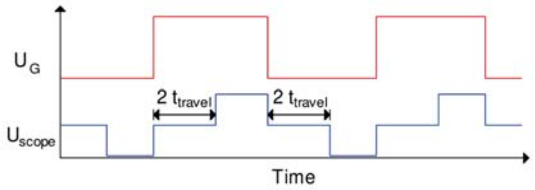

Figure 4.9: In an ideal system without multiple reflections and without ringing on the transmission line the maximum measurement signal frequency is given by the length of the line and the resulting travel time of the signal on the line.

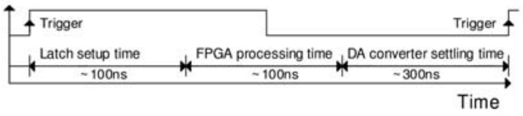

Figure 4.10: Timing diagram for one complete loop cycle. Major delays within the loop are the sampling comparator latch setup time, the FPGA processing time and the DA converter output settling time.

long acquisition time when a high virtual resolution is required. Therefore on the first view it looks attractive to choose a high measurement signal frequency. However, there are commonly two more practical limitations for the measurement signal frequency. First limitation is the travel time of the signal on the transmission line. It is desired to excite a new pulse into the line only when the previous pulse is over and the line is free in order to avoid superposing of multiple pulses. For a transmission line with e.g. 10 m length as often used in soil moisture measurement applications the travel time in one direction will be approximately 50 ns depending on the exact line characteristics. For 50 ns travel time the theoretical limit of the measurement signal frequency is $1/(4\ t_{travel}) = 5$ MHz. The resulting waveform for an ideal system according to Fig. 4.2 B with an open ended line is shown in Fig. 4.9. The period of the measurement signal must be greater than 4 times the travel time of the signal into one direction of the line.

The second practical limit for the measurement signal frequency is given by the timing of one closed loop cycle according to Fig. 4.10. One complete loop cycle is illustrated in Fig. 4.10. First time constant in the loop after exciting the trigger signal (which is a latch signal for the sampling comparator) is a mandatory fixed delay which must be waited for in order to ensure a stable and settled comparator output. Since the integrator is continuously virtually tracking the input voltage level the differential input signal of the comparator at the latch signal moment is always very low and in the mV range. Therefore the comparator latch setup time always becomes relatively large. In the developed prototype design we allow for a 100 ns latch setup time which is a factor of at least 10 compared to the typical latch setup times of a few nanoseconds of fast bipolar comparators. After the setup time the output of the comparator is read by the FPGA where the digital counter is implemented. For internal synchronization and processing 5 FPGA-clock-ticks are required which is equal to 100 ns in our design. Then the DA-converter is updated with the new integrator value. The DA-converter and following amplifiers require a certain settling time until the analog output value is stable. In total the loop-time is 500 ns in our circuit which limits the maximum trigger signal frequency to $1/500$ ns $= 2$ MHz. As a compromise between acquisition time, temporal resolution and transmission line length we choose 1 MHz as fundamental repetition frequency of the TDR signal. A detailed investigation of the expected measurement accuracy and resolution is presented in the experimental section.

Due to the time constant of the integrator in the feedback loop there is another theoretical limitation. On one hand it is desired that the amplitude resolution of the captured waveform is good (e.g. in the range of 8...12 bit). On the other hand it is desired that the DM can follow signals with a high slew rate such as the sharp rising edges of the

Dieses Werk ist copyrightgeschützt und darf in keiner Form vervielfältigt werden noch an Dritte weitergegeben werden.
Es gilt nur für den persönlichen Gebrauch.

injected square wave signal. In case of a DM the behaviour of the integrator in the feedback loop does not allow for optimizing the circuit in such a way that both requirements are fulfilled at the same time. In practical applications it is necessary to make a compromise between the maximum slew rate and the amplitude resolution of the feedback signal. The only applicable solution to increase the amplitude resolution while keeping a defined maximum slew rate is to increase the sampling resolution t_{res} of the system. This is theoretically possible by adjusting the delta frequency Δf but will lead to a longer acquisition time as already discussed above (see Fig. 4.7). The minimum rise time t_{rise} of a full scale step signal which can still be followed by an n-bit integrator which can perform n-1 steps is

$$t_{rise} = (2^n - 1) \cdot t_{res} \tag{4.7}$$

The graph in Fig. 4.11 illustrates this behavior for several amplitude resolutions as a function of the temporal sampling resolution. For a sinusoidal signal with an amplitude equal to the dynamic range of the DM circuit this means a maximum frequency f_{max} which can be captured by the system is

$$f_{max} = \frac{1}{\pi(2^n - 1) \cdot t_{res}} \tag{4.8}$$

Higher frequency sinusoidal signals can only be captured by reducing their amplitude but this results in less amplitude resolution because then the fixed dynamic range of the feedback loop is not fully used. The graph in Fig. 4.12 shows the maximum theoretical frequency for sinusoidal signals with full amplitude which can be captured as a function of the temporal resolution for different amplitude resolutions.

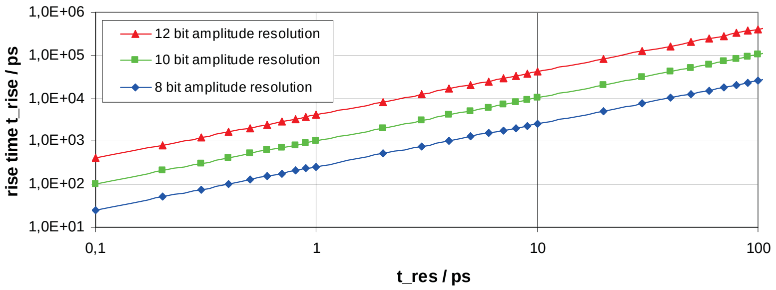

Figure 4.11: Minimum full scale step signal rise time which can be tracked by the delta modulator loop as a function of the temporal sampling resolution t_{res} for different amplitude resolutions.

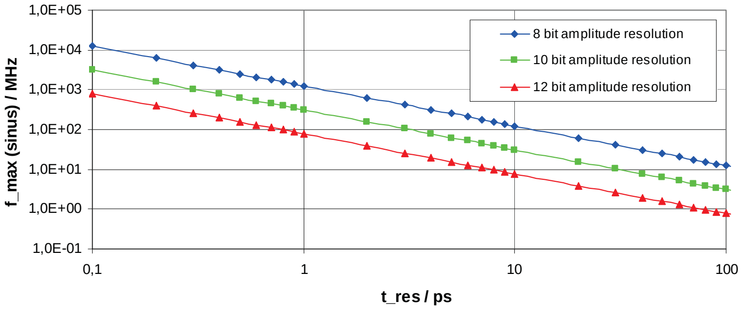

Figure 4.12: Maximum frequency f_{max} as a function of the temporal sampling resolution t_{res} which can be sampled in case of a sinusoidal measurement signal with an amplitude covering the full dynamic range of the integrator in the feedback loop.

Dieses Werk ist copyrightgeschützt und darf in keiner Form vervielfältigt werden noch an Dritte weitergegeben werden.
Es gilt nur für den persönlichen Gebrauch.

As mentioned above a square wave signal with 1 MHz as fundamental frequency and a temporal resolution of 1 ps is chosen as a compromise between the resulting amplitude resolution and the required acquisition time. Fig. 4.13 shows the resulting theoretical minimum full scale step rise time as a function of the achievable amplitude resolution according to equation 4.7. However, in our circuit the rise time of the signal is limited by the slew rate of the line driver circuit for amplitude resolutions below 11 bit. For amplitude resolutions above 11 bit the rise time is limited by the integrator.

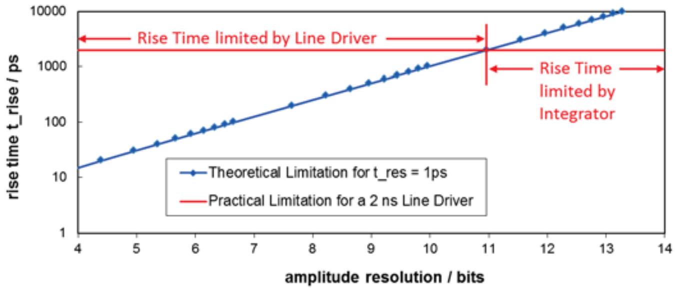

Figure 4.13: Minimum rise time as a function of the achievable amplitude resolution for a virtual temporal sampling resolution of 1 ps. In the developed circuit the rise time is limited to 2 ns by the line driver slew rate for amplitude resolutions below 11 bit. For amplitude resolutions above 11 bit the rise time is limited by the integrator time constant.

4.1.3 Electronic Circuit

The developed prototype circuit is divided into three subcircuits. The main circuit contains a small size FPGA, a microcontroller for system control and operation, SRAM memory, a real time clock and some interface components for connecting the digital processing hardware to the analog frontend. The analog frontend consists of a line driver circuit which is able to excite pulses into a transmission line as well as the comparator based DM sampling circuit. For data storage and connection to a computer a separate circuit board with various communication interfaces such as USB, RS-485 and 868 MHz wireless transceivers is developed. An on-board micro-SD card allows for storing up to 2 GB of measurement data. Fig. 4.14 shows a photograph of the developed circuit boards. Fig. 4.15 shows a comprehensive block schematic of the TDR- meter. Almost all important system functions are implemented within the FPGA except for the external large SRAM memory for temporary data storage and a "housekeeping" microcontroller. The microcontroller controls the FPGA via a custom SPI interface. The microcontroller is connected to a programmable real time clock (RTC) which allows for using the TDR-meter as an independent remote measurement device which can perform measurements on a cyclic basis. The microcontroller is waked up by an RTC interrupt and organizes a full measurement cycle. After completing a measurement cycle and storing the obtained data the microcontroller shuts down the power supply for most components on the PCB and falls back to a power saving sleep mode. While sleeping the total current consumption at a supply voltage of 6 V is below 10 μA which allows for a long time supply via a small battery pack. During active measurement with a 50 Ohm transmission line connected to the output the current consumption is approximately 190 mA, but only for a period of approximately 1 second until the TDR- meter circuit is switched off by the microcontroller again. In order to save power it is desired to keep the acquisition time as short as possible.

Dieses Werk ist copyrightgeschützt und darf in keiner Form vervielfältigt werden noch an Dritte weitergegeben werden.
Es gilt nur für den persönlichen Gebrauch.

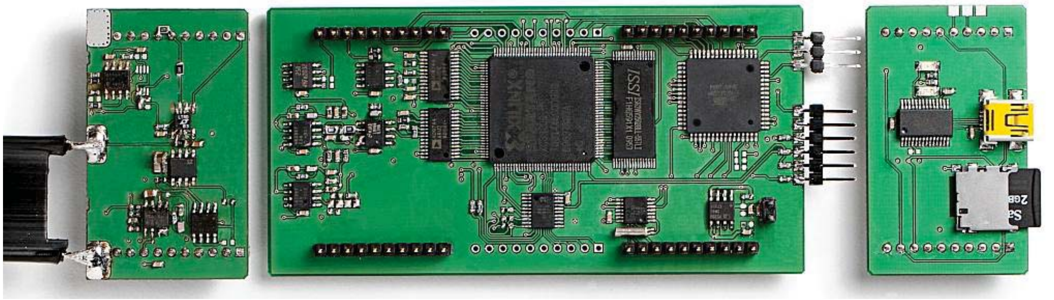

Figure 4.14: Photograph of the developed miniaturized TDR-meter circuit. The size of the main board in the middle is 100 x 50 mm. The two circuit boards on the side (left: line driver and sampling circuit, right: communication interfaces) are designed as header boards and can be mounted on top of the mainboard.

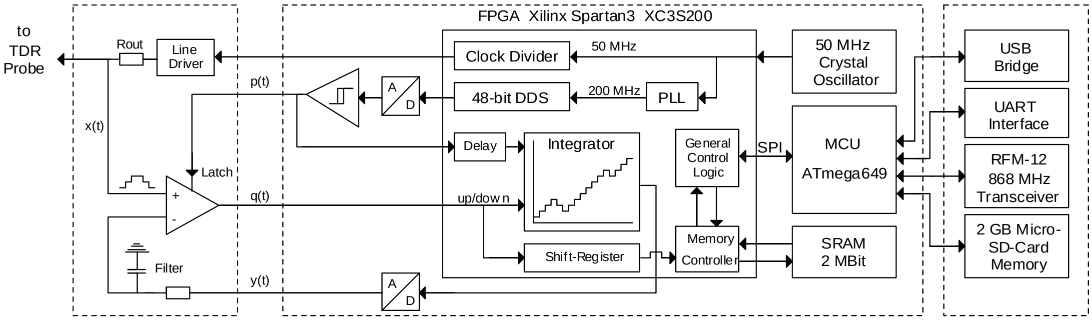

Figure 4.15: Block schematic of the complete electronic TDR-meter circuit. Almost all measurement functionalities are implemented inside a small standard FPGA. A microcontroller controls all functionalities including the FPGA, the SRAM memory readout, data storage and data transmission via various interface types. The small analog part consists of a line driver circuit and the sampling comparator based Delta-Modulator circuit.

According to equation 4.4 and Fig. 4.8 the delta frequency Δf between the measurement signal and the trigger signal must be very small when a high temporal resolution is required. For a 1 MHz measurement signal Δf must be 1 Hz when a virtual resolution of 1 ps is desired which is equal to 1 ppm relative frequency tuning accuracy. The fundamental measurement signal frequency f_{pulse} is derived from the 50 MHz FPGA system clock by a decimal divider counter. The trigger signal is also derived from the same 50 MHz clock time base but can be precisely adjusted by a Direct Digital Synthesizer (DDS) which is also implemented inside the FPGA. The frequency tuning accuracy is defined by the 48-bit wide internal phase accumulator of the DDS and the DDS clock frequency which is 4 x 50 MHz = 200 MHz. The resulting tuning accuracy is 200 MHz / 248 = 0.71 μHz. The output of the DDS related DA- converter (AD9744) is filtered by a good LC-bandpass filter with a quality factor Q = 80 in order to further reduce harmonics and therefore reduce the sampling jitter. The filtered DDS output signal is converted to a square wave signal by a Schmitttrigger circuit using a fast comparator (LT1711). The pulse code modulated serial bitstream q(t) which represents the sampled signal is processed by a memory controller unit and is transferred to an external SRAM for temporary storage. Up to 2 Mbit can be stored inside the SRAM which is equal to a recording time of 2 μs with a resolution of 1 ps. This long recording time is sufficient for

Dieses Werk ist copyrightgeschützt und darf in keiner Form vervielfältigt werden noch an Dritte weitergegeben werden.
Es gilt nur für den persönlichen Gebrauch.

transmission lines having a length of up to approximately 200 m which is already much longer than used in most practical applications.

The line driver circuit is shown in Fig. 4.16. The square wave measurement signal is shaped by a fast bipolar comparator (LT1711). The comparator reaches a rise time of 2 ns for a pulse with an amplitude of 5 V. The generated 5 V pulse is reduced to a 3 V pulse by a voltage divider and then buffered by a following fast current feedback amplifier. Reduction of the pulse amplitude is necessary to keep the signal amplitude within a certain input voltage range of the sampling comparator. The transmission line is connected to the output of the buffer amplifier via an additional output resistor R_{out}. This resistor can easily be replaced by any resistor (greater than 50 Ohm) for achieving an optimized impedance matching between the TDR-meter output impedance and the characteristic line impedance. The achieved rise time of 2 ns is slower than many state-of-the-art TDR-meters can reach according to their datasheets. In some applications this may not be acceptable e.g. if a short coaxial probe is used as transmission line. However, in the field of geological and agricultural soil monitoring applications the used transmission lines are usually long and in the range of several meters. In addition the specified short rise time of state-of-the-art TDR- meters is often a more theoretical value which can be measured directly at the output of the TDR-meter. If the TDR- meter is connected to a flat ribbon cable via a 50 Ohm coaxial feeding line (e.g. RG 58), the rise time of the injected pulse is significantly degraded within the first few meters of the coaxial line. In addition there are often RF-Multiplexers used to connect multiple sensor lines to one TDR-meter. Inserting such an additional RF-Multiplexer causes additional slew rate degradation. However, in most practical target applications for the new TDR-meter a 2 ns rise time is fully acceptable. On the other hand the use of a standard comparator as a pulse source offers the great advantage of having a large step signal amplitude of 3 V which is approximately a factor of 10 higher than in most other TDR-meters. In theory the pulse amplitude is not so important, but in case of the above presented sampling circuit this is an advantage because the input hysteresis of the sampling comparator is very small compared to the signal amplitude. In the laboratory we figured out that most fast bipolar comparators have an internal input hysteresis in the range of 1 to 3 mV which is often not fully specified in the datasheet. In the case of a low signal amplitude this effect may degrade the sampling amplitude resolution. In the case of a 3 V step signal we can almost ignore this minor effect as it becomes only relevant if high amplitude resolutions better than approximately 10 bit are required for the raw data acquisition.

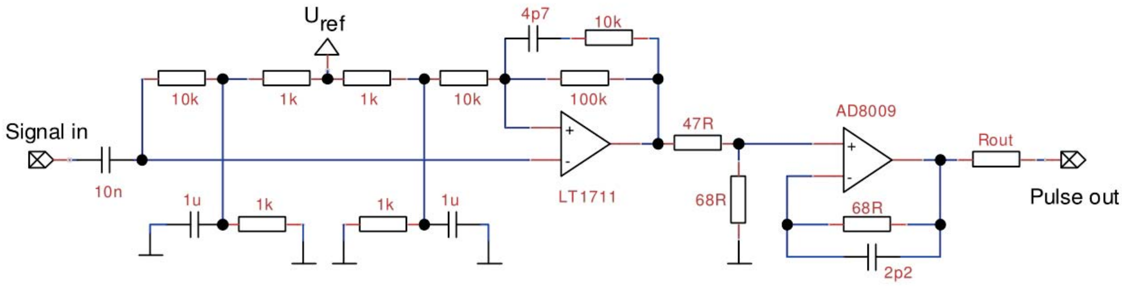

Figure 4.16: Schematic of the line driver circuit. A fast bipolar comparator is used to form a square wave with sharp rising edges from the input signal. The achieved slew rate is approximately 2 ns for a 5 V step signal. The comparator output is buffered by a fast current feedback amplifier which drives the connected transmission line via the matched output resistor R_{out}.

Dieses Werk ist copyrightgeschützt und darf in keiner Form vervielfältigt werden noch an Dritte weitergegeben werden.
Es gilt nur für den persönlichen Gebrauch.

The sampling circuit comparator requires only few components and is illustrated in Fig. 4.15 on the left side as a part of the analog header board. The comparator must have a high analog input bandwidth, a wide input voltage range, a latch input with short latch setup time (a few nanoseconds are preferred) and a short propagation delay to ensure fast sampling and readout. In the prototype circuit we successfully used the LT1711 comparator. The analog feedback signal y(t) is low pass filtered with a filter located close to the input pin of the comparator in order to reduce coupled EMC noise caused by the fast switching components on the PCB. Cutoff frequency of the low pass filter is 5 MHz to ensure that there is no significant additional phase shift between the analog DM output signal and the comparators input at the time of the rising edge of each latch signal. In addition to a careful PCB layout every analog comparator and amplifier is supplied by an individual stabilized power regulator in order to prevent ripple on the individual power rails and thus reduce induced noise in the circuit to a minimum. The result is a very clean excitation signal without noticeable distortion caused by short switching peak currents. This short time stability of the signals is mandatory for correctly capturing a repetitive signal without distortion. Long time stability issues such as temperature drift do not play a significant role during one measurement cycle because the acquisition time is only a fraction of a second.

4.1.4 Laboratory Experiments

The developed TDR-meter circuit is tested in the laboratory. The laboratory experiments are done to investigate the general system accuracy, repeatability and resolution. In addition to the laboratory experiments the developed circuit has been successfully used within two field measurement applications as described in chapter 3.

Experiment 1: Accuracy and Resolution

The first experiment is a comparison to a conventional laboratory setup as shown in Fig. 4.1. Goal of the experiment is to test the amplitude accuracy of the system at different fundamental excitation signal frequencies. Especially the behaviour of the sampling comparators input stage is of major interest since the input signal level covers the entire input voltage range. Typical effects such as (virtual) offset voltages and gain errors caused by the limited common mode rejection ratio of the sampling comparator have to be evaluated.

The output resistor R_{out} is set to 50 Ohm which allows for comparing the device to other standard laboratory equipment having 50 Ohm outputs. In addition it allows for connecting a 50 Ohm coaxial cable for defined and reproducible measurements. For this experiment the amplitude resolution is set to 10 bits and the virtual sampling resolution is set to 1 ps. According to Fig. 4.11 a full scale step pulse with a minimum rise time of 1 ns can be captured with these settings. The generated pulse has a measured rise time of approximately 2 ns so there is still some margin to ensure that the integrator can virtually track the input signal despite the presence of some jitter. The experiment is done four times. In each experiment the fundamental excitation signal frequency and thus the required trigger frequency are changed. We are investigating the system behaviour at 100 kHz, 500 kHz, 1 MHz and 2 MHz. Frequencies lower than 100 kHz lead to extremely long acquisition times and are not acceptable in our target applications. Even at 100 kHz the acquisition time is already 100 seconds when a temporal resolution of 1 ps is desired. Frequencies higher than 2 MHz cannot be handled by our electronic circuit mainly because of the required loop time for each sample (see Fig. 4.10). In

Dieses Werk ist copyrightgeschützt und darf in keiner Form vervielfältigt werden noch an Dritte weitergegeben werden.
Es gilt nur für den persönlichen Gebrauch.

the experiment the transmission line is an open ended RG-58 type coaxial cable with 50 Ohm characteristic wave impedance. For reference the TDR signal is captured with a fast digital oscilloscope (LeCroy Waverunner 104Xi). The vertical resolution of the oscilloscope is 10 bit. 10 curves are recorded and averaged. Both traces are compared to each other and the difference is computed to see if there are deviations from each other. As an example Fig. 4.17 shows two resulting averaged waveforms in one plot. The data was obtained at 1 MHz. Both curves are almost identical and are matching very well. Fig. 4.18 shows the difference between the curves sampled with the TDR-meter and the oscilloscope for all four tested frequencies. It is obvious that there is a gain error of a few millivolts. The gain error is not constant but increases at higher input signal levels. Especially at higher fundamental frequencies the increase in the measured gain error is higher. At 2 MHz the measured error is already in the range of 9 mV. A test of the sampling comparator shows that its DC input offset voltage is approximately 4 mV. In order to exclude a frequency dependent excitation signal degradation or distortion of the signal source we compare the excitation signal full scale output level sampled with the oscilloscope at 100 kHz and 2 MHz. The difference is shown in Fig. 4.19. The visible noise is in the range of +/- 3 mV which is equal to 1 bit at 3 V excitation signal amplitude and a full scale vertical resolution of 10 bit of the oscilloscope. Since there is no remarkable difference, the signal source is stable over the tested frequency range and the observed gain error is most likely caused by a slightly decreased performance of the comparators input stage at higher frequencies and at higher common mode levels of the input signal. However, in total this experiment shows that the vertical accuracy of the developed TDR-meter is in the range of 8 bit without any offset or gain error compensation and approximately 9 bit when we mathematically reduce the measured gain error by subtracting a constant offset (the DC offset voltage) of the comparator. The ripple found on all four sampled curves in Fig. 4.18 is approximately 1 mV. As stated above the curves are averaged curves from 10 measurement cycles. In theory the ripple is at least one LSB of the feedback loop resolution which is approximately 4.0 mV in this experiment for 4.0 Volt full scale DAC amplitude and 10 bit amplitude quantization. It can be concluded that the sampling resolution of the system is in the same range as the integrator resolution in the feedback loop.

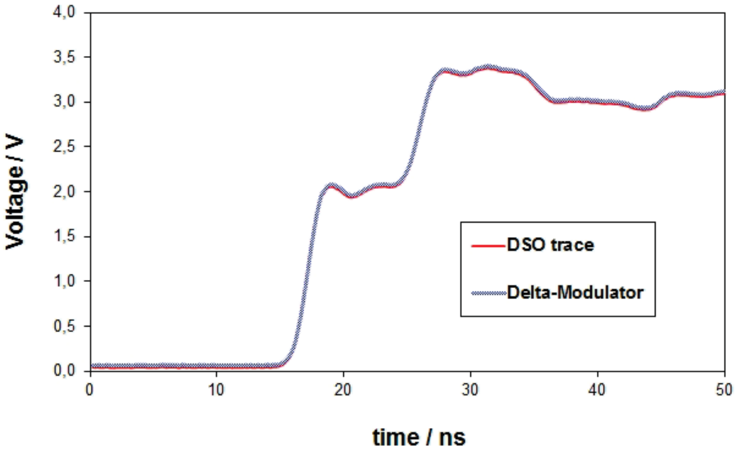

Figure 4.17: Comparison of the captured waveforms of a TDR measurement using an open ended coaxial cable. One curve is sampled with an oscilloscope (LeCroy Waverunner 104 Xi) and the second curve is captured with the new developed TDR-meter.

Dieses Werk ist copyrightgeschützt und darf in keiner Form vervielfältigt werden noch an Dritte weitergegeben werden.
Es gilt nur für den persönlichen Gebrauch.

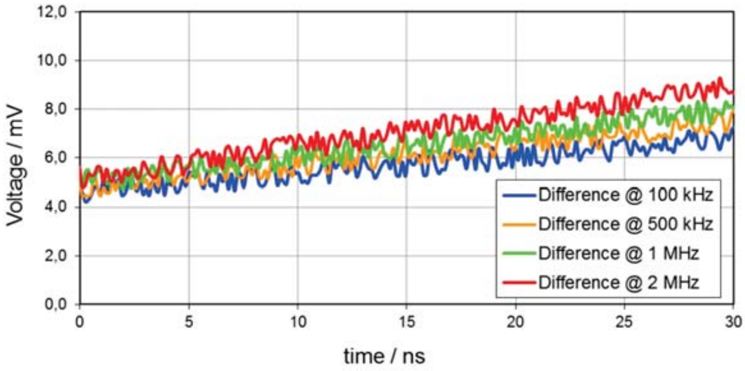

Figure 4.18: Difference between sampled curves. For each frequency one curve is sampled with a digital oscilloscope and the other curve is sampled with the TDR-meter circuit. The graph shows a gain error of approximately 5 to 9 mV and additionally superposed noise with an amplitude in the range of 1 mV.

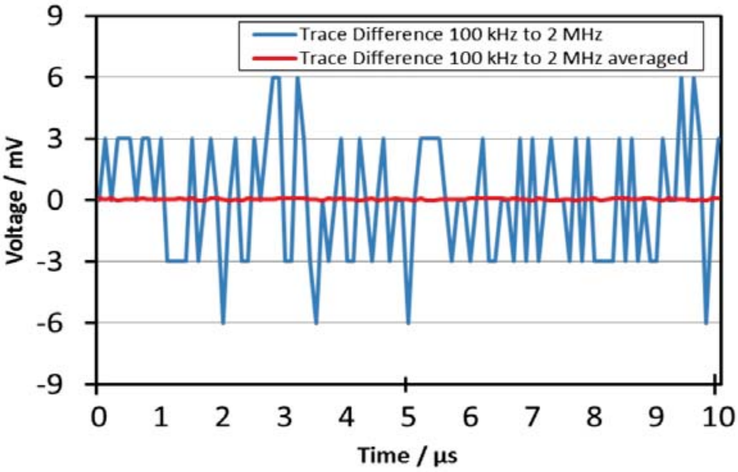

Figure 4.19: Difference between two sampled curves of the excitation signal. One curve is sampled at a fundamental excitation signal frequency of 100 kHz, the second curve is sampled at 2 MHz. Both curves are sampled with the digital oscilloscope. Applying a moving averaging filter with a width of 128 samples to the raw data shows that the difference is almost perfectly zero which means that the excitation source is stable at the tested frequencies.

Dieses Werk ist copyrightgeschützt und darf in keiner Form vervielfältigt werden noch an Dritte weitergegeben werden.
Es gilt nur für den persönlichen Gebrauch.

Experiment 2: Accuracy and Load

In a second laboratory experiment the amplitude accuracy is further verified under different load conditions. In this experiment a resistor is directly soldered to the output pads of the TDR-meter circuit instead of a transmission line and forms a voltage divider with the output resistor Rout of the TDR- meter circuit. The sampled voltage level is compared to the theoretical voltage level which we expect for the known voltage divider. The amplitude error between theoretical and measured signal is computed. As explained above the output resistor of the TDR-meter can be varied in order to adapt to different transmission lines with different characteristic line impedances. In this experiment we set R_{out} to nominal values of 50 Ohm, 100 Ohm and 200 Ohm which is in the range of typical TDR transmission lines. As a load resistor in each case we connect nominal values of 0 Ohm, 50 Ohm, 100 Ohm, 200 Ohm and 1 kOhm. Since all resistors have initial tolerances, the resistors are measured and the test results shown in Fig. 4.20 are computed with the exact values. The presented result is always the error in percent with respect to the theoretical value. All measured combinations show an amplitude error below +/- 0.5 %, many samples below +/- 0.25 % which is equal to an amplitude accuracy in the range of 8 bits for all tested load and frequency combinations.

R_out / Ohm	R_load / Ohm	Error % @ 100 kHz	Error % @ 500 kHz	Error % @ 1 MHz	Error % @ 2 MHz
49.2	0	-0,40	-0,03	-0,33	-0,10
	50.5	0,06	-0,16	-0,38	0,13
	102.1	0,27	-0,37	-0,16	0,16
	204.4	0,48	0,39	0,27	0,39
	1019.1	0,38	0,20	0,18	0,40
101.6	0	-0,30	-0,41	0,27	-0,48
	50.5	0,34	0,00	0,48	-0,17
	102.1	0,21	-0,39	0,17	-0,44
	204.4	-0,43	0,46	0,23	0,15
	1019.1	-0,32	-0,21	-0,43	0,19
199.0	0	-0,16	-0,49	0,33	0,14
	50.5	-0,09	-0,27	0,05	-0,22
	102.1	-0,40	-0,06	-0,31	0,33
	204.4	-0,42	-0,42	0,44	-0,34
	1019.1	-0,11	0,47	0,08	-0,21

Figure 4.20: The table shows the measured amplitude error based on different combinations of the TDR-meter output resistance and attached load resistance.

Experiment 3: Time Base Linearity

In a third laboratory experiment the linearity of the time base of the new circuit is tested. At the beginning of the experiment an open ended 50 Ohm coaxial cable with a length of 200 cm is connected to the TDR-meter. The travel time of the signal is measured and averaged 10 times by capturing the TDR waveform and comparing the captured signal level to the two threshold values of 1/4 UG and 3/4 UG in order to locate the two rising edges of the characteristic double step signal. Then the coaxial cable is shortened by 10 cm and the measurement is repeated. The experiment was done 10 times until the cable was shortened to 100 cm. Shortening the cable can be done with high accuracy and ensures that other components such as the connectors remain constant during the experiment. The measurement result is presented in Fig. 4.21. With R2 = 0.9994 the circuit shows an excellent linearity. One reason for the achieved excellent linearity is the continuously running sampling concept based on a DDS clock generation. In contrast

Dieses Werk ist copyrightgeschützt und darf in keiner Form vervielfältigt werden noch an Dritte weitergegeben werden.
Es gilt nur für den persönlichen Gebrauch.

to delay lines there is no inherent nonlinearity present. The only source of timing errors created by the DDS clock system are spurs in the DDS output spectrum which occur due to a limited DDS sampling frequency, limited amplitude resolution of the DA-converter and jitter of the DDS driving clock signal. The implemented DDS synthesizer has a measured spurious free dynamic range of approximately 70 to 75 dB when generating output frequencies in the range of 100 kHz to 2 MHz. All spurs are further reduced by a sharp LC bandpass filter. The remaining spurs will directly be translated to sampling jitter by the following comparator which forms a square wave out of the sinusoidal DDS output. The square wave signal is required for triggering the latch input of the sampling comparator. The jitter effects are analysed and discussed below.

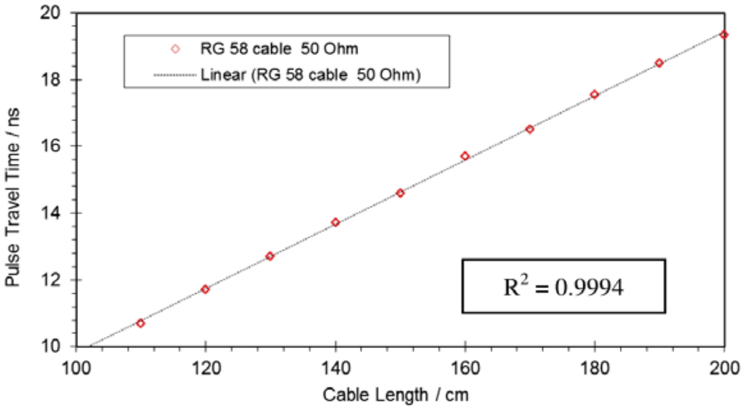

Figure 4.21: Measured pulse travel time as a function of the cable length. The cable is shortened by 10 cm for each measurement. The expected graph is a linear function. With R2 = 0.9994 the TDR-meter circuit shows an excellent linearity.

Experiment 4: Jitter Estimation

Jitter will affect the effective sampling resolution, accuracy and potentially will limit the minimum rise time of a step signal which the integrator must be able to follow. In this system the relevant sampling jitter means timing imperfections of the latch signal relative to the measurement pulses. In the system there are several sources which potentially cause timing jitter. As mentioned above, the most important sources are spurs in the DDS output signal and switching jitter caused by the comparator which converts the sinusoidal DDS output to a square wave signal. In addition there is switching jitter of the line driver circuit, jitter caused by a non constant latch setup time of the sampling comparator and of course initial jitter from the crystal oscillator and the following FPGA clock distribution and clock management modules such as internal PLL and the clock divider. All timing jitter effects add up in the system and may randomly cancel out each other or result in a worst case jitter scenario where all jitter effects add up into one direction. Since it is difficult to directly measure each source of jitter without influencing the circuit, we performed a further experiment to investigate the total amount of jitter. Within the test the output resistance Rout was set to 50 Ohm and an open ended coaxial cable of type RG-58 with a length of 2 m and a characteristic wave impedance of 50 Ohm was connected. 50 Ohm is the lowest output resistance which can be driven by the line driver. The fast switching output currents are high in this case and therefore the switching noise is expected to be high as well. We use this configuration as a worst case scenario. The experiment is done three times with the fundamental excitation frequencies

Dieses Werk ist copyrightgeschützt und darf in keiner Form vervielfältigt werden noch an Dritte weitergegeben werden.
Es gilt nur für den persönlichen Gebrauch.

100 kHz, 1 MHz and 2 MHz in order to investigate the frequency dependence of the jitter effects. During each experiment the TDR-meter circuit performed 1500 complete measurements of the resulting characteristic curves (see Fig. 4.3 B). The equivalent time between the internal start signal for the excited pulse and the first matching of the sampled signal amplitude with a compare value of 3/4 UG was recorded. Out of the 1500 performed measurements a jitter histogram for each sampling frequency was derived. Fig. 4.22 shows the envelope curves of the three histograms. It can be seen that the resulting jitter effects are lower at 100 kHz than at 1 MHz or 2 MHz. One reason is that the DDS generator has a higher oversampling rate in this case which leads to a better spurious free dynamic range. Another reason is that transients in the circuit such as fast switching currents at 100 kHz have 20 times more time to decay than at 2 MHz. However, the difference between the derived envelope functions is of minor importance for the overall performance of the TDR-meter with respect to the requirements set by our target application. The shape of the histograms is not a perfect Gaussian function. However, the total amount of jitter is significantly smaller than the required sampling resolution of the target application of approximately 50 ps. For this reason it is not necessary to further investigate the individual jitter sources.

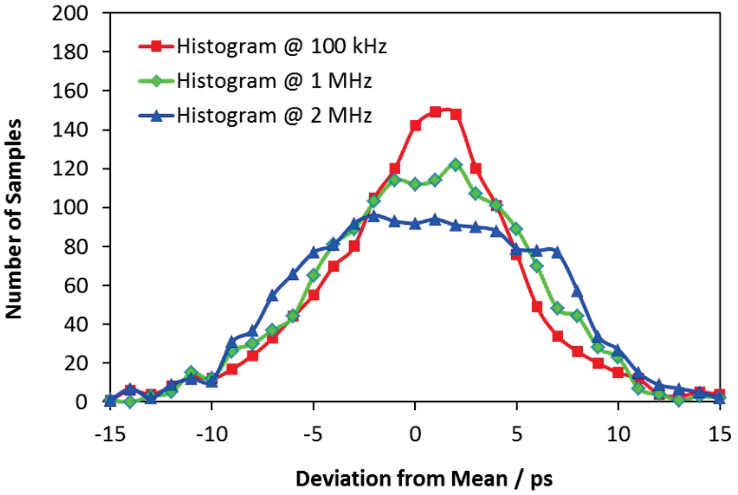

Figure 4.22: Envelope functions of the jitter histograms for the two fundamental excitation frequencies 100 kHz and 2 MHz. The resulting jitter is slightly lower at 100 kHz but the difference in the two envelope functions is of minor importance with respect to the required accuracy of the TDR-meter within the target applications.

The measured jitter is bigger than the actual virtual sampling resolution of 1 ps. However, it is still useful to keep the 1 ps resolution in the system in order to allow the integrator to track rising edges with a rise time as low as approximately 1-2 ns while keeping the amplitude resolution at a level of 10 bit. The amplitude resolution in the system is better than the accuracy. In several applications this is absolutely useful when only the ratio between two amplitudes is important and the absolute value is of minor interest. As discussed above the integrator in an ideal system can track signals with a rise time of 1 ns with an amplitude resolution of 10 bits when a virtual temporal sampling resolution of 1 ps is adjusted. The implemented line driver is limited to a rise time of 2 ns but it is still useful to keep 1 ps virtual resolution in order to suppress rise time limitations caused by jitter and to have some margin to the theoretical boundary. From Fig. 24 it is obvious that the sampled output of the system cannot be used for applications where a real 1 ps resolution is required. However, the sampling

Dieses Werk ist copyrightgeschützt und darf in keiner Form vervielfältigt werden noch an Dritte weitergegeben werden.
Es gilt nur für den persönlichen Gebrauch.

specification for the target application "moisture measurement and detection" is in the range of approximately 50 ps which is equal to a spatial resolution of approximately 2,5 cm along the transmission line. In addition to the resulting high amplitude resolution of the system the oversampled waveform allows for an optional additional low pass filtering by applying a moving averaging filter with a limited width. If the width of the filter is smaller than the number of samples which occur during the step rise time, there is almost no remarkable effect on the slew rate degradation.

4.1.5 Conclusions

The new developed miniaturized TDR-meter circuit is based on several well known methods such as equivalent time sampling, delta modulation and precise DDS frequency generation. The overall circuit concept combines many attractive advantages of these single techniques in a smart way. The result is a very flexible and scalable measurement unit which can easily be adapted to application specific needs in terms of virtual sampling rate, fundamental step signal frequency, amplitude resolution and acquisition time. The fundamental measurement signal frequency of the repetitive excitation signal can be adjusted independently of the temporal resolution, only the acquisition time will vary. The equivalent time sampling scheme is a trade-off between the acquisition time and a very high virtual temporal sampling rate. Advantage of the sequential sampling method is the low overall complexity and low real-time data rate which must be processed by the circuit. A new digital sampling circuit based on a DM architecture further reduces the overall system complexity and the resulting amount of sampled raw data by pulse code modulation. Due to the mainly digital character of the system and the reduced complexity it is possible to integrate the bigger part of the design into a small FPGA. In the implemented prototype circuit we tested frequencies in the range of 100 kHz to 2 MHz. Frequencies below 100 kHz result in a very long acquisition time. Frequencies above 2 MHz cannot be processed by the developed circuit due to timing limitations. The laboratory experiments show that the jitter effects become more visible at higher fundamental excitation signal frequencies. However, we decided to choose 1 MHz fundamental measurement signal frequency and 1 ps virtual temporal resolution for our field experiment as a compromise. The accuracy and resolution at 1 MHz fulfil our target application requirements. Advantage of the 1 MHz excitation signal frequency is that the acquisition time is by a factor of 100 lower than at 100 kHz while keeping the same temporal resolution. In our target application where the TDR- meter is supplied by a battery this saves a great amount of energy. The new TDR-meter circuit eliminates all major conceptual drawbacks of delay-line based sampling systems such as a limited recording time or fixed sampling resolution by using continuous signals with fine relative frequency adjustment options given by the DDS. The rise time of the generated step output signal is approximately 2 ns when driving a 3 V step signal into a 50 Ohm cable. The rise time is currently limited by the line driver stage which is based on a fast comparator and a fast operational amplifier. For the targeted measurement applications in many geological and agricultural experiments the achieved slew rate is sufficient. Besides the limited slew rate the only further trade-off compared to established laboratory TDR-meters is the slower acquisition speed, but in many cases this is not relevant.

Dieses Werk ist copyrightgeschützt und darf in keiner Form vervielfältigt werden noch an Dritte weitergegeben werden.
Es gilt nur für den persönlichen Gebrauch.

4.2 High Precision Phase Measurement

The above described electronic circuit for the miniaturized TDR-meter which is capable of tracking a repetitive signal with very high (virtual) sampling resolution can also be used for measuring the phase shift of two signals with very high accuracy and resolution. The following sections show how the developed circuit has to be modified and how the operating scheme for low frequencies has to be varied. In principle the circuit structure is still the same, only some parameters have to be changed. The derived concept for measuring a phase shift with high accuracy and resolution has been published as a regular conference paper at the ICEBI2010 conference. The following sections are based on this conference paper and parts of the following text cite this publication. The text flow, the introduction and the conclusions have slightly been modified to fit in the context and the text flow of this dissertation. The numbering of the subsections, figures and references are adapted to the overall numbering of this dissertation. A detailed description of the originally published work and the individual contributions of the author and the co-authors is given below.

D. Trebbels, D. Woelki, R. Zengerle:

High Precision Phase Measurement Technique for Cell Impedance Spectroscopy
ICEBI 2010, 14th International Conference on Electrical Bioimpedance, Journal of Physics: Conference Series 224 (2010) 012159, Gainesville/Florida, April 4-8, 2010

Contributions to this publication:

1. D. Trebbels: Literature Reserach, Development of the System Concept, Development of Prototype Circuits and Software, Laboratory Measurements, Supervision of Daniel Woelki (Student) and Manuscript Preparation
2. D. Woelki: Support during Experiments and Measurements (as Part of his Student Internship and Masterthesis)
3. R. Zengerle: Discussion of Results, Scientific Advice during Manuscript Preparation

Dieses Werk ist copyrightgeschützt und darf in keiner Form vervielfältigt werden noch an Dritte weitergegeben werden.
Es gilt nur für den persönlichen Gebrauch.

4.2.1 Overview and Target Application

In general the developed phase measurement circuit can be used in any technical application, but focus of this thesis are biomedical applications such as complex cell impedance measurement and dielectric tissue analysis. In many of the named applications it is necessary to measure the complex dielectric constant of a sample as a function of frequency. Therefore the developed system is capable of measuring amplitude and especially high precision phase of the measurement signal over a wide frequency range from approximately 10 Hz to 10 MHz. The experimental result of the developed circuit shows a phase resolution of up to 0.01 degree at 1 MHz and 0.1 degree at 10 MHz. The excellent phase measurement resolution is achieved by a virtual "time transformation" of the sinusoidal measurement signal by using an appropriate sampling scheme adjusted to the measurement frequency. The functional principle of the digital sampling circuitry is based on Delta − Modulation and is implemented inside a cheap standard FPGA. A prototype circuit board of the phase measurement system has been developed and is successfully tested within the target application "HCT-measurement" where the (quasi)static dielectric properties of a blood sample have to be analysed which flows inside a standard medical plastic tubing. The application HCT-measurement is described in detail in chapter 2 of this thesis.

4.2.2 State of the Art in Broadband Phase Measurement Circuits

There are many methods and concepts available for precise phase measurement based on different modulation schemes such as e.g. IQ-modulation. However, almost all of the traditionally known methods for phase measurement either do work for low frequency signals or for high frequency signals only. In most situations it is very difficult or even impossible to cover several decades of frequency with one of the traditionally used phase measurement methods. For this reason in the field of broadband Impedance Spectroscopy a conventional voltage divider approach is often found as illustrated in Fig. 4.23. In such a circuit a sinusoidal measurement signal is generated and fed to the unknown impedance (MUT) via a well known reference impedance Z. The injected sinusoidal signal will cause a current flow and thus a characteristic phase shift between current and voltage across the unknown MUT. In many conventional systems these signals are captured by conventional AD-converter based sampling circuits and processed. This method is straight forward and simple to understand, but it becomes clear that this concept only works with high precision for low frequency signals. In each AD-converter based circuit there is a maximum sampling rate. The higher the measurement signal frequency is compared to the fixed AD-converter sampling frequency, the lower is the resulting oversampling rate and thus the expected accuracy and resolution of the measurement. The only way for increasing the system accuracy and resolution for high frequency measurement signals is to also increase the AD-converter sampling rate. However, this causes an enormous amount of effort when sampling in the range of several ten or hundred MHz and the circuit must be capable to process the resulting large amount of raw data. Of course such a system is possible in theory but it is not attractive for integration into a cost sensitive product.

4.2.3 Delta Modulator based Sampling Circuit Concept

In order to eliminate the above mentioned drawbacks of a conventional AD-converter based sampling scheme it is proposed to replace the AD-converter by a Delta-Modulator. A detailed description and performance analysis of a Delta Modulator has been given

Dieses Werk ist copyrightgeschützt und darf in keiner Form vervielfältigt werden noch an Dritte weitergegeben werden.
Es gilt nur für den persönlichen Gebrauch.

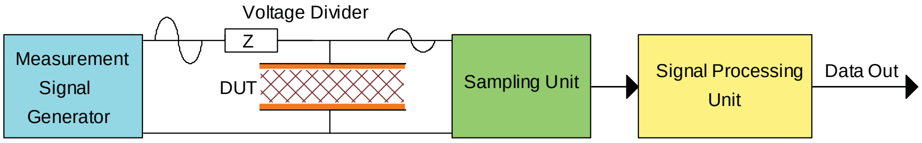

Figure 4.23: Typical measurement setup for measuring complex dielectric properties of biological cells and tissue inside a test cell. Two conductive plates encapsulate the sample material (MUT) and serve as a capacitor. The attached measurement setup generates sinusoidal measurement signals and measures amplitude distortion and phase shift caused by the sample material inside the test cell.

above in the documentation of the developed TDR-meter circuit and is not repeated here again. Fig. 4.24 shows the corresponding block schematic of the developed phase measurement circuit based on a Delta Modulator. The circuit components of this architecture are described in the following sections.

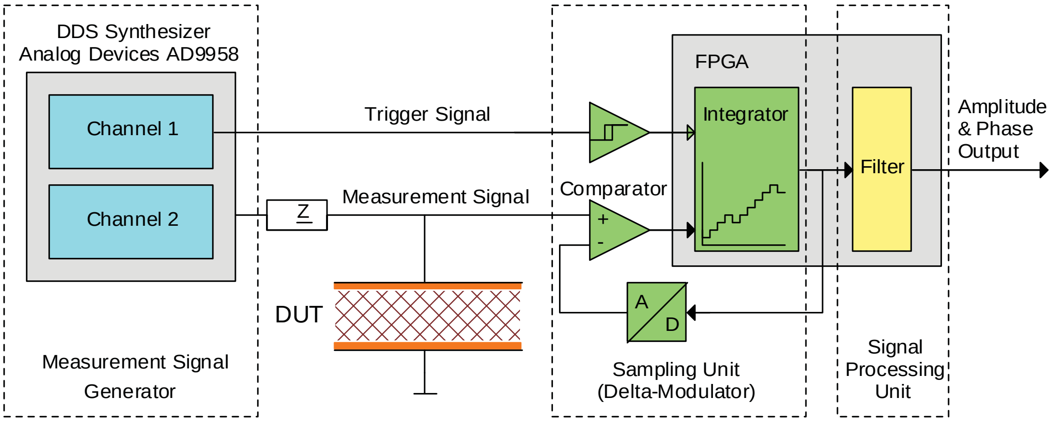

Figure 4.24: Block schematic of the new phase measurement system based on Delta-Modulation. The measurement signal is generated by a DDS-Synthesizer. The sampling unit consists of a comparator which acts as a 1 bit A/D-Converter followed by a digital integrator / counter which is triggered by an independent channel of the DDS-Synthesizer.

Measurement Signal Generator

The measurement signal generator module is implemented by using an off-the-shelf Direct Digital Synthesizer (DDS) Chip. The Synthesizer provides two independent output channels. Channel 2 generates the actual sinusoidal measurement signal while channel 1 generates an adjustable trigger signal for the integrator circuit inside the FPGA (Xilinx Spartan3 XC3S400). The DDS-Synthesizer is internally driven by a high frequency 500 MHz clock signal and therefore allows for generating measurement signals with a good SNR within a frequency range up to 1 MHz (even up to 10 MHz). The phase accumulator width is $N = 32$ bit for both channels which leads to a fine frequency resolution of each output channel of 0.12 Hz. In the circuit of the TDR-meter there was only one DDS channel for generating a defined frequency, the second frequency was generated by a binary counter divider within the FPGA logic. However, the use of two DDS channels allows for generating virtually any desirable frequency combination on channel 1 and

Dieses Werk ist copyrightgeschützt und darf in keiner Form vervielfältigt werden noch an Dritte weitergegeben werden.
Es gilt nur für den persönlichen Gebrauch.

channel 2 which is required by the implemented sampling scheme and which allows for precise adjustment of the measurement signal frequency if required.

Sampling Unit

The developed digital sampling circuitry is the main component of the phase measurement system. The sampling circuitry is based on a pure digital Delta-Modulator (DM) structure and replaces a conventional A/D-Converter. It digitizes the sinusoidal measurement signal which has been affected by the MUT. The DM-module mainly consists of a digital 12-bit counter inside the FPGA which serves as an integrator. Depending on the output state of the external comparator the counter counts either up or down on each rising edge of the trigger signal provided by channel 1 of the DDS-Synthesizer. The actual state of the integrator is converted into a corresponding analog voltage signal and fed back to the inverting input of the comparator. The high impedance positive input of the comparator is directly connected to the voltage divider of the reference impedance Z and the test cell. As a matter of principle the integrator is forced to track the sinusoidal signal on the comparators positive input. An example of the typical pattern of the integrator curve is shown in Fig. 4.25. By setting the trigger frequency, the number of samples taken in each period of the measurement signal can be adjusted. Using appropriate values, an oversampling rate of up to 10^6 can be achieved which leads to a high theoretical SNR of up to 120 dB for the DM-structure [13].

Signal Processing Unit

The output data of the Delta Modulator is the integrators curve which represents the phase shifted signal. Since the comparator inside the sampling system acts as a 1-bit A/D-converter the sampled raw data on the output of the integrator contains high frequency components. In Fig. 4.25 these high frequency components appear as ripple on the sampled sine wave. A simple digital moving averaging filter implemented inside the FPGA removes these high frequency components. Since it is possible to highly oversample the measurement signal with this circuit structure, the resulting additional phase shift of a low pass filter can be neglected if the filter width is kept in a reasonable size.

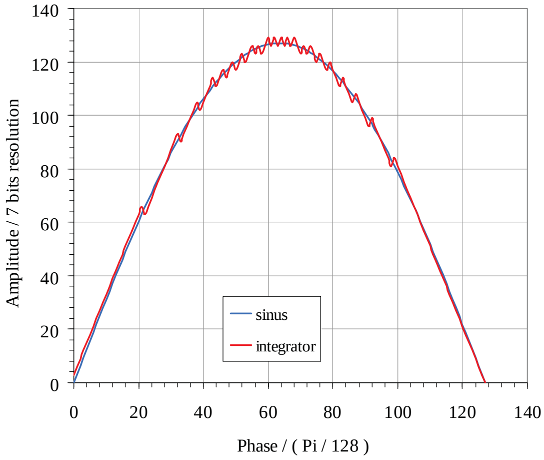

Figure 4.25: Simulation of the delta modulator illustrates the basic behavior of the integrator curve which tracks the ideal sinusoidal input signal. The simulation is performed for a 7 bit amplitude resolution system for better visualization.

Dieses Werk ist copyrightgeschützt und darf in keiner Form vervielfältigt werden noch an Dritte weitergegeben werden.
Es gilt nur für den persönlichen Gebrauch.

4.2.4 Sampling Concept for Low and High Frequency Signals

The phase measurement system is used to measure amplitude and phasing of sinusoidal signals in a frequency range from 10 Hz to 10 MHz. Due to this wide range of six decades, the operation mode of the sampling unit has to be switched between a conventional oversampling mode for digitizing low measurement frequencies and an undersampling mode for high measurement frequencies.

Oversampling Mode

The oversampling mode is used to digitize signals at low frequencies in the range of 10 Hz to 10 kHz. In this operation mode the output frequency of channel 1 is set to the absolute maximum which can be processed by the FPGA. In this operation mode all measurement samples are taken during a single period of the sinusoidal measurement signal generated by channel 2. Since the trigger signal frequency is always set to a constant maximum value which is limited by the FPGA speed, this sampling method causes a varying number of samples taken during a single sinusoidal measurement signal period dependent on the measurement signal frequency. The graph in Fig. 4.27 illustrates this effect for an assumed maximum frequency of 10 MHz which can be handled by the used FPGA logic.

Undersampling Mode

The undersampling mode is used if the measurement frequency is in the range of 10 kHz to 10 MHz. In this operation mode channel 1 also generates the measurement signal which is directed to the MUT. In contrast to the oversampling mode channel 1 generates a trigger signal frequency just slightly above the measurement frequency. Due to the fine frequency resolution of the DDS-Synthesizer the delta frequency between both channels can easily be adjusted to values in the range of a few Hz or even below 1 Hz. For the undersampling mode the graph in Fig. 4.27 assumes the trigger frequency to be exact 10 Hz above the measurement signal frequency. As a matter of principle in the undersampling mode the shape of the measurement signal is captured by sampling many repetitive measurement signals. On each incoming sine wave of the measurement signal exactly one sample is taken at a slightly delayed point. The trigger process is illustrated in Fig. 4.26. The undersampling mode allows for digitizing the sinusoidal measurement signal with a virtual high temporal resolution depending on the settings of the trigger frequency and the measurement frequency. Amplitude and phasing are measured with high accuracy by transforming the real measurement frequency to a lower frequency.

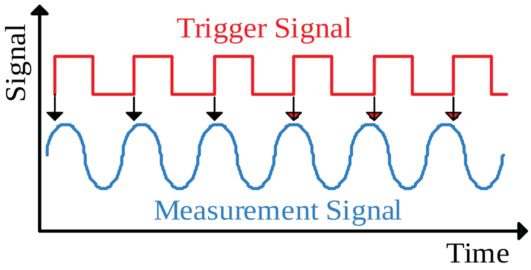

Figure 4.26: Sampling technique in the undersampling mode for capturing the signal out of multiple repetitive sine waves. The undersampling scheme is identical to the sampling scheme used in the TDR-meter circuit.

Dieses Werk ist copyrightgeschützt und darf in keiner Form vervielfältigt werden noch an Dritte weitergegeben werden.
Es gilt nur für den persönlichen Gebrauch.

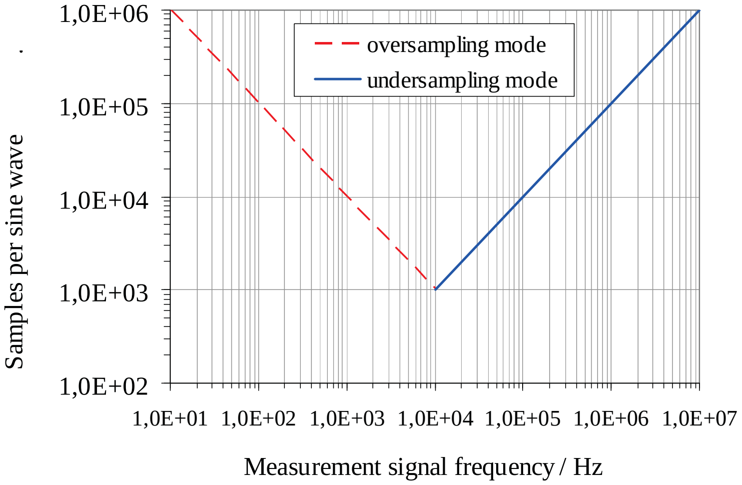

Figure 4.27: The graph shows the number of samples taken per sine wave as a function of the measurement frequency. The trigger frequency is assumed to be constant at 10 MHz for the oversampling mode. For the undersampling mode the delta frequency is assumed to be constant at 10 Hz between the trigger- and the measurement frequency.

4.2.5 Prototype Circuit and Test Results

A prototype circuit board has been constructed for the developed phase measurement concept as shown in Fig. 4.28. The prototype has been used in the laboratory for measurement of the phase shift caused by a capacitive HCT-sensor (see chapter 2). Within these laboratory experiments the developed circuit has been used in parallel to a conventional laboratory LCR-Meter in order to compare the obtained measurement results to each other. Fig. 4.29 shows one typical plot. The measurement result of the Delta Modulator circuit almost perfectly matches the curve of the expensive laboratory LCR-meter. Within all experiments done with the prototype circuit the achieved accuracy (compared to the LCR-meter as a reference) was better than 0.28 degree.

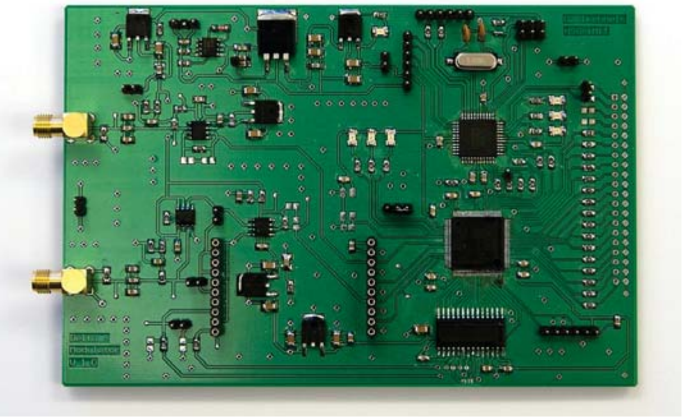

Figure 4.28: Developed prototype circuit board (100 mm x 160 mm) of the Delta Modulator based phase measurement concept. The circuit has been successfully used within real laboratory applications and is intended to be used for HCT-measurement sensors as described in chapter 2.

Dieses Werk ist copyrightgeschützt und darf in keiner Form vervielfältigt werden noch an Dritte weitergegeben werden.
Es gilt nur für den persönlichen Gebrauch.

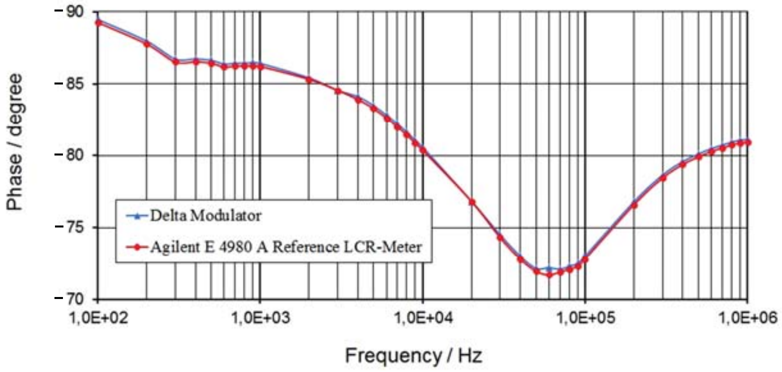

Figure 4.29: Experimental measurement data derived within laboratory experiments within a real application. For HCT-measurement blood is measured in a capacitive sensor construction and the dielectric losses inside the blood sample cause a typical frequency dependent phase shift of the measurement signal. As reference method a state-of-the-art LCR-meter from Agilent (E4980A) is used.

4.2.6 Conclusions

The developed precision phase measurement circuit is based on a Delta Modulator sampling circuit which replaces an conventional AD-converter. By switching the sampling concept between conventional oversampling mode for low frequency signals and undersampling mode for high frequency measurement signals an excellent phase resolution is gained within the tested frequency range up to 1 MHz. The Delta-Modulator based sampling circuit is very cheap and the resulting amount of raw data is small. This allows for a lightweight broadband measurement circuit which can be used within many biomedical applications where a (quasi)static impedance has to measured. Especially higher measurement frequency signals in the range of 100 kHz to 1 MHz can be measured with an outstanding phase resolution of better than 0.01 degree (for 1 MHz) which is in the range of conventional expensive laboratory equipment such as the Agilent E 4980A LCR-Meter. The employed Delta-Modulator circuitry allows for reconstructing high frequency measurement signals out of many repetitive sine waves which is equal to a time transformation of the measurement signal.

Dieses Werk ist copyrightgeschützt und darf in keiner Form vervielfältigt werden noch an Dritte weitergegeben werden.
Es gilt nur für den persönlichen Gebrauch.

4.3 Fast Chirp Signal based Impedance Measurement Platform

Within this last section of chapter 4 the developed circuit and measurement concept is described which is used for fast broadband measurement of a unknown impedance. In this thesis such a measurement system is required by the needle guidance application where the exact type of tissue has to be recognized in front of the needle tip and where only fractions of a second are allowed for measuring the complete impedance spectrum covering a bandwidth of a few kHz up to approximately 1 MHz. The developed system is different to the developed Delta Modulator based platform which can only be used in static applications. In the case of a fast and broadband measurement certain additional effort is required in order to obtain and process the required amount of data within a given short amount of time. However, by using modern components the resulting overall system can still be kept in a reasonable size, complexity and cost. Most functionality is implemented inside a mid range standard FPGA (Altera Cyclone III). This allows for a simple adaptation of the developed system to other applications by changing the FPGA configuration and/or corresponding software of the integrated softcore CPU (Nios II). The developed platform uses linear chirp signals as broadband excitation signals. The mathematical description of a chirp signal and a discussion of the advantageous signal properties is already given in chapter 1 and chapter 2 and therefore is not repeated here.

4.3.1 Potential Target Applications for fast broadband Impedance Measurement

Measuring the sensor impedance at more than just one fixed frequency is not necessary in all fast sensor applications, but it can give significant additional information about the sensor element and therefore enables to derive additional parameters. For instance, the sensor temperature drift can be compensated for or multiple parameters of a comprehensive equivalent electrical schematic of the sensor element can be derived. In many cases researchers report on interesting sensor principles and proof the concept using expensive wideband laboratory measurement equipment, but the new sensor principle is often not used in real applications due to the need for a sophisticated wideband measurement electronic. Especially time critical applications such as high speed sensors in industrial high throughput applications or sensing of a time dependent impedance [36] demand for a very fast sensor read-out and processing strategy. Examples for such time critical applications are single cell analysis [47], time dependent impedance of breathing lungs and beating hearts [36], dynamic processes such as needle insertion into human tissue [194, 195], microbiological applications [92], quality measurement in the food industry [25], electrochemistry [196], piezosensors [22], gas sensors and multiphase flow sensors [17, 18] and fast multichannel impedance tomography systems [133]. In all listed applications it is crucial to measure and process the impedance over a wide frequency range within a short period of time. The chirp signal based measurement platform which is presented within this thesis can potentially be used in all listed applications after changing a few parameters such as e.g. required bandwidth or signal duration.

4.3.2 System Concept for measuring with Chirp Signals

The developed system architecture is shown in Fig. 4.30. Most components are implemented inside a standard FPGA (Altera Cyclone III), only certain analog components are external and have to be adjusted depending on the target application (e.g. slight

Dieses Werk ist copyrightgeschützt und darf in keiner Form vervielfältigt werden noch an Dritte weitergegeben werden.
Es gilt nur für den persönlichen Gebrauch.

modification of amplifier circuits). The chirp signal is generated within the FPGA by a DDS core and converted to a corresponding analog signal by a standard 12 bit DA-converter. The generated chirp signal is then fed through a known serial resistor R_{ref} and the unknown impedance Z. The resistor is used for measuring the current which flows through the serial combination of R and Z by measuring the voltage drop across the resistor. The developed voltage across Z is also measured. For the measurement of both voltage signals a synchronous two-channel AD-converter with differential inputs is used which can sample two channels at the same time after getting a trigger signal. This ensures that there is no additional delay between the samples which would look like a phase shift in the measurement result. The maximum sampling speed of the employed AD-converter is 40 MHz while having an amplitude resolution of 12 bits. For adjusting the input voltage range of the two-channel AD-converter to the measurement signal range an amplifier circuit is placed in between. Each amplifier circuit is based on fully differential operational amplifiers and amplifies only the difference in the input voltage but not the common mode signal at the input. The captured raw data is then processed by the FPGA and the transfer function of the unknown impedance Z is output to the user.

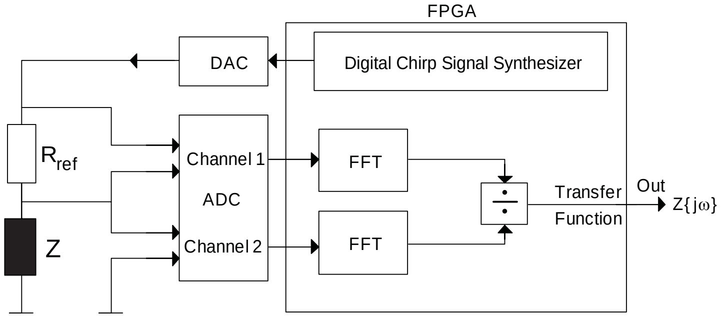

Figure 4.30: Block schematic of the developed chirp signal based platform for fast broadband impedance measurement. Most components are implemented inside a standard FPGA which allows for a flexible overall circuit which can be adapted to different applications.

4.3.3 Signal Processing of the Chirp Signals

General Signal Processing Concept

The processing of the sampled current and voltage signals is straight forward. The impedance spectrum of the unknown impedance Z is the quotient of the voltage signal spectrum and the current signal spectrum as given by equation 4.9. The spectrum of the sampled signals can easily be calculated by two parallel FFT-Blocks developed inside the FPGA logic.

$$Z(\omega) = \frac{FFT(U(t))}{FFT(I(t))} \tag{4.9}$$

The calculation of the quotient requires to divide one value by each other. However, a real division is difficult or even impossible to implement in hardware and most available development tools do not support such operations. For this reason a free version of the 32-bit Nios II softcore CPU is implemented in the FPGA which operates at a frequency of 80 MHz. This fast processor core can easily do the required division in a very short

Dieses Werk ist copyrightgeschützt und darf in keiner Form vervielfältigt werden noch an Dritte weitergegeben werden.
Es gilt nur für den persönlichen Gebrauch.

amount of time for each frequency bins of the computed spectrum. In addition this CPU can replace an external microcontroller and can be used for certain "housekeeping" functionalities and for serial data communication to e.g. a host computer.

Sampling Boundary Conditions

On the first view the proposed signal processing chain in Fig. 4.30 looks straight forward and easy to implement. But in case of broadband measurement signals, there are some theoretical and practical boundary conditions which must be fulfilled in order to obtain a useful measurement result. The first key consideration is the minimum duration of the chirp excitation signal. It is well-known that the resulting frequency resolution $\Delta\text{f} = 1/T_{chirp}$ is inverse to the measurement time. Fig. 4.31 illustrates the frequency resolution. Therefore in broadband measurements the lowest frequency component in the desired spectrum f_{min} determines the corresponding minimum excitation signal duration $T_{chirp-min}$. Assumed that at least 10 spectral lines per decade are desired for the computed transfer function, we obtain the following simple equation for $T_{chirp-min}$:

$$T_{chirp-min} = \frac{1}{f_{min}} \tag{4.10}$$

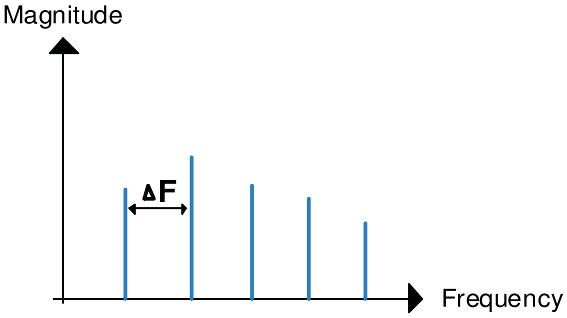

Figure 4.31: Illustration for the resulting frequency resolution Δf of the computed spectrum. In order to have a sufficient number of points per decade in the resulting impedance spectrum the chirp duration must have a minimum length.

The second key consideration is the required sampling rate of the two synchronous AD-converters used for capturing stimulus and response signal. According to the Shannon theorem the minimum sampling rate must be higher than twice the frequency of the highest frequency component in the signal. Therefore the maximum frequency component f_{max} in the chirp signal dictates the minimum sampling frequency $f_{sample-min}$ of both AD-converters according to equation

$$f_{sample-min} > 2 \cdot f_{max} \tag{4.11}$$

The resulting minimum total number of samples N_{min} required to capture one full chirp excitation signal can be calculated by combining equations 4.10 and 4.11 and expresses as

$$N_{min} = f_{sample-min} \cdot T_{chirp-min} = 2 \cdot \frac{f_{max}}{f_{min}} \tag{4.12}$$

For broadband signals covering multiple decades we always deal with the problem that f_{max} is much higher than f_{min} and therefore according to equation 4.12 we automatically obtain a very large number of samples which must be processed by the FFT algorithm.

Dieses Werk ist copyrightgeschützt und darf in keiner Form vervielfältigt werden noch an Dritte weitergegeben werden.
Es gilt nur für den persönlichen Gebrauch.

The number of samples increases exponentially with the number of frequency decades covered by the chirp signal. For instance, a chirp signal covering 3 decades requires at least $2 \cdot 10^3$ samples whereas a chirp covering 6 decades requires at least $2 \cdot 10^6$ samples.

Signal Processing Time

In most continuously running practical applications there is a maximum measurement time window given by the specific requirements of the sensor or measured process. This time window includes signal excitation/recording and following digital signal processing. In order to maximize the SNR of a measurement, the excited measurement signal energy should be as high as possible. This means that the excitation time should be as long as possible within the given window and as a result the processing time must remain very short. In other words a chirp measurement system has to be designed in such a way that the excitation time is significantly larger than the processing time to be effective. Despite the signal processing scheme presented in Fig. 4.30 is a straight forward method it would take quite a long time when processed in software using a microcontroller or a similar platform. A sample chirp signal with a duration of 200 μs covering a bandwidth of 3 decades from 1 kHz to 1 MHz already results in a minimum number of 2000 samples. The next matching power of 2 for the FFT algorithm is 2048 samples. Calculating two FFT's on 2048 data points with 12 bit amplitude resolution takes approximately 42 milliseconds on our reference design using an 8-bit ATmega128 microcontroller running at 16 MHz and 5.2 ms using a 32-bit Cortex-M3 controller running at 50 MHz. Compared to the original chirp duration of only 200 μs both microcontroller based processing solutions are slow which results in a very inefficient measurement system where most of the time is wasted by computing instead of exciting a signal. The proposed signal processing concept based on FFT computation inside an FPGA offers two great advantages compared to conventional software signal processing. First advantage is the fact that both channels can be processed in parallel which already reduces the computation time to only 50 %. Second great advantage is the wide variety of available IP-cores for signal processing which provide "pipelined architectures" for FFT processing. In a pipelined architecture the FFT unit does not have to wait for a completed sampling process. The FFT computation can already start after a short delay (a few clock ticks) after starting the sampling process. Then sampling and processing of the remaining samples is done in parallel as well. The table shown in Fig. 4.32 lists the resulting required processing time for a conventional Block-FFT and a fast Pipelined-FFT for different input array sizes. The values have been obtained by simulation with the Altera Software Package QUARTUS and the MegaCore Builder under the assumption that the FPGA is running at 100 MHz which is realistic for such a design. On the left side the conventional block mode is shown, on the right side the pipelined mode is shown. It becomes clear that this processing method is extremely fast. The developed platform is capable of processing chirp signals which cover a bandwidth of 4 decades while keeping the required signal processing time lower than approximately 10% of the complete measurement cycle. A wider bandwidth than 4 decades is theoretically possibly but would require a larger FPGA with extended Block-RAM memory on board for temporarily storing the sampled raw data.

4.3.4 Prototype Circuits and Test Measurements

A prototype circuit board has been developed and successfully used within fast tissue discrimination experiments. The complete system has intentionally been subdivided into two PBCs which can be mounted on top of each other. The lower circuit board mainly

Dieses Werk ist copyrightgeschützt und darf in keiner Form vervielfältigt werden noch an Dritte weitergegeben werden.
Es gilt nur für den persönlichen Gebrauch.

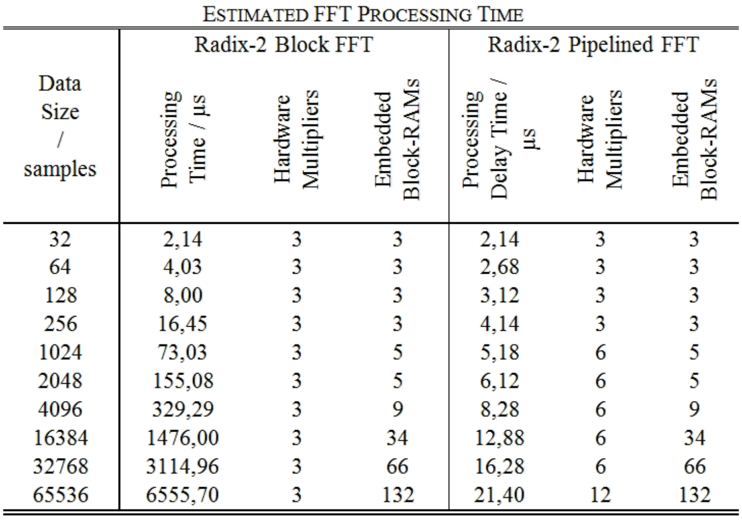

ESTIMATED FFT PROCESSING TIME

Data Size / samples	Radix-2 Block FFT			Radix-2 Pipelined FFT		
	Processing Time / µs	Hardware Multipliers	Embedded Block-RAMs	Processing Delay Time / µs	Hardware Multipliers	Embedded Block-RAMs
32	2,14	3	3	2,14	3	3
64	4,03	3	3	2,68	3	3
128	8,00	3	3	3,12	3	3
256	16,45	3	3	4,14	3	3
1024	73,03	3	5	5,18	6	5
2048	155,08	3	5	6,12	6	5
4096	329,29	3	9	8,28	6	9
16384	1476,00	3	34	12,88	6	34
32768	3114,96	3	66	16,28	6	66
65536	6555,70	3	132	21,40	12	132

Figure 4.32: Simulated processing time for FFT blocks inside the used FPGA. On the left side a standard Block-FFT is used where all data must be sampled first before the computation of the FFT can start. On the right side a pipelined FFT is simulated which operates in parallel to most of the sampling time.

contains the digital parts and is shown in Fig. 4.33. The upper circuit board shown in Fig. 4.34 mainly contains the analog components such as the fully differential amplifier circuits and the AD-converter. This modular design allows for adjusting especially the analog front end part to the specific needs of potential new target applications without the need for a complete redesign of the more complex digital circuit board which contains the FPGA.

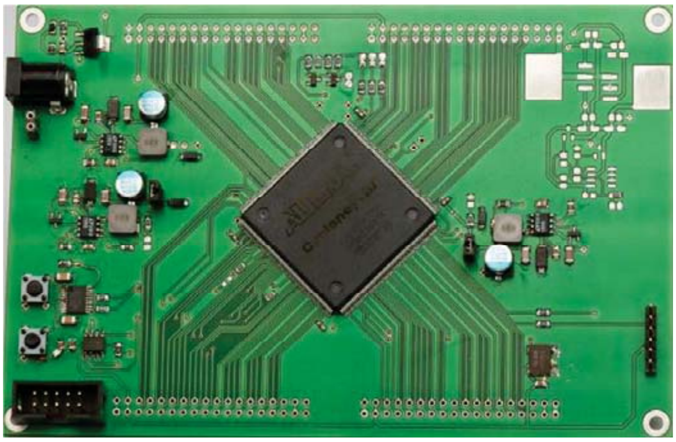

Figure 4.33: Photograph of the digital circuit board (100 mm x 160 mm) of the developed prototype design. The digital board mainly contains the FPGA and some associated components such as FLASH memory and a suitable power supply circuit.

The developed circuit is used to replace the laboratory measurement equipment (oscilloscope and signal generator)for the chirp signal based tissue discrimination as presented in chapter 2. Since such an extremely fast and broadband measurement of an impedance is not a common task, there is no laboratory measurement device available which could directly serve as a "reference" for benchmarking the new circuit. In addition the resulting SNR depends on multiple parameters such as the excited chirp signal amplitude,

Dieses Werk ist copyrightgeschützt und darf in keiner Form vervielfältigt werden noch an Dritte weitergegeben werden.
Es gilt nur für den persönlichen Gebrauch.

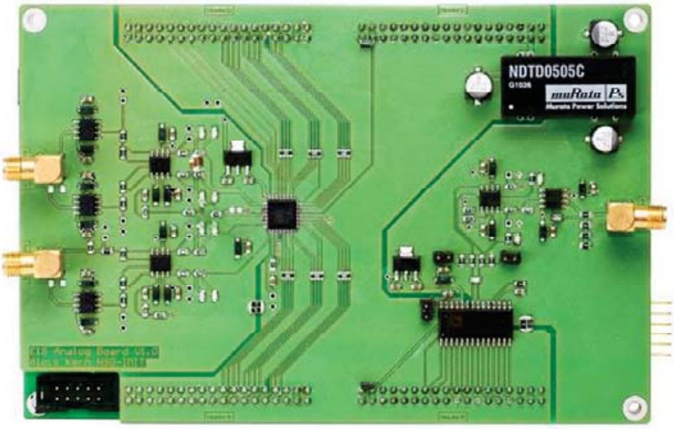

Figure 4.34: Photograph of the analog circuit board (100 mm x 160 mm) of the developed prototype design. The analog board mainly contains the differential amplifier and the AD-converter as well as the DA-converter for the signal generation. An isolated DC-DC converter allows for generating a symmetric and offset free excitation signal.

the covered bandwidth and the signal duration. All these parameters make it difficult to specify the accuracy of the system in a general way. However, in order to derive a practical result for the target application of this thesis, a direct comparison of the new circuit is made with the existing laboratory setup. As a load an RC-circuit combination is used which simulates the typical behaviour of biological tissue as presented in chapter 2 of this thesis (see Fig. 2.3). The chosen circuit parameters are $R_i = 1k\Omega$, $R_p = 1k\Omega$ and $C_M = 1nF$. The simulated theoretical Bode Diagram of this circuit is shown in Fig. 4.35. For current measurement a serial resistor with a value of 1 kOhm has been chosen, so there is a resulting voltage divider with a factor of 2 for low frequencies which is equal to -6 dB. The generated and excited chirp measurement signal is captured with an oscilloscope and a spectrum analyser (FSP from Rohde *and* Schwarz). The generated chirp signal is shown in Fig. 4.36 in time domain and in frequency domain. As expected from the theory the amplitude spectrum remains flat within the defined chirp bandwidth. The resulting computed transfer functions (Bode Diagram) of the measured virtual "Test Tissue" are shown in Fig. 4.37. On the left side the computed transfer function is shown which raw data has been measured with the laboratory setup. On the right side the computed transfer function is shown which raw data has been measured with the developed circuit. In all diagrams the presented curves show the average of 10 recorded transfer functions. Chirp signal duration (50 μs) and processing of the captured data is accomplished within approximately 100 μs for each single measurement. Thus the presented averaged curves require a total acquisition time of approximately 1 ms which is very fast compared to traditional measurement methods. The achieved measurement results based on the developed electronic circuit shows less noise especially at higher frequencies than the results based on the oscilloscope measurements. Major reason is the better amplitude resolution of the used AD-converter which is 12 bit in the circuit and only 8 bit in the oscilloscope. In addition the capacitive losses of the coaxial cables and the input capacitance of the oscilloscope cause an offset especially at higher frequencies. In contrast the parasitic capacitances of the electronic circuit are smaller and the resulting offset is almost negligible.

Dieses Werk ist copyrightgeschützt und darf in keiner Form vervielfältigt werden noch an Dritte weitergegeben werden.
Es gilt nur für den persönlichen Gebrauch.

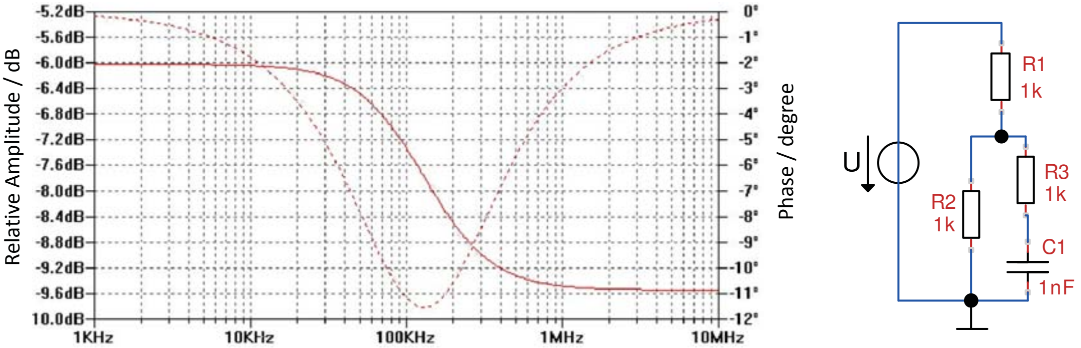

Figure 4.35: Simulated transfer function of the test circuit which is used as a complex load for comparing the developed chirp measurement circuit with the oscilloscope based laboratory setup. In series to the tissue dummy (R2, R3 and C1) a measurement resistor R1 of $1k\Omega$ is used for current measurement. At low frequencies there is the voltage divider effect caused by R1 and R2 only (C1 is high impedance) resulting in a relative amplitude of U/2 across the tissue dummy which is equal to -6 dB. At very high frequency R2 and R3 are in parallel connection because C1 becomes low impedance. The relative amplitude ratio approaches U/3 which is equal to approximately -9.6 dB.

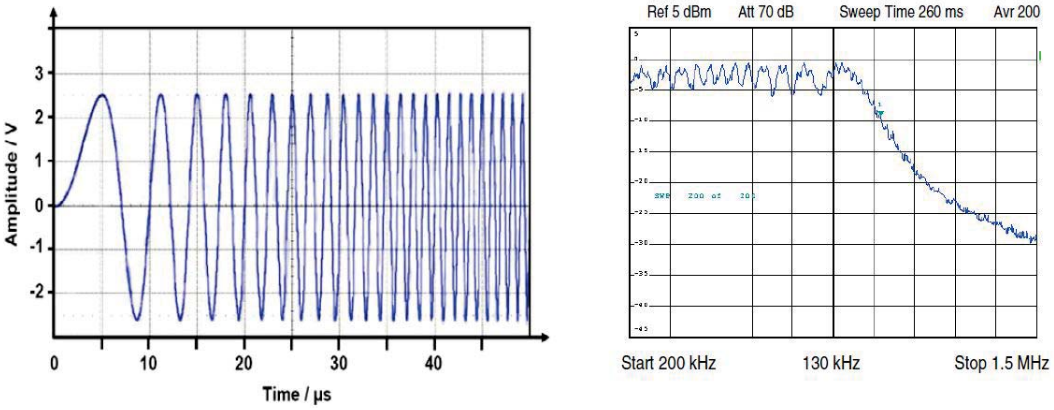

Figure 4.36: The generated and excited chirp measurement signal in time domain (left) and frequency domain (right). As expected from the theory the amplitude spectrum remains flat up to the upper bandwidth of the chirp.

Dieses Werk ist copyrightgeschützt und darf in keiner Form vervielfältigt werden noch an Dritte weitergegeben werden.
Es gilt nur für den persönlichen Gebrauch.

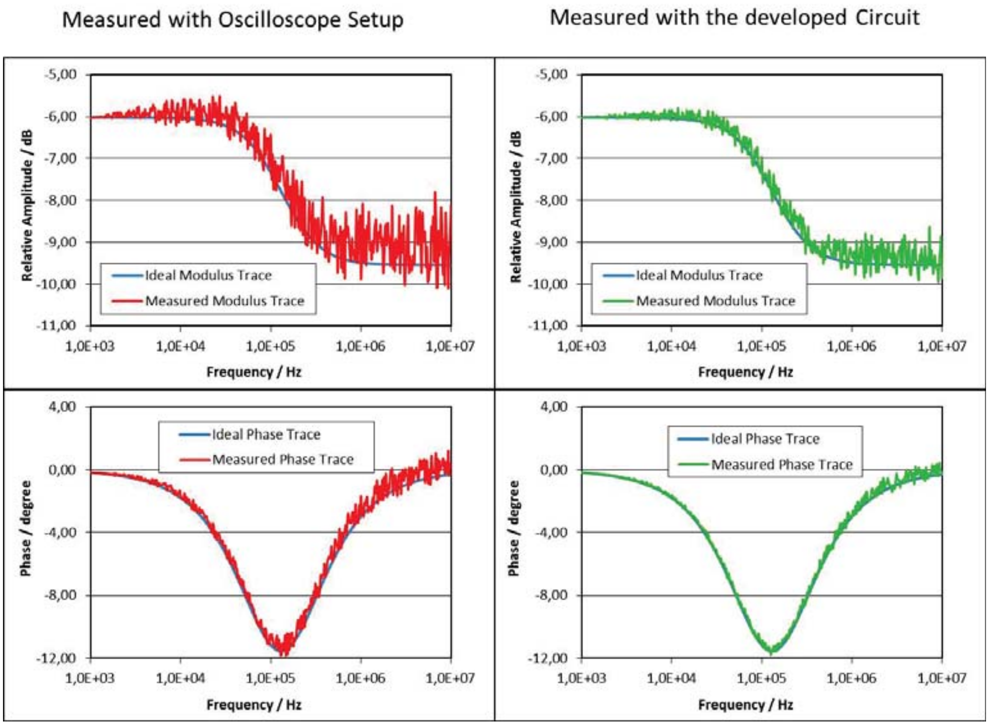

Figure 4.37: Comparison of the Bode Diagram obtained by the laboratory measurement setup, the developed circuit and the computed theoretical curve. It can be seen that the measured traces match the theoretical curve very well, only additional noise is present because of the distribution of the measurement signal energy within a wider bandwidth.

4.3.5 Discussion and Conclusions

The developed chirp signal measurement platform shows that it is possible to build a lightweight measurement system which can replace expensive standard laboratory equipment such as a fast sampling oscilloscope and an arbitrary signal generator. In addition the full signal processing is done within the circuit (FPGA) and no external computer is required. This enables the developed platform for being integrated into standalone products. Great advantage of the used chirp signals is the excellent scalability of the circuit to other applications. The concept can always remain the same, only parameters such as the signal bandwidth, amplitude and duration have to be adjusted. The mainly digital platform character allows for simply changing the processing parameters of the signal processing hardware with no modifications to the circuit board itself. However, there are mainly two limitations for this concept: the first limitation is the maximum bandwidth which is currently limited to 20 MHz (the AD-converter is sampling at 40 MHz). Increasing the sampling rate would require extensive additional effort for the data storage and processing. The selected FPGA is a mid-range FPGA which is available at very low cost. Increasing the bandwidth would mean to exchange the FPGA by a larger one which currently has several drawbacks. First the price is still relatively high for large FPGAs, second the large FPGAs are available in BGA-housings only which automatically leads to increased circuit board complexity and cost and last but not least the power consumption of high-end FPGAs is often so high that it is not realistic to build a battery supplied circuit which might be required by certain applications.

Dieses Werk ist copyrightgeschützt und darf in keiner Form vervielfältigt werden noch an Dritte weitergegeben werden.
Es gilt nur für den persönlichen Gebrauch.

5 Conclusions of the Thesis and Outlook

The presented work and the achieved research results cover a wide range of aspects such as application specific requirements, measurement signals, measurement devices, circuits, concepts and systems. The research field of "Impedance Spectroscopy" is a very large and complex field and there is a lot of potential for future applications based on smart measurement concepts, smart electronic circuits and of course smart processing of the raw data.

The obtained results and laboratory measurements showed that in all cases it is necessary to start from scratch for each target application and systematically investigate the frequency depending properties and the frequency range of interest. Having these parameters is already a first step into a solution for the target application. Based on the laboratory measurements usually a sensor frontend has to be developed while each specific application requires its individual and optimized frontend. In case of the HCT-measurement application a capacitive sensor has been constructed, analysed and optimized. For the tissue discrimination at the needle tip a galvanically coupled electrode system has been used and in case of the Time Domain Reflectometry based moisture detection system an electrically isolated transmission line was used. The obtained results for optimized frontends to these three applications are of course specific in each case and most likely will not be useful without modification for other applications. This is mainly caused by the individual physical, physiological and chemical properties of each sample material which has to be analysed. Such an individual optimization of the frontend can most likely never be replaced by one "universal frontend" which fits all requirements or which can be adjusted to different applications with ease. The fact that each target application requires an extensive amount of research and development in the laboratory first makes it very attractive to have at least a universal electronic measurement circuit available which can be attached to any frontend with no modifications or only very little modifications. Having such universal circuits available is already a huge step from the laboratory into the direction of a real product. Development time and cost is usually critical, especially because of the always required preliminary cost intensive laboratory work. The remaining budget for any electronic circuit is limited in most cases.

The two circuit concepts developed within this thesis may of course not fully cover all measurement requirements given by all potential applications in the wide field of impedance spectroscopy, but at least for a large number of target applications the proposed solutions could dramatically enhance a product development and reducing the system cost. Both systems have been developed in such a way that the universal and scalable character of each concept is kept. The delta modulator based sampling circuit can be used for sampling almost all signals reaching from narrow band sine wave signals up to broadband pulse signals with sharp rising edges containing higher frequency harmonics in the range of several 100 MHz. Despite the flexibility towards the shape of the signal the frequency and the sampling resolution can be chosen as required by the application and are independent from each other. In case of the broadband chirp signal the shape of the excitation signal is fixed, but all resulting parameters such as bandwidth, duration and signal amplitude can still be varied randomly and therefore be adapted to different applications with no hardware modifications to the processing circuit. Only a

Dieses Werk ist copyrightgeschützt und darf in keiner Form vervielfältigt werden noch an Dritte weitergegeben werden.
Es gilt nur für den persönlichen Gebrauch.

few software parameters and configurations of the employed FPGA have to be changed which can be done in almost no time.

While keeping the full desired flexibility and scalability both developed platforms are designed in such a way that a cheap construction without critical components or single-source components is possible. The "quality" (and this often means the cost) of the selected electronic components can be randomly selected depending on the targeted accuracy, resolution and maximum measurement frequency of interest. The signal processing can be done in virtually any available programmable logic device and is not fixed to a special product of a single-source manufacturer. The delta modulator structure itself can even be integrated within a very cheap and tiny standard CPLD. In this case the delta modulator would only track the input signal and of course there would be no remaining "signal processing logic" available. But the sampled signal is still reconstructed and fed back to the sampling comparator in an analog way. This gives the option for e.g. interfacing the AD-converter of a cheap standard microcontroller and capturing the "time transformed" original signal on a much lower time scale. If the resulting resolution and accuracy is sufficient within the target application, then this would even eliminate the need for a more expensive FPGA and the resulting increased circuit complexity. In case of the chirp measurement platform there is also a lot of room for flexibility. Especially the design of the amplifier stage which forms the frontend to the "sensor" can be simplified if a lower bandwidth is acceptable. In the simplest case a standard single ended AD-converter could be used which digitized the output voltage of a transimpedance amplifier circuit which "measures" the current through the MUT and develops a corresponding voltage signal on its output.

While many measurement systems have only one channel, both developed solutions of this thesis can easily be modified in such a way that multiple channels can be sampled either in a multiplexed fashion or in parallel. The use of programmable logic allows for a simple "drop in" of a previously designed and tested module and processing of the additional channels is done in parallel. This circumstance is a great advantage for multi-channel systems such as often found in biological applications where cells are monitored.

In each chapter of the thesis there is a short summary with conclusions given for the developed applications. These conclusions will not be repeated here in detail, but certain important achievements are worth to be mentioned here again especially in the context of the above mentioned key points "flexibility" and "low system cost".

The first investigated target application was the HCT-measurement task. Blood has to be analysed inside a plastic tubing with no direct contact to the blood. The developed optimized capacitive sensor approach solves the "contact-problem" by placing the blood in a fringing field with a reasonable field strength. The blood indirectly interacts with the applied measurement signals and changes in the permittivity and the conductivity of the blood can be seen in the resulting measured values capacitance and phase angle. In the medical field such a sensor has good potential for further applications with other liquids as well. Inherent advantage of the developed system is the fact that the medium in the tubing remains sterile and vice versa the sensor is not affected by the media itself. Besides medical target applications such a sensor shows good potential for being used in the drug and food and beverage industry as well as in the chemical industry where either a contamination of the medium inside the tubing has to be avoided or alternatively where the medium is difficult to handle (e.g. acids).

The second investigated target application was the needle and cannula guidance approach by classifying the exact type of biological tissue in front of a needle tip. The developed hollow coaxial design shows a very good spatial resolution, better than any

Dieses Werk ist copyrightgeschützt und darf in keiner Form vervielfältigt werden noch an Dritte weitergegeben werden.
Es gilt nur für den persönlichen Gebrauch.

other pure impedance based approach or system which has been published yet. Despite it can not replace traditional imaging based needle steering systems, it has the great advantage of being simple, small and cheap. In combination with the developed electronic chirp signal measurement system a portable solution could be brought to the market which might have impact in the field of medical first aid where large and expensive systems can not be used. In such a case the system can be used for precisely getting access to a defined vessel e.g. for catheter insertion. In addition such a "sensor needle" with a sensitive tip can potentially be used for monitoring the quality of food which often consists of biological cells or at least a mixture of cells and liquids.

Last but not least a miniaturized TDR-meter has been constructed which is already very close to a real product. So far the developed circuit is the cheapest and smallest TDR-meter which is "available on the market" while keeping the measurement accuracy and resolution in the same range as conventional expensive TDR-meters. The developed circuit could be manufactured in a small series at a cost which is a factor of 10 lower than other TDR-meters. In addition the developed circuit can be used for a completely independed remote operation which further reduces the overall system cost in monitoring applications. It is the first TDR-meter which also contains a large memory for storing measurement data and various interface systems for simple data transmission. Furthermore the low price and the small size of the TDR-meter enables to use it in applications where it was previously not possible. Because of the mentioned advantages it becomes now attractive to install one dedicated TDR-meter at the end of each transmission line sensor instead of connecting multiple sensor lines via a multiplexer to the TDR-meter. One of the biggest resulting advantages is then the fact that there is no cabling required to the sensor line. The low stand-by current consumption and the integrated data storage options and the wireless interface allow for placing the TDR-meter at any position e.g. within a building and it can be powered from a battery pack for several month or even years (depending on the measurement interval).

The success of the three projects can also be seen based on the interest of other companies and institutions on this technology. The proposed HCT-sensor design is further developed into a real product at the HSG-IMIT together with industrial partners in order to derive a real medical product for dialysis machines. The developed tissue classification method for needles and cannulas is further investigated in collaboration with a second partner in the field of medical systems and is also intended to be used for dialysis applications. A more detailed description of the target applications can unfortunately not be given here because of existing NDA agreements.

Last but not least the produced TDR-meters have already been installed in two target applications for remote ground water level monitoring and moisture detection in buildings. Especially the proposed solution for the moisture detection in buildings shows great potential and the project partners especially from the Technical University of Darmstadt have significant interest in these applications.

However, last but not least there is always some room for future ideas which might further enhance the technical properties of the achieved developments. As described above it is easily possible to scale the developed circuits and it became clear that at least some minor electronic components have to be adjusted which form the interface to the frontend. But the digital structure of the core itself remains always identical. This makes it potentially extremely attractive to develop an integrated circuit which contains either the components for a (multichannel) delta modulator or alternatively for a (multichannel) chirp based measurement systems. Integration into one single chip would dramatically reduce the overall size of the resulting application circuit as well as

Dieses Werk ist copyrightgeschützt und darf in keiner Form vervielfältigt werden noch an Dritte weitergegeben werden.
Es gilt nur für den persönlichen Gebrauch.

the power consumption which is a very important key factor in many target applications. Due to the digital character of both systems it would either be possible to build a digital chip only which does only contain the logic cores of the FPGA or alternatively it would be possible to develop a complete measurement system on one single chip including analog components such as e.g. the AD-converters, DA-Converters, the latched sampling comparator or amplifiers for the analog input signal.

Dieses Werk ist copyrightgeschützt und darf in keiner Form vervielfältigt werden noch an Dritte weitergegeben werden.
Es gilt nur für den persönlichen Gebrauch.

Dieses Werk ist copyrightgeschützt und darf in keiner Form vervielfältigt werden noch an Dritte weitergegeben werden.
Es gilt nur für den persönlichen Gebrauch.

List of Abbreviations

AC	Alternating Current
AD-Converter	Analog-Digital-Converter
BGA	Ball Grid Array
CPLD	Complex Programmable Logic Device
CPU	Central Processing Unit
CT	Computer Tomography
DA-Converter	Digital-Analog-Converter
DC	Direct Current
DDS	Direct Digital Synthesis
DM	Delta Modulator
DSO	Digital Storage Oscilloscope
DSP	Digital Signal Processor
DUT	Device Under Test
EIT	Electrical Impedance Tomography
EMC	Electro Magnetic Coupled
FEM	Finite Element Method
FFT	Fast Fourier Transform
FPGA	Field Programmable Gate Array
HCT	Hematocrit
IS	Impedance Spectroscopy
KIT	Karlsruhe Institute of Technology
LAN	Local Area Network
LSB	Least Significant Bit
MCU	Microcontroller Unit
MLS	Maximum Length Sequence
MRI	Magnetic Resonance Imaging
MSB	Most Significant Bit
MUT	Material Under Test
PCB	Printed Circuit Board
PE	Polyethylene
PEEK	Polyetheretherketone
PTFE	Polytetrafluorethylene
PVC	Polyvinyl Chloride
RF	Radio Frequency
RTC	Real Time Clock
SNR	Signal to Noise Ratio
SPI	Serial Peripheral Interface
SRAM	Static Random Access Memory
TDR	Time Domain Reflectometry
TF	Transfer Function
US	Ultrasound
USB	Universal Serial Bus
ZW	Warburg Impedance
Z_W	Characteristic Wave Impedance

Dieses Werk ist copyrightgeschützt und darf in keiner Form vervielfältigt werden noch an Dritte weitergegeben werden.
Es gilt nur für den persönlichen Gebrauch.

Bibliography

[1] Uwe Tröltzsch. *Modellbasierte Zustandsdiagnose von Gerätebatterien.* Dissertation, Universität der Bundeswehr München, 2005.

[2] Jung-Suk Yoo, Inja Song, Ji-Hun Lee, and Su-Moon Park. Real-Time Impedance Measurements during Electrochemical Experiments and Their Application to Aniline Oxidation. *Analytical Chemistry*, 75:2962–2968, 2003.

[3] Wolfgang Fichtner. *Impedanzmessungen in organischen Flüssigkeiten geringer Leitfähigkeit und ihr Einsatz zur Untersuchung von Schmierölen.* Dissertation, TU Dresden, 2002.

[4] Tetsuya Osaka and Katsuhiko Naoi. Application of On-Line Impedance Measurement Using Fast Fourier Transform to Electochemical Systems. *Bulletin of the Chemical Society of Japan*, 55:36–40, 1982.

[5] Ruben H. Milocco. Minimal Measurement Time In Electrochemical Impedance Identification. *Electrochemical Acta*, 39:1433–1439, 1994.

[6] T.J. Vyncke, F.M.L.L. De Belie, R.K. Boel, J.A.A. Melkebeek, Cheng Yonghua, and P. Lataire. Identification of PM synchronous machines in the frequency domain by broadband excitation. In *Power Electronics, Electrical Drives, Automation and Motion, 2008. SPEEDAM 2008. International Symposium on*, pages 1253 –1258, 11-13 2008.

[7] A. Palani and V. Jayashankar. An Adaptive High Resolution Measuring System for Charcaterizing Transformers Subjected to Broadband Excitation. In *TENCON 2005 2005 IEEE Region 10*, pages 1 –5, 21-24 2005.

[8] A. Ganji, P. Guillaume, R. Pintelon, and P. Lataire. Induction motor dynamic and static inductance identification using a broadband excitation technique. *Energy Conversion, IEEE Transactions on*, 13(1):15 –20, mar 1998.

[9] M. Mabwe Badileshi, D. Cristian, and G.-A. Capolino. Broadband excitation signal techniques for electric machine diagnostics. In *Diagnostics for Electric Machines, Power Electronics and Drives, 2003. SDEMPED 2003. 4th IEEE International Symposium on*, pages 236 – 241, 24-26 2003.

[10] Jie Wu, Yuxing Ben, and Hsueh-Chia Chang. Particle detection by electrical impedance spectroscopy with asymmetric-polarization AC electroosmotic trapping. *Micofluid Nanofluid*, 1:161–167, 2005.

[11] Shady Gawad, Karen Cheung, Urban Seger, Arnaud Bertsch, and Philippe Renaud. Dielectric spectroscopy in a micromachined flow cytometer: theoretical and practical considerations. *Lab on a Chip*, 4:241–251, 2004.

[12] Olfa Kanoun, Andrey Tetyuev, and Hans-Rolf Tränkler. Bodenfeuchtemessung mittels Impedanzspektroskopie. *Technisches Messen*, 71:475–485, 2004.

Dieses Werk ist copyrightgeschützt und darf in keiner Form vervielfältigt werden noch an Dritte weitergegeben werden.
Es gilt nur für den persönlichen Gebrauch.

[13] Rolf Becker. *Spatial Time Domain Reflectometry for Monitoring Transient Soil Moisture Profiles.* Dissertation, Universität Fridericiana zu Karlsruhe, 2004.

[14] Wencheng Xiong and Yun Shao. Models for imaginary part of dielectric constant of moisture and salt soil. In *Geoscience and Remote Sensing Symposium, 2004. IGARSS '04. Proceedings. 2004 IEEE International*, volume 6, pages 4302 – 4305 vol.6, 20-24 2004.

[15] Andrey Tetyuev and Olfa Kanoun. Method of Soil Moisture Measurement by Impedance Spectroscopy with Soil Type Recognition for In-Situ Applications. *Technisches Messen*, 73:404–412, 2006.

[16] T. Flaschke and H.-R. Trankler. Dielectric soil water content measurements independent of soil properties. In *Instrumentation and Measurement Technology Conference, 1999. IMTC/99. Proceedings of the 16th IEEE*, volume 1, pages 37 –41 vol.1, 1999.

[17] Marco Jose da Silva. *Impedance Sensors for Fast Multiphase Flow Measurement and Imaging.* Dissertation, Technische Universität Dresden, 2008.

[18] Marco Jose Da Silva, Eckhard Schleicher, and Uwe Hampel. A Novel Needle Probe Based on High-Speed Complex Permittivity Measurements for Investigation of Dynamic Fluid Flows. *IEEE Transactions on Instrumentation and Measurement*, 56:1249–1256, 2007.

[19] A. Scheuermann and C. Huebner. On the Feasibility of Pressure Profile Measurement With Time-Domain Reflectometry. *IEEE Transactions on Instrumentation and Measurement*, 58:467–474, 2009.

[20] N. E. Hager. Monitoring of cement hydration by broadband time-domain-reflectometry dielectric spectroscopy. *Journal of Applied Physics*, 96:5117–5128, 2004.

[21] J. Scherbel, P. H. Nguyen, G. Paasch, W. Brütting, and M. Schwoerer. Temperature dependent broadband impedance spectroscopy on poly(-p-phenylene-vinylene) light-emitting diodes. *Journal of Applied Physics*, 83:5045–5055, 1998.

[22] T. Saar, O. Märtens, M. Reidla, and A. Ronk. Chirp-based impedance spectroscopy of piezo-sensors. In *Electronics Conference, 2010. BEC 2008. 12th International Biennial Baltic*, pages 339–342, 2010.

[23] D. Popovic, L. McCartney, C. Beasley, M. Lazebnik, M. Okoniewski, S. C. Hagness, and J. H. Booske. Precision open-ended coaxial probes for in vivo and ex vivo dielectric spectroscopy of biological tissues at microwave frequencies. *IEEE Transactions on Microwave Theory and Techniques*, 53(5):1713–1722, 2005.

[24] M. Altmann, U. Pliquett, R. Suess, and E. von Borell. Prediction of lamb carcass composition by impedance spectroscopy. *J Anim Sci*, 82:816–825, 2004.

[25] Uwe Pliquett. Bioimpedance: A Review for Food Processing. *Food Eng Rev*, 2:74–94, 2010.

[26] S. Dado. Tissue Morphology and Cell Impedance Based Biosensors for Toxicity Testing. *Measurement Science Review*, 9:105–108, 2009.

Dieses Werk ist copyrightgeschützt und darf in keiner Form vervielfältigt werden noch an Dritte weitergegeben werden.
Es gilt nur für den persönlichen Gebrauch.

[27] A. Cataldo, M. Vallone, L. Tarricone, G. Cannazza, and M. Cipressa. TDR Moisture Estimation for Granular Materials: An Application in Agro-Food Industrial Monitoring. *IEEE Transactions on Instrumentation and Measurement*, 58:2597–2605, 2009.

[28] Gyula Simon and Johan Schoukens. Robust broadband periodic excitation design. In *Instrumentation and Measurement Technology Conference, 1999. IMTC/99. Proceedings of the 16th IEEE*, volume 2, pages 1217 –1221 vol.2, 1999.

[29] B. Sanchez and R. Bragos. Multifrequency simultaneous bioimpedance measurements using multitone burst signals for dynamic tissue characterization. *Journal of Physics: Conference Series*, 224:1–4, 2010.

[30] U. Pliquett and T. Nacke. Process relevant impedance measurement: fast and robust. In *Electronics Conference, 2010. BEC 2008. 12th International Biennial Baltic*, pages 227–230, 6-8 2010.

[31] J. Schoukens and T. Dobrowiecki. Design of broadband excitation signals with a user imposed power spectrum and amplitude distribution. In *Instrumentation and Measurement Technology Conference, 1998. IMTC/98. Conference Proceedings. IEEE*, volume 2, pages 1002 –1005 vol.2, 18-21 1998.

[32] Toivo Paavle, Mart Min, Jaan Ojarand, and Toomas Parve. Short-Time Chirp Excitations for Using in Wideband Characterization of Objects: An Overview. In *Electronics Conference, 2010. BEC 2008. 12th International Biennial Baltic*, pages 253–256, 2010.

[33] Toivo Paavle, Mart Min, and Toomas Parve. Using of chirp excitation for bioimpedance estimation: Theoretical aspects and modeling. In *Electronics Conference, 2008. BEC 2008. 11th International Biennial Baltic*, pages 325 –328, 6-8 2008.

[34] J. Ojarand, P. Annus, R. Land, T. Parve, and M. Min. Nonlinear Chirp Pulse Excitation for the Fast Impedance Spectroscopy. *Electronics and Electrical Engineering*, 4:73–76, 2010.

[35] Manoochehr Nahvi and Brian S. Hoyle. Electrical Impedance Spectroscopy Sensing for Industrial Processes. *IEEE Sensors Journal*, 9:1808–1816, 2009.

[36] Mart Min, Raul Land, Toivo Paavle, Toomas Parve, and Paul Annus. Broadband spectroscopy of a dynamic impedance. *J. Phys.: Conf. Ser.*, 224, 2010.

[37] M Min, U Pliquett, Nacke, A Barthel, P Annus, and R Land. Broadband excitation for short-time impedance spectroscopy. *Physiol. Meas.*, 29:185–192, 2008.

[38] M. Min, U. Pliquett, T. Nacke, A. Barthel, P. Annus, and R. Land. Signals in bioimpedance measurement: different waveforms for different tasks. *IFMBE Proceedings*, 17:181–184, 2007.

[39] K. Darowicki and P. Ślepski. Influence of the analyzing window on electrode impedance measurement by the continuous frequency scanning method. *Journal of Electroanalytical Chemistry*, 533:25–31, 2002.

Dieses Werk ist copyrightgeschützt und darf in keiner Form vervielfältigt werden noch an Dritte weitergegeben werden.
Es gilt nur für den persönlichen Gebrauch.

[40] W.D.T. Davies. Using the binary maximum length sequence for the identification of system dynamics. *Electrical Engineers, Proceedings of the Institution of*, 114(10):1582 –1584, october 1967.

[41] Shady Gawad, Tao Sun, Nicolas G. Green, and Hywel Morgan. Impedance spectroscopy using maximum length sequences: Application to single cell analysis. *Review of Scientific Instruments*, 78:054301–2 – 054301–7, 2007.

[42] T. J. Hamilton, A. van Schaik, and B. Cornell. Measuring the impedance of a tethered bilayer membrane biosensor. In *Biomedical Circuits and Systems Conference, 2008. BioCAS 2008. IEEE*, pages 361 –364, 20-22 2008.

[43] L. Rufer, S. Mir, E. Simeu, and C. Domingues. On-chip testing of MEMS using pseudo-random test sequences. In *Design, Test, Integration and Packaging of MEMS/MOEMS 2003. Symposium on*, pages 50 – 55, 5-7 2003.

[44] J. Sachs, P. Peyerl, and M. Rossberg. A new UWB-principle for sensor-array application. In *Proc. 16th IEEE IMTC/99 Instrumentation and Measurement Technology Conf*, volume 3, pages 1390–1395, 1999.

[45] J. Sachs, P. Peyerl, M. Kmec, and F. Tkac. Digital Ultra-Wideband-Sensor Electronics integrated in SiGe-Technology. In *Proc. 32nd European Microwave Conf*, pages 1–4, 2002.

[46] Tao Sun, Shady Gawad, Nicolas G Green, and Hywel Morgan. Broadband Impedance Spectroscopy for Single Particles in High Throughput Microfluidic Cytometer using Pseudorandom Noise. In *International Conference on Bio-Nano-Informatics Fusion & International Forum on Biochip Technologies*, 2006.

[47] Tao Sun, Shady Gawad, Catia Bernabini, Nicolas G Green, and Hywel Morgan. Broadband single cell impedance spectroscopy using maximum length sequences: theoretical analysis and practical considerations. *Meas. Sci. Technol.*, 18:2859–2868, 2007.

[48] Tao Sun, David Holmes, Shady Gawad, Nicolas G. Green, and Hywel Morgan. High speed multi-frequency impedance analysis of single particles in a microfluidic cytometer using maximum length sequences. *Lab on a Chip*, 7:1034–1040, 2007.

[49] Ai Hui Tan and Keith R. Godfrey. The generation of binary and near-binary pseudorandom signals: an overview. *IEEE Transactions on Instrumentation and Measurement*, 51(4):583 – 588, aug 2002.

[50] Yuxiang Yang, Minhang Kang, Yong Lu, Jian Wang, Jing Yue, and Zonghai Gao. Design of a wideband excitation source for fast bioimpedance spectroscopy. *Meas. Sci. Technol.*, 22:1–8, 2011.

[51] Yuxiang Yang, Minhang Kang, Yong Lu, Jian Wang, Jing Yue, and Zonghai Gao. Design of a wideband excitation source for fast bioimpedance spectroscopy. *Meas. Sci. Technol.*, 22:1–8, 2011.

[52] Uwe Pliquett, Dieter Frense, Markus Schönfeldt, Christian Frätzer, Yong Zhang, Brian Cahill, Michael Metzen, Andreas Barthel, Thomas Nacke, and Dieter Beckmann. Testing miniaturized electrodes for impedance measurements within the Beta-Dispersion - a practical approach. *J Electr Bioimp*, 1:41–55, 2010.

Dieses Werk ist copyrightgeschützt und darf in keiner Form vervielfältigt werden noch an Dritte weitergegeben werden.
Es gilt nur für den persönlichen Gebrauch.

[53] A. Searle and L. Kirkup. A direct comparison of wet, dry and insulating bioelectric recording electrodes. *Physiol. Meas.*, 21:271–283, 2000.

[54] H. P. Schwan. Electrode Polarization Impedance and Measurements in Biological Material. *Annals of the New York Academy of Sciences*, 148:191–209, 1968.

[55] P. A. Cirkel, J. P. M. van der Ploeg, and G. J. M. Koper. Electrode effects in dielectric spectroscopy of colloidal suspensions. *Physica A*, 235:269–278, 1997.

[56] U. Pliquett, E. Gersing, and F. Pliquett. Evaluation of Fast Time-domain Based Impedance Measurements on Biological Tissue. *Biomedizinische Technik*, 45:6–13, 2000.

[57] J Kozlowska, B Rigaud, E Martinez, M Granie, and J P Morucci. Determination of impedance of tissue in the frequency range 10E-6 - 20 MHz: preliminary results. *Clin. Phya. Physiol. Meas.*, 13:73–75, 1992.

[58] Buli Xu and Victor Giurgiutiu. Efficient electromechanical (E/M) impedance measuring method for active sensor structural health monitoring. In *Proceedings of the Smart Structures and Materials 2005: Sensors and Smart Structures Technologies for Civil, Mechanical, and Aerospace Systems*, pages 271–280, 2005.

[59] O. Märtens, T Saar, M. Min, R. Landis, and M. Reidla. Fast Impedance Spectroscopy of Piezosensors for Structural Health Monitoring. *Electronics and Electrical Engineering*, 7:31–34, 2010.

[60] Jerzy Hoja and Grzegorz Lentka. Fast Impedance Spectroscopy Method Using Squared Pulse Excitation. In *2th IMEKO TC1 & TC7 Joint Symposium on Man Science & Measurement, Annecy, France*, 2008.

[61] Grzegorz Lentka and Jerzy Hoja. Fast impedance measurement method using Laplace transformation. In *5th IMEKO TC4 Symposium on Novelties in Electrical Measurements and Instrumentation*, 2007.

[62] David Yelamos, Oscar Cascas, Ramon Bragos, and Javier Rosell. Improvement of a Front End for Bioimpedance Spectroscopy. *Annals of the New York Academy of Sciences*, 873:306–312, 1999.

[63] K. R. Aroom, M. T. Harting, C. S. Cox, R. S. Radharkrishnan, C. Smith, and B. S. Gill. Bioimpedance analysis: a guide to simple design and implementation. *J. Surg. Res.*, 153:23–30, May 2009.

[64] Dale E. Mathis and Richard P. Buck. High-speed Cross-Correlator for Broad-Band Impedance Measurements. *Analytical Chemistry*, 48:2033–2035, 1976.

[65] John J. Almasi and Otto H. Schmitt. Automated Measurement of Bioelectric Impedance at Very Low Frequencies. *Computers And Biomedical Research*, 7:449–456, 1974.

[66] F. Seoane, R. Bragos, and K. Lindecrantz. Current Source for Wideband Electrical Bioimpedance Spectroscopy Based on a Single Operational Amplifier. *IFMBE Proceedings*, 14:707–710, 2007.

Dieses Werk ist copyrightgeschützt und darf in keiner Form vervielfältigt werden noch an Dritte weitergegeben werden.
Es gilt nur für den persönlichen Gebrauch.

[67] J J A van Weereld, D A L Collie, and M A Player. A fast resistance measurement system for impedance tomography using a bipolar DC pulse method. *Measurement Science and Technology*, 12:1002–1011, 2001.

[68] F. Thiel and C. Hartung. Multikanalsystem zur nichtinvasiven Funktions- und Zustandsanalyse von Organen und Gewebe. *Biomed. Technik*, 49:233–237, 2004.

[69] Alex Hartov, Robert A. Mazzarese, Fred R. Reiss, Todd E. Kerner, K. Sunshine Osterman, Dinise B. Williams, and Keith D. Paulsen. A Multichannel Continuously Selectable Multifrequency Electrical Impedance Spectroscopy Measurement System. *IEEE Transactions on Biomedical Engineering*, 47:49–58, 2000.

[70] T. Nacke, R. Land, A. Barthel, J. Friedrich, P. Peyerl, M. Helbig, J. Sachs, M. Schafer, and U. Pliquett. Process instrumentation for impedance spectroscopy - a modular concept. In *Electronics Conference, 2008. BEC 2008. 11th International Biennial Baltic*, pages 235 –238, 6-8 2008.

[71] T. Nacke, A. Barthel, J. Friedrich, M. Helbig, J. Sachs, M. Schäfer, P. Peyerl, and U. Pliquett. A new hard and software concept for impedance spectroscopy analysers for broadband process measurements. In *IFMBE Proceedings 17*, 2007.

[72] Thomas Nacke, Andreas Barthel, Dieter Beckmann, Uwe Pliquett, Jürgen Friedrich, Peter Peyerl, Marko Helbig, and Jürgen Sachs. Messsystem für die impedanzspektroskopische Breitband-Prozessmesstechnik. *Technisches Messen*, 78:3–14, 2011.

[73] Thomas Schneider. *Wideband impedance spectrum analyzer with arbitrary fine frequency resolution for in situ sensor applications.* Dissertation, Otto-von-Guericke-Universität Magdeburg, 2008.

[74] Mart Min. Embedded Signal Processing in Impedance Spectroscopy. In *NORCHIP, 2008.*, pages 47 –52, 16-17 2008.

[75] P. Annus, M. Min, and J. Ojarand. Shortened square wave waveforms in synchronous signal processing. In *Instrumentation and Measurement Technology Conference Proceedings, 2008. IMTC 2008. IEEE*, pages 1259 –1262, 12-15 2008.

[76] Olev Märtens, Mart Min, Raul Land, and Paul Annus. Multi-frequency and Multi-channel Bio-impedance Measurement Solution. In *Signal Processing Symposium, 2006. NORSIG 2006. Proceedings of the 7th Nordic*, pages 178 –181, june 2006.

[77] Peeter Ellervee, Paul Annus, and Mart Min. High Speed Data Preprocessing for Bioimpedance Measurements: Architectural Exploration. In *NORCHIP, 2009*, pages 1–4, 2009.

[78] R Patz, S Watson, C Ktistis, M Hamsch, and A J Peyton. Performance of a FPGA-based Direct Digitising Signal Measurement module for MIT. *Journal of Physics: Conference Series*, 224:12–17, 2010.

[79] Pil Joong Yoo, Dae Hyun Lee, Tong In Oh, and Eung Je Woo. Wideband Bio-impedance Spectroscopy using Voltage Source and Tetra-polar Electrode Configuration. *Journal of Physics: Conference Series*, 224, 2010.

Dieses Werk ist copyrightgeschützt und darf in keiner Form vervielfältigt werden noch an Dritte weitergegeben werden.
Es gilt nur für den persönlichen Gebrauch.

[80] L Beckmann, M Jacob, C Hoog Antink, A Cordes, R Pikkemaat, N Jungbecker, T Gries, and S Leonhardt. Portable Bioimpedance Spectroscopy device and textile electrodes for mobile monitoring applications. *J. Phys.: Conf. Ser.*, 224, 2005.

[81] R. G. Lerch, E. Spiegel, R. Kakerow, R. Hakenes, H.Kappert, H. Kohlhaas, N. Kordas, M. Buchmann, T. Franke, Y. Manoli, and J. Mueller. A Programmable Mixed-Signal ASIC for Data Acquisition Systems in Medical Implants. *Proceedings of the IEEE International Solid-State Circuits Conference*, pages 162–163, 1995.

[82] Analog Devices. AD5933 – Technical Data Sheet, 2005.

[83] Raúl Macías Macías. Towards Wearable Spectroscopy Bioimpedance Applications. Master's thesis, University of Boras, 2009.

[84] Martin Israel. BioChip-Impedanzspektroskopie / Entwicklung eines Impedanzmessgerätes auf Basis des AD5933. Master's thesis, TU München, 2007.

[85] Jerzy Hoja and Grzegorz Lentka. Portable Analyzer For Impedance Spectroscopy. In *XIX IMEKO World Congress Fundamental and Applied Metrology September 6-11, 2009, Lisbon, Portugal*, 2009.

[86] Alberto Yúfera and Adoración Rueda. A CMOS Bio-Impedance Measurement System. In *Proceedings of the 2009 12th International Symposium on Design and Diagnostics of Electronic Circuits&Systems*, pages 252–257, 2009.

[87] C M Kurz, H Büth, and H Thielecke. Influence of transfection process on single cell impedance. In *Proceedings of the XIVth International Conference on Electrical Bioimpedance*, 2010.

[88] Hsin-Hung Li, Jen-Yu Jao, Ming-Kun Chen, Ling-Sheng Jang, and Yi-Chu Hsu. Open-ended MEMS Probes for Dielectric Spectroscopy of Biological Cells at Radio Frequencies. *Piers Online*, 5:251–255, 2009.

[89] Raj M. Pugo, Steven C. Deane, Carl Glasse, Michael R. Burcher, Hywel Morgan, and Christian H. Reccius. Flow Speed Particle Focussing in Microfluidic Impedance Measurements. In *Proceedings of the 14th International Conference on Miniaturized Systems for Chemistry and Life Sciences*, 2010.

[90] Shishuang Sun, Pommerenke D.J., Drewniak J.L., Genda Chen, Liang Xue, Brower M.A., and Koledintseva M.Y. A Novel TDR-Based Coaxial Cable Sensor for Crack Strain Sensing in Reinforced Concrete Structures. *IEEE Transactions on Instrumentation and Measurement*, 58:2714–2725, 2009.

[91] T. Lanz, S. Hafizovic, J. Rothe, R. Streichan, N. Goedecke, F. Heer, and A. Hierlemann. Differential Impedance Spectrometer and Vision System for Analysis of Single Cells. In *Transducers*, June 2009 2009.

[92] Hagen Thielecke. Impedanzspektroskopie für gewebebasierte Biosensoren. *Technisches Messen*, 72:609–616, 2005.

[93] A.A. Pilla, P.R. Nasser, and J.J. Kaufman. Gap junction impedance, tissue dielectrics and thermal noise limits for electromagnetic field bioeffects. *Bioelectrochemistry and Bioenergetics*, 35:63–69, 1994.

Dieses Werk ist copyrightgeschützt und darf in keiner Form vervielfältigt werden noch an Dritte weitergegeben werden.
Es gilt nur für den persönlichen Gebrauch.

[94] Thomas Nacke, Mario Anhalt, Dieter Frense, and Dieter Beckmann. Anwendungsmöglichkeiten der Impedanzspektroskopie in der Biotechnologie. *Technisches Messen*, 69:12–18, 2002.

[95] Daniel Gomez Abad. Development of a Capacitive Bioimpedance Measurement System. Master's thesis, RWTH Aachen, 2009.

[96] Mandi J Bossingham, Nadine S Carnell, and Wayne W Campbell. Water balance, hydration status, and fat-free mass hydration in younger and older adults. *Am J Clin Nutr*, 81(6):1342–1350, Jun 2005.

[97] Paul W Chamney, Peter Wabel, Ulrich M Moissl, Manfred J Müller, Anja Bosy-Westphal, Oliver Korth, and Nigel J Fuller. A whole-body model to distinguish excess fluid from the hydration of major body tissues. *Am J Clin Nutr*, 85:80–89, 2007.

[98] M. Dittmar and H. Reber. New equations for estimating body cell mass from bioimpedance parallel models in healthy older Germans. *Am J Physiol Endocrinol Metab*, 281(5):E1005–E1014, Nov 2001.

[99] Carrie Earthman, Diana Traughber, Jennifer Dobratz, and Wanda Howell. Bioimpedance Spectroscopy for Clinical Assessment of Fluid Distribution and Body Cell Mass. *Nutr Clin Pract*, 22:389–405, 2007.

[100] Ulrich Moissl, Peter Wabel, Steffen Leonhardt, and Rolf Isermann. Modellbasierte Analyse von Bioimpedanz-Verfahren. *Automatisierungstechnik*, 52:270–279, 2004.

[101] Ji-Jer Huang, Kuo-Sheng Cheng, and Cheau-Jane Peng. Temperature-Compensated Bioimpedance System for Estimating Body Composition. *IEEE Engineering In Medicine and Biology*, 19:66 – 73, 2000.

[102] Gilbert B. Forbes. Methods for determining composition of the human body. *Pediatrics*, 29:477–494, 1962.

[103] Subrata Ghosh, Doris Meister, Stephen Cowen, W. James Hannan, and Anne Ferguson. Body composition at the bedside. *European Journal of Gastroenterology & Hepatology*, 9:783–788, 1997.

[104] K.-P. Herm. Methoden der Körperfettbestimmung. *Deutsche Zeitschrift für Sportmedizin*, 54:153–154, 2003.

[105] Earl C. Hoffer, Clifton K. Meador, and David C. Simpson. Correlation of whole-body impedance with total body water volume. *Journal of Applied Physiology*, 27:531–534, 1969.

[106] Tao Dai and Andy Adler. In Vivo Blood Characterization From Bioimpedance Spectroscopy of Blood Pooling. *IEEE Transactions on Instrumentation and Measurement*, 58:3831–3838, 2009.

[107] Blagoy P. Iliev, Gheorghe A. M. Pop, and Gerard C. M. Meijer. In-vivo Blood Characterization System. In *Proceedings of the 2006 Instrument and Measurement Technology Conference*, pages 1781–1785, 2006.

[108] Jocelyn Songer. Tissue Ischemia Monitoring Using Impedance Spectroscopy: Clinical Evaluation. Master Thesis, Worcester Polytechnic Institute, 2001.

Dieses Werk ist copyrightgeschützt und darf in keiner Form vervielfältigt werden noch an Dritte weitergegeben werden.
Es gilt nur für den persönlichen Gebrauch.

[109] Edwin D. Trautman and Ronald S. Newbower. A Practical Analysis of the Electrical Conductivity of Blood. *IEEE Transactions on Biomedical Engineering*, BME-30:141–154, 1983.

[110] Y. Uelgen and M. Sezdi. Electrical parameters of human blood. In *Proceedings of the 20th Annual International Conference of the IEEE Engineering in Medicine and Biology Society*, volume 6, pages 2983 –2986 vol.6, November 1998.

[111] Helen Berney and J.J. O'Riordan. Impedance Measurement Monitors Blood Coagulation. *Analog Dialogue*, 42:1–3, 2008.

[112] Kichul Cha, Elaine F. Brown, and Douuglas W. Wilmore. A new bioelectrical impedance method for measurement of the erythrocyte sedimentation rate. *Physiol. Meas.*, 15:499–508, 1994.

[113] Tyna A Hope and Siân EIles. Technology review: The use of electrical impedance scanning in the detection of breast cancer. *Breast Cancer Res*, 6:69–74, 2004.

[114] A. Malich, T. Boehm, M. Facius, M. Freesmexer, M. Fleck, R. Anderson, and W.A. Kaiser. Differentiation of Mammographically Suspicious Lesions: Evaluation of Breast Ultrasound, MRI Mammography and Electrical Impedance Scanning as Adjunctive Technologies in Breast Cancer Detection. *Clinical Radiology*, 56:278–283, 2001.

[115] Gonzalo Martin, Rocio Martin, Maria Jesus Brieva, and Luis Santamaríia. Electrical impedance scanning in breast cancer imaging: correlation with mammographic and histologic diagnosis. *Eur Radiol*, 12:1471–1478, 2002.

[116] Natasha Shah, Albert Cerussi, Charlotta Eker, Jenny Espinoza, John Butler, Joshua Fishkin, Rene Hornung, and Bruce Tromberg. Noninvasive functional optical spectroscopy of human breast tissue. *Proceedings of the National Academy of Sciences of the United States of America*, 98:4420–4425, 2001.

[117] F. Thiel, M. Helbig, U. Schwarz, C. Geyer, G. Rimkus, W. A. Kaiser, I. Hilger, M. Hein, J. Sachs, and F. Seifert. Implementation of ultra-wideband sensors for biomedical applications. *Frequenz*, 63:9–10, 2009.

[118] Y. Zou and Z. Guo. A review of electrical impedance techniques for breast cancer detection. *Medical Engineering & Physics*, 25:79–90, 2003.

[119] Javier Rosell, Josep Colominas, Pere Riu, Ramon Pallas-Areny, and John G. Webster. Skin Impedance From 1 Hz to 1 MHz. *IEEE Transactions on Biomedical Engineering*, 35:649–651, 1998.

[120] N Pavselj, M Mitar, FX Hart, and D Miklavèiè. Characterization of the mechanical behavior of human skin by means of impedance spectroscopy. In *Proceedings of the XIVth International Conference on Electrical Bioimpedance*, 2010.

[121] Ingrid Nicander, Lennart Emtestam, Peter Aberg, and Stig Ollmar. Twelve years evolution of skin as seen by electrical impedance. In *Proceedings of the XIVth International Conference on Electrical Bioimpedance*, 2010.

[122] E. T. McAdams, J. Jossinet, A. Lackermeier, and F. Risacher. Factors affecting electrode-gel-skin interface impedance in electrical impedance tomography. *Med. & Biol. Eng. & Comput.*, 34:397–408, 1996.

Dieses Werk ist copyrightgeschützt und darf in keiner Form vervielfältigt werden noch an Dritte weitergegeben werden.
Es gilt nur für den persönlichen Gebrauch.

[123] Gorm Krogh Johnsen, Ø.G. Martinsen, and S. Grimnes. Estimation of In Vivo Water Content of the Stratum Corneum from Electrical Measurements. *The Open Biomedical Engineering Journal*, 3:8–12, 2009.

[124] Gorm Krogh Johnsen, Anne Berit Haugsnes, Ørjan G. Martinsen, and Sverre Grimnes. A new approach for an estimation of the equilibrium stratum corneum water content. *Skin Research and Technology*, 16:142–145, 2010.

[125] G K Johnsen, Ø G Martinsen, and Sverre Grimnes. Sorption studies of human keratinized tissues. In *Proceedings of the XIVth International Conference on Electrical Bioimpedance*, 2010.

[126] A. Jabbari, B. Johnsen, S. Grimnes, and Ø.G. Martinsen. Simultaneous measurement of skin potential and conductance in electrodermal response monitoring. In *Proceedings of the XIVth International Conference on Electrical Bioimpedance*, 2010.

[127] C. OB́rien, A. J. Young, and M. N. Sawka. Bioelectrical Impedance to Estimate Changes in Hydration Status. *Int J Sports Med*, 23:361–366, 2002.

[128] J. C. Wells, N. J. Fuller, O. Dewit, M. S. Fewtrell, M. Elia, and T. J. Cole. Four-component model of body composition in children: density and hydration of fat-free mass and comparison with simpler models. *Am J Clin Nutr*, 69(5):904–912, May 1999.

[129] LT Ho, RF Kushner, DA Schoeller, R Gudivaka, and DM Spiegel. Bioimpedance analysis of total body water in hemodialysis patients. *Kidney International*, 46:1438–1442, 1994.

[130] B.A. Shanholtzer and S.M. Patterson. Fluid Hydration Status Assessment in Behavioral Medicine Research: Seven-Day Test-Retest Reliability. *Annals of Behavioral Medicine*, 24:133–135, 2002.

[131] M Kraemer, C Rode, and V Wizemann. Detection limit of methods to assess fluid status changes in dialysis patients. *Kidney International*, 69:1609–1620, 2006.

[132] Markus Osypka and Eberhard Gersing. Tissue impedance spectra and the appropriate frequencies for EIT. *Physiol. Meas.*, 16:A49–A55, 1995.

[133] M Nahvi and B S Hoyle. Wideband electrical impedance tomography. *Meas. Sci. Technol.*, 19:1–9, 2008.

[134] Amit K. Gupta. Respiration Rate Measurement Based on Impedance Pneumography. Texas Instruments Application Report, February 2011.

[135] Peter M. Edic, Gary J. Saulnier, and Jonathan C. Newell. A Real-Time Electrical Impedance Tomograph. *IEEE Transactions on Biomedical Engineering*, 42:849–859, 1995.

[136] Kevin R. Cooper, Matthew Smith, and Derek Johnson. Development and Demonstration of Measurement-Time Efficient Methods for Impedance Spectroscopy of Electrode and Sensor Arrays. *Sensors*, 8:1774–1796, 2008.

Dieses Werk ist copyrightgeschützt und darf in keiner Form vervielfältigt werden noch an Dritte weitergegeben werden.
Es gilt nur für den persönlichen Gebrauch.

[137] Martin Brühl and Martin Hanke-Bourgeois. Kann Mathematik der elektrischen Impedanztomographie zum Durchbruch verhelfen? *Forschungsmagazin der Johannes Gutenberg Universität Mainz*, 2001.

[138] V. E. Arpinar and B. M. Eyuboglu. Microcontroller controlled, multifrequency electrical impedance tomograph. In *Engineering in Medicine and Biology Society, 2001. Proceedings of the 23rd Annual International Conference of the IEEE*, pages 2289 – 2291, 2001.

[139] H. P. Schwan. Electrical Properties of Tissue and Cell Suspensions. *Advanced Phys. Med. Biol.*, 5:147–209, 1957.

[140] H. P. Schwan. Electrical characteristics of tissues: A survey. *Biophysik*, 1:198–202, 1963.

[141] S. Grimnes and O.G. Martinsen. Cole electrical impedance model - a critique and an alternative. *IEEE Transactions on Biomedical Engineering*, 52:132–135, 2005.

[142] U. Pliquett. Electricity and biology. In *Electronics Conference, 2008. BEC 2008. 11th International Biennial Baltic*, pages 11 –20, 6-8 2008.

[143] Claudia H. Riedel. *Planare induktive Impedanzmessverfahren in der Medizintechnik.* PhD thesis, TU Karlsruhe, 2004.

[144] Sun-Young Lee, Heon-Jeong Lee, Yong-Ku Kim, Seung-Hyun Kim, Leen Kim, Min Soo Lee, Sook-Haeng Joe, In-Kwa Jung, Kwang-Yoon Suh, and Hyung-Kyu Kim. Neurocognitive function and quality of life in relation to hematocrit levels in chronic hemodialysis patients. *Journal of Psychosomatic Research*, 57:5–10, 2004.

[145] R. Klinke, H.-C. Pape, A. Kurtz, and S. Silbernagel. *Physiologie.* Thieme, Stuttgart, ISBN: 3137960061, 2009.

[146] Joel M. Bartfield, Debra Robinson, and John Lekas. Accuracy of Microcentrifuged Hematocrits in the Emergency Department. *The Journal of Emergency Medicine*, 11:673–676, 1993.

[147] J. Walters and P. Garrity. Performance Evaluation of the Sysmex XE-2100 Hematology Analyzer. *Laboratory Hematology*, 6:83–92, 2000.

[148] D. Schneditz, H. Pogglitsch, J. Horina, and U. Binswanger. A blood protein monitor for the continuous measurement of blood volume changes during hemodialysis. *Kidney International*, 38:342–346, 1990.

[149] D. Schneditz and N. Levin. Non-invasive Blood Volume Monitoring During Hemodialysis: Technical and Physiological Aspects. *Seminars in Dialysis*, 10:166–169, 1997.

[150] D. Schneditz and N. Levin. Non-invasive Blood Volume Monitoring During Hemodialysis. *Nephrol Dial Transplant*, 13:2098–2103, 1998.

[151] Shiori Oshima and Yoshiyuki Sankai. Simulator with Photon and Arbitrarily Arranged RBC for Hematocrit Estimation. In *Proceedings of the 29th Annual International Conference of the IEEE EMBS*, pages 3623–3628, 2007.

Dieses Werk ist copyrightgeschützt und darf in keiner Form vervielfältigt werden noch an Dritte weitergegeben werden.
Es gilt nur für den persönlichen Gebrauch.

[152] Shiori Oshima and Yoshiyuki Sankai. Optical Measurement of Blood Hematocrit on Medical Tubing with Dual Wavelength and Detector Model. In *Proceedimgs of the 31st Annual International Conference of the IEEE EMBS*, 2009.

[153] N. Kordas, Y. Manoli, W. Mokwa, and M. Rospert. A CMOS-Compatible Monolithic Conductivity Sensor with Integrated Electrodes. *Proceedings of the International Conference on Solid-State Sensors, Actuators and Microsystems*, pages 466–469, 1993.

[154] Ernesto F. Treo, Carmelo J. Felice, Mónica C. Tirado, Max E. Valentinuzzi, and Daniel O. Cervantes. Comparative Analysis of Hematocrit Measurements by Dielectric and Impedance Techniques. *IEEE Trans. Biomed. Eng.*, 52:549–552, 2005.

[155] E. F. Treo, D. O. Cervantes, C. J. Felice, M. Tirado, and M. E. Valentinuzzi. Hematocrit Measurement by Dielectric Spectroscopy. In *Proceedings of the Second Joint EMBS BMES Conference*, pages 1750–1751, 2002.

[156] Anca Roxana Varlan, Paul Jacobs, and Willy Sansen. Novel Design of a Planar Conductometric Hematocrit Sensor. In *Proceedings of the 8th International Conference on Solid-State Sensors and Actuators*, pages 475–478, 1995.

[157] Yekta Uelgen and Manâ Sezdi. Hematocrit Dependence of the Cole-Cole Parameters of Human Blood. In *Proceedings of the 2nd International Biomedical Engineering Days*, pages 71–74, 1998.

[158] Akikazu Sakudo, Yukiko Hakariya Kato, Hirohiko Kuratsune, and Kazuyoshi Ikuta. Non-invasive prediction of hematocrit levels by portable visible and near-infrared spectrophotometer. *Clinica Chimica Acta*, 408:123–127, 2009.

[159] Masamichi Nogawa, Shinobu Tanaka, and Ken ichi Yamakoshi. Development of an optical arterial hematocrit measurement method: pulse hematometry. In *Proceedings of the 2005 IEEE Engineering in Medicine and Biology*, 2005.

[160] Ken-Ichi Yamakoshi, Hideaki Shimazu, Tatsuo Togawa, Masakazu Fukuoka, and Hiroshi Ito. Noninvasive Measurement of Hematocrit by Electrical Admittance Plethysmography Technique. *IEEE Transactions on Biomedical Engineering*, 27:156–161, 1980.

[161] Wojciech Secomski, Andrzej Nowicki, Robert Olszewski, Jerzy Adamus, Paolo Fidanzati, and Piero Tortoli. Doppler Multigate Measurements of Ultrasonic Scattering, Attenuation and Hematocrit of Blood in the Human Artery. *IEEE Ultrasonics Symposium*, 2005.

[162] W. Secomski, A. Nowicki, F. Guidi, P. Tortoli, and P.A. Lewin. Non-invasive measurement of blood hematocrit in artery. *Bulletin of the Polish Academy of Sciences, Technical Sciences*, 53(3), 2005.

[163] D. Meeker. FEMM4.2. *www.femm.info, 10.02.2013.*

[164] M. Vosseler, M. Jugl, and R. Zengerle. A smart interface for reliable intradermal injection and infusion of high and low viscosity solutions. *Pharm. Res.*, 28:647 – 661, 2011.

Dieses Werk ist copyrightgeschützt und darf in keiner Form vervielfältigt werden noch an Dritte weitergegeben werden.
Es gilt nur für den persönlichen Gebrauch.

[165] Y. Thakur, J. S. Bax, D. W. Holdsworth, , and M. Drangova. Design and performance evaluation of a remote catheter navigation system. *IEEE Trans. Biomed. Eng.*, 56:1901 – 1908, 2009.

[166] H.Saito and T.Togawa. Detection of puncturing vessel wall for automatic blood sampling. In *Proceedings of First Joint EMBS BMES Conf.*, 1999.

[167] R. Alterovitz, J. Pouliot, R. Taschereau, I. Hsu, and K. Goldberg. Simulating needle insertion and radioactive seed implantation for prostate brachytherapy. *Stud. Health Tech. Informat.*, 94:19–25, 2003.

[168] R. Viard, N. Betrouni, J. Rousseau, S. Mordon, O. Ernst, and S. Maouche. Needle positioning in interventional MRI procedure: Real time optical localisation and accordance with the roadmap. In *Proc. 29th Annu.IEEE Int. Conf. Eng. Med. Biol. Soc. (EMBS)*, 2007.

[169] G. Fichtinger, A. Deguet, K. Masamune, E. Balogh, G. S. Fischer, H.Mathieu, R. H. Taylor, S. J. Zinreich, and L. M. Fayad. Image overlay guidance for needle insertion in CT scanner. *IEEE Trans. Biomed. Eng.*, 52:1415 – 1424, 2005.

[170] B. Bascle, N. Navab, M. Loser, B. Geiger, and R. Taylor. Needle placement under X-ray fluoroscopy using perspective invariants. In *Proc. IEEE Workshop Math. Methods Biomed. Image Anal.*, 2000.

[171] R. S. Singh, S. Natarajan, M. Lee, A. E. Dann, B. P. Cox, D. B. Bennett, E. R. Brown, H. Lee, W. S. Grundfest, and M. O. Culjat. Development of an ultrasound imaging system for needle guidance. *Proc. IEEE Int. Ultrason. Symp. (IUS)*, pages 1852 – 1855, 2009.

[172] S.Cochran, G.A.Corner, K.J.Kirk, D.I.A.Lines, and M.J.Watson. P5C5 design and validation of an ultrasound array optimised for epidural needle guidance. In *Proc. IEEE Ultrason. Symp.*, 2007.

[173] A. Haddadi, O. Goksel, S. E. Salcudean, and K. Hashtrudi-Zaad. On the controllability of dynamic model-based needle insertion in soft tissue. In *Proc. 2010 IEEE Annu. Int. Conf. Eng. Med. Biol. Soc. (EMBC)*, 2011.

[174] A.Majewicz, T.R.Wedlick, K.B.Reed, and A.M.Okamura. Evaluation of robotic needle steering in ex vivo tissue. In *Proc. 2010 IEEE Int. Conf. Robot. Autom. (ICRA)*, 2010.

[175] W. Yang, A. Bonvilain, T. Alonso, A. Moreau Gaudry, and S. Basrour. Modeling and characterization of an instrumented medical needle insight of new microsensor design for its insertion guidance. In *Proceedings of the 2010 IEEE EMBC conference*, 2010.

[176] H. Kalvoy, O. G. Martinsen, and S. Grimnes. Determination of tissue type surrounding a needle tip by electrical bioimpedance. In *Proceedings of the 30th IEEE EMBC conference*, 2008.

[177] Havard Kalvøy, Lars Frich, Sverre Grimnes, Ørjan G Martinsen, Per Kristian Hol, and Audun Stubhaug. Impedance-based tissue discrimination for needle guidance. *Physiol. Meas.*, 30:129–140, 2009.

Dieses Werk ist copyrightgeschützt und darf in keiner Form vervielfältigt werden noch an Dritte weitergegeben werden.
Es gilt nur für den persönlichen Gebrauch.

[178] S. Schlaeger. A fast TDR-inversion technique for the reconstruction of spatial soil moisture content. *Hydrol. Earth Sys. Sci. Discuss.*, 2:971 – 1009, 2005.

[179] Scott B. Jones, Jon M. Wraith, and Dani Or. Time domain reflectometry measurement principles and applications. *Hydrological Processes*, 16:141–153, 2002.

[180] A Scheuermann, C Hübner, H Wienbroer, D Rebstock, and G Huber. Fast time domain rflectometry (TDR) measurement approach for investigating the liquefaction of soils. *Measurement Science and Technology*, 21:1–11, 2010.

[181] C. Huebner. *Entwicklung hochfrequenter Messverfahren zur Boden- und Schneefeuchtebestimmung.* Dissertation, Universität Fridericiana zu Karlsruhe, 1999.

[182] R. Becker, A. Brandelik, C. Huebner, C. Schaedel, A. Scheuermann, and S. Schlaeger. Soil and Snow moisture measurement system with subsurface transmission lines for remote sensing and environmental applications. In *Prooceedings of the Open Symposium on Propagation and Remote Sensing, Garmisch Partenkirchen*, 2002.

[183] M. Malicki and J. Kotlinski. Dielectric Determination of Moisture of Wood using Time Domain Reflectometry. *Int. Agrophysics*, 12:217–220, 1998.

[184] Campbell Scientific. Website accessed on February 12th, 2013, http://www.campbellsci.com/soil-science.

[185] Donghwan Lee, Jinho Sung, and Jaehong Park. A 16ps-resolution Random Equivalent Sampling circuit for TDR utilizing a Vernier time delay generation. In *Nuclear Science Symposium Conference Record, 2003 IEEE*, volume 2, pages 1219–1223, 2003.

[186] Shi Xudong, Zheng Jianzhong, Jing Tao, and Wang Liwen. Design of Aircraft Cable Intelligent Fault Diagnosis and Location Sytem Based on Time Domain Reflection. In *Proceedings of the 8^{th} World Congress on Intelligent Control and Automation July 6-9 2010, Jinan, China*, pages 5856–5860, 2010.

[187] Miguel Carlo L. Purisima, Joel S. Marciano Jr., Roberto D. De Joya Jr., Paula P. Mogatas, and Carmela A. Salazar. FPGA Implementation of a Time Domain Reflectometry (TDR) System for Slope Monitoring Applications. In *Proceedings of TENCON 2010*, pages 1198–1202, 2010.

[188] Catalin Negrea and Marius Rangu. Sequential Sampling Time Domain Reflectometer. In *Proceedings of SIlTME2009 - 15^{th} International Symposium for Design and Technology of Electronics Packages*, pages 367–371, 2009.

[189] Ove Schimmer, B. Oberheitmann, F. Baumann, and R. Knoechel. Instantaneous Distinction between double and single frozen Fish using a new handheld Time Domain Reflectometer. In *ISEMA 2007 Conference Proceedings*, 2007.

[190] Ove Schimmer. *Ein Ultra-Breitband Messverfahren zur Bestimmung ausgewaehlter Materialeigenschaften von Naturstoffen.* Dissertation, University of Kiel, 2006.

[191] T. Sokoll and O. Schimmer. A High-Precision Time Domain Reflectometer with 75ps Rise-Time. In *ISEMA2011 Conference Proceedings*, 2011.

Dieses Werk ist copyrightgeschützt und darf in keiner Form vervielfältigt werden noch an Dritte weitergegeben werden.
Es gilt nur für den persönlichen Gebrauch.

[192] A. Scheuermann, C. Huebner, S. Schlaeger, N. Wagner, R. Becker, and A. Bieberstein. Spatial time domain reflectometry and its application for the measurement of water content distributions along flat ribbon cables in a full-scale levee model. *Water Resour. Res.*, 45:W00D24, 2009.

[193] A. Cataldo and E. De Benedetto. Broadband Reflectometry for Diagnostics and Monitoring Applications. *IEEE Sensors Journal*, 11:451–459, 2011.

[194] D. Trebbels, M. Jugl, and R. Zengerle. Real-time cannula navigation in biological tissue with high temporal and spatial resolution based on impedance spectroscopy. In *Proceedings of the IEEE EMBC conference*, 2010.

[195] D. Trebbels, F. Fellhauer, M. Jugl, G.Haimerl, M. Min, and R. Zengerle. Online Tissue Discrimination for Transcutaneous Needle Guidance Applications Using Broadband Impedance Spectroscopy. *IEEE Trans. Biomed. Eng.*, 59, 2012.

[196] G. S. Popkirov. Fast Time-Resolved Electrochemical Impedance Spectroscopy For Investigations Under Nonstationary Conditions. *Electrochimica Acta*, 41:1023–1027, 1996.

Dieses Werk ist copyrightgeschützt und darf in keiner Form vervielfältigt werden noch an Dritte weitergegeben werden.
Es gilt nur für den persönlichen Gebrauch.

Dieses Werk ist copyrightgeschützt und darf in keiner Form vervielfältigt werden noch an Dritte weitergegeben werden.
Es gilt nur für den persönlichen Gebrauch.

Dieses Werk ist copyrightgeschützt und darf in keiner Form vervielfältigt werden noch an Dritte weitergegeben werden.
Es gilt nur für den persönlichen Gebrauch.

Dieses Werk ist copyrightgeschützt und darf in keiner Form vervielfältigt werden noch an Dritte weitergegeben werden.
Es gilt nur für den persönlichen Gebrauch.